5-15-2015

Estimation of Earthquake Input Energy, Hysteretic Energy and its Distribution in MDOF Structures

Mebrahtom Gebrekirstos Mezgebo
Syracuse University

Follow this and additional works at: https://surface.syr.edu/etd

Part of the Engineering Commons

ABSTRACT

Current seismic codes for building design often utilize a force or a displacement-based approach in their implementation. In a force-based approach, a structure is designed to ensure it possesses sufficient strength to resist the maximum forces imparted to it by an earthquake.   In a displacement-based approach, a target displacement is calculated or identified and the structure is proportioned to achieve a specified performance level, defined by strain or drift limits, under a specified level of seismic intensity.   A third approach, which has gained momentum in the earthquake engineering community, is the energy-based approach. In this approach, a design is considered satisfactory if the capacity of a structure to absorb or dissipate energy exceeds its energy demand from an earthquake.   In the present research, a new energy-based approach is proposed in which velocity index (VI), obtained as the product of two ground motion indexes - peak ground velocity (PGV) and cumulative absolute velocity (CAV), is used to normalize input energy spectra.   The use of VI as a normalization factor not only allows for the creation of dimensionless input energy spectra, but can result in smaller values of coefficients of variation when compared to other normalization factors currently being used.

Earthquake input energy spectra for four site classes (Site Class B, C, D and E as per IBC 2012 soil classifications) and four hysteretic models (bilinear plastic, stiffness degradation, bilinear flag and bilinear slip) are developed for five ductility levels (μ=1, 2, 3, 4, 5) using ground motion ensembles of 38, 42, 38 and 26 recorded at site classes B, C, D and E, respectively. For purpose of design, the normalized input energy spectra are divided into three regions – short period, intermediate period and long period – that are consistent with the customary design response spectra contained in various seismic codes and standards. A close examination of these spectra

has shown that regardless of the hysteretic models used, the normalized seismic input energy decreases as ductility increases, and increases as the soil gets softer. For each site class, empirical ductility dependent input energy expressions are developed, and hysteretic to input energy ratio relationships are formulated. The proposed design input energy spectra are validated using six major earthquakes and are found to reasonably match the spectra generated using time history analysis.

Since the input energy spectra are developed for single-degree-of-freedom (SDOF) systems, to facilitate the implementation of the proposed method in the design of multi-degree-of-freedom (MDOF) systems, simple expressions that relate earthquake input and hysteretic energies for MDOF system to its equivalent single-degree-of-freedom (ESDOF) systems are formulated. The energy relationships are verified using four (a three story, a five story, a seven story and a nine story) frames each subjected to six earthquakes wherein a very good estimate for the three- and five- story and a reasonably acceptable estimate for the seven-, and nine-story frames were obtained. A new method for distributing hysteretic energy over the height of moment resisting frames is also proposed. The new distribution scheme was used in determining the energy demand (hysteretic energy) component of an energy-based seismic design (EBSD). EBSD is a story-wise optimization design procedure developed using the relationship that exists between energy dissipating capacity and plastic analysis/design of structures. Finally, the entire process of determining the input energy for ESDOF systems to the distribution of hysteretic energy over the height of MDOF structures using the proposed EBSD design procedure is demonstrated using two design examples: a three-story one-bay frame and a five-story two-bay frame.

ESTIMATION OF EARTHQUAKE INPUT ENERGY, HYSTERETIC

ENERGY AND ITS DISTRIBUTION IN MDOF STRUCTURES

by

Mebrahtom Gebrekirstos Mezgebo

B. Sc , Addis Ababa University, Ethiopia, 2000

M. Tech, Indian Institute of Technology Bombay, India, 2004

DISSERTATION

Submitted in partial fulfillment of the requirement for the degree of

Doctor of Philosophy in Civil Engineering

Syracuse University

Syracuse, New York

May 2015

ACKNOWLEDGMENTS

I express my sincere gratitude towards my advisor Professor Eric M. Lui whose enthusiasm in guiding me throughout the course of the study never faltered. His brilliant ideas and helpful suggestions were invaluable. His extreme patience with me in this protracted journey and his help in arranging a remote access that enabled me to do part of my research remotely was much felt and appreciated. I consider myself incredibly lucky to have had him as my advisor.

I am grateful to Professor D. Negussey for opening my eyes to the opportunities at Syracuse University and his instrumental help in my admission. I would like also to thank and recognize my qualifying, and/ or dissertation committee members: Professors R. Aboutaha, S. Bhatia, S. Clemence, A. Levy, V. Murthy, D. Negussey and R. Perkins. I am grateful for their time and their inputs for the dissertation work are appreciated. I am grateful to Ms. E. Buchanan, who was very supportive and never complained whenever I needed her help.

My special thanks to Atsede Negussey who helped me to stand on my feet during my first year at SU. Many thanks to the Ethiopian graduate students at SU who were my family away from home. I would like also to thank my fellow doctoral students and officemates for the wonderful times we had together.

Last but not least my endless gratitude to my father and mother who showered and continue to awash me with endless blessings and keep me in their prayers all the time. My wife Hiwot and my Sisters, your daily support and encouragement have borne a fruit.

TABLE OF CONTENTS

LIST OF TABLES

LIST OF FIGURES

To my parents

Gebrekirstos Mezgebo and Lemlem Gebremedhin

To my wife

Hiwot Kidanemariam

To my sisters

Tirfe, Tsega, Mulu, Tsigewoini, Senait and Birhan

1. INTRODUCTION

1.1 Background

Earthquake is the result of ground shaking caused by movement of tectonic plates. The severity

of earthquakes can be expressed in terms of a magnitude (the Richter's scale, surface-wave

magnitude, body-wave magnitude, moment magnitude) or an intensity (the modified Mercalli

scale). Both are related to the amount of energy released by the earthquake. This energy, if not

properly dissipated, could cause severe damage to or even destruction of natural or man-made

structures. The damage could result in both social and economic mishaps. Ground failures such

as earth flows, landslides and liquefaction could be easily triggered by earthquakes. Engineered

structures such as buildings, bridges, highways and dams are not exceptions; they can be

damaged or brought to failure during large earthquakes. In cases where there are no early

warning systems or where earthquake magnitudes cannot be adequately predicted, structural and

ground failures could result in substantial fatalities. Table 1.1 shown below lists the largest and

deadliest earthquakes since 2000 and the number of fatalities they inflicted as documented by the

United Stated Geological Survey (USGS). However, when structures are designed against

earthquakes, the property damage and related fatalities could be substantially reduced.

The unpredictability of the nature, occurrences and magnitudes of earthquakes makes it rather

difficult to design structures to be completely earthquake proof. Practicing engineers and

researchers agree that when it comes to earthquake design, "one needs to design the structure as

per the best practices available and pray that a monster earthquake wouldn't strike".   Currently,

seismic design procedures stipulated in earthquake design codes such as ASCE and IBC are

widely used by practicing engineers to design structures that can resist earthquake forces with an

acceptable damage (referred to as damage levels in FEMA 356). These procedures are also called performance base design procedures. Research is being continuously conducted in order to develop a more sound seismic design procedure that takes into account the energy imparted by an earthquake onto a structure. It is in this area that the present study attempts to make a contribution.

Table 1.1 Largest and Deadliest Earthquakes Since 2000

Year	Date	Magnitude	Fatalities	Region
2014	1-April	8.2	6	Iquique, Chile
2013	24-Sept	7.7	825	Barochistan, Pakistan
2012	6-Feb	6.7	113	Negros-Cebu region, Philippines
2011	11-Mar	9	20896	Near the East Coast of Honshu, Japan
2010	27-Feb	8.8	507	Offshore Maule, Chile
2010	12-Jan	7	316000	Haiti
2009	29-Sept	8.1	192	Samoa Islands region
2009	30-Sept	7.5	1117	Southern Sumatra, Indonesia
2008	12-May	7.9	87587	Eastern Sichuan, China
2007	15-Aug	8	514	Near the Coast of Central Peru
2006	26-May	6.3	5749	Java, Indonesia
2005	8-Oct	7.6	80361	Pakistan
2005	28-Mar	8.6	1313	Northern Sumatra, Indonesia
2004	26-Dec	9.1	227898	Off West Coast of Northern Sumatra
2003	26-Dec	6.6	31000	Southeastern Iran
2002	25-Mar	6.1	1000	Hindu Kush Region, Afghanistan
2001	26-Jan	7.7	20023	India
2000	4-Jun	7.9	103	Southern Sumatera, Indonesia

Source (http://earthquake.usgs.gov/earthquakes/eqarchives/year/byyear.php)

1.2 Commonly Used Seismic Design Procedures

Albeit some limitations and uncertainties, performance-based design procedures present the means to designing structures to resist seismic forces with an acceptable damage. The two most widely used conventional performance-based design procedures are the forced–based design and displacement-based design methods. They are both fundamentally nonlinear static procedures (NSPs).

In the force-based design (FBD) method, a design seismic force for a target structure is specified on the basis of an elastic acceleration response spectrum. This seismic design force is called the design base shear. To account for the inelasticity (ductility effect), the design force of the target structure obtained from the elastic acceleration response spectrum is divided by a force-reduction factor. The structure is then designed for the reduced force, and the displacement can be checked so that the code-specified serviceability limits are met. Regardless, the FBD method is not without limitations and drawbacks. Smith and Tso *(2002)* through their study on a large class of reinforced concrete members such as piers, flexural walls and ductile moment resisting fames claimed that force-based design procedure is inconsistent. They argued the assumption that the stiffness of the lateral force resisting elements is essentially independent of their strength is inconsistent as strength and stiffness are usually related. Moreover, the problems associated with this method, as pointed out by Priestley *et al. (2007)* are:

- The elastic stiffness is not known at the start of the design process, and very approximate values have to be used.
- Foundation effects are generally ignored in force-based design, and are difficult to incorporate in the design process as they affect both the elastic period, and displacement ductility demand.

- Even though the design force is calculated from an allowable displacement ductility factor, it does not properly address the force-displacement relationship of the structure.

The displacement-based design (DBD) method, which is generally accepted to be a better alternative to the FBD method, takes displacement as a design parameter as opposed to using base shear as in the case for FBD. As a result, the important task in a displacement-based design approach is to estimate the maximum displacement demand in a structure with reasonable simplicity and accuracy as a function of its local mechanical characteristics, such as member strain and deformation limits. FEMA 440's *(2005)* displacement-based Coefficient Method is one of the currently available displacement-based seismic design methods. The Coefficient Method modifies the linear elastic response of an equivalent single degree of freedom (SDOF) system by multiplying it by a series of coefficients to estimate a global displacement, commonly termed as the target displacement. This method uses an idealized force-displacement curve (pushover curve), which is a plot (for a given damping coefficient) of base shear versus roof displacement developed for a multiple degree of freedom (MDOF) structure. A corresponding spectral value for an effective period, T_e, of an equivalent SDOF system is then obtained from an elastic response spectrum corresponding to a design ground motion. The target displacement is then calculated using an empirical formula that involves modifying coefficients and the spectral value for the corresponding effective period. The effective period is obtained from an initial period of the structure and accounts for the loss of stiffness in the transition from elastic to inelastic behavior.

The accuracy of the DBD method is highly dependent on how closely the equivalent SDOF system and its corresponding MDOF system are related through the idealized pushover curve.

Recently, researchers have identified glitches in the use of roof displacement-based pushover curve. Enrique-Hernandez Montes *et al. (2004)* noted that the use of roof displacement in generating the capacity curve can be misleading because the capacity curve so obtained sometimes tends to show the structure as a source of energy rather than absorbing energy. They suggested that an energy-based pushover analysis be used instead whereby the lateral force is plotted against a displacement which is a function of energy. Manoukas *et al. (2011)* also developed an energy-based pushover procedure for estimating structural performance under strong earthquakes. They showed through numerical examples that their procedure provides better results compared to those produced by other similar procedures.

In addition, neither the FBD method that uses base shear as a design parameter nor the DBD method that uses displacement as a design parameter can directly consider the cumulative damage effect that result from numerous inelastic cycles of the ground motion due to deterioration of the structure's hysteretic behavior. Moreover, the effect of earthquakes on structures should be interpreted not just as a force or displacement quantity, but as a product of both, i.e., in terms of input energy. This is the underlying concept for the inception of the energy-based seismic design (EBSD) method. EBSD is believed by many to be the next generation of seismic design methods.

1.3 Energy – Based Seismic Design (EBSD) and its Current Status

The equation of motion for a single-degree-of-freedom (SDOF) inelastic system subjected to a ground motion is given by

$$m\ddot{u} + c\dot{u} + f_s = -m\ddot{u}_g \qquad (1.1)$$

where m= mass of the system; c= damping coefficient; f_s = restoring force; $\ddot{u}_g$= ground acceleration, and $\ddot{u}, \dot{u}, u$ are the relative acceleration, velocity, and displacement of the system with respect to the ground, respectively.

According to Uang and Bertero *(1990)* the energy balance equation for an SDOF structure based on relative motion can be written as

$$\int_0^t m\ddot{u}\,\dot{u}\,dt + \int_0^t c\dot{u}\,\dot{u}\,dt + \int_0^t f_s\,\dot{u}\,dt = -\int_0^t m\ddot{u}_g\,\dot{u}\,dt \qquad (1.2)$$

Equation (1.2) can be rewritten as

$$E_{kr} + E_d + E_a = IE \qquad (1.3)$$

where

$$E_{kr} = relative\,kinetic\,energy = \int_0^t m\ddot{u}\,\dot{u}\,dt = \frac{1}{2}m\dot{u}^2$$

$$E_d = damping\,energy = \int_0^t c\dot{u}^2 dt$$

$$E_a = absorbed\,energy = \int_0^t f_s\,\dot{u}\,dt$$

$$IE = relative\,input\,energy = -\int_0^t m\ddot{u}_g\dot{u}\,dt$$

E_{kr} in Equation (1.3) vanishes when the structure ceases to vibrate. E_d is related to the inherent viscous damping of the structure and/or by any supplemental damping mechanism provided by the presence of any damping devices in the system. E_a consists of two different types of energy: elastic strain energy, E_s, and hysteretic energy, HE. Elastic strain energy does not cause permanent damage to the structure. As its name indicates it occurs as a result of elastic deformation of the structure and becomes zero when vibration of the structures stops. Hysteretic energy is related to the inelastic deformation the structure undergoes during the ground motion. Unless otherwise dissipated through some mechanism, hysteretic energy could inflict permanent damage to the structure.

The philosophy of EBSD thus primarily focuses on ensuring that structures are designed to meet the energy demand of an earthquake, i.e., the hysteretic energy. In EBSD, if the hysteretic energy demand of a structure due to an earthquake can be dissipated through a controlled inelastic deformation of the structure, the design is said to be satisfactory. Therefore, hysteretic energy is considered to be the main design parameter in energy-based seismic design. Also, EBSD is believed to be a rational design approach for seismic design because it takes into account the accumulated earthquake induced damage in the design procedure. Conversely, the viability of EBSD depends on the accuracy in developing inelastic design spectra for SDOF as well as the virtue of the equations that relate the input energy and hysteretic energy. Moreover, for MDOF structures, the way the hysteretic energy is distributed over the different levels of the structure is equally important to the accuracy in the estimation of the input and hysteretic energies.

In summary, EBSD attempts to ensure that the seismic energy demand is less than or at most equal to the capacity of the structure to dissipate it. The seismic energy demand is the total

hysteretic energy whereas the capacity of the structure is the allowable plastic energy of the structure. In lieu of any supplementary damping devices, the plastic energy is the amount of energy consumed in forming plastic hinges in the structure.

1.4 Problem Statement and Objectives of the Research

The hysteretic energy and input energy expressions for inelastic SDOF proposed so far by different researchers mostly targeted structures with an elasto-plastic or a bilinear hysteretic model. However, structures do exhibit different kinds of hysteretic behavior, among which are the Bilinear Plastic, Stiffness Degradation, Bilinear flag and Bilinear Slip models. The description of these four different hysteretic models is presented below.

Bilinear plastic (Figure 1.1 (a)), which is the same as the elasto-plastic hysteretic model, is one of the most commonly used hysteretic models to describe the cyclic behavior of reinforced concrete and steel frame structures that are not expected to undergo strength or stiffness degradation during a seismic event. Figure 1.1(b) shows the stiffness degradation (modified Clough stiffness degradation) model, which is more appropriate to model the structural behavior that exhibits stiffness degradation and has less energy dissipation capacity than its elasto-plastic counterpart.

Self-centering isolation systems and special bracing systems are used in the design of new or the rehabilitation of existing structural systems against earthquake induced actions. These systems, such as slender unreinforced masonry shear walls and precast post-tensioned reinforced concrete elements, have little hysteretic energy dissipation capacity. Their cyclic behavior can neither be accurately modeled using the bilinear plastic model (which has the highest energy dissipation capacity among the hysteretic models) nor the bilinear elastic (theoretically, zero energy

dissipation capacity) model. The bilinear flag (Figure 1.1(c)), which combines the bilinear elastic and the bilinear plastic models, is more appropriate to capture the cyclic behavior of such systems.
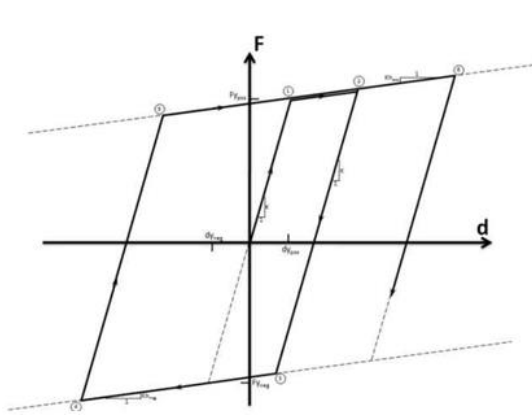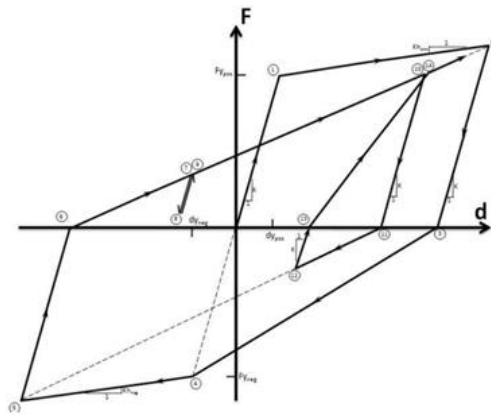
a) Bilinear –Plastic   b) Modified Clough Stiffness Degradation
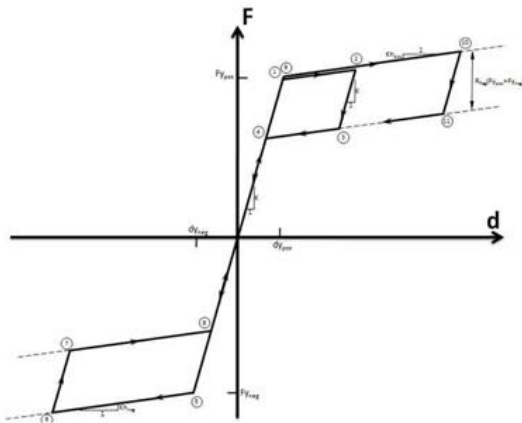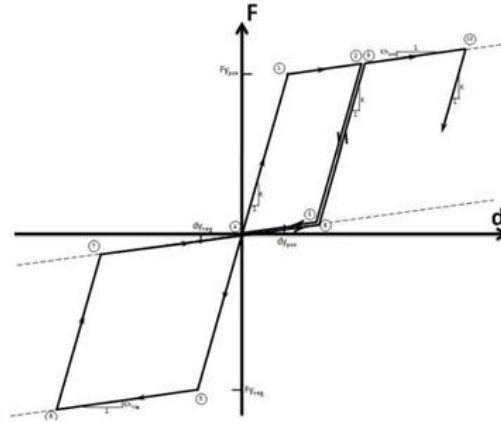
c) Bilinear Flag   d) Bilinear Slip

Figure 1.1 Hysteretic Models (source http://www.eqsols.com)

9

Low-rise steel frame buildings, wood, reinforced structures and other composite structures that are mainly subjected to shearing action may suffer from bond failure or slip. For such structures their hysteretic behavior can be captured using the bilinear slip hysteretic model (Figure 1.1(d)).

Thus far, research performed on determining hysteretic energy for multi-degree-of-freedom (MDOF) structures is quite limited and the outcome of this research is not conclusive and exhaustive. Hysteretic energy for MDOF structures can be obtained from their equivalent SDOF (ESDOF) systems. Hysteretic energy obtained using the ESDOF are accurate enough for cases where the seismic response of the MDOF is highly dominated by the first mode. However, for structures in which the seismic response is influenced by higher modes, hysteretic energy obtained using the ESDOF system approach has shown errors. These errors can be minimized if multi-mode methods are adopted, in which the total hysteretic energy for the MDOF system is obtained by summing up the energy contribution of a series of ESDOF systems representing each mode and adjusted by a corresponding modal participation factor.

It is important to highlight that by using energy-based seismic design, the overall objective is to design structures so that the energy-dissipation capacity (plastic deformation energy) is greater than the energy-dissipation demand (hysteretic energy). Therefore, this research aims to make contribution to the ongoing research on developing a sound energy-based seismic design procedure for structures by addressing the following two objectives.

Objective 1:

As stated above, structures do exhibit different hysteretic behavior apart from the relatively simple and more researched elasto-plastic hysteretic model. Therefore, the first objective of this research would be to propose expressions for hysteretic and input energies of inelastic SDOF systems for different hysteretic models and compare their accuracy with the existing formulas.

Objective 2:

As has pointed out by Ye *et al. (2009)*, very little research has been performed on determining hysteretic energy and its distribution in MDOFs systems, and so more widely applicable and simple methods are needed. Thus, the second objective of this research is to propose improved expressions for determining hysteretic energy for MDOF structures and its distribution.

The above objectives are achieved through numerical studies and the results are presented in this thesis as follows: A literature review of research on input and hysteretic energies for SDOF systems is presented in Chapter 2. This is followed by a discussion of the proposed input energy spectra and hysteretic energy spectra for SDOF systems in Chapter 3 and Chapter 4, respectively. Extending the concept to MDOF systems, the estimation of the input energy for MDOF systems is presented in Chapter 5, and a proposed procedure for distributing this energy to multi-story frames is given in Chapter 6. The last chapter summarizes the essence of the present findings with conclusions and some suggestions for future research.

2. INPUT AND HYSTERETIC ENERGIES OF SDOF SYSTEMS: LITERATURE REVIEW

2.1 Energy Spectra for an Inelastic SDOF System

Equation 1.3 is a statement of energy balance for an SDOF system. Alternatively, the energy balance can be expressed in terms of the total displacement of the SDOF system and in this case the resulting input energy is called an absolute/total input energy, IE_a, and is given by Equation 2.1.

$$IE_a = -\int_0^t m\, \ddot{u}_g \dot{u}_t \, dt \tag{2.1}$$

where $\dot{u}_t$ is the total velocity of the system; m, $\ddot{u}_g$ are as defined before.

Bruneau and Wang *(1996)* in their study on closed-form energy expression for an SDOF system subjected to rectangular and harmonic base excitations observed that there exists a close relationship between relative input energy and relative displacement. As a result, they recommended that a relative input energy formulation is preferred over an absolute formulation for assessing earthquake damage on structures. Henceforth, the relative input energy, *IE*, is used to quantify the energy content of an earthquake and is simply referred to as the input energy in this study.

Before Uang and Bertero *(1990)* introduced the energy balance concept, a number of researchers have recommended different empirical formulae to estimate earthquake input energy. For instance, Housner *(1956)* computed the input energy per unit mass of an SDOF system as follows

$$\frac{IE}{m} = \tfrac{1}{2}(PSV)^2 \tag{2.2}$$

where m is mass of the structure and PSV is the pseudo-spectral velocity. He was also the first to use an energy approach for seismic design. He used it in the design of an elevated water tank to resist a 1940 S00E component El Centro accelerogram, and concluded that his equation is valid for both elastic and inelastic SDOF systems.

Akiyama *(1985),* using Japanese design earthquakes, proposed the input energy per unit mass of an elastic SDOF structure due to a given earthquake as

$$\frac{IE}{m} = \frac{1}{2}(V_e)^2 \tag{2.3}$$

where the value of the equivalent velocity, V_e (cm/s), is given by

$$\begin{aligned} V_e &= 250 T_n & for\ T_n \leq T_g \\ V_e &= 250 T_g & for\ T_n \geq T_g \end{aligned} \tag{2.4}$$

where T_n is the natural period of vibration of the structure (in second) and T_g is the predominant period of the ground motion (in second). He showed that the predominant period of the ground motion is dependent on site soil characteristics.

Kuwamura and Galambos *(1989)* proposed different expressions for V_e in Equation (2.3) that took into account the severity and duration of an earthquake. Their expressions are given as follows

$$\begin{aligned} V_e &= \frac{1}{2}\sqrt{\frac{I_e}{T_g}}T_n & for\, T_n \leq T_g \\ V_e &= \frac{1}{2}\sqrt{T_g I_e} & for\, T_n \geq T_g \end{aligned} \tag{2.5}$$

where I_e is the intensity of the accelerogram computed as $I_e = \int_0^t \ddot{u}_g \, dt$ and t is duration of the earthquake.

Fajfar *et al. (1989)* used 40 accelerograms and studied structures that fall within the constant velocity region of the response spectra. From their study, they proposed the expression given in Equation (2.4) for estimating earthquake input energy in such structures.

$$\frac{IE}{m} = 2.2 \, t_{di}^{\,0.5} \, PGV^2 \tag{2.6}$$

where t_{di} is the duration of strong motion as defined by Trifunac and Brady *(1975)* and *PGV* is the peak ground velocity of the ground motion.

Out of curiosity, the different input energy expressions (Equations (2.2), (2.3) and (2.6)) were compared to the 'exact' input energy expression of Equation (2.1). For this purpose a 1994 Northridge earthquake recorded at Leona Valley station has been used and the corresponding input energies are shown in Figure 2.1. The earthquake has the following characteristics: site soil class C, $t_{di} = 12.5$ s, $I_e = 602$ in.^{2}/s^3, $T_g = 0.38$ s, $PGV = 2.92$ in./s, $a_{rms} = 4.35$ in./s^2 (0.011g). From Figure 2.1 it can be clearly seen that, expressions by Akiyama (1985) and Fajfar *et al. (1989)* give an overestimated value of input energy ('exact' input energy is shown as RTH in the figure) by a large margin. Expressions by Housner *(1956)* and Kuwambura and Galambos *(1989)*, on the other hand, underestimated the input energy. It is also important to note that these expressions do not take into account structural behavior, e.g., ductility, which is an important parameter in earthquake design.
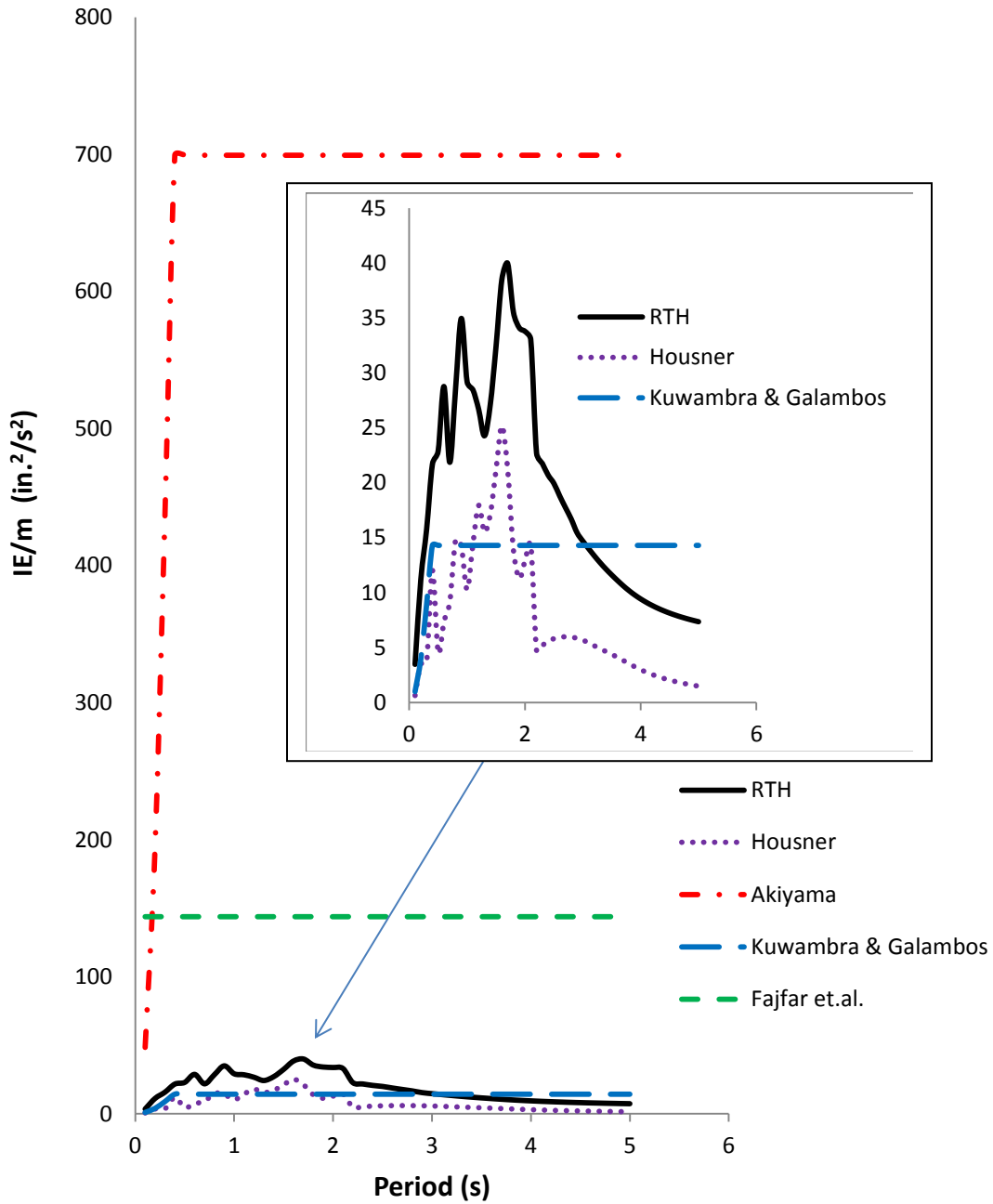
Figure 2.1 Input energy spectra for 1994 Northridge earthquake recorded at the Leona Valley station

Uang and Bertero *(1990),* using five accelerograms and the absolute input energy expression IE_a, concluded that Housner's *(1956)* expression for input energy reflects the maximum elastic energy stored in the structures but does not include the damping energy. Uang and Bertero's

(1990) conclusion is in agreement with what is observed from Figure 2.1. Based on their

finding, for a structure with ductility $\mu = 5$ and damping of 5%, they proposed an expression for

the absolute input energy per unit mass as

$$\frac{IE_a}{m} = \frac{1}{2}(1+0.12t_{di})^2 \, PGV^2 \tag{2.7}$$

Manfredi *(2001),* using 244 accelerograms, proposed an expression for input energy spectra for

structures with period of vibration that falls in the constant velocity region as follows

$$\frac{IE}{m} = 0.45\left(\frac{1}{\sqrt{\mu_c -1}}+0.23I_d\right)\left(\frac{Sa}{\omega}\right)^2 \tag{2.8}$$

$\frac{Sa}{\omega}$ denotes pseudo spectral velocity (in which S_a = pseudo-acceleration, ω = natural frequency

of the system), μ_c is the cyclic ductility, and I_d is a damage index given by

$$I_d = \frac{I_e}{PGA \times PGV} \quad and \quad \mu_c = 1+\frac{\Delta x_m}{u_y} \tag{2.9}$$

where $I_e = \int_0^t \ddot{u}_g dt$ is a measure of earthquake intensity, *PGA* is the peak ground acceleration,

PGV is the peak ground velocity, Δx_m is the maximum cyclic plastic deformation, and u_y is the

yield deformation.

Khashaee *(2004)* proposed the following expression for estimating seismic input energy

$$\frac{IE}{m} = \bar{f} \, f_T \frac{1}{2} (\frac{Sa}{\omega})^2 \tag{2.10}$$

where $\bar{f}$ is a factor accounting for the ductility and ground motion characteristics, f_T is a period factor. By using regression analysis of 160 accelerograms, Khashaee also proposed expressions for the period factor f_T and for the factor $\bar{f}$ as

$$
\begin{aligned}
f_{\scriptscriptstyle T} &= 0.572\, e^{(-4.283 T_n)} + 0.6 \qquad &&for\ \mu = 1 \\
f_{\scriptscriptstyle T} &= 1 \qquad &&for\ \mu = 2,3,4,5 \qquad &&(2.11) \\
\bar{f} &= \frac{4.256}{\sqrt{\mu - 0.5}} + 0.318\, I_C
\end{aligned}
$$

where μ is the ductility and I_c an intensity index proposed by Park and Ang *(1985)* as

$$
I_c = \left(a_{rms}\right)^{1.5} (t_{di})^{0.5} \qquad\qquad (2.12)
$$

where a_{rms} (g) is the root-mean-square ground acceleration and t_{di} is the duration of strong motion as defined by Trifunac and Brady *(1975)*

Khashaee *(2004)* proposed input energy expression and compared it with Manfredi's *(2001)* expression and concluded that the two matched reasonably well. An advantage of Khashaee's method over that of Manfredi's is that there is no need to determine the cyclic ductility of the structure being designed.

It is of interest to investigate the performance of the ductility dependent input energy expressions given in Equations (2.8) and (2.10). For this purpose, they are graphically presented in Figure 2.2 along with an "exact" input energy obtained from a time history analysis (RTH) for the 1994 Northridge earthquake recorded at Leona Valley Station. The results show that, the expression by Khashaee *(2004)* overestimates the input energy by about 150 % on average for SDOF structures with initial periods of 0.5-2.5 s. Whereas, Uang and Bertero *(1990)* expression underestimates the input energy by about 40% on average in the same period range. It should be

noted that the fundamental period of most medium to high-rise story structures fall in this range. The observations made from Figures 2.1 and 2.2 clearly show that there exists an inconsistency and inaccuracy in estimating the input energy for SDOF structures with various ductility and period of vibration properties. This presents a persuasive reason to revisit the existing research findings and come up with new input energy expressions that take into account the ground motion characteristics, structural behavior including ductility and site soil conditions.
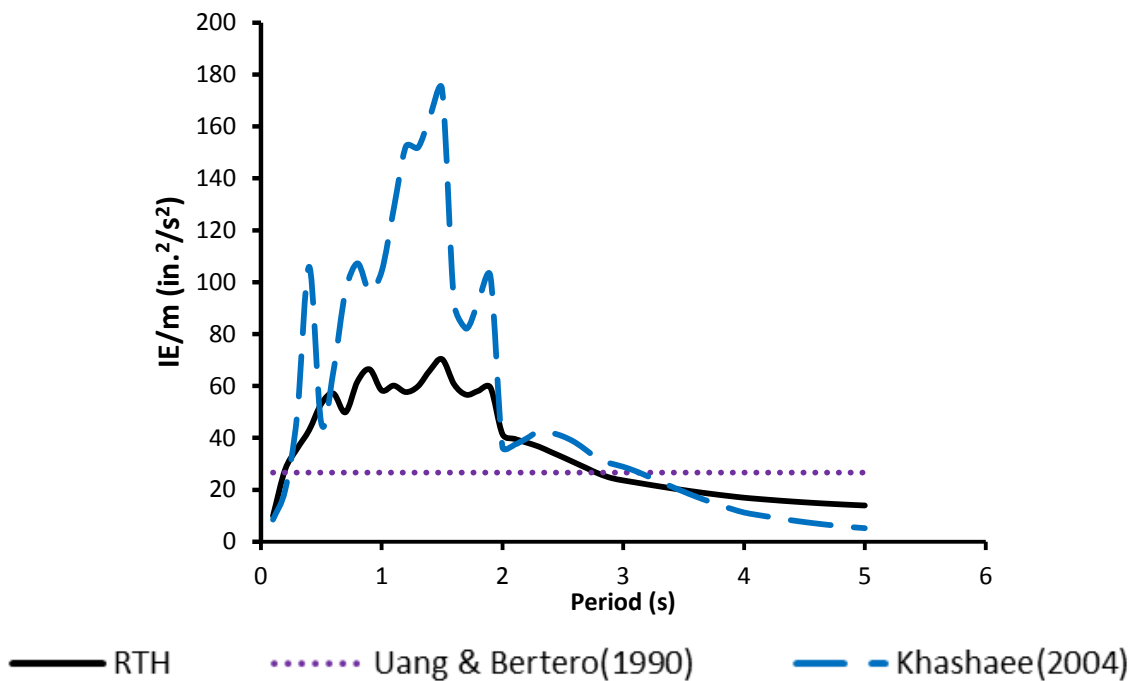
Figure 2.2 Input energy spectra for 1994 Northridge earthquake recorded at Leona Valley station, SDOF (μ=5 and ζ=5%)

As mentioned in Section 1.3, hysteretic energy is by far the most appropriate parameter to quantify the energy dissipation capacity of structures subjected to earthquake excitations. Hysteretic energy is an important parameter used to measure the plastic cumulative damage of structures during an earthquake. Knowing the amount of energy needed to be dissipated through inelastic deformation helps with the design if a structure that possesses sufficient energy dissipation capacity to avoid collapse. For a given earthquake and a SDOF system, hysteretic

18

energy can be estimated from the corresponding input energy. Its accuracy primarily depends on the accuracy of the expressions used for estimating the input energy. Unlike input energy, hysteretic energy is independent of the energy formulation used in the energy balance equation. A literature review of research conducted thus far on estimating hysteretic energy of SDOF systems from the corresponding SDOF input energy is presented below.

2.2 Hysteretic Energy for SDOF System

Housner *(1956)* defined input energy that contributes to the damage of a structure as total seismic input energy, *IE,* less energy dissipated through inherent damping, E_d. According to his definition, the damage energy, E_D, can be written as

$$E_D = IE - E_d \qquad (2.13)$$

Theoretically, per Housner's *(1956)* definition, the damage energy is the sum of the absorbed and kinetic energy. However, at the end of ground motion duration, the kinetic energy becomes small; consequently, the absorbed energy, E_a, can be assumed to be approximately equal to the damage energy, E_D. The expressions for the input energy, *IE,* and damage energy, E_D, normalized by mass *m* and expressed in terms of equivalent velocities are given as follows

$$V_E = \sqrt{2E_i / m} \qquad : \quad V_D = \sqrt{2E_D / m} \qquad (2.14)$$

Akiyama *(1985)*, based on analysis of SDOF systems with elastic-perfectly plastic restoring force characteristics, proposed the following relationship between normalized input and damage energies as

$$\frac{V_D}{V_E} = \frac{1}{1 + 3\zeta + 1.2\sqrt{\zeta}} \qquad (2.15)$$

where ζ is the damping ratio.

Fajfar and Vidic *(1994)* did a parametric study on nonlinear elasto-plastic SDOF systems subjected to five different ground motions from different countries and proposed the following expression for systems with $\zeta = 0.05$.

$$\frac{V_D}{V_E} = \sqrt{\frac{0.9(\mu-1)^{0.95}}{\mu}} \tag{2.16}$$

For a structure with damping ratio $\zeta = 0.05$, Manfredi *(2001)* recommended the following expression be used to estimate hysteretic energy, *HE*, per unit mass

$$\frac{HE}{m} = \frac{(\mu_c - 1)}{\left[1 + 1.5(\mu_c - 1)^{0.8}\right]^2}\left(1 + 0.23I_d\sqrt{\mu-1}\right)\left(\frac{Sa}{\omega}\right)^2 \tag{2.17}$$

He further suggested that for damping $\zeta = 0.05$, the input energy and hysteretic energy can be related by

$$HE = 0.72\frac{(\mu_c - 1)}{\mu_c}IE \tag{2.18}$$

Khashaee *(2004)*, with the intention of eliminating the cyclic ductility variable in Equation (2.18), applied regression analysis on input and hysteretic energies data obtained from 160 accelerograms and proposed the following expressions

$$\begin{aligned} HE &= 0 && \text{for } \mu = 1 \\ HE &= 0.72(1-\mu^{-1})^{0.7}IE && \text{for } \mu = 2,3,4,5 \end{aligned} \tag{2.19}$$

In order to get an insight into the performance of the damage/hysteretic energy expressions given in Equations (2.14) through (2.19), they have been compared to the hysteretic energy obtained from a time history analysis. The Northridge earthquake used above was also used here and the results are shown below.

20
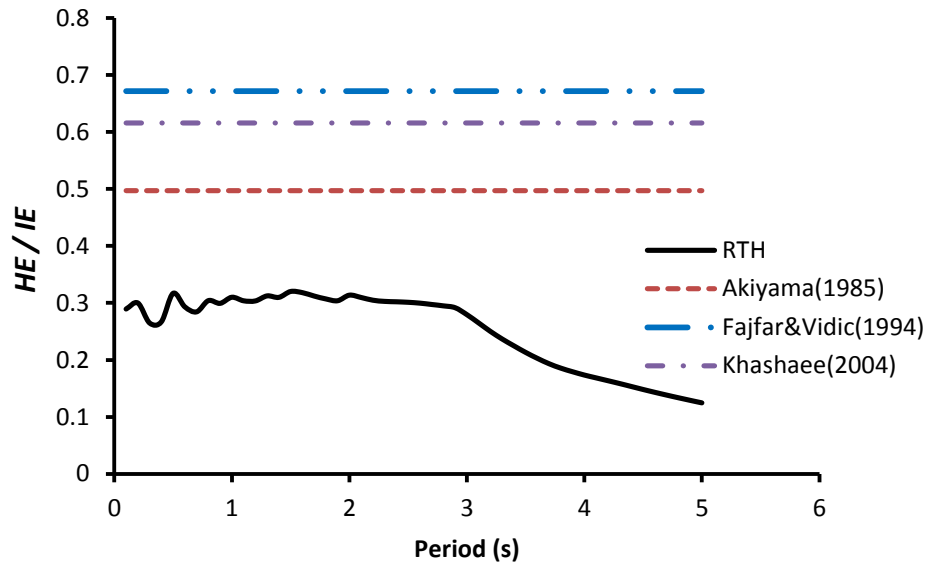
Figure 2.3 Hysteretic energy to input energy ratio for Northridge earthquake recorded at the Leona Valley station, (SDOF: μ =5 and ζ=5%)

Figure 2.3 indicates that the ratio of hysteretic energy to input energy for an SDOF structure (μ =5 and ζ=5%) with bilinear-plastic hysteretic behavior does not significantly depend on the period of vibration of the structure. It can be clearly seen that hysteretic-to-input energy ratio expressions proposed by Akiyama *(1985)*, Fajfar and Vidic *(1994)* and Khashaee *(2004)* overestimate the hysteretic/damage energy. More hysteretic energy means more demand is placed on structural detailing to ensure that it has sufficient ductility to undergo inelastic displacement and rotations. In other words, structures designed based on these expressions often turn out to be overly conservative.

3   PROPOSED INPUT ENERGY SPECTRA OF SDOF SYSTEMS

3.1 Introduction

In seismic design, especially when time history analysis is required, the selection of a set of

design earthquakes is an important part of the design process. Without the proper selection of

the design earthquakes, the design is deemed inadequate. The same is true for developing

seismic design spectra. In this study, the selection was done for four ground motion ensembles

based on site soil classes B, C, D and E, and the procedure is detailed in Section 3.2. The ground

motion ensemble for each site was selected from the Pacific Earthquake Engineering Research

Center (PEER) ground motion record data that contains a very large set of ground motions

recorded worldwide. Section 3.2 presents a description of the proposed SDOF system input

energy spectra characteristics such as ductility, damping and range of period of vibration.

Hysteretic behavior dependent constant ductility spectra are procedurally developed for site soil

classes B, C, D and E in sections 3.4, 3.5, 3.6 and 3.7, respectively.

The effects of hysteretic behavior and soil condition on the input energy of SDOF systems are

addressed in Sections 3.8 and 3.9, respectively. As described in Section 3.8, regardless of the

hysteretic behavior of the SDOF system, when the soil gets softer the input energy decreases in

the short period region of the spectra and increases in the intermediate and long period regions.

In Section 3.10, the validity of the proposed input energy spectra for SDOF systems was tested

by comparing it with the results of the more exact time history analysis. Overall, the validation

tests show that the proposed mean+σ and mean+2σ (where σ is the standard deviation) produce a

fairly conservative result.

3.2 Selection of Ground Motion Ensemble

In practice, when structures are designed to resist earthquakes, the effect of soil-structure interaction is accounted for by categorizing the soil into site classes based on seismic soil profiling. Much research has been dedicated to study soil-structure interaction and its effect on seismic design. Research conducted by Luco *(1982)*, Stewart *et al.* (1999), Poland *et al. (2000)*, Spyrakos and Vlassis *(2002)*, Tongaonkar and Jangid *(2003)* and Gazetas *(2006)* are a few of them. In this study, without giving emphasis on the details, the soil-structure interaction effect on seismic design was accounted for by investigating the effect of soil site class on the seismic input energy. This was achieved by grouping the ground motion records used in this study into different soil categories.

On the basis of the shear wave velocity of the upper 100ft (30m) depth of a soil profile, site soils are seismically categorized into stiff, soft, medium, etc. Such grouping is well documented in current codes such as ASCE/SEI 7-10 *(2010),* International Building Code (IBC *2012*), and the Euro Code, just to mention a few. For this study, site soil classification based on IBC 2012 has been adopted. According to IBC 2012 soil sites classes are categorized as shown in Table 3.1. Ground motion records were selected from the Pacific Earthquake Engineering Research Center (PEER) database for each site class. Additional criteria such as magnitude of earthquake, site distance to source, and target spectra have been used to further refine the data of earthquake records to be used in the study. A description of these additional criteria is presented below.

Table 3.1 Soil site classification according to IBC 2012

Soil Site Class	Soil Description	Shear wave velocity, V_s (ft/s)
A	Hard rock	> 5000
B	Rock	$2500 < V_s \leq 5000$
C	Very dense soil and soft rock	$1180 < V_s \leq 2500$
D	Stiff soil	$590 < V_s \leq 1180$
E	Soft soil	$490 < V_s \leq 590$

Magnitude: Magnitude and intensity of earthquake are two of the most widely accepted indicators of the size of an earthquake. Magnitude is a measure of an earthquake in terms of the released energy whereas intensity is a measure of the observed effect of an earthquake. Charles Richter in 1935 developed the widely used magnitude scale called the Richter's scale. In this study, ground motion records of magnitudes 6-8 based on Richter's Magnitude Scale are selected. This range of magnitude covers earthquakes labeled as strong to major earthquakes.

Distance (km): Effect of near-source ground motions on structures is more pronounced compared to that of far-source ground motions. Hall *et al. (1995)*, Campbell *(1997)*, Bazzurro and Luco *(2005)*, have suggested that pronounced effect of near-source ground motions need to be addressed differently during design. In other words, the result of a study based on a mix of near-source and far-source ground motion records is likely to give misleading conclusions. As a result, this study has excluded near-source ground motion records in the selected ground motion ensemble and is primarily focused on far-source ground motion effects. Near-source and far-source ground motion records are considered to have an epicentral distance of less than 15 km and greater than 30 km, respectively, to the site of the structure or recording station. It is also important to note that far-source ground motions with longer epicentral distances are

characterized by low intensity and small magnitudes. Therefore, this study has tried to narrow down the epicentral distance to a range of 30-80 km.

Target Spectra: In developing design spectra, it is desirable to have the group of selected ground motion records exhibit similar spectral characteristics. The mean spectra developed using such similar spectra should give a smaller standard deviation. However, because ground motions that occur at different sites have different magnitudes, peak values and durations and when averaged, the resulting standard deviations could still be high. To minimize the anticipated high discrepancies and variations, ground motions are often scaled to match some target spectra before they are used in time history analysis. In this study, ground motion records were selected and scaled to match soil site-based response spectra. The soil-site based spectra were generated by geometrically combining the Pacific Earthquake engineering Research Center's Next Generation Attenuation (PEER-NGA) ground motion models developed by Abrahamson and Silva (A & S) *(2008)*, Campbell and Bozorginia (C & B) *(2008)*, Boore and Atkinson (B & A) *(2008)*, and Chiou and Youngs (C & Y) *(2008)*. The target spectra developed for each site based on these models represent an 84th percentile of the geometric mean. The selection and scaling of the ground motions has been made in such a way that the selected ground motion spectra match the target spectra in the period range 0.1 to 3.5 s with equal weights. This range of period of vibration was chosen because most medium- to high-rise buildings have fundamental periods of vibrations of 0.3 to 3.0 s according to the PEER manual, and most bridges have fundamental periods of vibrations in the 0.2 to1.2 s range according to Kunde and Jangid *(2003)*.

Most structures are not built on hard rocks. Even though it cannot be verified by collected data, the majority of structures are founded on soil types C and D and some on soil types B and E. Cognizant of this, only energy spectra for soil types B, C, D and E were developed in this study.

25

A total of 144 ground motion records selected based on the above criteria have been used. A summary of the ground motion records can be found in Appendix A.

3.3 Input Energy Spectra

Input energy spectra that are hysteretic model and soil site class dependent have been developed in this study. Traditionally, the design of earthquake-resistant structures is based on soil site class dependent elastic response spectra generated using a damping ratio of 5%. It is also common to use 5% damping to capture the damping behavior of structures that exhibit inelastic behavior when subjected to dynamic loading. Thus, a damping value of 5% was used in this study to develop the site class and hysteretic specific input energy spectra. If an energy spectrum with different damping ratio is required, it can theoretically be generated by dividing the 5% damping spectra by a damping coefficient factor similar to a damping coefficient factor suggested by Ramirez *et al. (2002)* to modify the response spectrum for higher damping. Ductility plays an important role in response of structures to dynamic loading. As a rule of thumb, the more ductile a structure is, the less it will experience catastrophic damage during a major seismic event. Constant ductility spectra developed by Peng and Conte *(1997)*, Inel *et al. (2002)* and Zhai and Xie *(2005)* supported the same hypothesis. According to Chopra and Goel *(1999),* constant ductility spectra are being use more often for seismic design. In view of this, the input energy spectra developed in this study were chosen to be constant ductility spectra with ductility values of 1, 2, 3, 4 and 5.

The force-displacement relationship or hysteretic behavior of a structure affects its seismic response and hence the energy spectra. Thus, it is important that the hysteretic behavior of a structure under design is known and considered in the determination of the input energy. In this study four different hysteretic models, namely: Bilinear Plastic (BP), Stiffness Degradation or Modified Clough (SD), Bilinear Flag (BF) and Bilinear Slip (BS) were considered. The

properties of these hysteretic models have been discussed in Section 1.4. In reality, structures after yielding do not plastify completely; some undergo strain-hardening and others go through strain-softening. In structural analysis, this effect is addressed through the use of a parameter called post- to pre-yield stiffness ratio, α. In this study a value of $\alpha =0.05$ was used; which is believed to represent the post yield stiffness behavior of most structures. The effect of the value of α on the shape or size of the input energy spectra is minor to insignificant. For instance, Nakashima *et al. (1996)* studied bilinear SDOF and MDOF structures with post to pre-yield stiffness ratio up to 0.75 and concluded the effect of α only have a minor effect on the input energy.

3.4 Input Energy Spectra for Site Class B

A total of 38 earthquake ground motion records have been selected and used in developing the energy spectra for site class B (see Appendix A1). The ground motions were selected to match a target spectrum, which was developed using the NGA models mentioned in Section 3.2 and shown in Figure 3.1. PEER's online beta-version web application was used to develop the spectrum and select relevant ground motions.
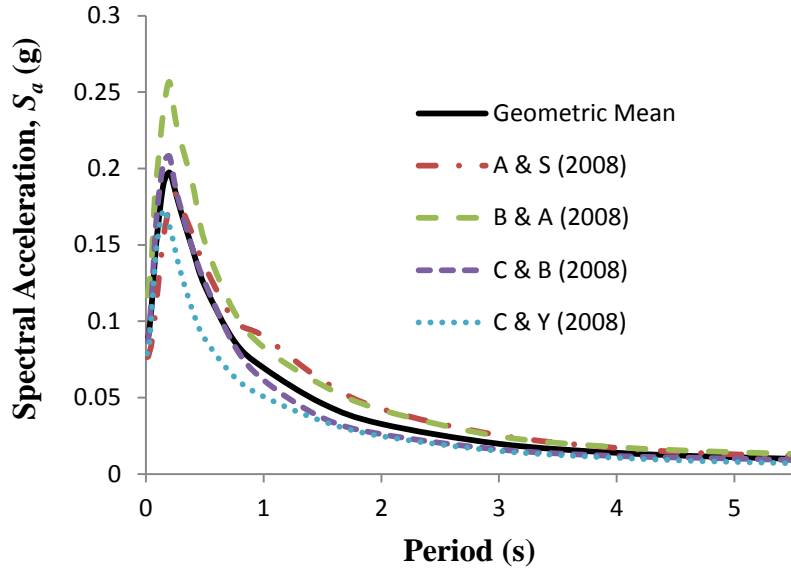
Figure 3.1 Target spectra for site class-B

The ground motions were selected and scaled in such a way that the response spectrum of the selected ground motion reasonably matches with the target spectra. Figure 3.2 shows the geometric mean and the arithmetic mean spectra of the selected ground motion records and the target spectra developed using the PEER-NGA spectra models. The target spectra is the geometric mean of four attenuation models (see Section 3.2) and is shown in Figure 3.1. The parity between the mean spectra and the target spectra clearly indicates that the selected ground motion records satisfactorily represent ground motions recorded at site class B. Statistical analysis also proves this observation; the correlation coefficient, ρ, between the target spectrum and the mean spectra is 0.99. A high value of correlation coefficient signifies that the selected ground motion ensemble is a good representative for site class B. Thus, this ensemble was used to develop realistic energy spectra for the site.
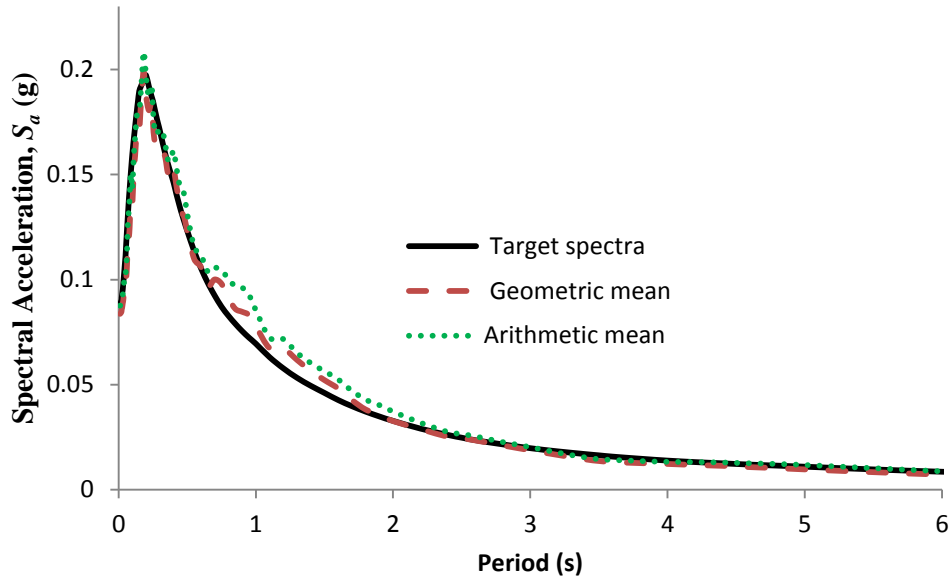
Figure 3.2 Correlation between target and mean spectra for site class-B

Once the representative ground motion records were selected, a series of nonlinear SDOF system time history analyses were performed using BISPEC *(2010)*. SDOF structures (with the different hysteretic models stated above) were each subjected to the 38 ground motion records selected for site class B. The results of these analyses and the steps involved in ultimately developing the energy spectra are discussed below.

3.4.1   Hysteretic Model -BP: Bilinear Plastic

Figure 3.3 shows input energy spectra for a SDOF system with BP hysteretic behavior subjected to a set of selected ground motion records for soil site B. The spectra were developed for ductility values of μ= 1, 2, 3, 4 and 5, and post to pre-stiffness ratio of α=0.05   Also shown in the figure are the mean, mean+σ (68 percentile) and mean+2σ (95 percentile) energy spectra. In most codes and standards, design spectra are either mean spectra or mean+σ spectra. In this study mean+σ and mean+2σ were developed with the idea of presenting a viable alternative for a conservative design, a tradition opted by most practicing engineers. The values shown for the

29

mean+σ and mean+2σ energy spectra in Figure 3.3 are dependent on structural properties (hysteretic model, period, ductility and damping), soil site characteristics and ground motion characteristics such as *PGA*, *PGV*, duration, etc. The structural properties and soil site effects are explicitly represented in the energy spectra (by hysteretic model, period, ductility and damping) and site class (site class B in this case), respectively. On the other hand, the ground motion characteristics, similar to commonly used acceleration response spectra, are represented implicitly in the final output. For a sound seismic design, the intensity of earthquake is an important parameter that needs to be considered when deciding which spectra are to be used. Therefore, the equations that define the input energy spectra should have a factor exclusively dedicated to representing the intensity of ground motions. Such spectra will allow the designer to use design spectra with intensity and magnitude that reflect the severity of the seismic events of interest.
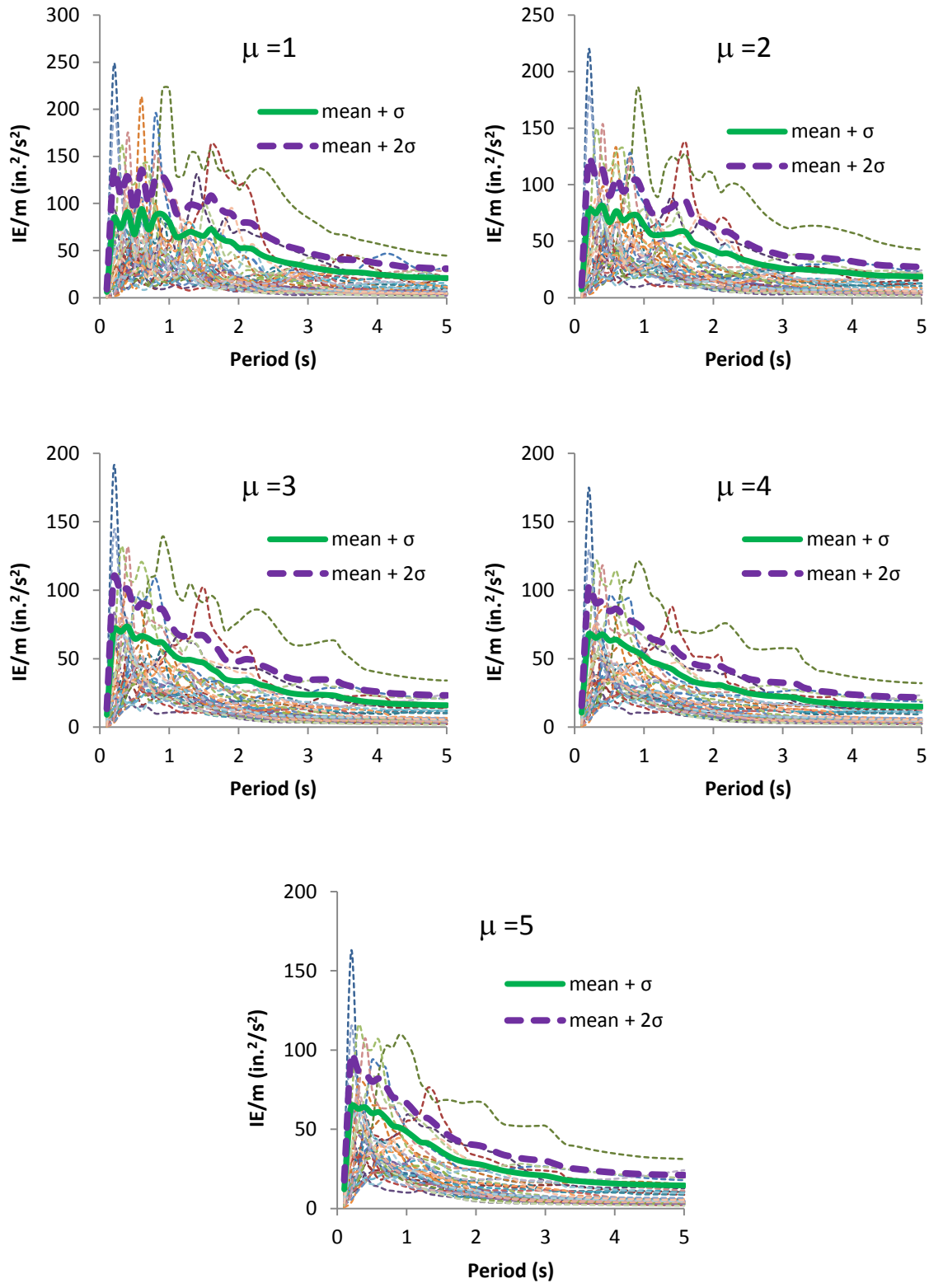
Figure 3.3 Input energy spectra for SDOF systems with bilinear plastic hysteretic model type (α= 0.05) and damping coefficient, ζ= 5%

One way of developing intensity dependent spectra is to normalize the energy spectra using seismic damage indices or quantities that are used to measure the intensity of seismic events. In this study, different damage indices of earthquake ground motion have been investigated in order to find a representative normalization parameter. The list of damage indices considered are as follows

- Cumulative absolute velocity (*CAV*), EPRC (*1988*) : $CAV = \int_0^t |\ddot{u}_g(t)| \, dt$

- Arias intensity (*I_A*), Arias (*1970*): $I_A = \frac{\pi}{2g} \int_0^t \ddot{u}_g^2(t) \, dt$

- Seismic damage index (*I_d*), Manfredi (*2001*): $I_d = \frac{1}{PGA \times PGV} \int_0^t \ddot{u}_g^2(t) \, dt$

- Velocity index (*VI*): $VI = CAV \times PGV$

where

$\ddot{u}_g(t)$ = ground motion acceleration time history

PGA = peak ground acceleration

PGV = peak ground velocity

t = duration of ground motion and

g = gravitational acceleration = 9.81 m/s^2 (32.2 ft/s^2)

In statistics, coefficient of variation is defined as the standard deviation divided by the average or mean. It is used to measure the dispersion of a data. A low value means less dispersion. Based on this fact, the coefficient of variation has been used to compare the degree of uncertainty involved in normalizing the input energies shown in Figure 3.3.
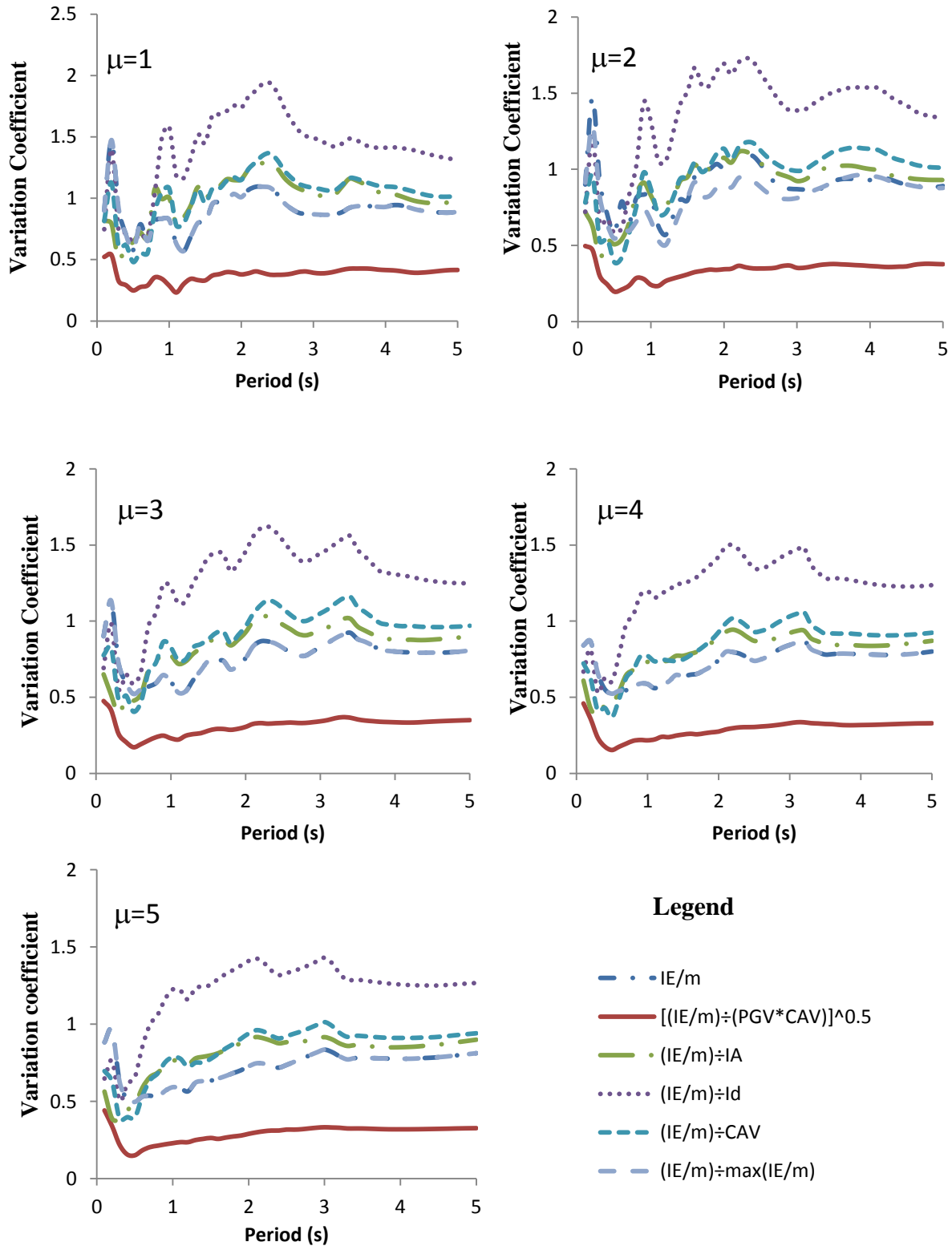
Figure 3.4 Coefficient of variation (hysteretic model- BP)

The input energies have been normalized by different normalizing parameters listed above and the results are shown in Figure 3.4. From the figure, it can be clearly seen that input energies normalized by the velocity index (*VI*) result in the smallest coefficient of variation. On the other hand, normalizing with respect to the damage index, I_d, produces larger values of coefficient of variation. From a statistics point of view, mathematical models obtained by regression analysis of more clustered data, i.e., data that has smaller coefficient of variation will result in equations that will better fit the data.

The unit of *VI* is [distance^2/ time^2] which is the same as that of energy per unit mass. Thus, normalization of the input energy per unit mass by *VI* results in an energy spectrum that is non-dimensional. Non-dimensional spectra have an added advantage that the designer can use whatever units of his choice. Moreover, for a given seismic site and soil zone, the two quantities *PGV* and *CAV* required to calculate *VI* can readily be obtained from the literature. Publications by Power *et al (2008)*, Campbell *et al (2010)* and Bradley *(2012)* are among some recent research findings that give *CAV* and *PGV* prediction equations. Based on the above findings and the relatively ample information available about site based *CAV* and *PGV* values, the velocity index *VI* was used as the normalization parameter for developing the input energy spectra.

The Normalized Energy (*NE*) which will be used in this study from now on is defined as the square root of input energy per unit mass, *IE/m*, divided by the velocity index, *VI*, i.e.,

$$NE = \sqrt{\frac{IE/m}{CAV \times PGV}}.$$
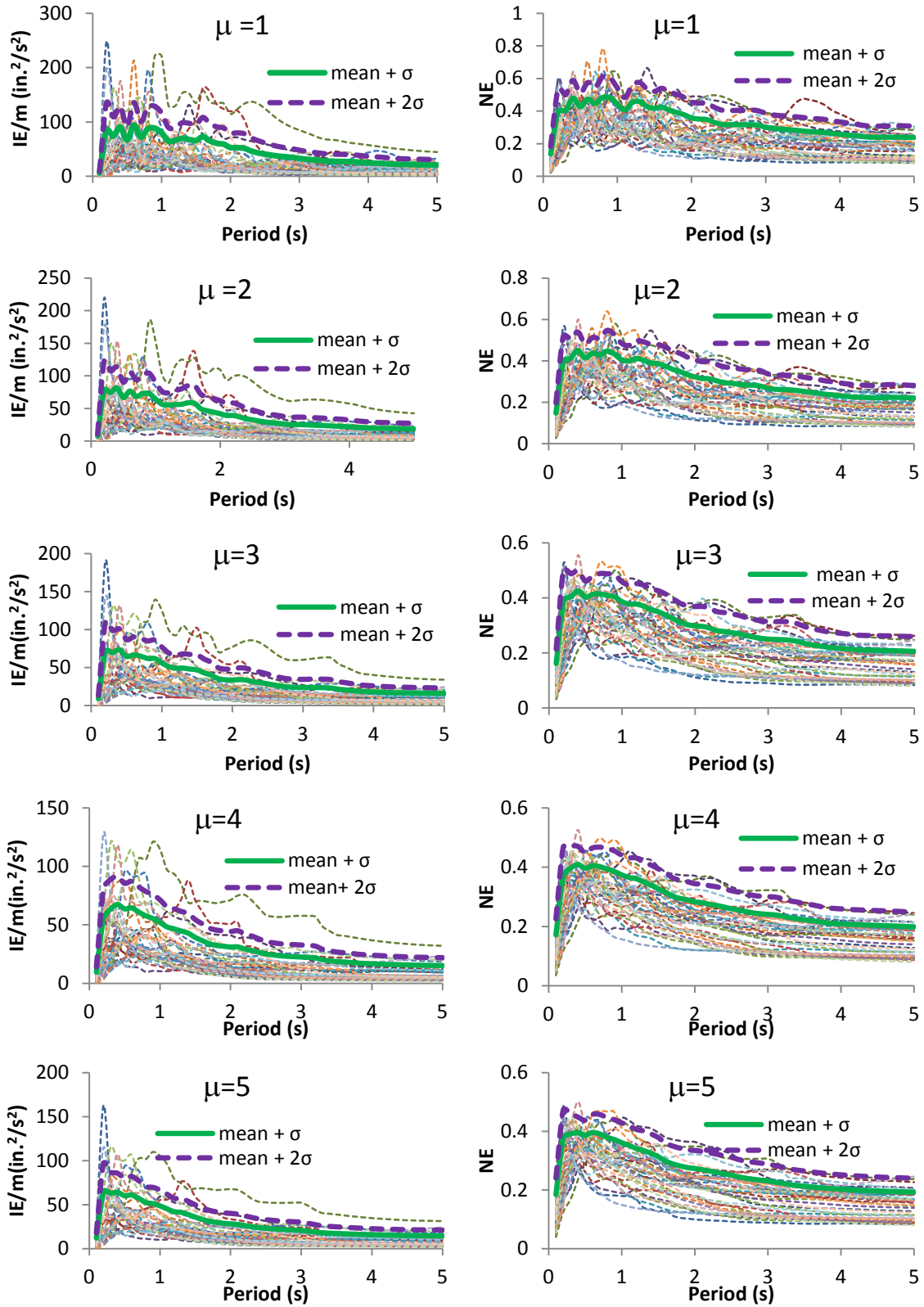
Figure 3.5 Actual (*IE/m*) and corresponding *VI* normalized input energy (*NE*) spectra

35

Besides simplifying the input energy spectra to non-dimensional quantity, input energy

normalized by *VI* gives values that are more narrowly banded (i.e., relatively smaller peaks and

valleys) when compared with the actual energy spectra. Figure 3.5 shows a comparison of the

actual input energy spectra, *IE/m* (left) and the *VI* normalized input energy spectra (*NE*) (right)

for SDOF structures with bilinear plastic hysteretic behavior, ductility values of μ=1,2,3,4,5 and

site class B. The figure clearly shows that, when normalized by *VI*, the peaks and valleys of the

input energy spectra are less pronounced, thus reducing the dispersion of the spectral values.

When the dispersion in a given set of data is reduced, the resulting standard deviation will be

smaller. Moreover, from the coefficient of variation plots of Figure 3.4, it can be observed that

the *VI* normalized input energies have smaller coefficient of variation values compared to those

of the actual input energies. Smaller and more uniform values for the coefficient of variation are

indictors that the mathematical model can provide a better fit for the given data.

Figure 3.5 shows that the mean+σ and mean+2σ spectra envelope quite a high percentage of the

input energy spectra for the selected ground motion records, particularly in the range of periods

from 0.5 to 5 s. Thus, it can be said that the *VI* normalization design input energy spectra would

likely lead to a rather safe and conservative design. Similar observations have been made for the

other three hysteretic models (Modified Clough Stiffness Degradation, Bilinear-Slip and

Bilinear-Flag hysteretic models) investigated in this study. Looking further, the shape of the *VI*

normalized energy spectra used to fit the mean+σ and mean+2σ spectra has been selected in such

a way that it will look familiar to most engineers engaged in seismic design work. A commonly

used response spectra shape can be found in codes and standards (such as IBC 2012, ASCE 7

2010, UBC 97, AASHTO 2011, EURO Code 8 2009, etc.) used by practicing engineers. A

similar general shape has been adopted and is shown in Figure 3.6. The general shape of the

spectra consists of three regions characterized by the following:

1. a straight line for structures in the short period range

2. a constant (plateau) for structures in the intermediate period range

3. a power curve for structures in the long period range.

Accordingly, the equations used to define the proposed *VI* normalized energy spectra, *NE*, are

given below.

$$NE = \begin{cases} sT + b & ; T \leq T_1 \\ C & ; T_1 \leq T < T_2 \\ kT^n & ; T \geq T_2 \end{cases} \tag{3.1}$$

where s and b are the slope and y-intercept of the linear part; C is the maximum value of the *NE*

spectra; T_1 and T_2 separate the short and long period regions from intermediate region.
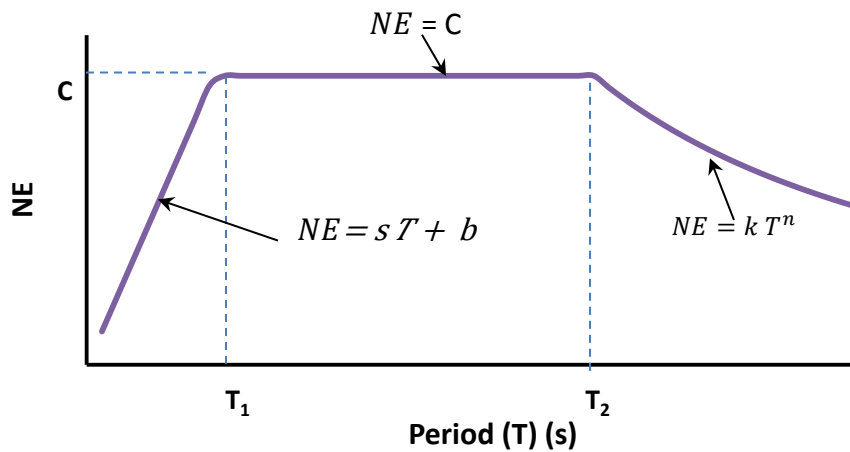
Figure 3.6 Proposed normalized energy, *NE*, spectra

Values of the variables *s, b, C, k, n, T₁* and *T₂* for the SDOF input energy spectra are obtained through a three part nonlinear regression analysis; one each for the short, intermediate and long period regions. The nonlinear regression analysis attempts to mathematically model the best fit equations to the mean+σ and mean+2σ input energy spectra of the selected set of earthquakes for each site class and each hysteretic model type. For site class B and hysteretic type BP these values are presented in Table 3.1. Plots of the smoothened spectra obtained using the values given in Table 3.1 are shown in Figure 3.7.

Table 3.1 *s, b, C, k, n, T₁* and *T₂* values: soil class B and hysteretic model BP

	μ	s	b	T_1	C	T_2	k	n
					Variable			
mean + σ	1	2.599	-0.124	0.234	0.484	1.276	0.549	-0.521
	2	2.446	-0.0969	0.224	0.451	1.122	0.476	-0.480
	3	2.259	-0.0643	0.217	0.425	1.010	0.427	-0.456
	4	1.979	-0.0261	0.220	0.409	0.947	0.399	-0.435
	5	1.928	-0.00875	0.210	0.396	0.907	0.380	-0.420
mean + 2σ	1	3.519	-0.169	0.222	0.611	1.306	0.701	-0.515
	2	3.210	-0.124	0.209	0.547	1.144	0.582	-0.453
	3	2.877	-0.074	0.200	0.501	1.090	0.521	-0.437
	4	2.414	-0.0156	0.202	0.471	0.984	0.468	-0.395
	5	2.321	0.008	0.200	0.473	0.882	0.450	-0.388
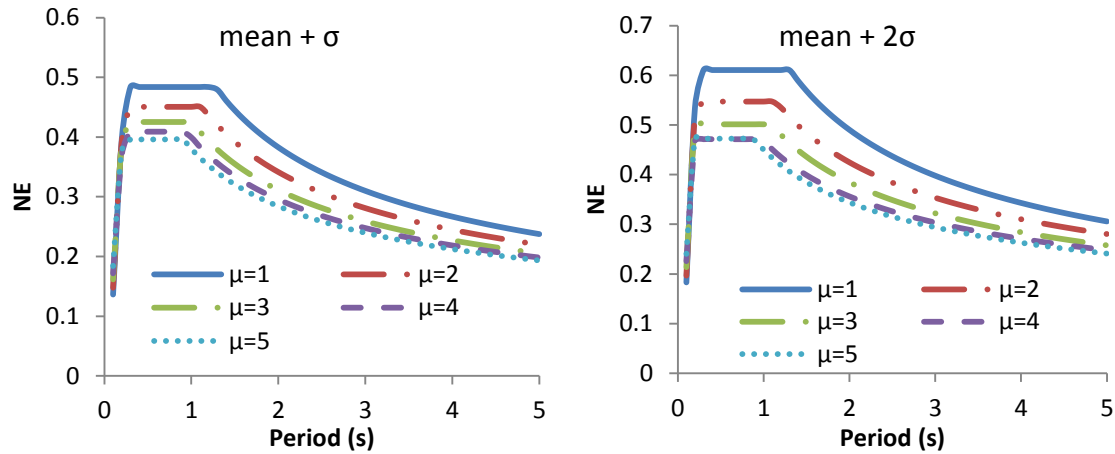
Figure 3.7 *NE* **spectra: hysteretic model BP and site class B**

From Figure 3.7, it can be seen that for a SDOF system with a given period of vibration, *T*, the mean+σ and mean+2σ input energy spectra values decrease as the ductility value of the structure increases. For instance, at a period of *T*= 2.0 s, the input energy spectral values are: 0.383, 0.341, 0.311, 0.295, 0.284 for the mean+σ, and 0.490, 0.425, 0.385, 0.356, 0.344 for mean+2σ, for ductility values of *μ*=1, 2, 3, 4, 5, respectively. Similar observation was also made by Chen *et al (2010)*. They used 56 earthquake records from four site classes and found that spectral values of the total input energy spectrum decrease with an increase in ductility coefficient. While this is the general trend, the decrease in spectral values with an increase in ductility values is not that significant beyond some level of ductility. For instance, Figure 3.7 shows that the input energy plots for ductility values 4 and 5 almost overlap each other. Further research can be performed to determine the limit of ductility value beyond which the change in input energy becomes insignificant.
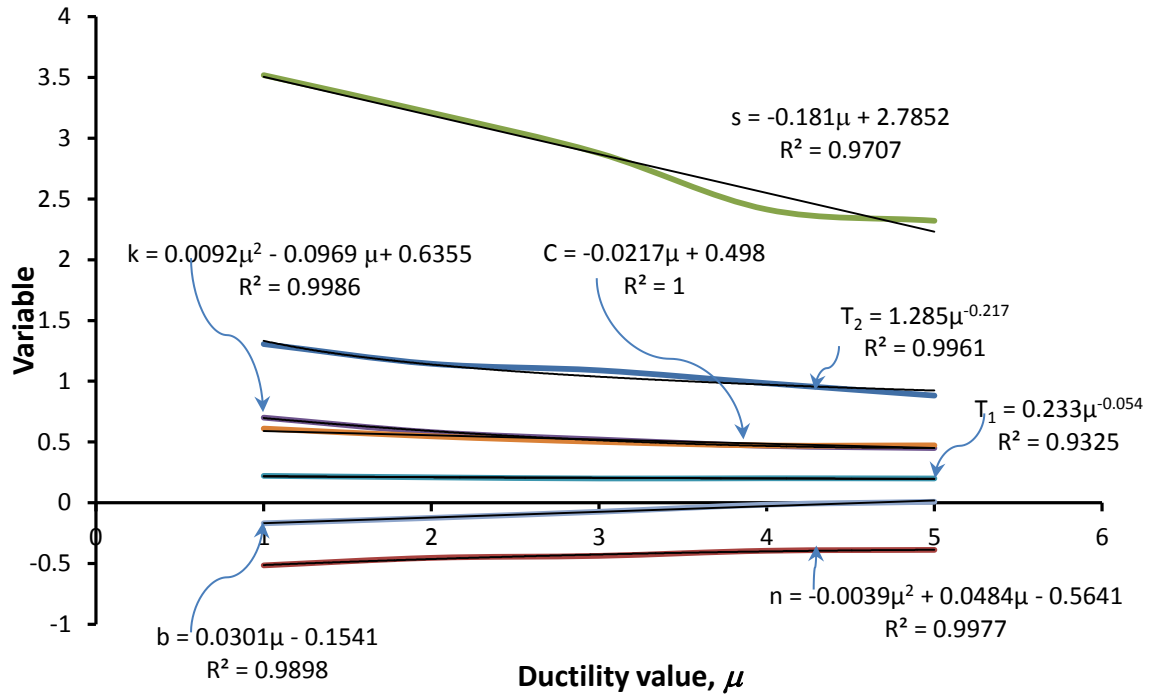
Figure 3.8 Ductility based single expressions: *NE* (mean+σ)

The chart contains the following annotations:

$s = -0.181\mu + 2.7852$
$R^2 = 0.9707$

$k = 0.0092\mu^2 - 0.0969\,\mu + 0.6355$
$R^2 = 0.9986$

$C = -0.0217\mu + 0.498$
$R^2 = 1$

$T_2 = 1.285\mu^{-0.217}$
$R^2 = 0.9961$

$T_1 = 0.233\mu^{-0.054}$
$R^2 = 0.9325$

$n = -0.0039\mu^2 + 0.0484\mu - 0.5641$
$R^2 = 0.9977$

$b = 0.0301\mu - 0.1541$
$R^2 = 0.9898$
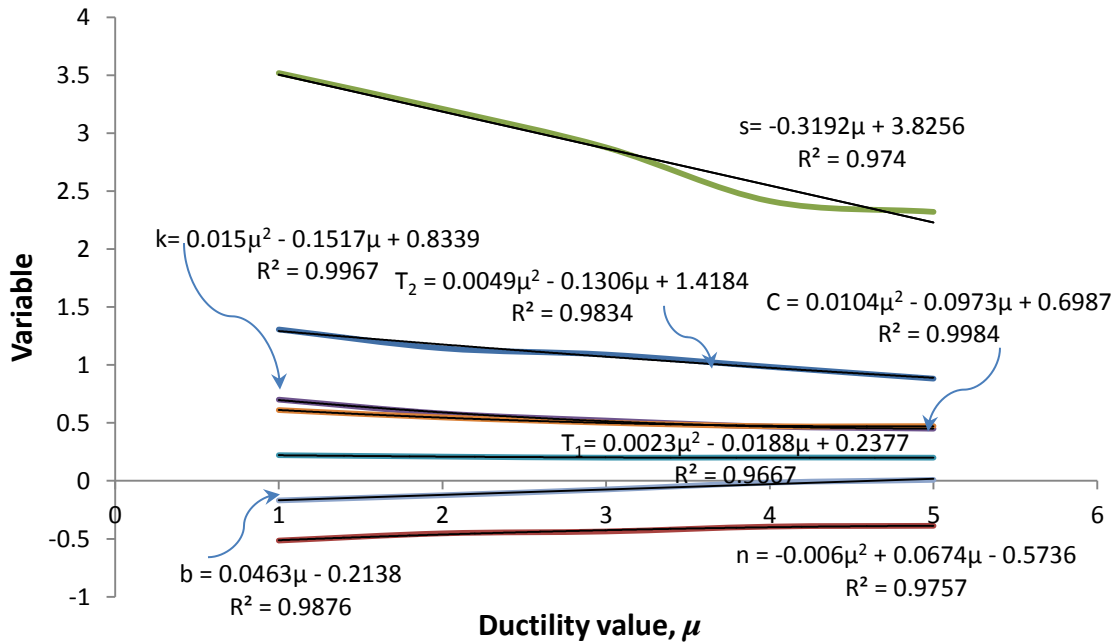
Figure 3.9 Ductility based single expressions: *NE* (mean+2σ)

The chart contains the following annotations:

$s = -0.3192\mu + 3.8256$
$R^2 = 0.974$

$k = 0.015\mu^2 - 0.1517\mu + 0.8339$
$R^2 = 0.9967$

$T_2 = 0.0049\mu^2 - 0.1306\mu + 1.4184$
$R^2 = 0.9834$

$C = 0.0104\mu^2 - 0.0973\mu + 0.6987$
$R^2 = 0.9984$

$T_1 = 0.0023\mu^2 - 0.0188\mu + 0.2377$
$R^2 = 0.9667$

$b = 0.0463\mu - 0.2138$
$R^2 = 0.9876$

$n = -0.006\mu^2 + 0.0674\mu - 0.5736$
$R^2 = 0.9757$

From a design perspective, it is more convenient to use simplified expressions to represent the variables given in Table 3.1. Using nonlinear regression analysis on the variables given in Table 3.1 for the mean+σ and mean+2σ input energy spectra as shown in Figures 3.8 and 3.9, respectively, curve-fitting equations were developed for the variables. They are given in Equation (3.2) as a function of ductility, μ.

$$
\begin{aligned}
s &= -0.181\mu + 2.785 & s &= -0.319\mu + 3.826 \\
b &= 0.0301\mu - 0.154 & b &= 0.0463\mu - 0.214 \\
T_1 &= 0.233\mu^{-0.054} & T_1 &= 0.220\mu^{-0.066} \\
C &= -0.0217\mu + 0.498 & C &= 0.0104\mu^2 - 0.0973\mu + 0.699 \\
T_2 &= 1.285\mu^{-0.217} & T_2 &= 1.333\mu^{-0.228} \\
k &= 0.0092\mu^2 - 0.0969\mu + 0.636 & k &= 0.015\mu^2 - 0.152\mu + 0.834 \\
n &= -0.0039\mu^2 + 0.0484\mu - 0.564 & n &= -0.006\mu^2 + 0.0674\mu - 0.574
\end{aligned}
\tag{3.2}
$$

$$\underbrace{\qquad\qquad\qquad}_{mean+\sigma} \qquad\qquad \underbrace{\qquad\qquad\qquad}_{mean+2\sigma}$$

From Figures 3.8 and 3.9, it can be seen that the R^2 values for the expressions given in Equation (3.2) are all very close to unity, indicating that they fit the data rather well. Equations 3.1 and 3.2 together can now be used to estimate the input energy per unit mass for SDOF systems with hysteretic type BP located in site class B for a given ductility value in the range $1 \leq \mu \leq 5$. To check the accuracy of the proposed equations, plots for different ductility values are presented in Figure 3.10. The comparison was carried out by evaluating the correlation coefficients given in the figure. For all ductility values the correlation coefficients were found to be close to unity for both the mean+σ and mean+2σ energy spectra. Thus, it can be concluded that Equations (3.1) and (3.2) can be used to estimate the normalized input energy spectra for SDOF systems with hysteretic behavior BP, ζ=5% and α=0.05 located in soil site class B. Recall that the input energy spectra was normalized by *VI*, and thus it is essential to note that the level of uncertainty

in the input energy estimates will also depend on the accuracy of determining the velocity index,

VI.

Likewise, similar procedures have been followed in developing the input energy spectra for the remaining three hysteretic models, namely; Strength Degradation or Modified Clough (SD), Bilinear- Slip (BS) and Bilinear- Flag (BF) considered in this study. For sake of brevity, the detailed procedures involved and performed in developing the energy spectra are left out and only the final *VI* normalized energy spectra are presented and discussed in subsequent sections. The mean+σ and mean+2σ energy spectra exhibited similar general shapes as that shown in figure 3.6. To be consistent, the same variables for each hysteretic model were used in defining the shape of each respective energy spectrum.
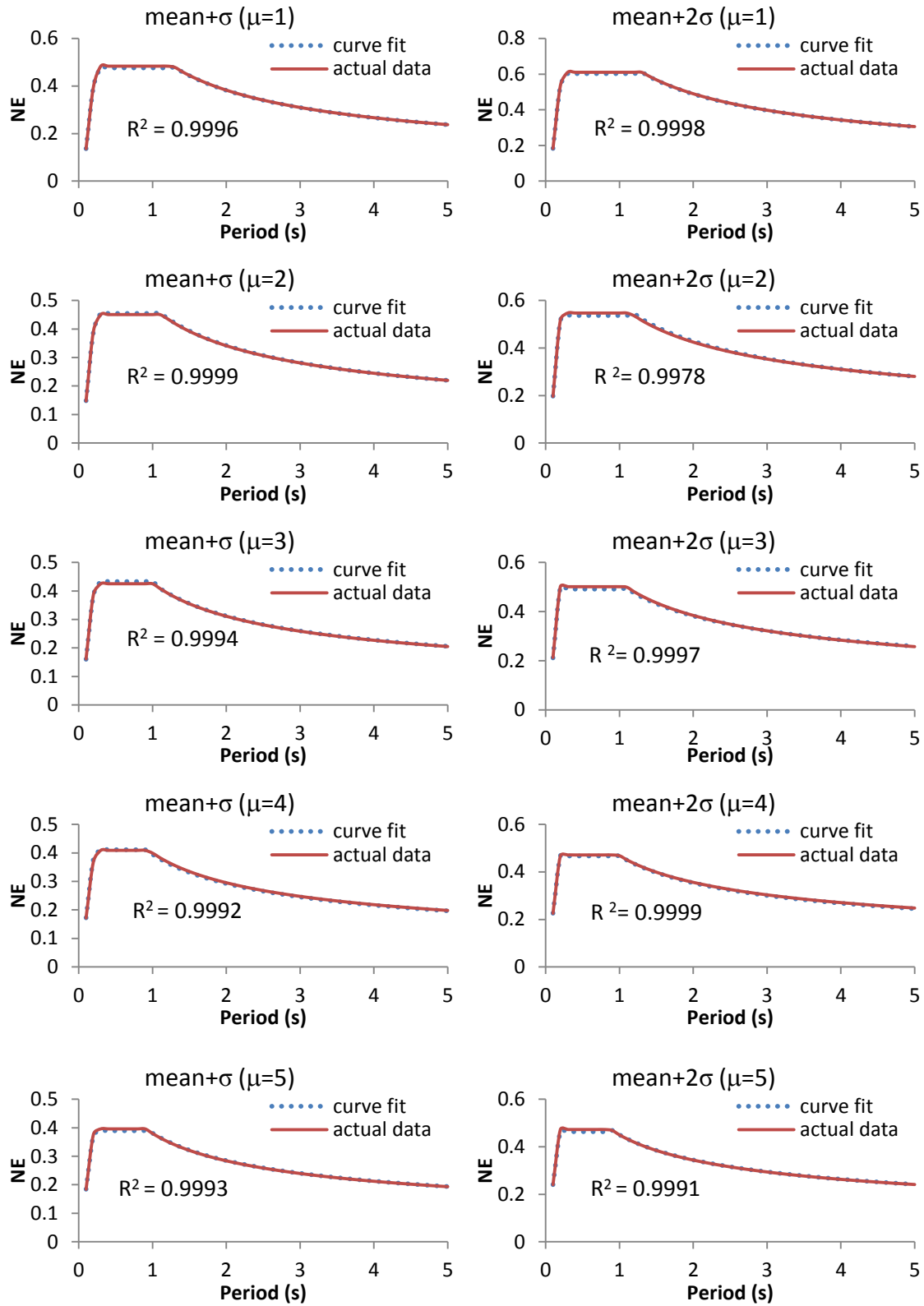
Figure 3.10 Comparison of *NE*: actual data and fitted curves

3.4.2 Hysteretic Model-SD: Strength Degradation (Modified Clough)

As stated in Section 1.4, when reinforced concrete and steel structures are subjected to cyclic

loading such as an earthquake, they tend to lose some strength and stiffness due to crack

formation, bond degradation, yielding, corrosion and fatigue, etc. The loss in stiffness, also

known as stiffness degradation, results in a structure having less energy dissipation capacity than

that of the bilinear plastic model. This loss of stiffness can be captured if the hysteretic behavior

of the structural system is modeled using the Stiffness Degradation (Modified Clough Stiffness

Degradation), SD, hysteretic model.

A time history analysis was carried out using the same set of 38 earthquake records selected for

site class B to develop the input energy spectra for SDOF systems with SD hysteretic behavior.

The resulting, *VI* normalized, mean+σ and mean+2σ input energy spectra are shown Figure 3.11.

It is interesting to see that the input energies display similar shapes as and the variation of input

energy with ductility are like that of the hysteretic model BP. The similarity also applies to the

range of energy spectra plateau, which gets smaller as ductility increases, and the periods at the

corner points of the spectra (T_1 and T_2) decrease with an increase in ductility. It is also observed

that the degree of decrease is more for T_2 than for T_1.

Figure 3.11 *NE* spectra: hysteretic model SD and site class B

Table 3.2 *s, b, C, k, n, T₁* and *T₂* values: soil class B and hysteretic model SD

	μ	s	b	T_1	C	T_2	k	n
					Variable			
mean + σ	1	2.599	-0.124	0.234	0.484	1.242	0.540	-0.511
	2	2.098	-0.0263	0.219	0.433	1.108	0.454	-0.450
	3	1.663	0.0487	0.219	0.413	0.957	0.405	-0.423
	4	1.433	0.094	0.215	0.402	0.869	0.380	-0.411
	5	1.255	0.131	0.210	0.395	0.821	0.365	-0.402
mean + 2σ	1	3.519	-0.169	0.222	0.611	1.262	0.686	-0.502
	2	2.631	-0.0222	0.205	0.516	1.212	0.560	-0.429
	3	1.935	0.0855	0.209	0.489	1.017	0.493	-0.399
	4	1.567	0.149	0.203	0.468	0.967	0.462	-0.389
	5	1.290	0.201	0.200	0.459	0.897	0.440	-0.382

Equation (3.3) gives mathematical expressions that define the variables of the energy spectra for soil site B and hysteretic model SD. The expressions are developed through regression analysis of the corresponding values of the variables listed in Table 3.2.

$$s = -0.335\mu + 2.816$$
$$b = 0.063\mu - 0.164$$
$$T_1 = 0.232\mu^{-0.059} + 0.001$$
$$C = 0.0069\mu^2 - 0.0624\mu + 0.536$$
$$T_2 = -0.108\mu + 1.323$$
$$k = 0.0119\mu^2 - 0.114\mu + 0.64$$
$$\underbrace{n = -0.0085\mu^2 + 0.0766\mu - 0.576}_{mean+\sigma}$$

$$s = 4.373e^{-0.252\mu}$$
$$b = 0.091\mu - 0.224$$
$$T_1 = 0.219\mu^{-0.056} + 0.004$$
$$C = 0.0126\mu^2 - 0.111\mu + 0.702 \qquad (3.3)$$
$$T_2 = -0.0975\mu + 1.364$$
$$k = 0.0175\mu^2 - 0.164\mu + 0.828$$
$$\underbrace{n = -0.0108\mu^2 + 0.0929\mu - 0.58}_{mean+2\sigma}$$

3.4.3   Hysteretic Model-BF: Bilinear Flag

Figure 3.12 shows the mean+σ and mean+2σ *VI* normalized energy spectra for site class B and hysteretic model type of Bilinear Flag (BF). The same ensemble of 38 earthquakes recorded on soil site B was used in developing the spectra. Like the cases for the BP and SD hysteretic models, the spectral values of the input energy decrease with an increase in the ductility of the structure. This may seem to contradict the argument that input energy is directly related to the area under the force displacement curve as was suggested by Hernandez-Montes *et al. (2004).* However, higher ductility does not necessarily mean large displacement; it can be a small maximum displacement over a relatively smaller yield displacement and thus resulting in a small amount of input energy. Unlike that of the hysteretic models BP and SD, the lower range of the plateau (value of T_1) remains almost the same regardless of the ductility value of the structure. On the other hand, the (value of T_2) shows a similar trend of decreasing value with an increase in ductility. Table 3.3 presents the variables used to define the *VI* normalized energy spectra for hysteretic model type BF, site class-B and ductility values μ=1, 2, 3, 4 and 5. For easier manipulation, expressions shown in equation (3.4) were developed to replace the variables list in Table 3.3.
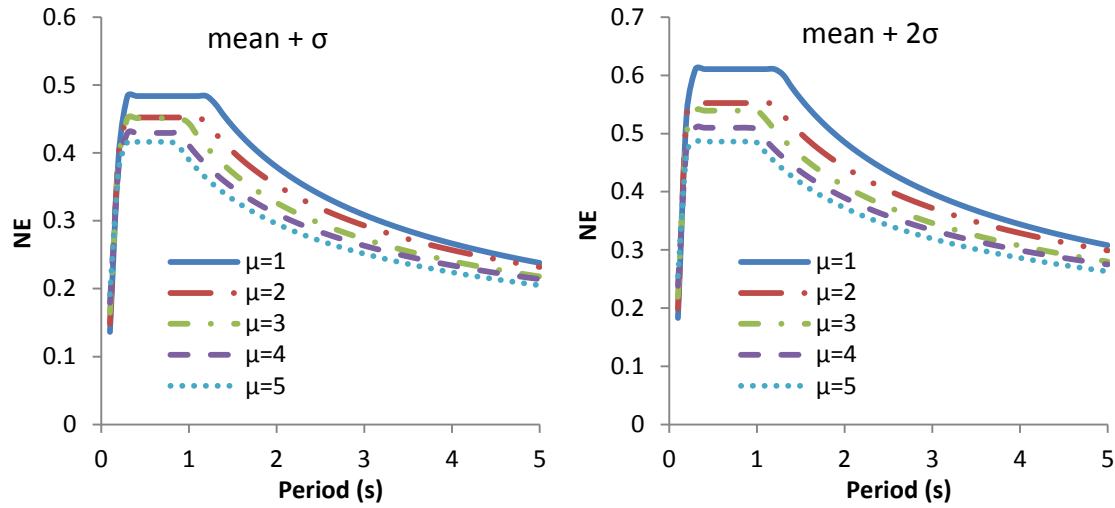
Figure 3.12 Normalized input energy spectra: hysteretic model BF and site class B

Table 3.3 *s, b, C, k, n, T₁* and *T₂* values: soil class B and hysteretic model BF

	μ	s	b	T_1	C	T_2	k	n
					Variable			
mean + σ	1	2.599	-0.124	0.234	0.484	1.241	0.540	-0.509
	2	2.523	-0.104	0.220	0.452	1.160	0.484	-0.457
	3	2.236	-0.0591	0.228	0.451	0.961	0.443	-0.441
	4	2.002	-0.0209	0.225	0.432	0.9	0.411	-0.406
	5	1.851	0.00667	0.221	0.416	0.849	0.39	-0.4
mean + 2σ	1	3.519	-0.169	0.222	0.611	1.258	0.684	-0.496
	2	3.336	-0.135	0.206	0.552	1.188	0.595	-0.427
	3	2.817	-0.0624	0.216	0.539	1.032	0.546	-0.415
	4	2.409	-0.00271	0.213	0.510	0.985	0.507	-0.380
	5	2.146	0.0403	0.208	0.486	0.991	0.484	-0.379

$$s = -0.202\mu + 2.848$$
$$b = 0.0343\mu - 0.163$$
$$T_1 = 0.232\mu^{-0.025}$$
$$C = 0.485\mu^{-0.085} + 0.003$$
$$T_2 = 1.284\mu^{-0.25}$$
$$k = -0.0372\mu + 0.565$$
$$\underbrace{n = -0.0051\mu^2 + 0.0057\mu - 0.559}_{mean+\sigma}$$

$$s = -0.367\mu + 3.947$$
$$b = -0.055\mu - 0.231$$
$$T_1 = 0.218\mu^{-0.028} + 0.01$$
$$C = 0.612\mu^{-0.134}$$
$$T_2 = 1.276\mu^{-0.169} + 0.08$$
$$k = 0.687\mu^{-0.216}$$
$$\underbrace{n = -0.0081\mu^2 + 0.0764\mu - 0.560}_{mean+2\sigma}$$

(3.4)

3.4.4 Hysteretic Model: Bilinear Slip, BS

The strength of reinforced concrete structures is dependent on the strength of concrete and reinforcing steel used. This is true provided that a strong bond exists between the concrete and the reinforcing steel. In cases where a strong bond does not exist between the concrete and the reinforcing steel, the structure could fail prematurely before the steel yields or the concrete crushes as a result of bond failure. Shear failure is also one of the failure mechanisms of reinforced concrete structures. Both shear and bond failures are triggered by a slip phenomenon. Bond slip affects the integrity of a structure and could result in a reduction in both stiffness and strength. A reduction in strength and stiffness means there is a corresponding reduction in energy dissipation capacity. This phenomenon cannot be captured by the hysteretic models BP, SD and BF discussed above, and a Bilinear Slip (BS) hysteretic model should be used instead.

Figure 3.13 shows the *VI* normalized mean+σ and mean+2σ input energy spectra for site class B and hysteretic model type BS. The effect of ductility on input energy for structures with hysteretic model BS was found to have similar nature as it was observed for the case of hysteretic model types BP, SD and BF except in the intermediate region. In the intermediate region of the mean+σ input energy spectra for hysteretic model BS, structures with a ductility value of μ=4 uncharacteristically tend to have slightly larger or almost the same spectral values

of input energy as those with a ductility level of $\mu = 3$. The mean+2σ even show higher values in the intermediate region for structures with a ductility value $\mu = 4$ as compared to those with $\mu=3$ and 2. An investigation into to the mean values; however, did not show such differences. Thus, this change in trend could be attributed to the combined effect of ductility and hysteretic model on the dispersion of input energy values obtained from the ensemble of earthquake records. Recall that highly dispersed data results in higher standard deviations.
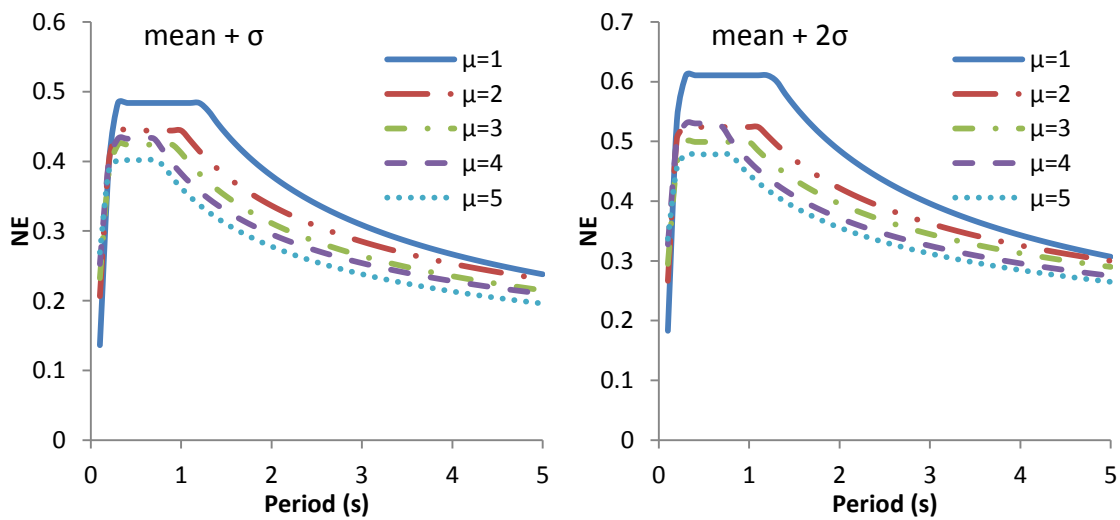
Figure 3.13 *NE* spectra: hysteretic model BS and site class B

Table 3.4 *s*, *b*, *C*, *k*, *n*, T_1 and T_2 values: soil class B and hysteretic model BS

	μ				Variable			
		s	*b*	T_1	*C*	T_2	*k*	*n*
mean + σ	1	2.599	-0.124	0.234	0.484	1.241	0.540	-0.509
	2	1.941	0.0125	0.222	0.444	1.017	0.447	-0.410
	3	1.525	0.0798	0.226	0.424	0.932	0.412	-0.404
	4	1.467	0.106	0.222	0.432	0.719	0.380	-0.372
	5	1.180	0.151	0.212	0.402	0.760	0.362	-0.381
mean + 2σ	1	3.519	-0.169	0.222	0.611	1.260	0.685	-0.499
	2	2.384	0.0282	0.208	0.524	1.115	0.546	-0.372
	3	1.693	0.126	0.221	0.499	1.008	0.501	-0.339
	4	1.732	0.154	0.217	0.530	0.678	0.467	-0.329
	5	1.194	0.218	0.218	0.478	0.796	0.444	-0.321

Expressions given in Equation (3.5) were developed using regression analysis of the values listed in Table 3.4. It is important to note that unlike the other three hysteretic models, the values of *b*, T_1, T_2 and *C* do not strictly decrease with an increase in ductility. Variables *b*, T_1, T_2 and *C* define the intermediate period region of the spectra and as discussed above the input energy variation with ductility in this region was not strictly decreasing or increasing. Consequently, higher (at least third) degree polynomials were used to achieve values of 0.95 or greater for the correlation coefficients.

$$s = 2.631\mu^{-0.469}$$
$$b = -0.0159\mu^2 + 0.16\mu - 0.259$$
$$T_1 = -0.0018\mu^3 + 0.0159\mu^2 - 0.0448\mu + 0.264$$
$$C = -0.0049\mu^3 + 0.0472\mu^2 - 0.153\mu + 0.595$$
$$T_2 = 0.0288\mu^2 - 0.299\mu + 1.514$$
$$k = 0.0107\mu^2 - 0.106\mu + 0.63$$
$$n = -0.0135\mu^2 + 0.111\mu - 0.598$$
mean+σ

$$s = 3.575\mu^{-0.624}$$
$$b = -0.024\mu^2 + 0.234\mu - 0.367$$
$$T_1 = 0.0027\mu^4 - 0.012\mu^3 + 0.148\mu^2 - 0.263\mu + 0.367$$
$$C = -0.012\mu^3 + 0.117\mu^2 - 0.363\mu + 0.871$$
$$T_2 = 0.0389\mu^4 - 0.432\mu^3 + 1.641\mu^2 - 2.626\mu + 2.638$$
$$k = 0.0176\mu^2 - 0.161\mu + 0.82$$
$$n = -0.0187\mu^2 + 0.152\mu - 0.622$$
mean+2σ

(3.5)

Some of the expressions in Equation (3.5) are too long and do not necessarily result in a significant change in the accuracy of the final values of the variables and thus the amount of input energy. Hence, alternative simpler and easier expressions with $R^2 > 0.9$ given in Equation (3.6) are recommended for use.

$$
\begin{array}{ll}
s = 2.631\mu^{-0.469} & s = 3.575\mu^{-0.624} \\
b = 0.0644\mu - 0.148 & b = 0.09\mu - 0.198 \\
T_1 = 0.234\mu^{-0.048} + 0.02 & T_1 = 0.217\mu^{-0.01} + 0.01 \\
C = 0.481\mu^{-0.102} + 0.003 & C = 0.596\mu^{-0.13} + 0.015 \\
T_2 = 1.261\mu^{-0.335} + 0.08 & T_2 = 1.324\mu^{-0.349} + 0.08 \\
k = 0.0107\mu^2 - 0.106\mu + 0.63 & k = 0.0176\mu^2 - 0.161\mu + 0.82 \\
\underbrace{n = -0.0135\mu^2 + 0.111\mu - 0.598}_{mean+\sigma} & \underbrace{n = -0.0187\mu^2 + 0.152\mu - 0.622}_{mean+2\sigma}
\end{array}
\qquad (3.6)
$$

3.5 Input Energy Spectra for Site Class C

A total of 42 earthquake records (Appendix A2) have been selected and scaled to develop input energy spectra for site class C. Using PEER *(2011)* NGA models, a target spectrum was developed in a similar manner as was done for site class B. The target spectrum was then used to select earthquakes recorded at site class C whose spectra match reasonably well with the target spectrum. The mean spectra of the selected ground motion records along with the target spectrum are presented in Figure 3.14 for easy comparison. The correlation coefficient between the geometric mean and the target spectra and that between the arithmetic mean and the target spectra are both equal to 0.99. Because a correlation coefficient close to one shows a strong match between two data sets, the ensemble of selected ground motion records can be considered as a reliable set of records that represents the nature of earthquakes recorded at site class C. Subsequently, this ensemble of 42 earthquakes was used to develop the input energy spectra for SDOF structures with the four different hysteretic models (BP, SD, BF and BS).

51
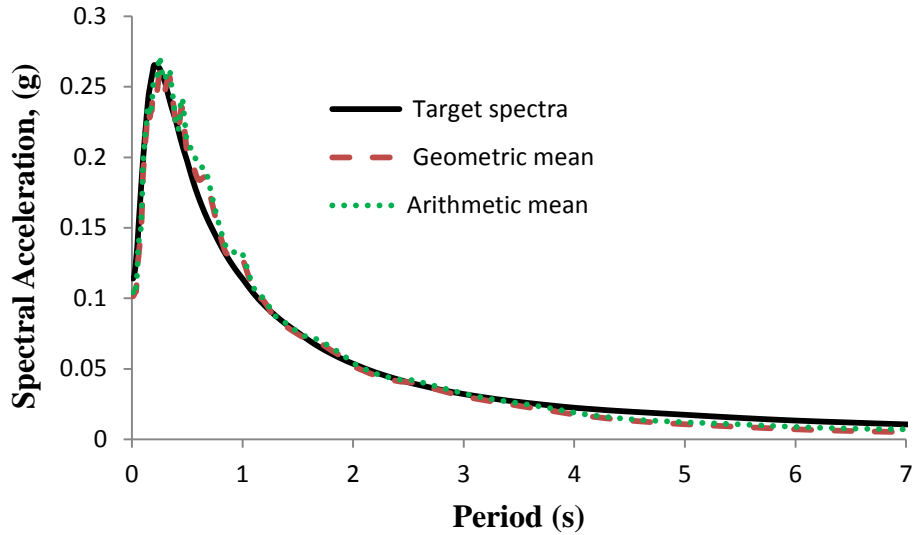
Figure 3.14 Relation between mean and target Spectra for site C

Like that of site class B, an extensive time history spectral analysis has been performed using BISPEC *(2010)* for SDOF structures (with hysteretic models: BP, SD, BF and BS) subjected to the 42 ground motion records selected for site class C. A summary of the analysis results and discussions for each hysteretic model type are presented below.

3.5.1 Hysteretic Model: Bilinear Plastic, BP

The *VI* normalized mean+σ and mean+2σ input energy spectra for ductility values of $\mu = 1, 2, 3, 4, 5$ are shown in Figure 3.15. The values of the different variables used to define the input energy spectral shape are listed in Table 3.5. Figure 3.15 shows that the ductility has a similar effect on input energy as it had for site class B. Input energy decreases with an increase in the ductility value for both the mean+σ and mean+2σ spectra.
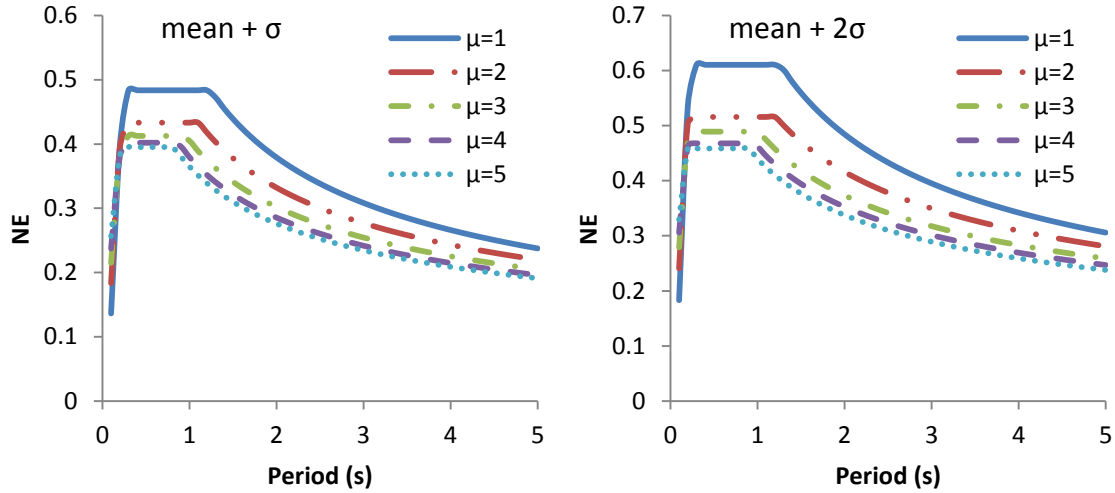
Figure 3.15 *NE* spectra: hysteretic model BP and site class C

Table 3.5 *s, b, C, k, n, T₁* and *T₂* values: soil class C and hysteretic model BP

	μ	s	b	T₁	C	T₂	k	n
					Variable			
mean + σ	1	1.461	-0.0415	0.374	0.505	1.847	0.811	-0.772
	2	1.418	-0.0321	0.346	0.459	1.838	0.761	-0.832
	3	1.367	-0.0168	0.324	0.426	1.648	0.614	-0.731
	4	1.300	-0.0002	0.319	0.415	1.556	0.568	-0.707
	5	1.266	0.011	0.312	0.406	1.48	0.530	-0.680
mean + 2σ	1	1.672	-0.0367	0.393	0.621	1.889	1.032	-0.798
	2	1.585	-0.0262	0.356	0.537	1.871	0.902	-0.826
	3	1.495	-0.00713	0.339	0.499	1.648	0.716	-0.723
	4	1.387	0.0146	0.334	0.478	1.585	0.661	-0.702
	5	1.335	0.0288	0.328	0.466	1.494	0.609	-0.667

In the range of ductility values from 3 to 5, the decrease in input energy is not as significant as the decrease in input energy observed for ductility values in the range of 1 to 3. This is true for both the mean+σ and mean+2σ spectra. Based on this, it can be inferred that for a given

earthquake (recorded at site class C) the effect of ductility on input energy of SDOF structures with hysteretic behavior type BP tends to be minimal for ductility values $\mu \geq 3$. It is also true for the case of input energy for hysteretic model BP and site class B (see section 3.4.1). The limit of the ductility value beyond which its effect on input energy becomes insignificant can be further researched by performing spectral analysis for ductility values (say 5 - 10). As for ductility values $\mu = 1, 2, 3, 4, 5$, ductility based VI normalized input energy expressions for SDOF systems with hysteretic behavior BP at soil site C are given in Equation (3.7).

$$
\begin{array}{ll}
\underbrace{\begin{aligned}
s &= -0.0507\mu + 1.515 \\
b &= 0.0137\mu - 0.0569 \\
T_1 &= 0.374\mu^{-0.116} \\
C &= 0.0069\mu^2 - 0.0657\mu + 0.563 \\
T_2 &= -0.102\mu + 1.978 \\
k &= 0.0089\mu^2 - 0.129\mu + 0.946 \\
n &= 0.0072\mu^2 - 0.0124\mu - 0.786
\end{aligned}}_{mean+\sigma}
&
\underbrace{\begin{aligned}
s &= -0.0873\mu + 1.757 \\
b &= 0.0172\mu - 0.0569 \\
T_1 &= 0.389\mu^{-0.113} \\
C &= 0.0115\mu^2 - 0.106\mu + 0.711 \\
T_2 &= -0.108\mu + 2.02 \\
k &= 0.0205\mu^2 - 0.232\mu + 1.253 \\
n &= 0.0031\mu^2 + 0.02\mu - 0.838
\end{aligned}}_{mean+2\sigma}
\end{array} \tag{3.7}
$$

3.5.2   Hysteretic Model: Stiffness Degradation (Modified Clough), SD

Shown in Figure 3.16 are the mean+σ and mean+2σ *VI* normalized input energy spectra for SDOF structures with hysteretic behavior type SD and site class C and ductility values $\mu = 1, 2, 3, 4, 5$. A decrease in input energy with an increase in ductility value is once again observed for SDOF structures with hysteretic behavior type SD. This decrease in the amount of input energy diminishes as the ductility value gets higher. For instance, in the constant region of the *VI* normalized mean+σ energy spectra, the decrease in values are 10%, 3%, 3%, and 1% between μ=1&2, μ=2&3, μ=3&4, and μ=4&5, respectively. The corresponding values for the mean+2σ spectra are 15%, 3.5%, 3.5 % and 1%, respectively.
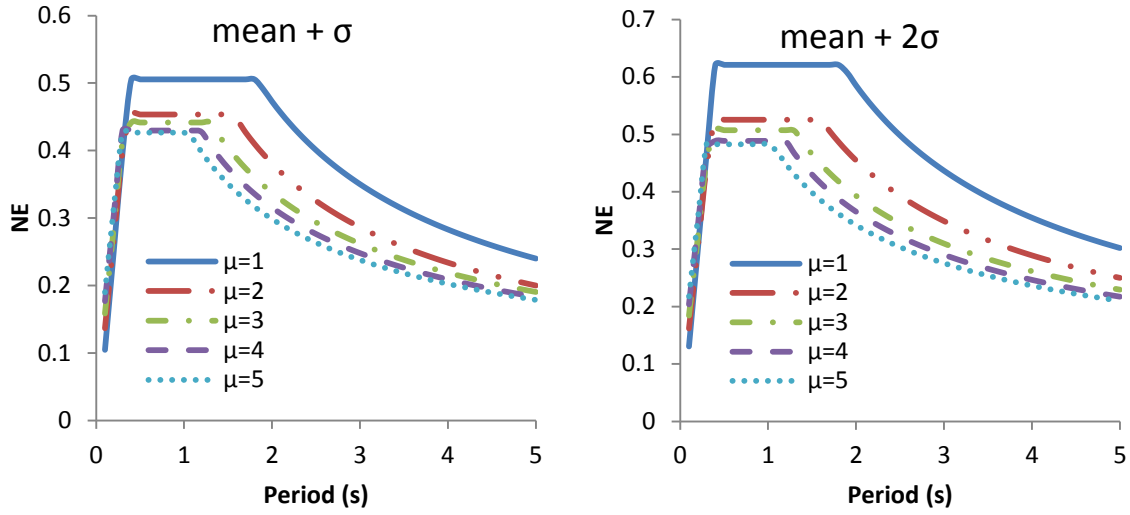
Figure 3.16 *NE* spectra: hysteretic model SD and site class C

Table 3.6 *s, b, C, k, n, T₁* and *T₂* values: soil class C and hysteretic model SD

	μ	s	b	T_1	C	T_2	k	n
					Variable			
mean + σ	1	1.461	-0.0415	0.374	0.505	1.826	0.789	-0.740
	2	1.308	0.00592	0.342	0.453	1.560	0.620	-0.703
	3	1.275	0.0311	0.322	0.442	1.301	0.520	-0.624
	4	1.273	0.0496	0.299	0.430	1.189	0.476	-0.594
	5	1.256	0.0644	0.288	0.427	1.057	0.440	-0.560
mean + 2σ	1	1.672	-0.0367	0.393	0.621	1.842	0.965	-0.722
	2	1.402	0.0216	0.359	0.525	1.602	0.715	-0.653
	3	1.347	0.0497	0.340	0.507	1.295	0.590	-0.587
	4	1.352	0.0686	0.311	0.489	1.198	0.541	-0.567
	5	1.343	0.0834	0.297	0.483	1.046	0.494	-0.532

Table 3.6 presents the different variables used to define the *VI* normalized mean+σ and mean+2σ

input energy spectra for SDOF of structures given in Figure 3.16. These values are curve-fitted

using nonlinear regression analysis to obtain the expressions given in Equation (3.8). From

Table 3.6 and Figure 3.16, it can be seen that the value of T_2 decreases as ductility value

increases resulting in a smaller constant region range. In other words, if the period of the

structure is closer to T_2, the input energy can be significantly reduced by increasing the ductility

of the structure.

$$
\begin{array}{ll}
s = 0.0218\mu^2 - 0.175\mu + 1.601 & s = 0.0416\mu^2 - 0.321\mu + 1.927 \\
b = 0.0255\mu - 0.0547 & b = -0.0069\mu^2 + 0.0699\mu - 0.0969 \\
T_1 = 0.379\mu^{-0.164} & T_1 = 0.34\mu^{-0.174} \\
C = 0.007\mu^2 - 0.0601\mu + 0.555 & C = 0.0128\mu^2 - 0.108\mu + 0.709 \qquad (3.8) \\
T_2 = -0.191\mu + 1.959 & T_2 = -0.2\mu + 1.995 \\
k = 0.023\mu^2 - 0.222\mu + 0.983 & k = 0.0345\mu^2 - 0.318\mu + 1.237 \\
\underbrace{n = 0.0468\mu - 0.784}_{mean+\sigma} & \underbrace{n = -0.0082\mu^2 + 0.0955\mu - 0.809}_{mean+2\sigma}
\end{array}
$$

3.5.3   Hysteretic Model: Bilinear Flag, BF

Figure 3.17 shows the mean+σ and mean+2σ *VI* normalized input energy spectra for SDOF

structures with hysteretic behavior type BF located at site class C. The general trend of a

decrease in the amount of input energy with an increase in ductility value continues to hold.

However, the amount of decrement is lower than that for the SD model. For instance, for the

mean+σ spectra the decrease in the amount of input energy is 6%, 2%, 4%, and ≈0% between

μ=1&2, μ=2&3, μ=3&4, and μ=4&5, respectively. The values of the variables that define the

input energy diagrams shown in Figure 3.17 are presented in Table 3.7. Equation (3.9) gives

expressions for input energy spectra expressed as a function of ductility.

Figure 3.17 *NE* spectra: hysteretic model BF and site class C

Table 3.7 *s, b, C, k, n, T₁* and *T₂* values: soil class C and hysteretic model BF

		Variable						
	μ	s	b	T_1	C	T_2	k	n
mean + σ	1	1.461	-0.0415	0.374	0.505	1.847	0.811	-0.771
	2	1.402	-0.0315	0.358	0.470	1.613	0.654	-0.689
	3	1.342	-0.0128	0.352	0.459	1.445	0.589	-0.679
	4	1.380	-0.00789	0.323	0.438	1.379	0.538	-0.640
	5	1.428	-0.0066	0.311	0.438	1.208	0.489	-0.577
mean + 2σ	1	1.672	-0.0367	0.393	0.621	1.889	1.032	-0.798
	2	1.552	-0.0242	0.375	0.558	1.638	0.770	-0.653
	3	1.435	0.00236	0.375	0.540	1.463	0.691	-0.647
	4	1.493	0.00529	0.347	0.523	1.364	0.632	-0.607
	5	1.569	0.00333	0.323	0.509	1.232	0.570	-0.538

$$s = 0.0223\mu^2 - 0.142\mu + 1.585$$
$$b = -0.0022\mu^2 + 0.0226\mu - 0.0636$$
$$T_1 = -0.016\mu + 0.392$$
$$C = 0.0043\mu^2 - 0.0427\mu + 0.543$$
$$T_2 = -0.151\mu + 1.952$$
$$k = 0.0163\mu^2 - 0.174\mu + 0.959$$
$$n = 0.0437\mu - 0.802$$
$$\underbrace{\qquad\qquad\qquad\qquad}_{mean+\sigma}$$

$$s = 0.0406\mu^2 - 0.27\mu + 1.908$$
$$b = -0.0037\mu^2 + 0.0335\mu - 0.0691$$
$$T_1 = -0.0028\mu^2 + 0.0001\mu + 0.394$$
$$C = 0.0071\mu^2 - 0.0685\mu + 0.677 \qquad (3.9)$$
$$T_2 = -0.159\mu + 1.993$$
$$k = 0.03\mu^2 - 0.286\mu + 1.268$$
$$n = -0.792\mu^{-0.218}$$
$$\underbrace{\qquad\qquad\qquad\qquad}_{mean+2\sigma}$$

3.5.4   Hysteretic Model: Bilinear Slip, BS

The mean+σ and mean+2σ *VI* normalized input energy spectra for SDOF systems represented by the bilinear slip hysteretic model are shown in Figure 3.18. Compared to SDOF structures with hysteretic models BP, SD and BF, not only are the values of T_1 and T_2 the lowest, but the ranges of the constant region are the narrowest as well (see Figure 3.19). The case of $\mu=1$ is an exception as it is independent of the hysteretic type considered and remains the same for all cases.
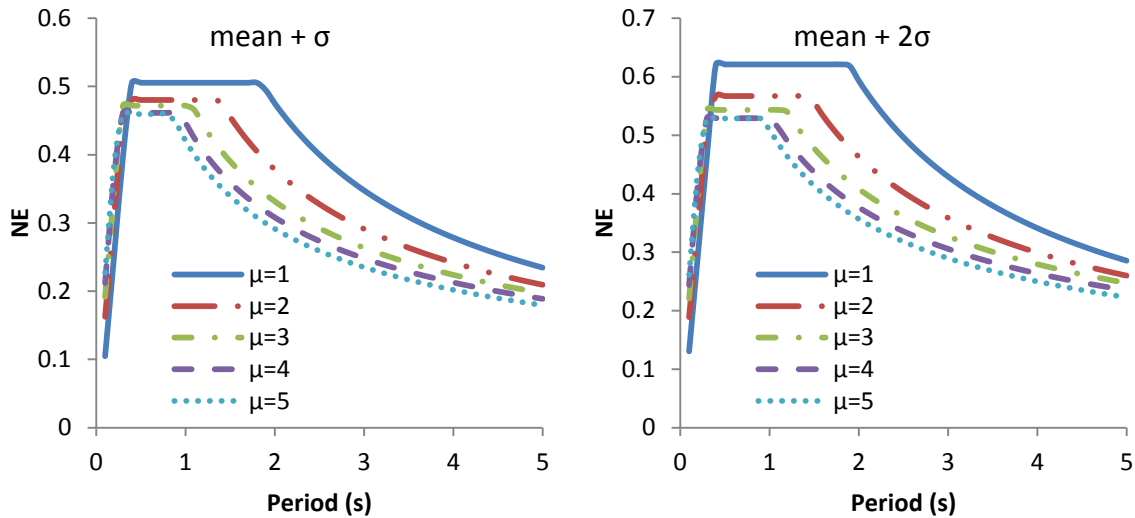
Figure 3.18 *NE* **spectra: hysteretic model BS and site class C**
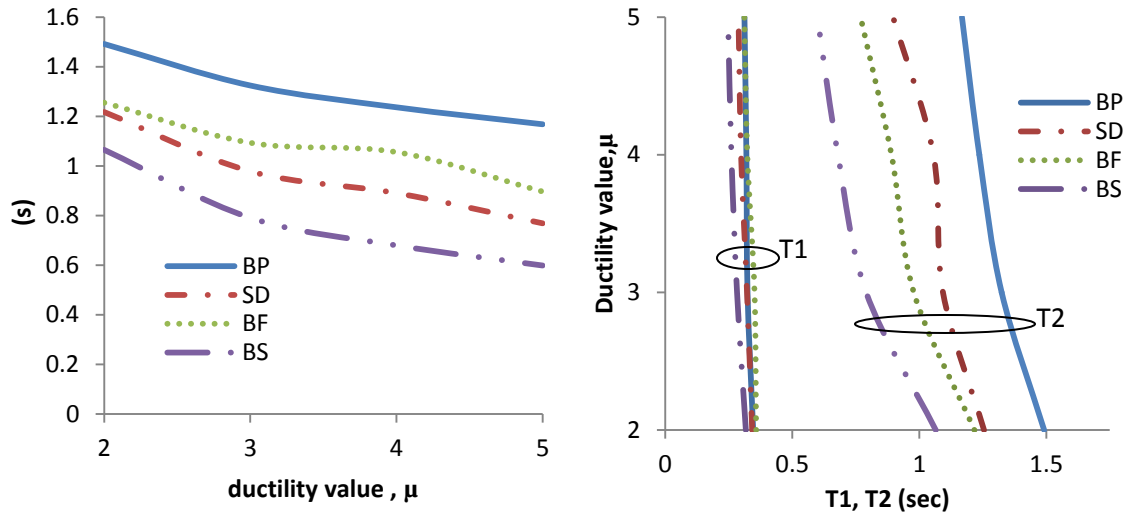
Figure 3.19 T_1, T_2 and constant region range comparison for hysteretic model types BP, SD, BF and BS

Values of the variables that define the *VI* normalized input energy spectra shape for hysteretic model type BS is shown in Table 3.8. The corresponding ductility based equations obtained using nonlinear regression analysis are given in Equation (3.10)

Table 3.8 *s, b, C, k, n, T_1* and *T_2* values: soil class C and hysteretic model BS

	μ	s	b	T_1	C	T_2	k	n
					Variable			
mean + σ	1	1.461	-0.0415	0.374	0.505	1.847	0.811	-0.771
	2	1.462	0.0164	0.317	0.480	1.382	0.592	-0.646
	3	1.534	0.0382	0.283	0.472	1.074	0.491	-0.567
	4	1.555	0.0564	0.26	0.461	0.940	0.446	-0.535
	5	1.578	0.0695	0.247	0.460	0.846	0.421	-0.529
mean + 2σ	1	1.672	-0.0367	0.393	0.621	1.889	1.032	-0.798
	2	1.653	0.0237	0.329	0.567	1.451	0.717	-0.630
	3	1.747	0.046	0.285	0.543	1.185	0.596	-0.546
	4	1.762	0.0678	0.262	0.529	1.033	0.538	-0.515
	5	1.802	0.081	0.248	0.529	0.930	0.509	-0.514

$$s = 0.0326\mu + 1.420$$
$$b = -0.0067\mu^2 + 0.0661\mu - 0.0973$$
$$T_1 = 0.376\mu^{-0.261}$$
$$C = 0.0032\mu^2 - 0.0303\mu + 0.531$$
$$T_2 = 0.0654\mu^2 - 0.637\mu + 2.409$$
$$k = 0.0316\mu^2 - 0.282\mu + 1.051$$
$$\underbrace{n = -0.0205\mu^2 + 0.183\mu - 0.931}_{mean+\sigma}$$

$$s = 0.037\mu + 1.617$$
$$b = -0.0068\mu^2 + 0.0686\mu - 0.0949$$
$$T_1 == 0.396\mu^{-0.292}$$
$$C = 0.0083\mu^2 - 0.0723\mu + 0.683 \qquad (3.10)$$
$$T_2 = 0.0559\mu^2 - 0.569\mu + 2.39$$
$$k = 0.0454\mu^2 - 0.395\mu + 1.363$$
$$\underbrace{n = -0.0275\mu^2 + 0.234\mu - 0.999}_{mean+2\sigma}$$

3.6 Input Energy Spectra for Site Class D

A total of 38 ground motion records has been selected and used in developing the energy spectra

for site class D. The PGA of the ensemble ranges from 0.11g to 0.22g, and the *PGV* ranges from

11.3 cm/s to 38.1 cm/s. The set of earthquakes was scaled to match the target spectrum which

was developed using PEER NGA models using parameters applicable to site class D. After

scaling, the *PGA* and *PGV* ranges were found to be 0.08g to 0.47g and 8.38 cm/s to 75.47 cm/s,

respectively. Upon scaling the lower limit in the range has decreased and this may seem to

contradict the expected result. This is acceptable because scaling is performed on the ground

motion, not on the ground motion components. In such cases one of the components might have

higher *PGA/PGV* compared to the other and upon scaling the lower values could be further

scaled down. Figure 3.20 shows the mean spectra of the selected ground motion records

ensemble and the target spectra used for scaling the ground motion records.
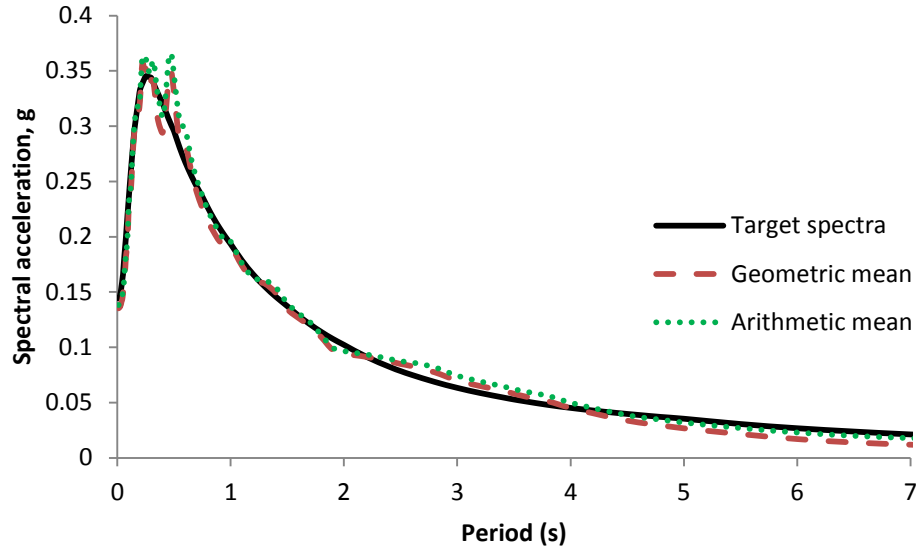
Figure 3.20 Relation between mean and target Spectra for site D

3.6.1 Hysteretic Model: Bilinear Plastic, BP

The mean+σ and mean+2σ *VI* normalized input energy spectra for SDOF structures with hysteretic model BP and ductility values of μ = 1, 2, 3, 4, 5 located in site class D are shown in Figure 3.21. The values of the variables used to define the input energy spectra are given in Table 3.9. Like that of site class B, the input energy spectral values decrease with an increase in ductility value for both the mean+σ and mean+2σ spectra. From Figure 3.21, it can be easily seen that the decrease in input energy with an increase in ductility value is more distinct at low ductility values (μ=1-3) than the rate of decrement decreases at higher ductility values (μ=3-5). This reinforces the observation made for class sites B and C that beyond some ductility value, the amount of input energy in SDOF systems can be considered to be insensitive to ductility. The values of the input spectra shape parameters in Table 3.9 were curve-fitted through nonlinear regression analysis. The resulting simple expressions are given in Equation (3.11).
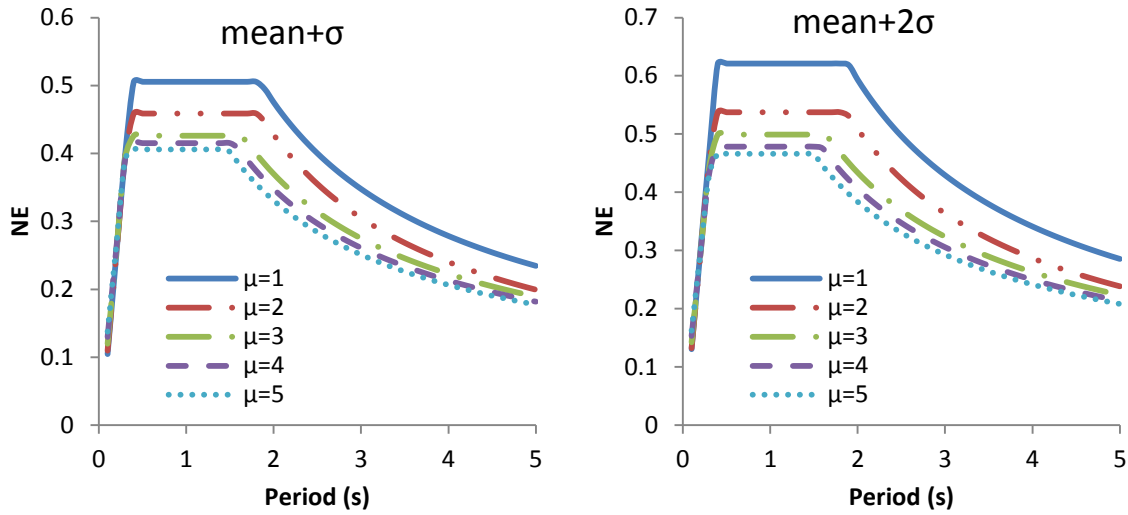
61

Figure 3.21 *NE* spectra: hysteretic model BP and site class D

Table 3.9 *s, b, C, k, n, T₁* and *T₂* values: soil class D and hysteretic model BP

	μ				Variable			
		s	b	T_1	C	T_2	k	n
mean+σ	1	1.021	-0.00796	0.569	0.573	2.186	0.80	-0.425
	2	1.041	-0.00607	0.498	0.512	2.083	0.731	-0.485
	3	1.021	0.00155	0.458	0.469	2.057	0.645	-0.441
	4	1.026	0.00688	0.428	0.446	2.047	0.647	-0.518
	5	1.023	0.0134	0.409	0.432	2.035	0.618	-0.505
mean+2σ	1	1.176	0.00671	0.593	0.704	2.182	0.904	-0.320
	2	1.187	0.00787	0.509	0.613	2.092	0.84	-0.428
	3	1.145	0.0172	0.466	0.551	2.055	0.728	-0.388
	4	1.137	0.0243	0.434	0.517	2.041	0.692	-0.408
	5	1.117	0.0332	0.415	0.497	2.045	0.68	-0.438

$$
\begin{aligned}
s &= -0.0011\mu + 1.03 \\
b &= 0.0056\mu - 0.0151 \\
T_1 &= 0.571\mu^{-0.206} \\
C &= 0.008\mu^2 - 0.0831\mu + 0.647 \\
T_2 &= 0.0142\mu^2 - 0.119\mu + 2.282 \\
k &= 0.0118\mu^2 - 0.116\mu + 0.905 \\
n &= -0.001\mu^2 - 0.0174\mu - 0.404
\end{aligned}
\qquad
\begin{aligned}
s &= -0.0168\mu + 1.203 \\
b &= 0.0069\mu - 0.0029 \\
T_1 &= 0.594\mu^{-0.224} \\
C &= 0.0122\mu^2 - 0.124\mu + 0.815 \\
T_2 &= 0.0151\mu^2 - 0.123\mu + 2.286 \\
k &= 0.0128\mu^2 - 0.137\mu + 1.038 \\
n &= 0.0067\mu^2 - 0.062\mu - 0.284
\end{aligned}
\qquad (3.11)
$$

$$\underbrace{}_{mean+\sigma} \qquad\qquad \underbrace{}_{mean+2\sigma}$$

3.6.2 Hysteretic Model: Stiffness Degradation, SD

Figure 3.22 shows the mean+σ and mean+2σ *VI* normalized input energy spectra for SDOF

structures with ductility values of $\mu = 1, 2, 3, 4, 5$ and hysteretic behavior type SD located in site

class D. The pattern of change in input energy with respect to ductility value was observed to be

similar to the pattern seen for SDOF structures with hysteretic behavior type BP. The amount of

input energy decreases with an increase in the ductility value. For instance, in the intermediate

region of the VI normalized mean+σ energy spectra, the decrease in the maximum values is

15%, 5%, 2%, and 2% between $\mu=1\&2$, $\mu=2\&3$, $\mu=3\&4$, and $\mu=4\&5$, respectively. The

corresponding values for the mean+2σ spectra are 18%, 6%, 3 % and 2.5%. Compared to

hysteretic model BP, the decrease in the input energy spectral values when ductility increases is

relatively higher for hysteretic model SD.

The values of the variable used to define the input energy spectra shown in Figure 3.22 are given

in Table 3.10. Through regression analysis, simple expressions expressed as a function of

ductility value are given in Equation (3.12).
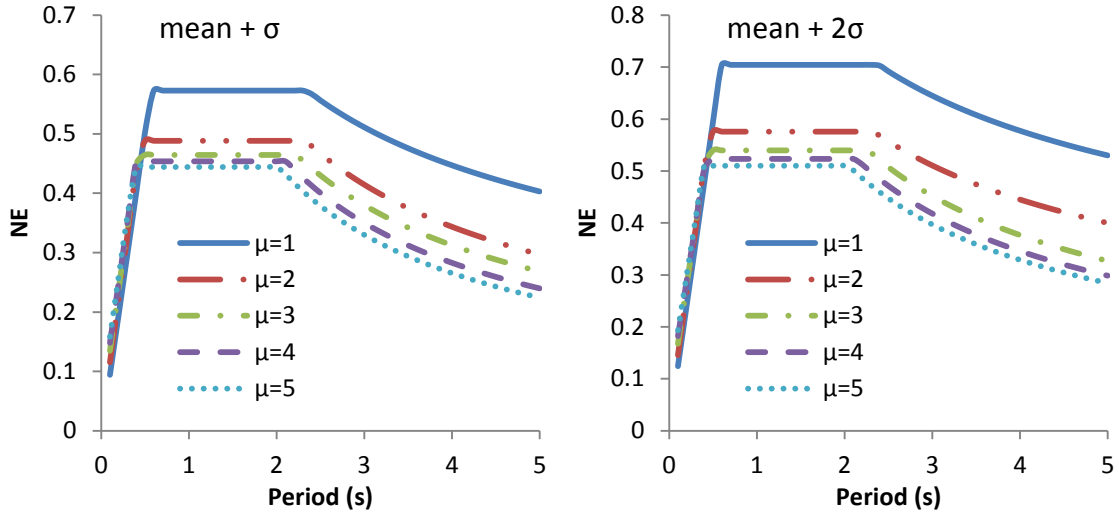
Figure 3.22 *NE* spectra: hysteretic model SD and site class D

Table 3.10 *s, b, C, k, n, T_1* and *T_2* values: soil class D and hysteretic model SD

	μ	s	b	T_1	C	T_2	k	n
					Variable			
mean + σ	1	1.021	-0.00796	0.569	0.573	2.348	0.852	-0.465
	2	1.075	0.00785	0.447	0.488	2.334	0.849	-0.653
	3	1.047	0.03	0.415	0.465	2.233	0.802	-0.680
	4	1.017	0.0463	0.401	0.454	2.113	0.79	-0.741
	5	1.024	0.0561	0.379	0.444	2.025	0.757	-0.756
mean + 2σ	1	1.176	0.00671	0.593	0.704	2.386	0.984	-0.384
	2	1.206	0.0249	0.457	0.576	2.335	0.864	-0.478
	3	1.136	0.0539	0.428	0.54	2.269	0.907	-0.634
	4	1.071	0.0751	0.419	0.523	2.133	0.862	-0.659
	5	1.068	0.0866	0.396	0.510	2.045	0.814	-0.654

$$s = -0.0053\mu + 1.053$$
$$b = 0.0167\mu - 0.0235$$
$$T_1 = 0.553\mu^{-0.245}$$
$$C = 0.0117\mu^2 - 0.0991\mu + 0.654$$
$$T_2 = -0.0119\mu^2 - 0.0156\mu + 2.388$$
$$k = -0.0017\mu^2 - 0.0148\mu + 0.873$$
$$\underbrace{n = 0.0222\mu^2 - 0.2\mu - 0.303}_{mean+\sigma}$$

$$s = -0.0351\mu + 1.237$$
$$b = 0.021\mu - 0.0136$$
$$T_1 = 0.571\mu^{-0.241}$$
$$C = 0.0179\mu^2 - 0.151\mu + 0.828 \qquad (3.12)$$
$$T_2 = -0.0101\mu^2 - 0.0276\mu + 2.428$$
$$k = 0.004\mu^2 - 0.0581\mu + 1.016$$
$$\underbrace{n = 0.0235\mu^2 - 0.213\mu - 0.182}_{mean+2\sigma}$$

3.6.3   Hysteretic Model: Bilinear Flag, BF

Figure 3.23 shows the mean+σ and mean+2σ input energy spectra for SDOF structures with hysteretic behavior type BF located at site class D. In the short period region, no significant difference in input energy for the different ductility values for both the mean+σ and mean+2σ input energy spectra is observed. It may be postulated that in the short period region (0.1-0.75 s approximately), ductility value does not significantly affect the input energy for SDOF structures with hysteretic behavior type BF. However, for longer periods, the input energy values tend to decrease with an increase in ductility value. For instance, for the mean+σ spectra the decrease in the amount of input energy is 11%, 7%, 3%, and 2% between $\mu=1\&2$, $\mu=2\&3$, $\mu=3\&4$, and $\mu=4\&5$, respectively. The corresponding values for the mean+2σ spectra are 14%, 9%, 3 % and 2%. Table 3.11 gives the values of the variables that define the input energy spectra shown in Figure 3.23 and Equation (3.13) gives expressions for those variables, obtained using nonlinear regression analysis, as a function of ductility.
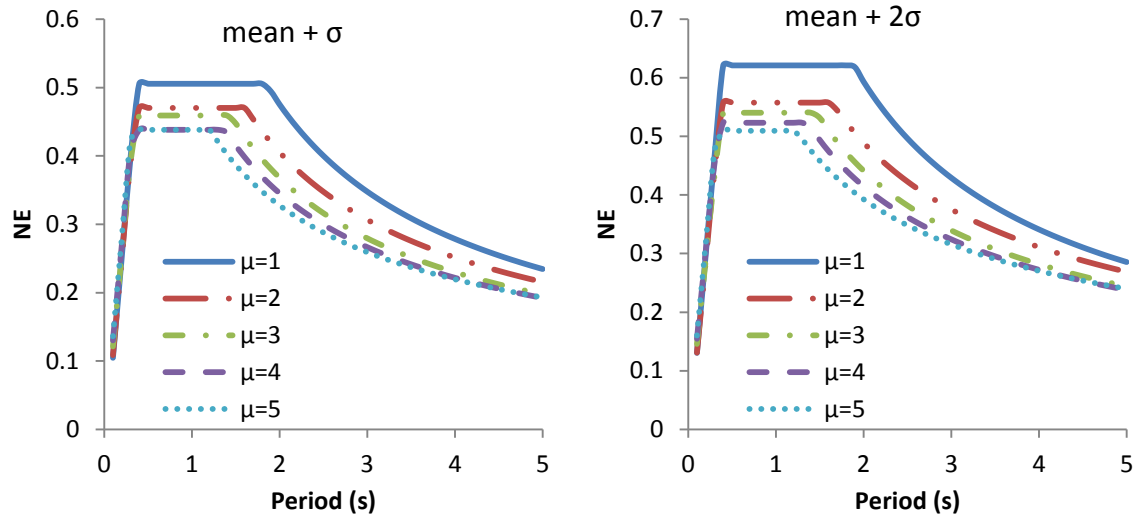
Figure 3.23 *NE* spectra: hysteretic model BF and site class D

Table 3.11 *s, b, C, k, n, T₁* and *T₂* values: soil class D and hysteretic model BF

	μ	s	b	T_1	C	T_2	k	n
					Variable			
mean + σ	1	1.021	-0.00796	0.569	0.573	2.884	1.201	-0.699
	2	1.092	-0.0105	0.473	0.506	2.661	1.03	-0.726
	3	1.122	-0.00803	0.428	0.472	2.511	0.92	-0.725
	4	1.087	0.0023	0.419	0.458	2.314	0.865	-0.759
	5	1.126	0.00463	0.395	0.449	2.235	0.861	-0.809
mean + 2σ	1	1.176	0.00671	0.593	0.704	2.748	1.175	-0.507
	2	1.256	0.00253	0.481	0.607	2.702	1.058	-0.56
	3	1.273	0.00596	0.428	0.551	2.676	0.986	-0.591
	4	1.205	0.0208	0.428	0.536	2.476	1.044	-0.735
	5	1.245	0.0236	0.405	0.528	2.398	1.071	-0.809

$$s = 0.0204\mu + 1.029$$
$$b = 0.0038\mu - 0.0153$$
$$T_1 = 0.561\mu^{-0.223}$$
$$C = 0.0097\mu^2 - 0.0879\mu + 0.649$$
$$T_2 = 0.0171\mu^2 - 0.267\mu + 3.134$$
$$k = 0.0277\mu^2 - 0.251\mu + 1.423$$
$$\underbrace{n = -0.0058\mu^2 + 0.0093\mu - 0.708}_{mean+\sigma}$$

$$s = -0.0117\mu^2 + 0.0793\mu + 1.123$$
$$b = 0.0018\mu^2 - 0.0057\mu + 0.009$$
$$T_1 = 0.579\mu^{-0.235}$$
$$C = 0.0156\mu^2 - 0.136\mu + 0.822 \qquad (3.13)$$
$$T_2 = -0.017\mu^2 + 0.0096\mu + 2.758$$
$$k = 0.0299\mu^2 - 0.202\mu + 1.343$$
$$\underbrace{n = -0.0111\mu^2 - 0.0114\mu - 0.484}_{mean+2\sigma}$$

3.6.4 Hysteretic Model: Bilinear Slip, BS

The mean+σ and mean+2σ *VI* normalized input energy spectra for SDOF structures with

hysteretic behavior type BS located at site class D are shown in Figure 3.24. The values of the

variables used to define the spectra are given in Table 3.12. These values were also used to

develop the simple expressions, an alternative to the tabulated values, given in Equation (3.14)

that define the design input energy for SDOF structures with hysteretic model BS and ductility

values of μ=1, 2, 3, 4, 5. Unlike the case of hysteretic models BP, SD and BF, input energy

spectral values in the short period range have been observed to increase with an increase in

ductility value. For instance, at a period of 0.3s, the spectral values for mean+σ are 0.3, 0.37,

0.41, 0.44, 0.46 and for mean+2σ the values are 0.36, 0.43, 0.47, 0.5, 0.52 for ductility values of

μ=1, 2, 3, 4, 5, respectively. Even though this increase in normalized spectral energy with an

increase in ductility value is minimal, it does signify that the relationship of ductility and input

energy of SDOF structures is not always inversely proportional. For SDOF with hysteretic type

BS, ductility amplifies the input energy in the short period region.
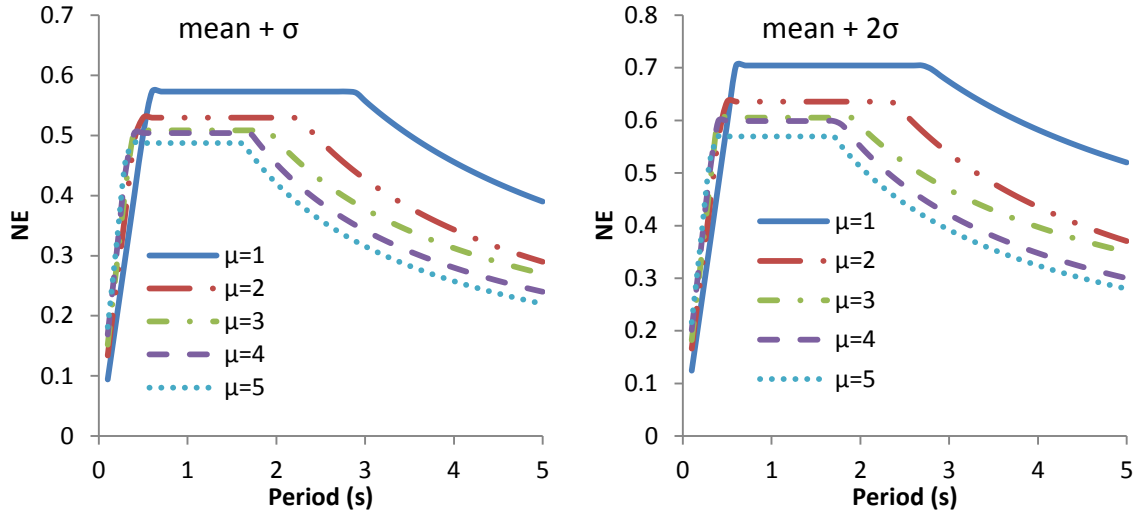
Figure 3.24 Normalized input energy spectra: hysteretic model BS and site class D

Table 3.12 s, b, C, k, n, T_1 and T_2 values: soil class D and hysteretic model BS

	μ	s	b	T_1	C	T_2	k	n
					Variable			
mean + σ	1	1.021	-0.00796	0.569	0.573	2.884	1.201	-0.699
	2	1.192	0.0148	0.432	0.529	2.261	0.984	-0.759
	3	1.30	0.022	0.374	0.508	2.130	0.928	-0.795
	4	1.351	0.0338	0.348	0.504	1.885	0.843	-0.813
	5	1.381	0.0433	0.321	0.487	1.831	0.816	-0.852
mean + 2σ	1	1.176	0.00671	0.593	0.704	2.748	1.175	-0.507
	2	1.329	0.0334	0.453	0.636	2.377	1.191	-0.725
	3	1.437	0.0386	0.394	0.605	2.237	1.114	-0.758
	4	1.478	0.054	0.369	0.599	1.992	1.044	-0.807
	5	1.507	0.0657	0.334	0.569	1.974	0.996	-0.823

$$s = 0.0878\mu + 0.986$$
$$b = 0.0122\mu - 0.0153$$
$$T_1 = 0.561\mu^{-0.352}$$
$$C = 0.005\mu^2 - 0.0498\mu + 0.615$$
$$T_2 = 0.0731\mu^2 - 0.687\mu + 3.454$$
$$k = 0.0251\mu^2 - 0.242\mu + 1.403$$
$$\underbrace{n = 0.0043\mu^2 - 0.0618\mu - 0.645}_{mean+\sigma}$$

$$s = 0.0811\mu + 1.142$$
$$b = 0.0139\mu - 0.0019$$
$$T_1 = 0.587\mu^{-0.349}$$
$$C = 0.0073\mu^2 - 0.0747\mu + 0.766 \qquad (3.14)$$
$$T_2 = 0.0428\mu^2 - 0.450\mu + 3.145$$
$$k = -0.0086\mu^2 + 0.0008\mu + 1.196$$
$$\underbrace{n = 0.0278\mu^2 - 0.238\mu - 0.316}_{mean+2\sigma}$$

3.7 Input Energy Spectra for Site Class E

A total of 26 earthquake records have been selected and used for developing the input energy spectra for site class E. Compared to the other soil site classes, there are very few earthquakes recorded at site class E, and among which only a few of these records meet the selection criteria set forth. As a result, only a small size ensemble of earthquakes was used. The target spectrum was developed in a similar manner as for the other site classes using PEER NGA models produced using relevant parameters for site class E. The mean spectra of the selected ensemble of ground motion records are presented along with the target spectrum in Figure 3.25 for easy comparison. The correlation coefficients between the geometric mean and the target spectra as well as between the arithmetic mean and the target spectra are both 0.97. The correlation coefficients are slightly less than those obtained for soil classes B, C, and D, but are high enough to ensure a strong correlation between the mean spectra of the models and the mean spectra of the ensemble of 26 earthquakes. These 26 earthquake records have been used to develop the input energy spectra for SDOF structures with the four different hysteretic models (BP, SD, BF and BS) located at soil site class E.
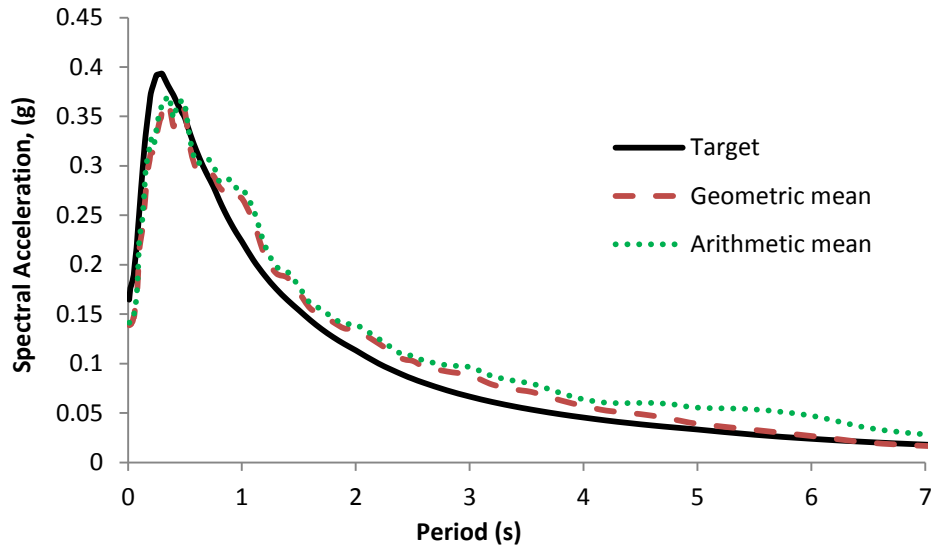
Figure 3.25 Relation between mean and target spectra for site class E

Similar to the previous cases, an extensive time history spectral analysis has been performed

using BISPEC (2010) for SDOF structures (with hysteretic models: BP, SD, BF and BS)

subjected to the 26 ground motion records selected for site class E. A summary of the analysis

results and discussions for each hysteretic model type are presented below.

3.7.1 Hysteretic Model: Bilinear Plastic, BP

The mean+σ and mean+2σ VI normalized input energy spectra for SDOF structures with

ductility values of $\mu = 1, 2, 3, 4, 5$ and hysteretic model BP located at site class E are shown in

Figure 3.26. These normalized input energy spectra were plotted using the spectral variables

given in Table 3.13. Note that the input energy spectral values decrease with an increase in

ductility value for both the mean+σ and mean+2σ spectra in the intermediate and long period

regions, i.e., they exhibit the same trend as those for site classes B, C, and D. However, the

decrease in input energy with an increase in ductility value is not uniform. The rate is higher at

low ductility values (μ=1-3) and diminishes at higher ductility values (μ=3-5). Similar

observations have been made for site classes B, C, and D. In an effort to develop simple

expressions for the input energy spectra, the values of spectral variables in Table 3.13 were curve-fitted using nonlinear regression analysis. The resulting expressions are given in Equation (3.15).
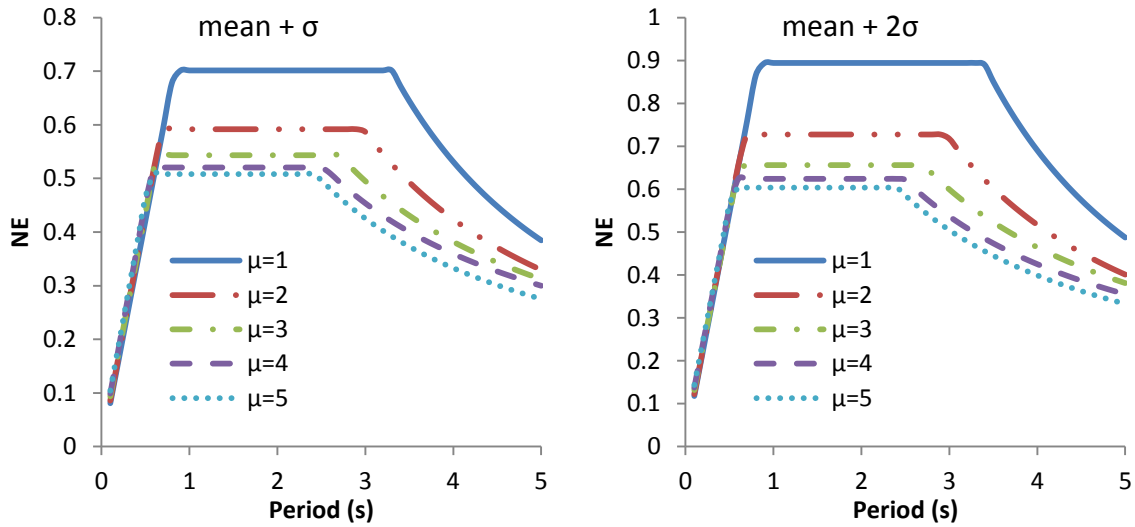
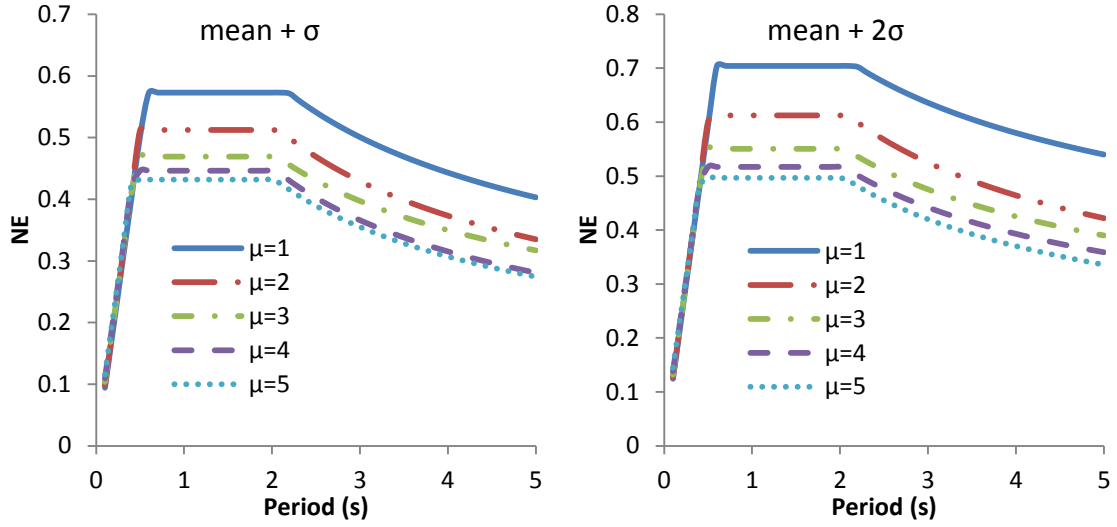**Figure 3.26** *NE* **spectra: hysteretic model BP and site class E**

Table 3.13 *s, b, C, k, n, T₁* and *T₂* values: soil class E and hysteretic model BP

	μ	s	b	T_1	C	T_2	k	n
					Variable			
mean + σ	1	0.853	-0.00445	0.828	0.701	3.301	3.952	-1.448
	2	0.873	-0.00147	0.68	0.592	2.978	2.031	-1.130
	3	0.856	0.008	0.625	0.543	2.706	1.334	-0.902
	4	0.891	0.00974	0.573	0.520	2.533	1.106	-0.811
	5	0.903	0.013	0.547	0.508	2.435	1.084	-0.852
mean + 2σ	1	1.069	0.011	0.827	0.894	3.390	6.027	-1.563
	2	1.068	0.0153	0.667	0.727	2.964	2.509	-1.139
	3	1.021	0.0297	0.613	0.656	2.71	1.588	-0.887
	4	1.046	0.0328	0.565	0.624	2.489	1.304	-0.808
	5	1.051	0.0383	0.538	0.604	2.407	1.235	-0.815

$$s = 0.0118\mu + 0.84 \qquad\qquad s = -0.0057\mu + 1.068$$
$$b = 0.0048\mu - 0.0092 \qquad\qquad b = 0.0072\mu + 0.0037$$
$$T_1 = 0.823\mu^{-0.257} \qquad\qquad T_1 = 0.818\mu^{-0.265}$$
$$C = 0.0157\mu^2 - 0.140\mu + 0.821 \qquad\qquad C = 0.0237\mu^2 - 0.211\mu + 1.073 \qquad (3.15)$$
$$T_2 = 3.338\mu - 0.194 \qquad\qquad T_2 = 3.413\mu^{-0.218}$$
$$k = 0.305\mu^2 - 2.495\mu + 6.033 \qquad\qquad k = 0.538\mu^2 - 4.308\mu + 9.536$$
$$\underbrace{n = -0.0609\mu^2 + 0.517\mu - 1.908}_{mean+\sigma} \qquad\qquad \underbrace{n = -0.0738\mu^2 + 0.626\mu - 2.107}_{mean+2\sigma}$$

3.7.2 Hysteretic Model: Stiffness Degradation, SD

Shown in Figure 3.27 are the mean+σ and mean+2σ *VI* normalized input energy spectra for

SDOF structures with ductility values of $\mu = 1, 2, 3, 4, 5$ and hysteretic behavior type SD located

in site class E.   Even though rather insignificant, the spectral values increase with an increase in

ductility value in the short period region. This indicates that highly stiff structures (structures

with short periods of vibration) located in site class E could experience more input energy with

an increase in ductility value. However, in the intermediate and long period regions, the spectral

values decrease with an increase in ductility value.   Also, it can be seen that the rate of

decrement in the amount of input energy decreases with an increase in the ductility value. For

instance, in the constant region of the mean+σ *VI* normalized energy spectra, the decrease in

spectral values by 17%, 6%, 2%, and 2% between $\mu=1\&2$, $\mu=2\&3$, $\mu=3\&4$, and $\mu=4\&5$,

respectively, is observed. The corresponding decreases for the mean+2σ spectra are 21%, 8%, 2

% and 2%, respectively.

The variables used to define the spectra shown in Figure 3.22 are given in Table 3.10. Through

nonlinear regression analysis, simple input energy spectra expressions expressed as a function of

ductility value and are given in Equation (3.16).
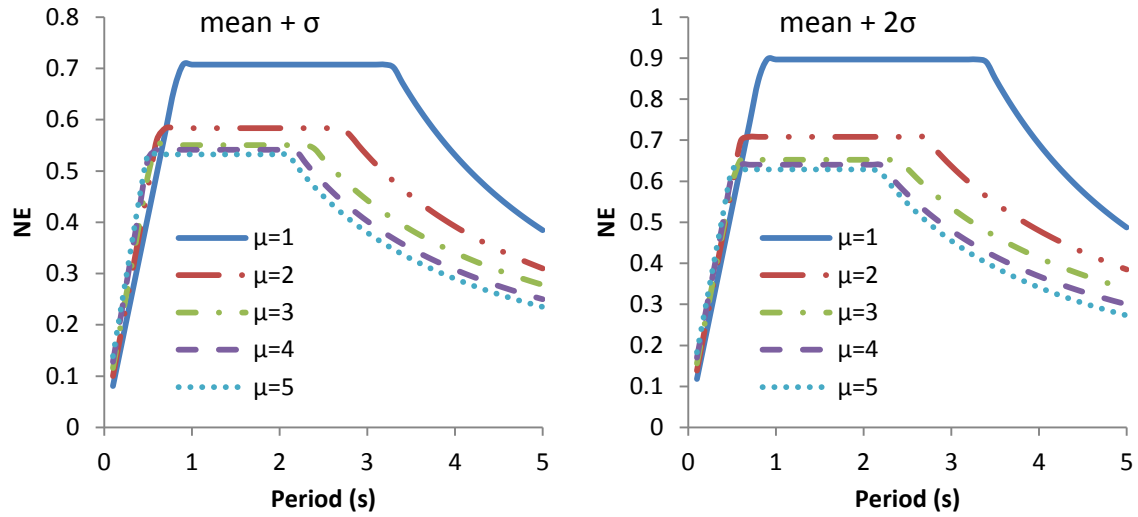
Figure 3.27 *NE* spectra: hysteretic model SD and site class E

Table 3.14 *s, b, C, k, n, T_1* and *T_2* values: soil class E and hysteretic model SD

	μ				Variable			
		s	*b*	*T_1*	*C*	*T_2*	*k*	*n*
mean + σ	1	0.828	-0.00211	0.857	0.707	3.282	3.952	-1.448
	2	0.920	0.00821	0.625	0.584	2.741	1.686	-1.052
	3	0.94	0.0217	0.563	0.550	2.365	1.207	-0.912
	4	0.988	0.0291	0.519	0.541	2.181	1.119	-0.931
	5	1.023	0.0366	0.485	0.532	2.095	1.067	-0.94
mean + 2σ	1	1.039	0.0142	0.849	0.897	3.385	6.027	-1.563
	2	1.119	0.0266	0.609	0.708	2.695	1.883	-0.986
	3	1.093	0.0467	0.554	0.652	2.410	1.441	-0.901
	4	1.110	0.059	0.523	0.640	2.196	1.322	-0.921
	5	1.131	0.07	0.494	0.629	2.171	1.365	-1

$$
\begin{aligned}
s &= 0.0456\mu + 0.803 \\
b &= 0.0098\mu - 0.0108 \\
T_1 &= 0.833\mu - 0.348 \\
C &= 0.0181\mu^2 - 0.148\mu + 0.828 \\
T_2 &= 3.293\mu^{-0.289} \\
k &= 0.344\mu^2 - 2.699\mu + 6.116 \\
n &= -0.069\mu^2 + 0.528\mu - 1.881
\end{aligned}
\qquad
\begin{aligned}
s &= -0.0053\mu^2 + 0.0493\mu + 1.009 \\
b &= 0.0144\mu \\
T_1 &= 0.815\mu^{-0.33} \\
C &= 0.0284\mu^2 - 0.231\mu + 1.085 \\
T_2 &= 3.336\mu^{-0.286} \\
k &= 0.621\mu^2 - 4.715\mu + 9.721 \\
n &= -0.101\mu^2 + 0.726\mu - 2.139
\end{aligned}
\qquad (3.16)
$$

$$\underbrace{}_{mean+\sigma} \qquad\qquad \underbrace{}_{mean+2\sigma}$$

3.7.3   Hysteretic Model: Bilinear Flag BF

Figure 3.28 shows the mean+σ and mean+2σ *VI* normalized input energy spectra for SDOF

structures with hysteretic behavior type BF and located at site class E. Similar to the BP

hysteretic model, the effect of ductility value on the input energy for SDOF structures is

insignificant in the short period region. A distinct effect of ductility; however, was observed in

the intermediate and long period regions of input energy spectra, especially when the ductility

value range is between $\mu=1$ and $\mu=3$. In these regions, the spectra input energy values decrease

with an increase in ductility value. For instance, in the intermediate period region, the decrease

in the amount of input energy for the mean+σ spectra is approximately 7%, 5%, 3%, and ≈0%

between $\mu=1\&2$, $\mu=2\&3$, $\mu=3\&4$, and $\mu=4\&5$, respectively. The corresponding decreases for

the *mean+2σ* spectra are 12%, 7%, 4 % and 2%, respectively. Table 3.15 gives values of the

variables that define the input energy spectra shown in Figure 3.28. Equation (3.17) gives

alternative simple expressions for the variables as a function of ductility developed using

nonlinear regression analysis of the corresponding values given in Table 3.15.
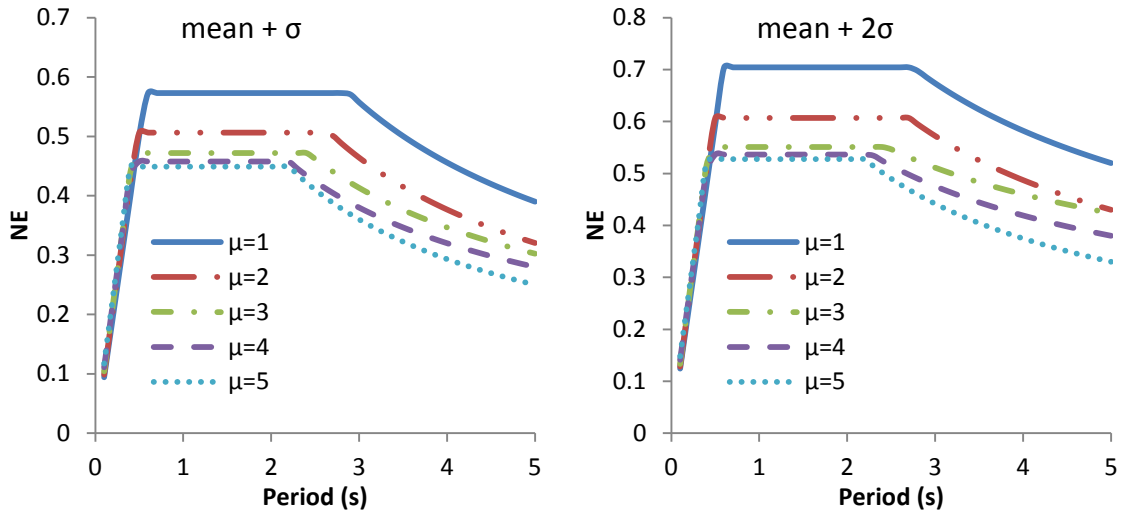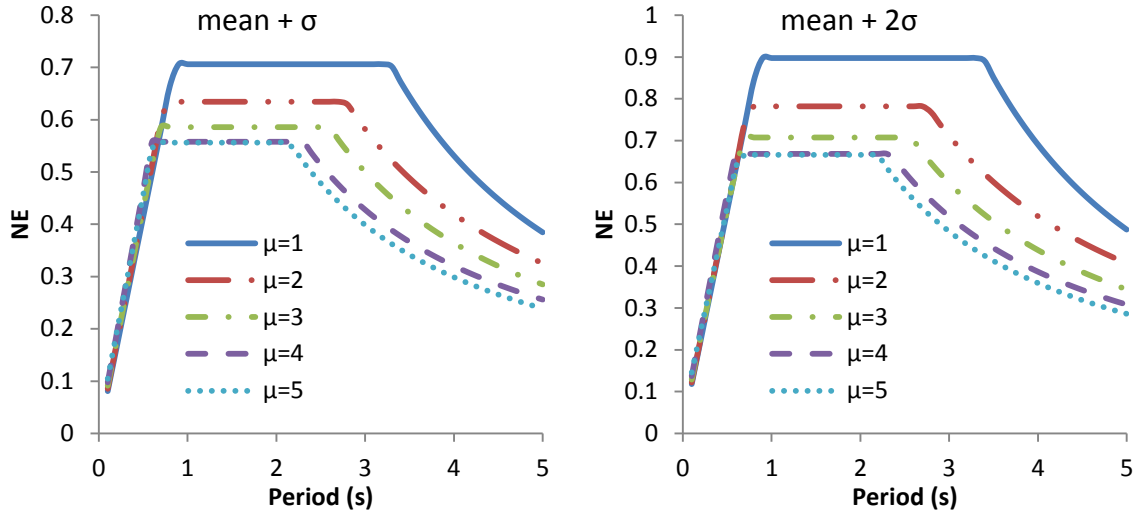
Figure 3.28 *NE* spectra: hysteretic model BF and site class E

Table 3.15 *s*, *b*, *C*, *k*, *n*, T_1 and T_2 values: soil class E and hysteretic model BF

	μ	*s*	*b*	T_1	*C*	T_2	*k*	*n*
					Variable			
mean + σ	1	0.833	-0.00243	0.850	0.706	3.286	3.952	-1.448
	2	0.857	-0.00038	0.740	0.634	2.780	2.029	-1.137
	3	0.849	0.0064	0.683	0.586	2.496	1.512	-1.037
	4	0.92	0.00566	0.6	0.558	2.304	1.291	-1.005
	5	0.879	0.0165	0.614	0.556	2.151	1.198	-1.
mean + 2σ	1	1.037	0.0143	0.852	0.897	3.383	6.027	-1.563
	2	1.038	0.018	0.736	0.782	2.752	2.366	-1.094
	3	1.01	0.0277	0.673	0.707	2.489	1.81	-1.03
	4	1.094	0.0275	0.586	0.668	2.339	1.59	-1.02
	5	0.985	0.0471	0.628	0.666	2.193	1.49	-1.025

75

$$s = 0.0154\mu + 0.821 \qquad\qquad s = -0.0047\mu + 1.047$$
$$b = 0.0044\mu - 0.008 \qquad\qquad b = 0.0075\mu + 0.0044$$
$$T_1 = 0.854\mu^{-0.22} \qquad\qquad T_1 = 0.85\mu^{-0.219}$$
$$C = 0.0115\mu^2 - 0.107\mu + 0.801 \qquad\qquad C = 0.0187\mu^2 - 0.17\mu + 1.048 \qquad (3.17)$$
$$T_2 = 33.308\mu^{-0.262} \qquad\qquad T_2 = 3.354\mu^{-0.266}$$
$$k = 0.283\mu^2 - 2.32\mu + 5.848 \qquad\qquad k = 0.533\mu^2 - 4.181\mu + 9.34$$
$$\underbrace{n = -0.0487\mu^2 + 0.395\mu - 1.774}_{mean+\sigma} \qquad\qquad \underbrace{n = -0.0716\mu^2 + 0.544\mu - 1.992}_{mean+2\sigma}$$

3.7.4 Hysteretic Model: Bilinear Slip, BS

The mean+σ and mean+2σ *VI* normalized input energy spectra for SDOF structures with

hysteretic behavior type of bilinear slip and site class E are shown in Figure 3.29. The graphs

were created using the values of the variables given in Table 3.16. These values were also used

to develop simple ductility based general expressions given in Equation (3.18) for five ductility

values of μ=1, 2, 3, 4, 5. Figure 3.29 shows that the input energy spectral values increase with an

increase in ductility value in the short period region. This energy-ductility relationship is similar

to that of the hysteretic model SD and to some extent to that of the hysteretic models BP and BF.

For instance, consider the input energy for a SDOF structure with a period of vibration of 0.3 s (a

point in the straight line portion of the spectra, i.e., the short period region) the mean+σ spectral

values are 0.25, 0.33, 0.36, 0.40, 0.43, and the mean+2σ spectral values are 0.33, 0.41, 0.44,

0.48, 0.51 for ductility values of μ=1, 2, 3., 4, 5, respectively.
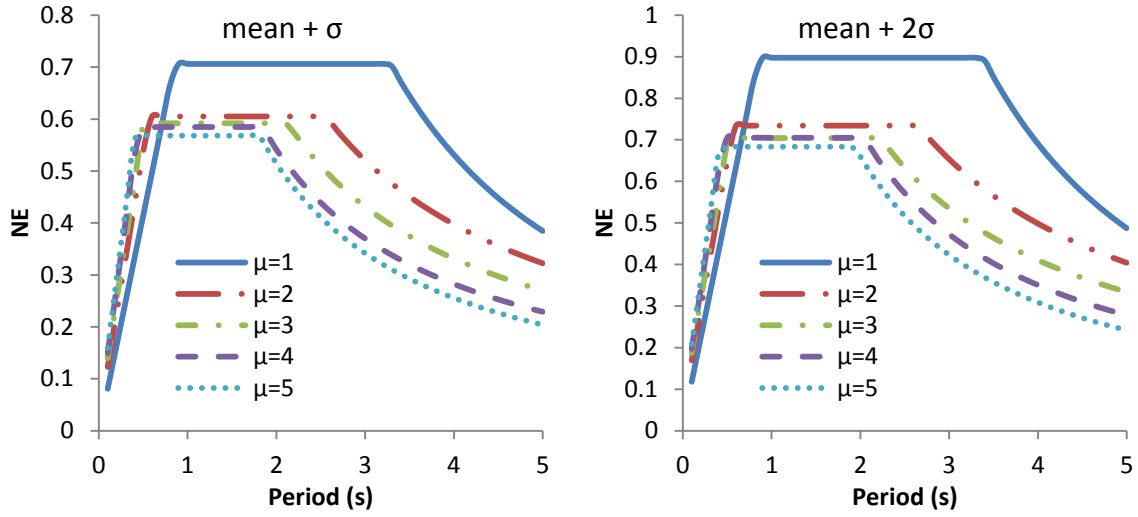
Figure 3.29 *NE* spectra: hysteretic model BS and site class E

Table 3.16 *s, b, C, k, n, T_1* and *T_2* values: soil class E and hysteretic model BS

		Variable						
	μ	s	b	T_1	C	T_2	k	n
mean + σ	1	0.833	-0.00243	0.850	0.706	3.286	3.952	-1.448
	2	1.037	0.0192	0.565	0.605	2.556	1.459	-0.938
	3	1.121	0.0271	0.504	0.592	2.125	1.182	-0.917
	4	1.261	0.0229	0.445	0.585	1.843	1.038	-0.939
	5	1.336	0.0256	0.406	0.568	1.813	1.036	-1.01
mean + 2σ	1	1.037	0.0143	0.852	0.897	3.383	6.027	-1.563
	2	1.199	0.0496	0.571	0.734	2.651	1.837	-0.941
	3	1.250	0.0622	0.513	0.704	2.227	1.474	-0.922
	4	1.412	0.0557	0.46	0.705	2.043	1.482	-1.04
	5	1.514	0.0572	0.414	0.683	1.937	1.409	-1.094

$$s = 0.123\mu + 0.749$$
$$b = 0.006\mu + 0.0005$$
$$T_1 = 0.822\mu^{-0.449}$$
$$C = 0.0125\mu^2 - 0.105\mu + 0.787$$
$$T_2 = 3.292\mu^{-0.39}$$
$$k = 0.365\mu^2 - 2.818\mu + 6.167$$
$$\underbrace{n = -0.0859\mu^2 + 0.603\mu - 1.914}_{mean+\sigma}$$

$$s = 0.117\mu + 0.932$$
$$b = 0.0092\mu + 0.0202$$
$$T_1 = 0.824\mu^{-0.434}$$
$$C = 0.0224\mu^2 - 0.180\mu + 1.039 \qquad (3.18)$$
$$T_2 = 3.368\mu^{-0.356}$$
$$k = 0.615\mu^2 - 4.647\mu + 9.625$$
$$\underbrace{n = -0.106\mu^2 + 0.722\mu - 2.108}_{mean+2\sigma}$$

3.8 Effect of Site Soil Characteristics on Input Energy

In the preceding sections, the mean+σ and mean+2σ *VI* normalized input energy spectra have been developed and discussed for SDOF systems with BP, SD, BF and BS hysteretic behavior for five levels of ductility μ=1, 2, 3, 4,and 5, and four soil site types B,C, D and E. Although it is not the intention of this study to investigate soil-structure interaction in details, it is of interest to see how different soil site classes can affect the input energy spectra. This can be accomplished by keeping the hysteretic type and ductility value the same while varying the soil category.

Figures 3.30 to 3.33 show the effect of soil site class on the *VI* normalized input energy spectra for SDOF systems with the four different hysteretic types considered in this study. For brevity, only figures corresponding to SDOF systems with two ductility values of μ=1 and 3 are presented here. The complete set of figures that encompasses all five ductility values of μ=1, 2, 3, 4, 5, the four soil site classes, and the four hysteretic models considered in this study can be found in Appendix B. It should be noted that for ductility value of μ=1, the input energy spectra remain the same regardless of the hysteretic type used. This is because when μ=1 the system is elastic, and so the input energy is independent of the hysteretic type.
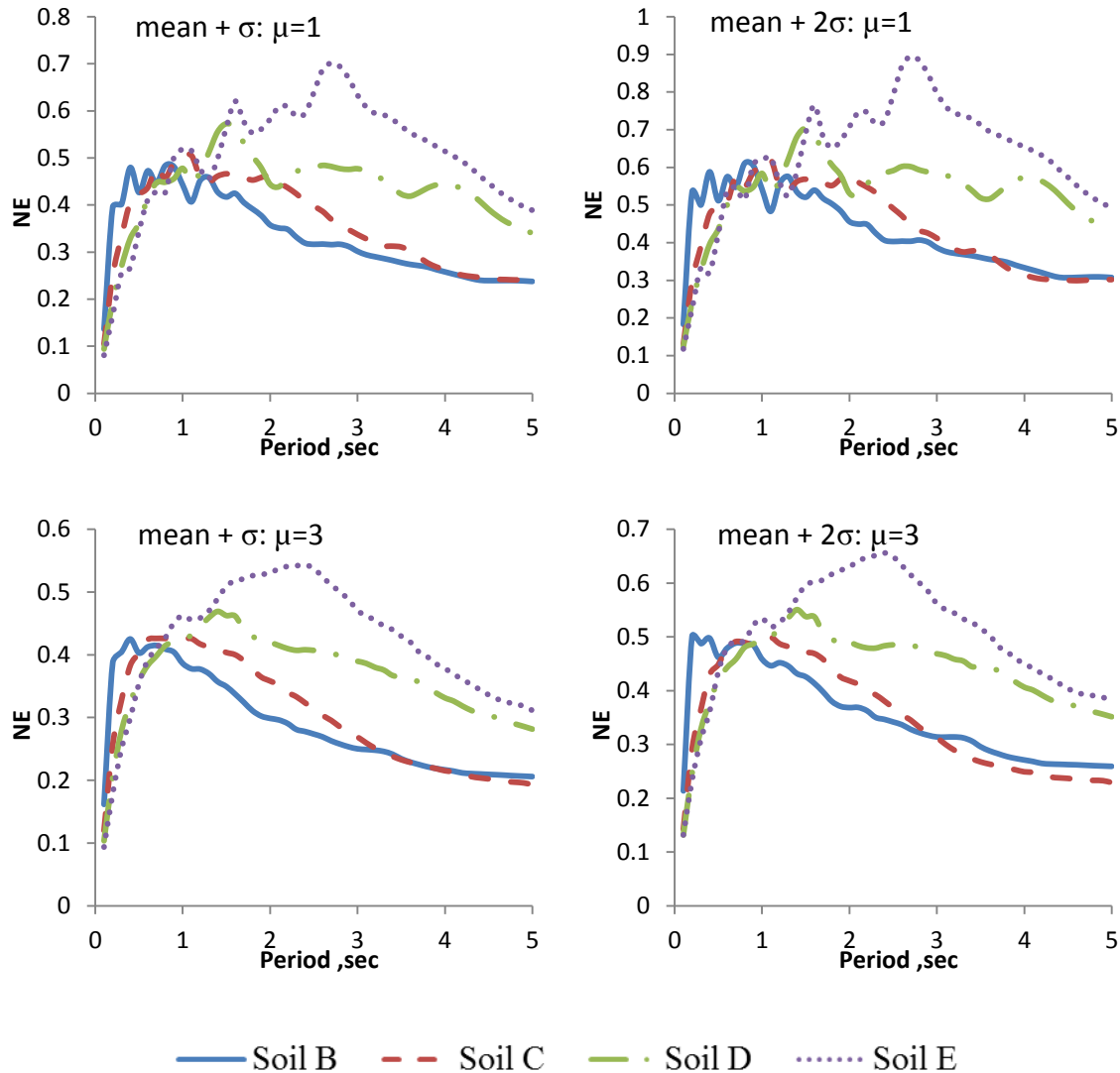
Figure 3.30 Effect of soil on input energy of SDOF structures: hysteretic model BP

As it can be seen in Figure 3.30, the maximum spectral value increases as the soil gets softer.

Both the mean+σ and mean+2σ exhibit similar responses for soil classes E and B in that they

produce the maximum and minimum spectral values, respectively. This trend is similar to the

effect of soil site on elastic design response spectrum (ASCE/SEI 7-12). This observation also

agrees with that made by Decanini and Mollaioli *(1998)*, who used different earthquake sets and

normalizing factors to study the elastic earthquake input energy spectra. They found that the

seismic input energy displays a definitive tendency to increase as the soil stiffness decreases. In

79

addition, it should be noted that the period of vibration for SDOF systems at which the input energy is a maximum increases as the soil gets softer. In other words, longer period (less stiff) structures founded on soft soils are likely to be subjected to a higher VI normalized input energy when compared to those founded on hard soils. For instance, for the BP hysteretic model at a ductility value μ=3, the maximum mean+σ input energy occurs approximately at periods of 0.7 s, 0.9 sec, 1.4 s and 2.4 s for site classes B, C , D and E, respectively. Moreover, as the soil gets softer the maximum value range (i.e., the intermediate period region in Figure 3.6) gets larger, i.e., a wider range of structures will be affected (see Table 3.17). This reinforces the theory that site conditions not only alter the characteristics of ground motion such as its amplitude, but they also affect the frequency content of the ground motion.

Time history analysis of SDOF structures with hysteretic behavior types SD, BF, and BS also show similar results (see Figures 3.31 through 3.33). For the ductility values considered in this study, SDOF systems built on softer soils are more likely to be subjected to higher input energy than those built on stiffer soils, especially for periods that range from 0.75 to 2.0 s. However, at higher periods of vibration (approximately greater than 2.5 s), SDOF systems for site class B tend to show higher values of input energy when compared to those for site class C. In the short period region (approximately 0.5 - 0.75 s) region, it is hard to draw definitive conclusion on the relationship between the soil site class and maximum input energy. Nevertheless, it can be generalized that at very short periods, SDOF structures founded on stiff soils are likely to be subjected to higher input energy as compared to those on soft soils. This phenomenon is more visible for cases with hysteretic models BP, SD and BF.

Table 3.17 Periods of maximum *NE*, value of the maximum *NE*, and range of intermediate region for *μ*=3

Hysteretic Model	Item	mean+σ				mean+2σ			
		B	C	D	E	B	C	D	E
BP	T (s)	0.7	0.9	1.4	2.4	0.2	1.1	1.4	2.4
	NE_{max}	0.415	0.426	0.469	0.543	0.5	0.499	0.551	0.656
	Range	0.8	1.32	1.6	2.08	0.89	1.31	1.59	2.09
SD	T (s)	0.3	0.6	1.3	1.6	0.3	0.6	1.3	1.6
	NE_{max}	0.413	0.442	0.465	0.55	0.489	0.507	0.539	0.645
	Range	0.74	0.98	1.82	1.80	0.81	0.96	1.84	1.86
BF	T (s)	0.6	0.8	1.1	2.2	0.6	0.6	1.3	2.2
	NE_{max}	0.451	0.457	0.465	0.586	0.539	0.54	0.551	0.707
	Range	0.73	1.09	1.98	1.81	0.82	1.09	2.02	1.82
BS	T (s)	0.4	0.5	1	1.4	0.9	0.5	1	1.4
	NE_{max}	0.424	0.472	0.508	0.592	0.499	0.543	0.605	0.704
	Range	0.71	0.79	1.53	1.62	0.79	0.9	1.51	1.71
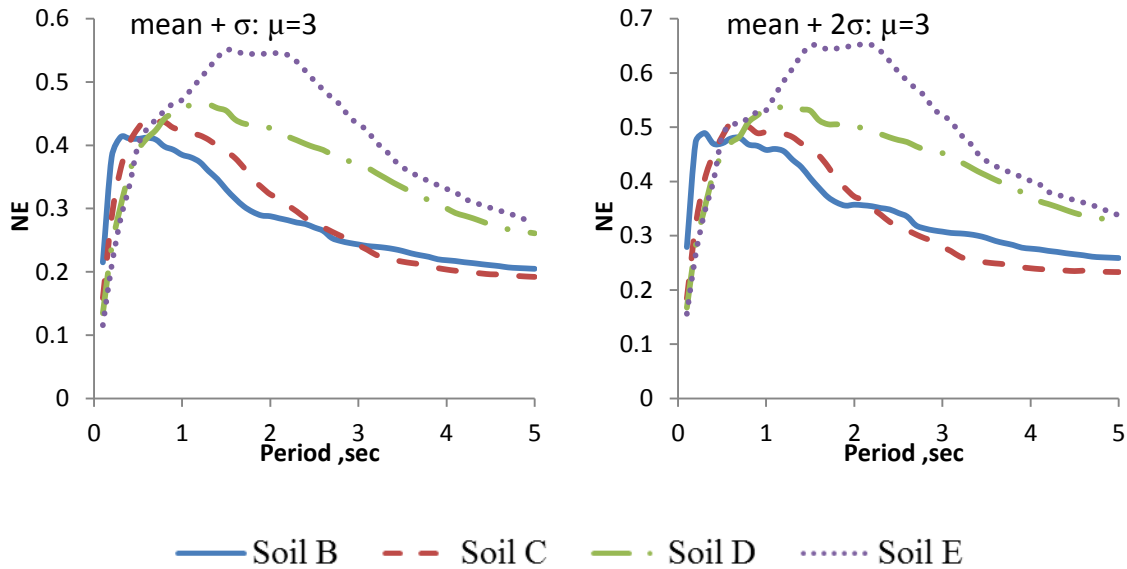
Figure 3.31 Effect of soil on input energy of SDOF structures: hysteretic model SD
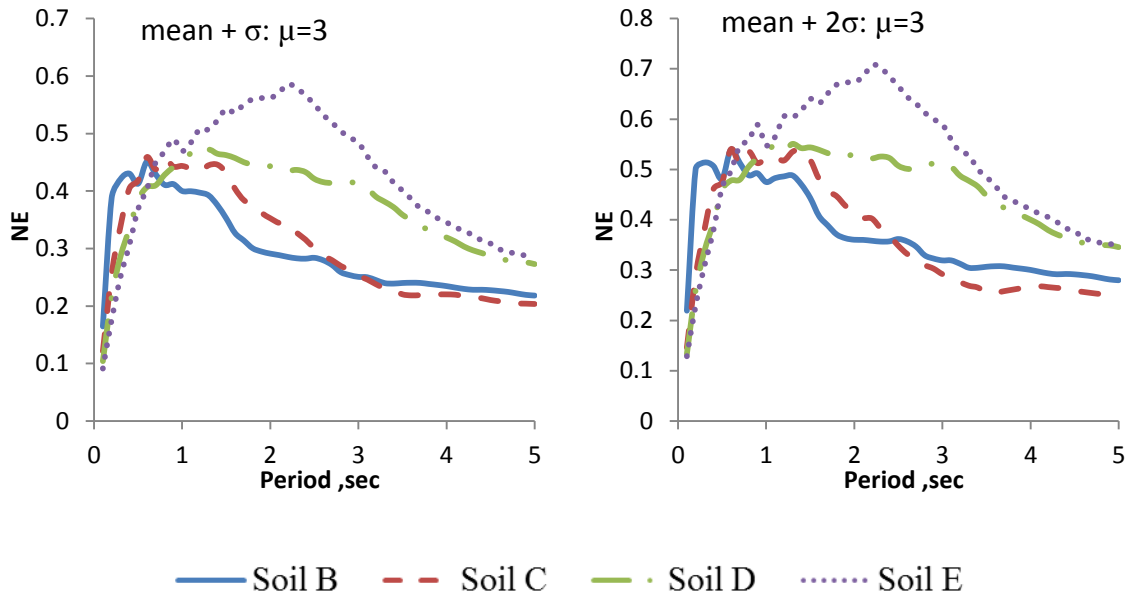
Figure 3.32 Effect of soil on input energy of SDOF structures: hysteretic model BF
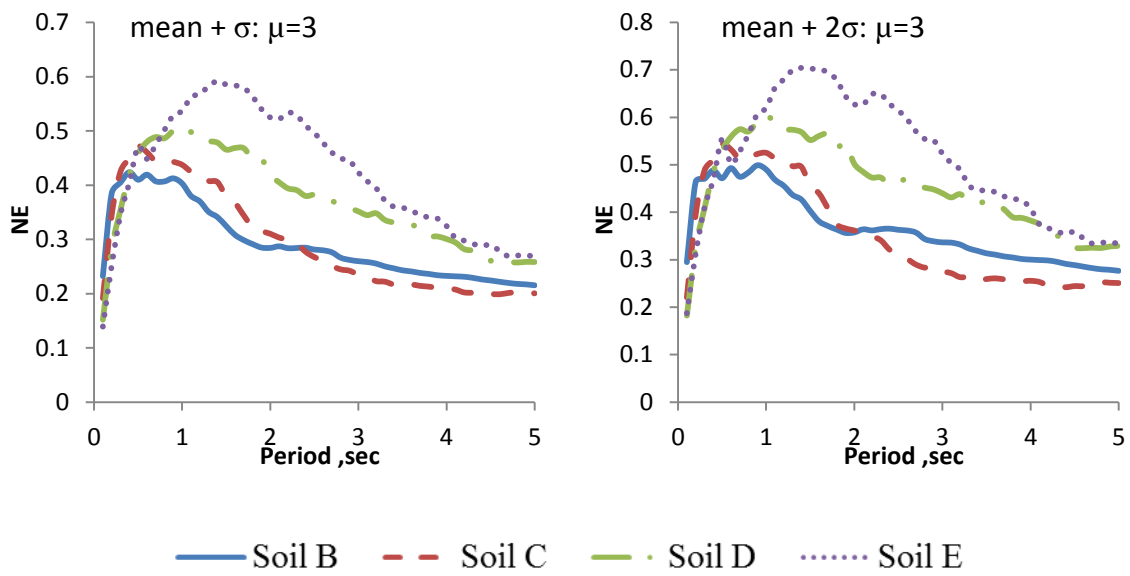
Figure 3.33 Effect of soil on input energy of SDOF structures: hysteretic model BS

3.9 Effect of Hysteretic Behavior

Figure 3.34 shows the effect of hysteretic behavior on the VI normalized input energy spectra for SDOF structures at a ductility value of $\mu=3$. Although it is expected that hysteretic behavior will have an effect on the input energy of SDOF structures, given a hysteretic behavior the input energy shapes for all ductility levels were found to possess similar characteristics. As a result, the ensuing discussions and conclusions drawn from SDOF structures with a ductility value of $\mu=3$ are applicable to ductility values of 1, 2, 4 and 5 as well.

The figure shows that for site classes B and C, irrespective of the hysteretic behavior the input energy spectra values in the short period region remain more or less the same. For site classes D and E; however, SDOF structures with hysteretic type BS exhibit higher values of input energies when compared to those with hysteretic behavior types BP, SD and BF. For periods of vibration greater than approximately 2 s, there appears to be some grouping of hysteretic behaviors that exhibit close values of input energies for all site classes: Hysteretic types BP & BF fall in one cluster and SD & BS in another. It is also important to note that hysteretic types SD & BS (both subjected to stiffness degradation; the former from the inherent property of the model and the latter due to bond slip) exhibit similar trend in input energy. In this range of vibration period, a distinct difference in input energy between the groupings has been observed - BP & BF produce higher input energy spectral values than SD & BS.
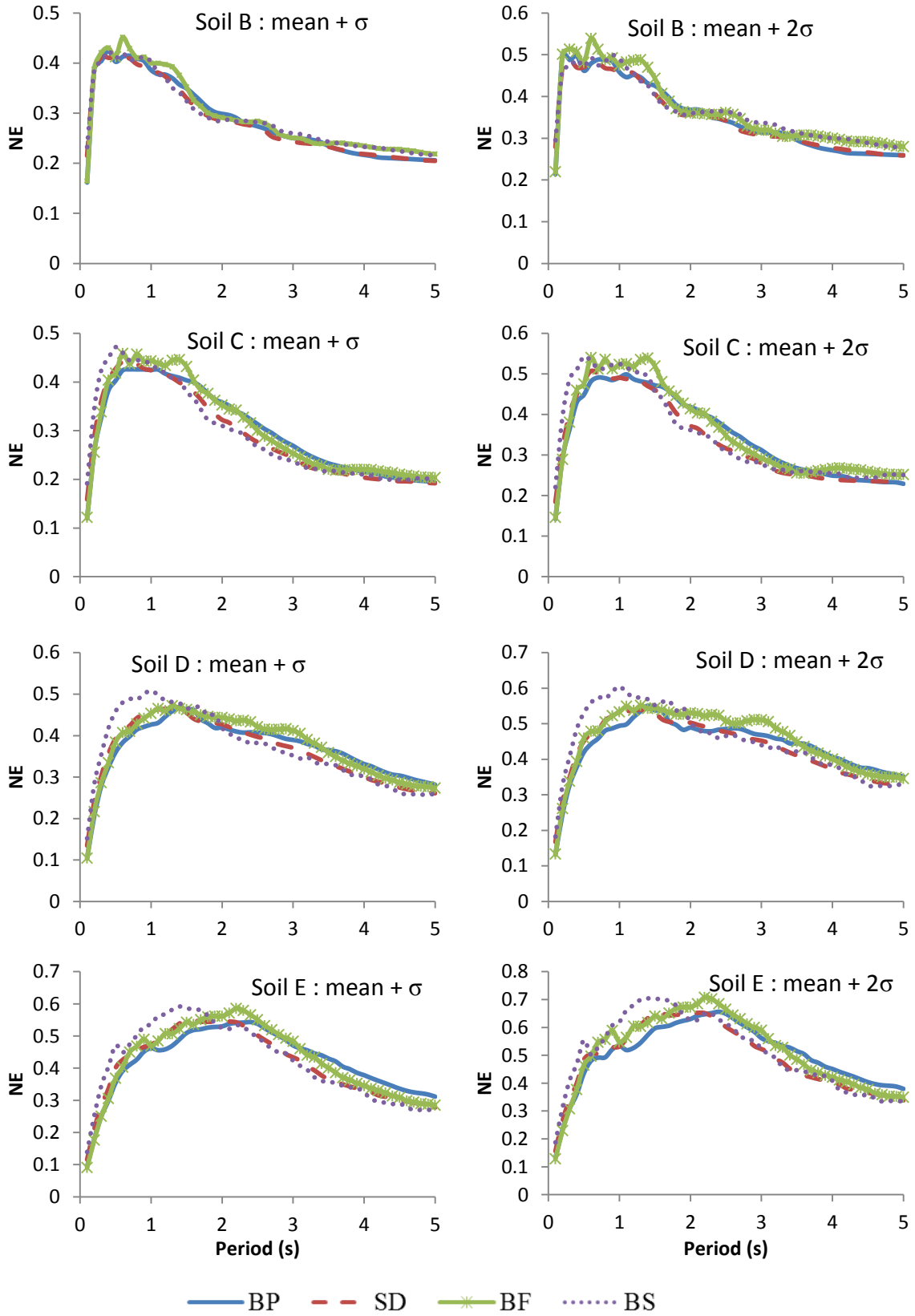
Figure 3.34 Effect of hysteretic behavior on input energy: ductility value, μ=3

3.10   Validation of Proposed Spectra

Validation or verification of any proposed models or procedures is a key process that precedes the use of new findings for their intended purpose. Validation can be done through a realistic comparison of the new finding with existing or commonly accepted procedures and/or with experimental results. In this study, the proposed spectra are compared with nonlinear time history analysis (exact) spectra. Nonlinear time-history analysis provides nonlinear evaluation of the dynamic response of a structure under an applied load that can vary according to a specified time function. For this purpose, three widely studied major ground motion records, each having two components (fault normal and fault parallel) for each soil category, were selected from the PEER ground motion database and used in the verification process. Particulars of the selected earthquake records are as detailed in Table 3.18. Earthquake records from the same events were selected for each soil category to facilitate the comparison of the relative performance of the proposed spectra among the different soil site types.

Table 3.18 Earthquake records selected for validation of proposed spectra

Soil type	Ground motion	Year	Magnitude	V_{s30}(m/s)	Station
B	Loma Prieta,	1989	6.93	1249.9	SF-Pacific Height
	Northridge-01,	1994	6.69	821.7	Anacapa Island
	Chi-Chi Taiwan,	1999	7.62	999.7	TCU085
C	Loma Prieta	1989	6.93	367.6	Fremont- Mission
	Northridge-01	1994	6.69	684.9	Leona Valley #1
	Chi-Chi Taiwan	1999	6.2	442.1	CHY 046
D	Loma Prieta	1989	6.93	271.1	Dublin- Fire Station
	Northridge-01	1994	6.69	234.9	Camarillo
	Chi-Chi Taiwan	1999	6.3	271.1	CHY037
E	Loma Prieta,	1989	6.93	155.1	Treasure
	Northridge-01,	1994	6.69	160.6	Carson
	Chi-Chi Taiwan 04,	1999	6.2	172.1	CHY054

V_{s30} : average shear wave velocity of the upper 30m depth of soil profile of a site

It is anticipated that the selected ground motion records for a given soil site will have different seismic characteristics such as *PGV*, *PGA* and *CAV*. Also, recall that the proposed energy spectra were developed based on a statistical measure (mean+σ and mean+2σ) of a set of ground motion records normalized by the velocity index, *VI*. Thus, to be consistent, the proposed spectra will be compared with the mean+σ and mean+2σ spectra of the time history analysis of the selected earthquakes for each soil. It is also important to note that the few number of earthquakes selected for the verification process might give a very high standard deviation which in turn could result in higher design spectra value. However, this statistical magnification can be minimized through proper scaling of the ground motion records, which is a necessary element in any nonlinear dynamic analysis that involves a group of ground motion records. Therefore, the selected sets of earthquake records for each site were scaled in accordance with the procedures

stated in FEMA P695 and PEER database technical manual. The ground motion indices and

scaling factors used in the analysis are listed in Table 3.19.

Table 3.19 Ground motion indices and scaling factor

Soil type	Ground motion	Fault normal component			Fault parallel component			Scale
		CAV*	*PGA**	*PGV**	*CAV**	*PGA**	*PGV**	
B	Loma Prieta	72.884	24.705	5.8945	53.332	15.286	2.3685	1.1492
	Northridge-01	90.824	25.216	1.2422	67.857	14.049	0.78222	1.6342
	Chi-Chi Taiwan	122.18	27.376	2.9556	107.47	19.958	2.875	1.2052
C	Loma Prieta	183.69	55.743	3.7364	213.17	52.545	5.3555	0.809
	Northridge-01	107.42	41.74	3.1088	73.527	17.685	2.4956	1.4067
	Chi-Chi Taiwan	161.88	45.674	3.545	162.21	39.876	3.4653	0.9199
D	Loma Prieta	143.96	28.165	2.8836	122.68	28.995	1.8559	1.6785
	Northridge-01	345.68	45.131	5.1424	343.07	37.716	4.3114	1.0296
	Chi-Chi Taiwan	235.07	45.629	4.9952	276.96	60.384	6.5801	0.8985
E	Loma Prieta,	136.37	49.57	10.704	127.67	58.431	9.0373	0.3826
	Northridge-01	189.46	29.409	2.8617	197.77	38.045	2.7483	0.6906
	Chi-Chi Taiwan	161.05	16.986	3.306	150.45	19.4	2.6742	1.0462

* all units are in inches and seconds
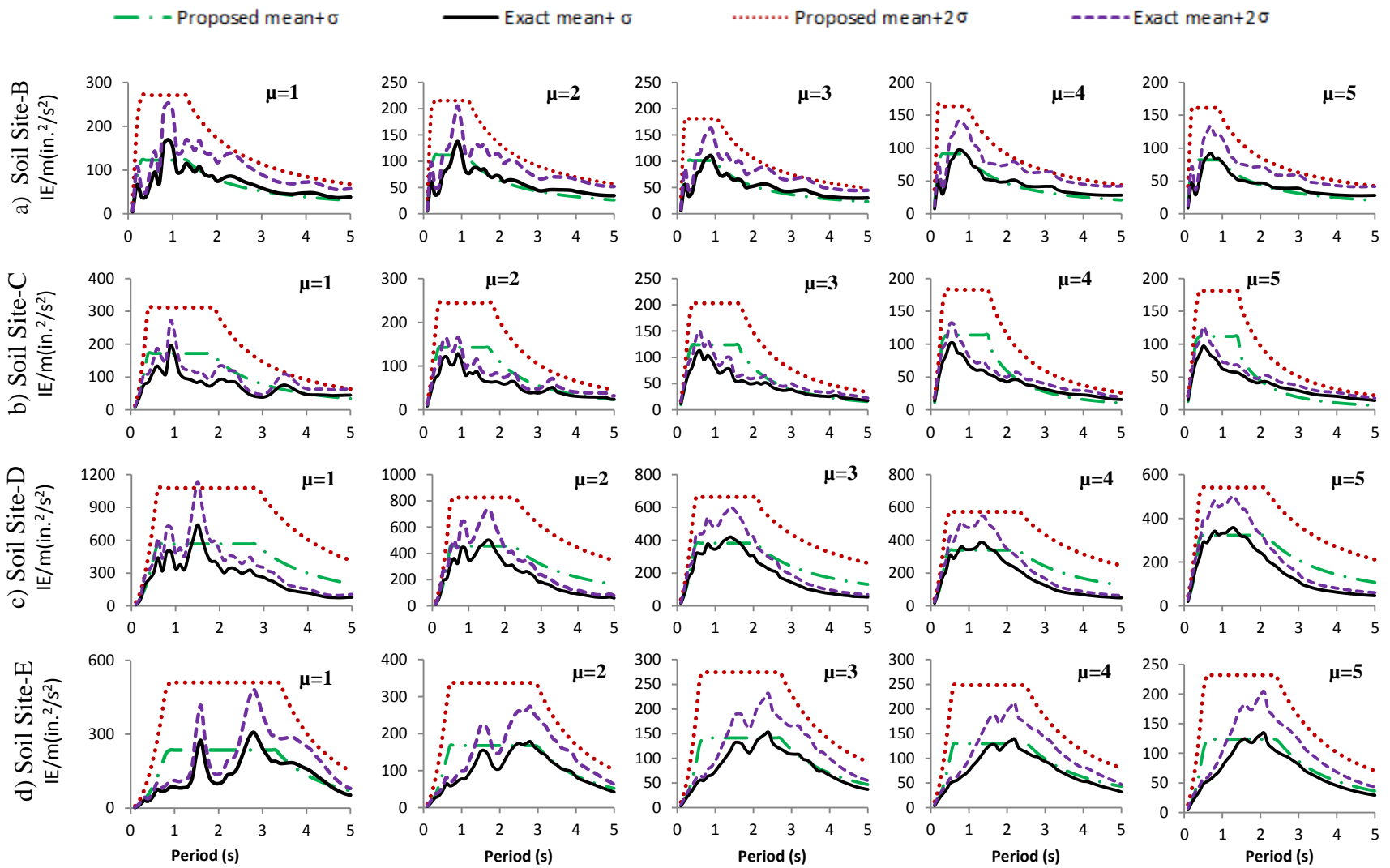
Figure 3.35 Verification of proposed spectra: hysteretic model BP (ζ=5%, α=0.05)

Figure 3.35 shows the mean+σ and mean+2σ input energy per unit mass spectra for both the "exact" time history analysis and the proposed spectra for a SDOF structure with bilinear plastic (BP) hysteretic behavior, pre-to-post yield stiffness ratio of α=0.05 and damping coefficient of ζ=5%. These spectra were developed for the different site classes using the site specific earthquakes listed in Table 3.18. The "exact" spectra are the mean+σ and mean+2σ input energy spectra obtained from time history analyses of the six earthquake records (three earthquakes with two components each) selected for each soil site. The scaling factors indicated in Table 3.19 have been applied to the corresponding ground motion records at the beginning of the analysis. It is important to realize that unlike that of linear analysis, scaling should be applied before the nonlinear analysis is performed, but not to the responses after the analysis. Similarly, scaling factors are applied to the *PGV* and *CAV* values before the mean+σ and mean +2σ normalizing factors, velocity indices, and *VI* are computed. Consistency in scaling used for both the "exact" and proposed procedures is essential if a sound conclusion is to be drawn from the ensuing results.

The solid black line and the pink dashed line in Figure 3.35 are the "exact" mean+σ and mean+2σ spectra, respectively. The green dash-dot line and the red dotted line show the proposed mean+σ and mean+2σ spectra. From this figure, it can be said that for soil sites B and E, and for all ductility values considered in this study, the proposed mean+σ spectra tend to give lower values than the "exact" mean+σ spectra, especially in the intermediate and long period regions; whereas in the short period region the opposite is true. On the other hand the proposed mean+2σ spectra give higher input energy values compared to the "exact" mean+2σ spectra in all regions of the input energy spectra.

For soil site C, the proposed mean+2σ spectra were found to be conservative especially in the intermediate region of the spectrum, whereas the mean+σ spectra fairly match the "exact" spectra both in the short and intermediate regions. However, the proposed mean+σ spectra underestimate the input energy in the long period region. For soil site D, in the short and intermediate period regions, the proposed mean+σ spectra underestimate the input energy whereas they give higher values than the "exact" spectra at longer period regions. On the other hand, the mean+2σ spectra produce conservative values in all regions of the spectra as compared to the "exact" mean+2σ spectra. The only exception to this observation is the case for ductility value μ=1 where the maximum value of the "exact" mean+2σ spectrum is greater than the maximum value of the proposed mean+2σ spectrum. This type of situation is expected as the proposed mean+σ and mean+2σ spectra only give spectral values that are higher than the spectral values for 68% and 95% of the earthquake ensemble used in the analysis, respectively.

Based on the above observations on the normalized input energy spectra for SDOF systems with hysteretic model BP, damping of ζ=5% and ductility values of μ=1, 2, 3, 4, and 5, the following conclusions can be drawn.

- For soil site classes B, C, D and E, the proposed mean+2σ spectra give conservative values in all regions, and if used for design they would give a larger factor of safety.
- The proposed mean+σ spectra fairly match the "exact" spectra in all regions for soil site classes B, C, D and E, except in the long period region for soil site class B and C, in which the proposed spectra values would underestimate the input energy values
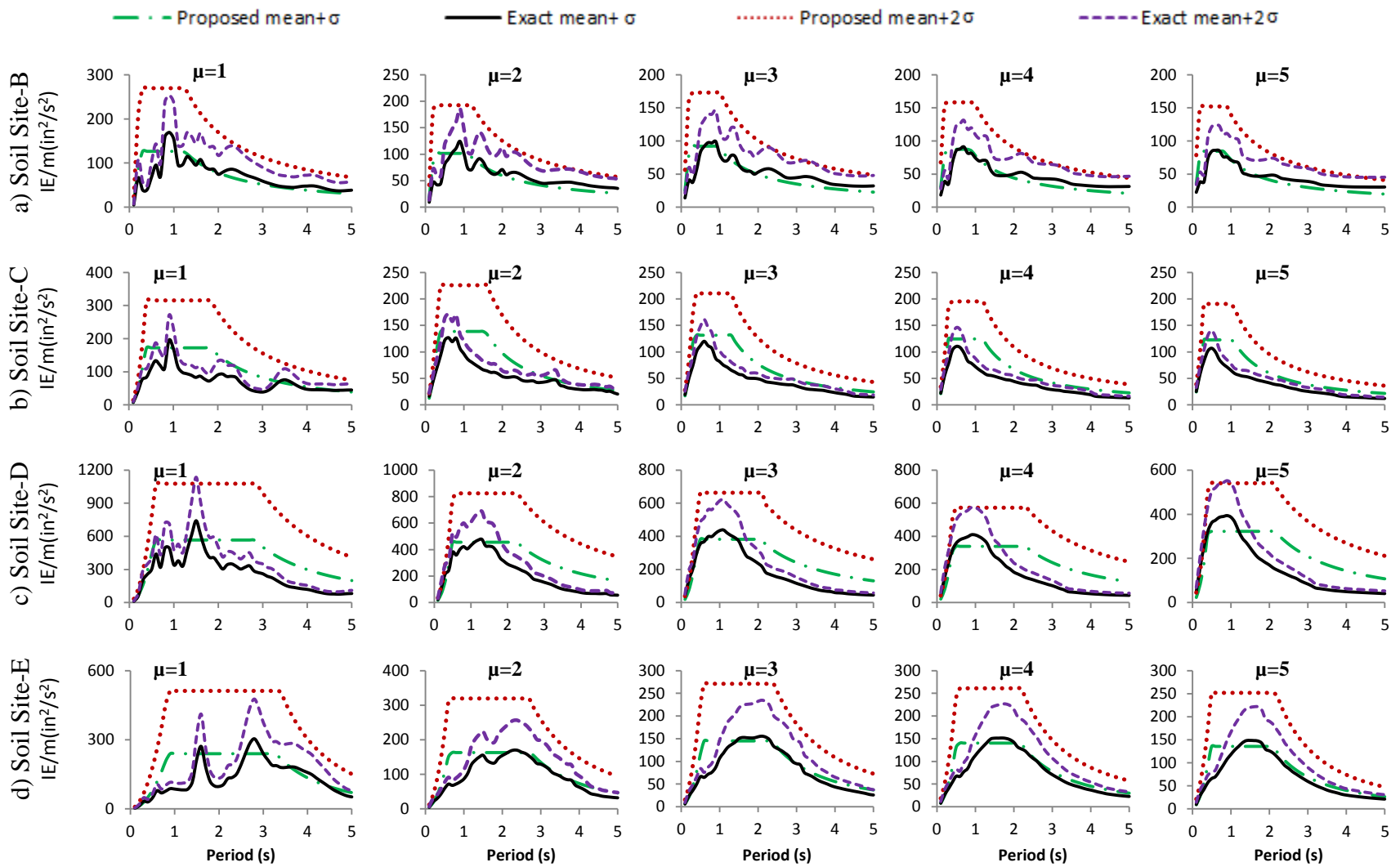
Figure 3.36 Verification of proposed spectra: hysteretic model SD (ζ=5%, α=0.05)

Figure 3.36 show the mean+σ and mean+2σ input energy per unit mass spectra for both the "exact" time history analysis and the proposed spectra for a SDOF structure with strength degradation (modified Clough) (SD) hysteretic behavior, pre-to-post yield stiffness of α=0.05, and damping coefficient of ζ=5%. Figures 3.36 (a) and (d) show the relationship between the proposed and "exact" mean+σ and mean+2σ spectra for soil site class B and E, respectively. For both site classes, except for μ=1 in the short period region, the proposed mean+σ spectra reasonably match the "exact" spectra for ductility values of μ= 2,3,4,5. The proposed mean+2σ spectra, on the other hand, result in higher spectral values and envelope the "exact" spectra in all regions of the spectra for ductility values of μ=1,2,3,4,5.

As can be seen from Figures 3.36 (b) and (c), the range of the intermediate region of the proposed mean+2σ spectra for site classes C and D is wider than that of the "exact" spectra. This may result in an overly conservative design for structures with periods of vibration close to the higher end of the intermediate region. For site class D, the mean+σ proposed spectra tend to underestimate the spectral values. In such cases, it is suggested that either a higher factor of safety or more earthquake records than the number specified by current design standards be used.

For SDOF structures behaving elastically at site classes B, C, D and E, the proposed mean+σ spectra underestimate the spectral values in the intermediate region. This may not be an issue when it comes to design as almost all structures exhibit some type of nonlinear behavior. However, if elastic spectra in conjunction with response modification factors are used for design, higher factors of safety should be used to overcome the lower values of the estimated input energy.
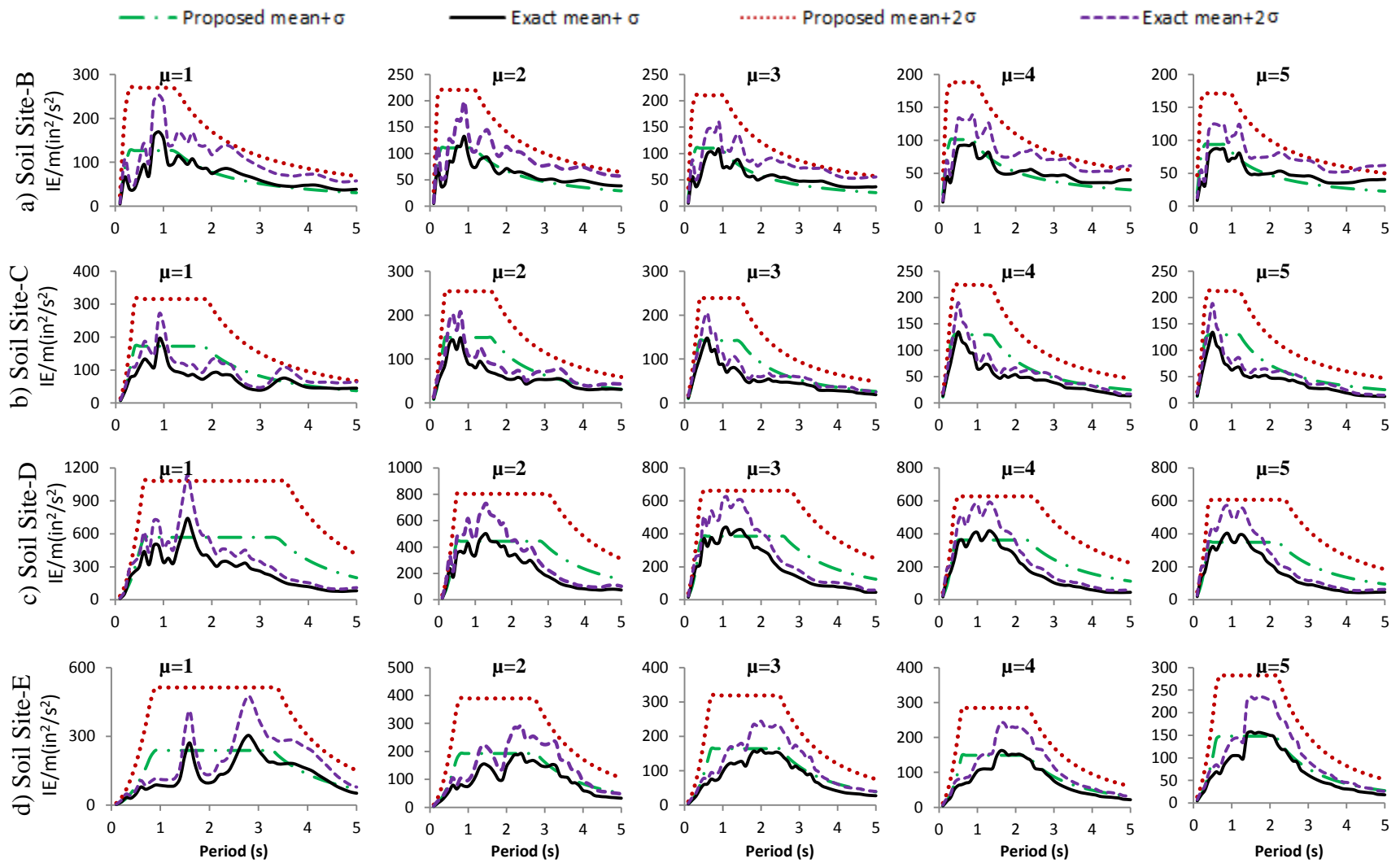
Figure 3.37 Verification of proposed spectra: hysteretic model BF (ζ=5%, α=0.05)

Comparison of the mean+σ and mean+2σ proposed spectra and the "exact" spectra of SDOF structures with hysteretic behavior BF for target ductility values of μ=1,2,3,4,5 and site classes B, C, D, and E are shown in Figure 3.37. For site classes B and E (Figure 3.28 (a) & (d)), the proposed mean+σ and mean+2σ spectra give a good match to the "exact" spectra for ductility values of μ= 2, 3, 4,and 5. Although the proposed spectra envelope the "exact" spectra in such cases, they are somewhat conservative for ductility values of μ= 3, 4, and 5 for site class B in the intermediate region. For site classes C and D both the spectral values of the proposed mean+σ and mean+2σ spectra reasonably match the spectral values of the "exact" spectra for ductility values of μ= 2, 3, 4 and 5. However, the proposed spectra overestimate the spectral values in the upper half of the intermediate region. This was more pronounced for site class C, where the peaks of the "exact" spectra are narrowly banded in a small range of vibration periods.

The verification diagrams for the proposed spectra for SDOF structures with hysteretic behavior BS are shown in Figure 3.38. For ductility values of μ=2, 3, 4, and 5, the proposed spectra show conservative estimates of the "exact" spectra for site classes B and C. For site classes D and E, the proposed mean+σ spectra underestimate the values at the point of maxima of the intermediate regions. On the other hand, the proposed mean+2σ spectra produce a very close estimate with the exception of ductility value of μ= 5, where the maximum values of the "exact" spectra exceed those of the proposed values only at specific periods of vibration.
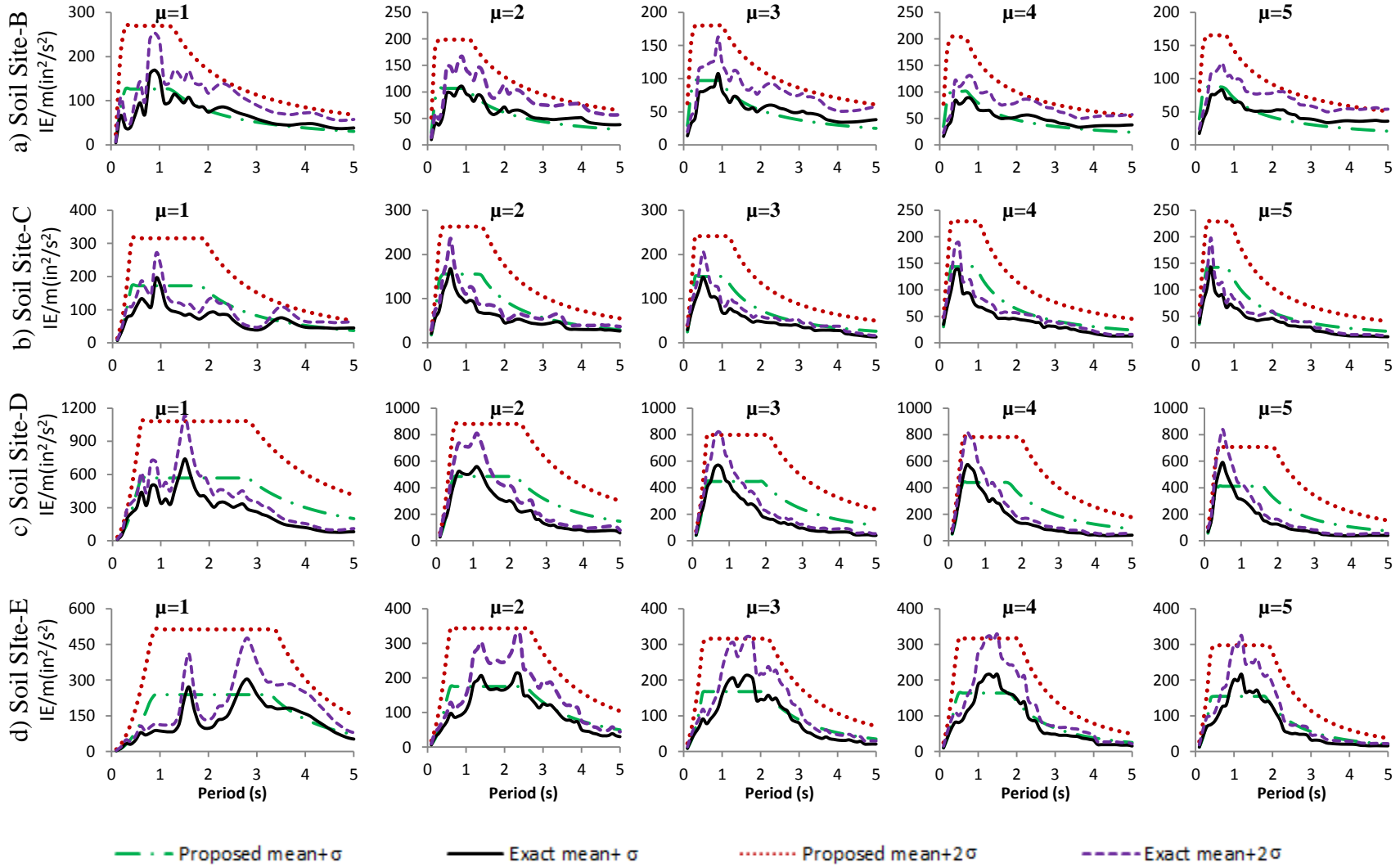
Figure 3.38 Verification of proposed spectra: hysteretic model BS (ζ=5%, α=0.05)

4   PROPOSED HYSTERETIC ENERGY SPECTRA FOR SDOF SYSTEMS

4.1 Introduction

One of the goals of this study is to develop hysteretic energy spectra for purpose of design. The proposed hysteretic energy spectra are intended to help engineers estimate the seismic energy demand of a structure and design it to withstand the seismic energy in the event of an earthquake. In this study, for reasons to be explained Section 4.2, the hysteretic to input energy ratio spectra rather than the explicit hysteretic energy spectra will be developed.

In Section 4.2 the procedure used to develop the proposed spectra for hysteretic to input energy ratio (*HE/IE*) are discussed and outlined. The proposed spectra are developed based on different site classes and hysteretic responses of SDOF systems. The hysteretic models considered are BP, SD, BF and BS for each of the following site classes: B, C, D and E. Details of these proposed *HE/IE* spectra are presented in Sections 4.3 through 4.6.

Sections 4.7 and 4.8 summarize a study of the effect of soil site characteristics and hysteretic behavior on the proposed *HE/IE* spectra. In general, for a given hysteretic model the effect of soil site characteristics on *HE/IE* spectra was found to be very minimal. On the other hand, for a given site class, SDOF systems with hysteretic behavior types BP and SD were found to produce higher *HE/IE* spectral values compared to SDOF systems with hysteretic behavior types BF and BS. The validation of the proposed *HE/IE* spectra is presented in Section 4.9. They were found to yield conservative spectral values when compared to the exact hysteretic energy spectra.

4.2 Proposed Hysteretic Energy Spectra Development Procedure

In the preceding chapter, input energy spectra for SDOF systems having four different hysteretic models (BP, SD, BF, and BS) have been proposed. These hysteretic behavior dependent input

energy spectra can be used in an energy-based seismic design (EBSD) of SDOF systems that takes into account the ductility requirement and site soil characteristics. The normalization parameter, Velocity Index (*VI*), used in the formulation of the input energy spectra provides designers with the flexibility to choose the intensity of the design earthquake.

It has been pointed out in chapter 1 that it is not the full amount of input energy imparted to a structure during a seismic event that causes damage. Per Equation (1.3), input energy is the sum of damping energy, kinetic energy and absorbed energy. Of these three energies, the one that causes damage is a part of the absorbed energy; namely hysteretic energy, *HE*. Therefore, a designer using EBSD method is required to estimate the total hysteretic energy generated and to design the structure with a mechanism to dissipate this destructive energy. Through statistical analysis it is possible to develop hysteretic energy spectra. However, the damage index or intensity of earthquakes has little or no direct relationships with hysteretic energy or hysteretic behavior of structural systems. Thus, it might be unrealistic to develop hysteretic energy spectra that can be scaled to a desired intensity of design earthquake. In Chapter 3, input energy spectra that can be scaled to a desired intensity of earthquake by using the normalization parameter, *VI*, have been developed. Moreover, Manfredi *(2001)* and Ye *et al (2009)* have claimed that input energy is a stable parameter for assessing structural response. Mollaioli *et al (2006)* also observed that most stable seismic parameters can be obtained by setting a relationship between the square root of input energy and displacement (which is dependent on hysteretic behavior) and asserted that input energy can be considered to effectively represent seismic demand in structural systems. Cognizant of this, instead of developing explicit hysteretic energy spectra, spectra that relate hysteretic energy (*HE*) to input energy (*IE*), i.e., hysteretic energy to input energy ratio (*HE/IE*) will be proposed in this study.

In developing the (*HE/IE*) spectra, the set of scaled earthquakes for the different site classes

listed in Appendix A are used. The same set of earthquake records have been used in developing

the proposed *NE* spectra in Chapter 3. For each site-class a hysteretic behavior dependent

mean+σ and mean+2σ *HE/IE* spectra have been proposed. The spectra were developed from the

energy ratios of the time history analysis results of scaled earthquakes selected for a given site-

class. For instance, *HE/IE* spectra for soil class-B shown in Figure 4.1 are obtained using the

following steps.

Step 1:

For a given hysteretic model and ductility value, the spectral values of input energies are

obtained from time history analysis using BISPEC for the selected set of earthquakes for site

class B and the corresponding mean+σ and mean+2σ of input energy spectral values are

calculated.

Step 2:

Similarly, using the same set of earthquakes, the mean+σ and mean+2σ hysteretic energy

spectral values for a given hysteretic model and ductility value are calculated using the hysteretic

energy spectral values obtained from BISPEC.

Step 3:

Hysteretic energy to input energy ratios, *HE/IE*, are then obtained as follows

$$\frac{HE}{IE}(mean+\sigma) = \frac{HE(mean+\sigma)}{IE(mean+\sigma)} \quad \text{and} \quad \frac{HE}{IE}(mean+2\sigma) = \frac{HE(mean+2\sigma)}{IE(mean+2\sigma)}$$

Step 4:

The values obtained in Step 3 are then used to generate *HE/IE* spectra like those shown in Figure 4.1.

Time history analyses for site classes C, D and E were found to have similar *HE/IE* spectral shapes like those shown in Figure 4.1. In other words, for a given hysteretic model, the mean+σ and mean+2σ *HE/IE* spectra exhibited similar variations in spectral values with period. This is true, irrespective of the soil site characteristics, for ductility values μ=2, 3, 4, and 5 considered in this study. However, as can be seen from Figure 4.1, the *HE/IE* spectral shapes do not show similar characteristics among the different hysteretic models considered in this study. As a result, the following hysteretic model dependent general shapes have been adopted in developing smoothened *HE/IE* spectra.
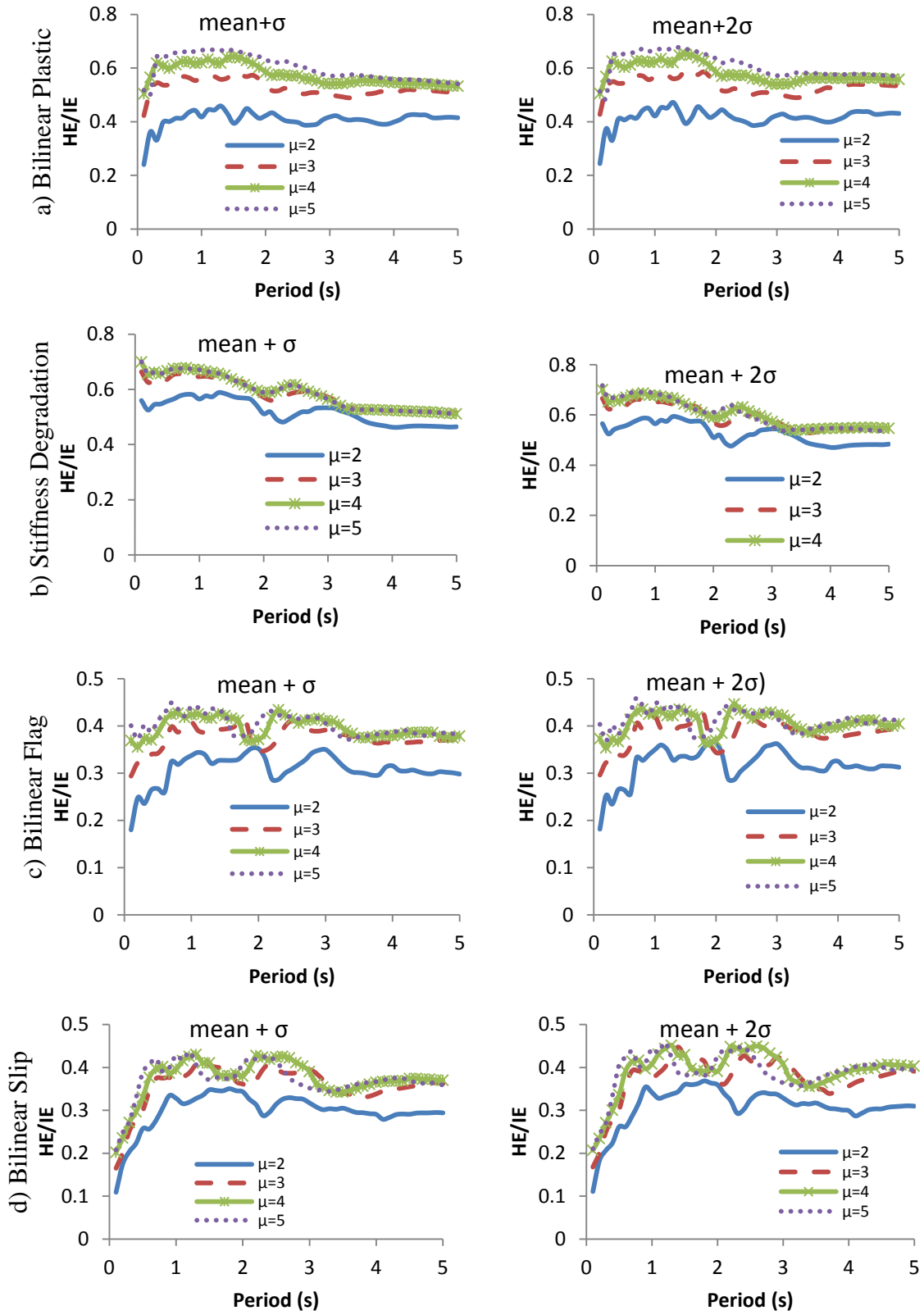
Figure 4.1 Actual *HE/IE* spectra: site class B

Hysteretic Model BP: Spectral values at the extreme left end of the short period region increase with period (albeit, for a very small period range) until the maximum value is reached (see Figure 4.1(a)). For instance, the periods that correspond to these maximum values are 0.28, 0.28, 0.32 and 0.35 sec for ductility values of μ=2, 3, 4, and 5, respectively. These values are well below the periods of vibrations for most civil engineering structures. Moreover, the spectral values in the short period region are not significantly lower than the maximum value. As a result, the maximum value in the intermediate regions was assumed to extend into the short period region. In the long period region the spectral values do not exponentially decrease and thus the values were considered to vary linearly. Accordingly, the smoothened spectra were considered to have the general shape shown in Figure 4.2.

Hysteretic Models SD and BF: Like hysteretic model BP, the general *HE/IE* spectral shape shown in Figure 4.2 is adopted for hysteretic models SD and BF. For these hysteretic models, the *HE/IE* spectral values in the short period do not strictly increase or decrease with period. They exhibit closer values to the maximum spectral value. Thus, extending the intermediate region (region of maximum value) to the short period will not greatly underestimate or overestimate the value of the resulting hysteretic energy.
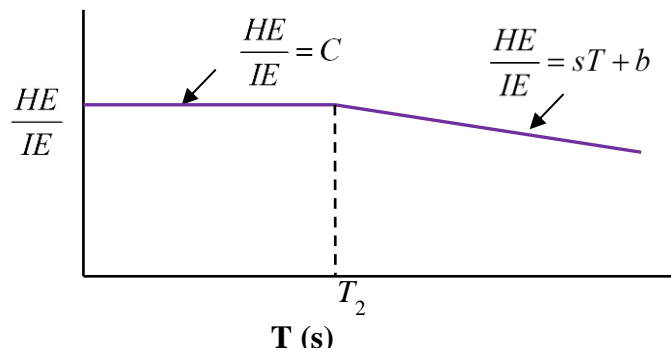
Figure 4.2 *HE/IE* spectra shape for hysteretic models BP, SD and BF

Hysteretic Model BS: The *HE/IE* spectra for hysteretic model BS (shown in Figure 4.1(d)) show a significant difference between the smallest value of the short period region and the maximum value of the intermediate region. Therefore, instead of extending the shape of the spectra in the intermediate region spectra into the short period region, a tri-linear shape as shown in Figure 4.3 is proposed.
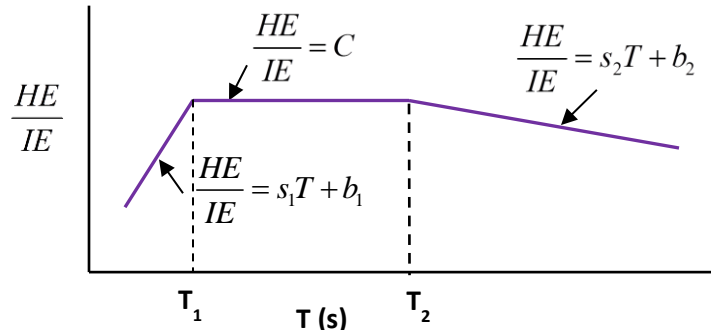
Figure 4.3 *HE/IE* **spectra shape for hysteretic model –BS**

Using the steps explained above and the specific general shapes adopted, hysteretic behavior dependent *HE/IE* spectra as a function of ductility were developed for site classes B, C, D and E and are presented below.

4.3 *HE/IE* Spectra for Site Class B

Table 4.1 list values of the constants indicated in Figures 4.2 and 4.3 needed to define the *HE/IE* spectra for SDOF systems with hysteretic behavior types BP, SD, BF, and BS located at site class B. These values were obtained for structures with pre-to-post yield stiffness ratio of $\alpha=0.05$, damping 5%, and ductility values of $\mu=2$, 3, 4, and 5. At ductility value of $\mu=1$, the SDOF systems remain elastic and the corresponding hysteretic energy is theoretically zero. Figure 4.4 presents mean+σ and mean+2σ *HE/IE* spectra generated using the respective values from Table 4.1 for each hysteretic model considered in this study.

Table 4.1 *HE/IE* spectral shape constants for site class B

	Hysteretic Model BP							
	mean+σ				mean+2σ			
μ	2	3	4	5	2	3	4	5
C	0.459	0.583	0.642	0.671	0.472	0.592	0.652	0.678
T_2	2.275	2.008	1.727	1.573	2.372	2.108	1.805	1.599
s	-0.0157	-0.0233	-0.0333	-0.0383	-0.0157	-0.02	-0.03	-0.0333
b	0.495	0.63	0.7	0.732	0.51	0.634	0.706	0.732

	Hysteretic Model SD							
	mean+σ				mean+2σ			
μ	2	3	4	5	2	3	4	5
C	0.588	0.656	0.678	0.684	0.593	0.663	0.686	0.691
T_2	1.565	1.306	1.096	1.041	1.685	1.479	1.104	1.129
s	-0.0362	-0.0377	-0.0423	-0.0464	-0.033	-0.0348	-0.0358	-0.0404
b	0.645	0.706	0.725	0.732	0.649	0.714	0.726	0.737

	Hysteretic Model BF							
	mean+σ				mean+2σ			
μ	2	3	4	5	2	3	4	5
C	0.353	0.413	0.434	0.449	0.366	0.425	0.446	0.46
T_2	3.115	2.73	2.492	2.124	3.179	2.775	2.481	2.135
s	-0.0291	-0.02	-0.022	-0.0225	-0.0291	-0.015	-0.016	-0.016
b	0.443	0.468	0.489	0.497	0.459	0.467	0.486	0.494

	Hysteretic Model BS							
	mean+σ				mean+2σ			
μ	2	3	4	5	2	3	4	5
s_1	0.66	0.362	0.338	0.406	0.724	0.328	0.274	0.349
b_1	0.043	0.129	0.168	0.167	0.0383	0.135	0.18	0.175
T_1	0.466	0.820	0.777	0.663	0.456	0.952	0.993	0.812
C	0.350	0.426	0.430	0.436	0.369	0.448	0.452	0.458
T_2	2.112	2.03	2.589	2.211	2.141	1.956	2.729	2.207
s_2	-0.0195	-0.0214	-0.0249	-0.028	-0.0205	-0.0186	-0.0212	-0.0236
b_2	0.392	0.469	0.495	0.498	0.412	0.484	0.509	0.510

For all four cases (Figures 4.4(a-d)), both the mean+σ and mean+2σ *HE/IE* spectral values increase with an increase in ductility. In chapter 3 it has been discussed that, in general, for SDOF systems the amount of input energy decreases with an increase in ductility. Inherently,

hysteretic energy increases as ductility increases and hence it is logical to observe an increase in the *HE/IE* spectral value when ductility value increases. It has also been observed that the effect of ductility on *HE/IE* spectra is not uniform throughout the range of ductility values considered in this study. Spectral values show insignificant change as the ductility values increase (see Figure 4.4). Especially in the long period region, the *HE/IE* spectra plots for ductility values $\mu=$ 3, 4, and 5 appear to overlap.

Another important finding is that, for a given hysteretic behavior and ductility value, the mean+σ and mean+2σ *HE/IE* spectral values show negligible differences (see Table 4.1). This indicates that the seismic parameter *HE/IE* is statistically stable, unlike input energy spectra where there is a significant difference between the *mean+σ* and *mean+2σ* values. This observation corroborates with the notion of determining hysteretic energy from input energy (a more global seismic parameter) instead of proposing explicit hysteretic energy spectra directly.
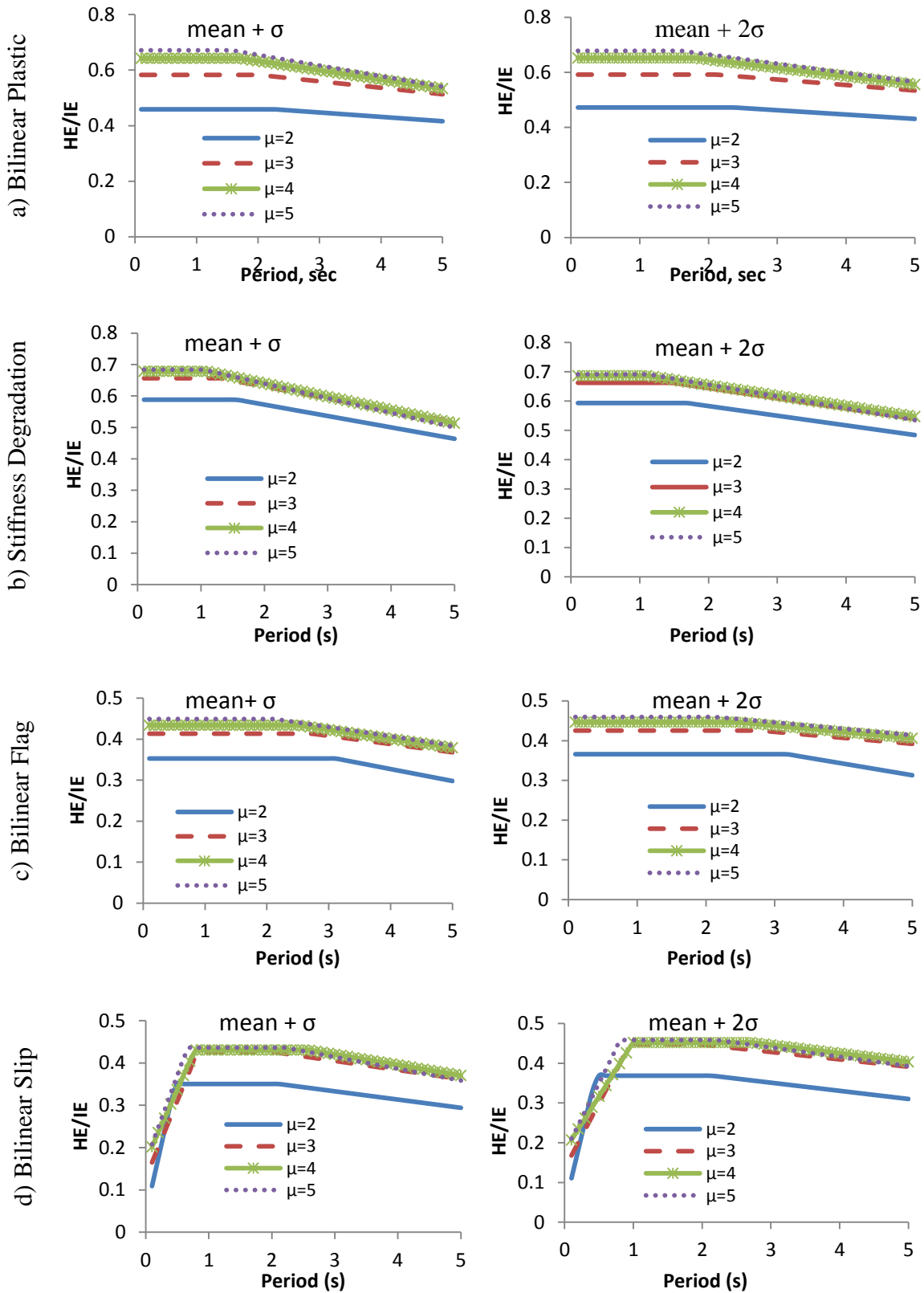
Figure 4.4 *HE/IE* **spectra: site class B**

4.4 *HE/IE* Spectra for Site Class C

Table 4.2 gives values of the constants used to define the *HE/IE* spectra for soil site class C.

Table 4.2 *HE/IE* spectral shape constants for site class C

	Hysteretic Model BP							
	mean+σ				mean+2σ			
μ	2	3	4	5	2	3	4	5
C	0.476	0.592	0.651	0.676	0.509	0.605	0.658	0.684
T_2	5	3.548	2.674	2.605	5	3.727	2.858	2.742
s		-0.0244	-0.0247	-0.0308		-0.0123	-0.0153	-0.0208
b		0.679	0.717	0.756		0.651	0.702	0.741
	Hysteretic Model SD							
	mean+σ				mean+2σ			
μ	2	3	4	5	2	3	4	5
C	0.6	0.667	0.699	0.711	0.607	0.667	0.697	0.718
T_2	5	5	2.441	1.848	5	5	3.244	2.11
s			-0.0363	-0.0388			-0.0275	-0.0275
b			0.787	0.783			0.787	0.776
	Hysteretic Model BF							
	mean+σ				mean+2σ			
μ	2	3	4	5	2	3	4	5
C	0.337	0.406	0.434	0.444	0.35	0.428	0.442	0.45
T_2	5	5	5	5	5	5	5	5
s								
b								
	Hysteretic Model BS							
	mean+σ				mean+2σ			
μ	2	3	4	5	2	3	4	5
s_1	0.351	0.39	0.458	0.424	0.355	0.395	0.466	0.436
b_1	0.0556	0.0892	0.102	0.119	0.0529	0.0871	0.098	0.113
T_1	0.732	0.745	0.642	0.644	0.772	0.806	0.681	0.707
C	0.312	0.38	0.396	0.392	0.327	0.406	0.416	0.421
T_2	5	5	5	5	5	5	5	5
s_2								
b_2								

HE/IE spectra for SDOF systems with hysteretic behavior types BP, SD, BF, and BS and ductility values of μ=2, 3, 4, and 5 located at site class C generated using these constants are shown in Figure 4.5. The pre-to-post yield stiffness ratio and damping coefficient used were α=0.05 and ζ=5%, respectively. Similar to what was observed for site class B, the same trend of an increase in *HE/IE* with an increase in ductility value is observed. In the long period region for hysteretic type SD (Figure 4.5 (b)), the proposed *HE/IE* values for ductility values μ=4&5 are seen to be greater than that for ductility values μ=2&3. This is in agreement with the actual *HE/IE* values, which are higher for μ=4&5 than for μ=2&3.

It should be noted that the variation of *HE/IE* with ductility value is not uniform. For instance, the percentage increases of the mean+σ *HE/IE* values are 27%, 10%, 5% for hysteric type BP; 11%, 5%, 2% for hysteric type SD; 20%, 7%, 2% for hysteretic type BF and 21%, 4%, 1% for hysteric type BS between ductility values 2&3, 3&4, 4&5, respectively. The values for the mean+2σ *HE/IE* are (27%, 10%, 4%), (10%, 5%, 3%), (22%, 3%, 2%) and (24%, 2%, 1%) for hysteretic models BP, SD, BF and BS, respectively. This observation indicates that the effect of ductility on *HE/IE* is more significant at lower ductility values (μ=2 to 3) than higher ductility values (μ=4 to 5). Compared to site class B, *HE/IE* values for site class C do not change significantly with period. For instance, for hysteretic models BP and SD (μ=2, 3) and in the long and intermediate regions of hysteretic models BF and BS (μ=2, 3, 4, 5) *HE/IE* values generally remained constant.
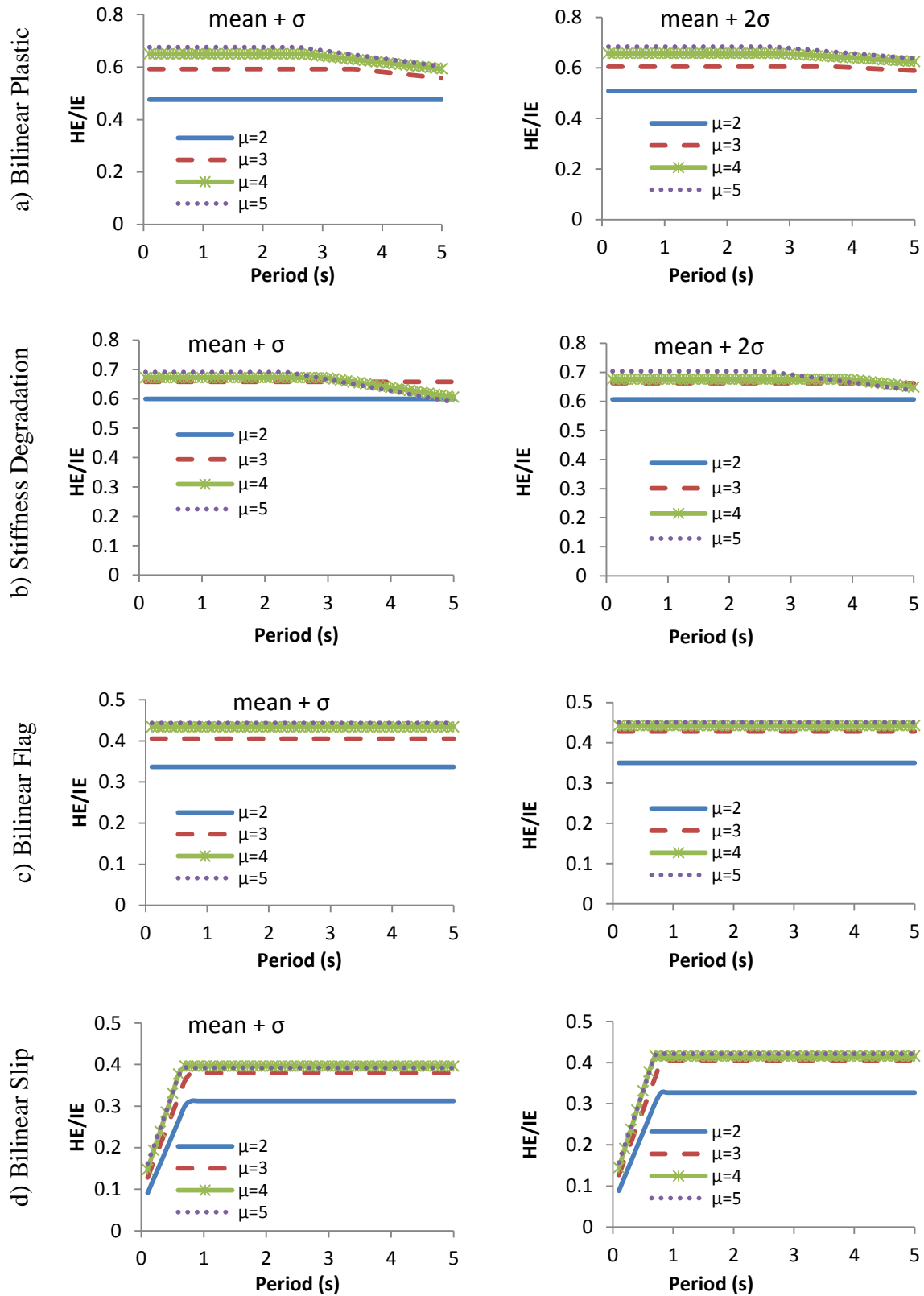
Figure 4.5 HE/IE spectra: site class-C

108

4.5 *HE/IE* Spectra for Site Class D

Table 4.3 gives values of the constants used to define the *HE/IE* spectra for soil site class D.

Table 4.3 *HE/IE* spectral shape constants for site class D

	Hysteretic Model BP							
	mean+σ				mean+2σ			
μ	2	3	4	5	2	3	4	5
C	0.512	0.623	0.668	0.696	0.531	0.637	0.677	0.703
T_2	5	5	3.48	3.094	5	5	3.6	3.061
s			-0.0256	-0.0289			-0.0244	-0.0233
b			0.757	0.785			0.765	0.775
	Hysteretic Model SD							
	mean+σ				mean+2σ			
μ	2	3	4	5	2	3	4	5
C	0.609	0.682	0.699	0.712	0.617	0.686	0.700	0.712
T_2	2.230	2.071	1.486	1.321	2.368	2.162	1.633	1.605
s	-0.0142	-0.0262	-0.0283	-0.0335	-0.0142	-0.0262	-0.0235	-0.0291
b	0.641	0.736	0.741	0.756	0.642	0.732	0.738	0.759
	Hysteretic Model BF							
	mean+σ				mean+2σ			
μ	2	3	4	5	2	3	4	5
C	0.336	0.417	0.442	0.460	0.349	0.426	0.45	0.469
T_2	5	5	5	2.99	5	5	5	3.066
s				-0.038				-0.0383
b				0.574				0.587
	Hysteretic Model BS							
	mean+σ				mean+2σ			
μ	2	3	4	5	2	3	4	5
s_1	0.367	0.437	0.408	0.395	0.373	0.473	0.448	0.427
b_1	0.0493	0.0813	0.111	0.127	0.0477	0.0752	0.105	0.121
T_1	0.755	0.678	0.696	0.680	0.773	0.659	0.671	0.682
C	0.326	0.377	0.395	0.395	0.336	0.387	0.405	0.412
T_2	5	5	5	5	5	5	5	5
s_2								
b_2								

Figure 4.6 shows the *HE/IE* spectra for SDOF systems with hysteretic behavior BP, SD, BF and

BS having a pre-to-post yield stiffness ratio of $\alpha=0.05$ and damping $\zeta=5\%$ located in site class D

generated using the spectral constants given in Table 4.3. Like that for site classes B and C,

HE/IE values increase as ductility value increases. The increment, however, is minimal beyond

some ductility value; in this case beyond $\mu=3$. For hysteretic type SD, in the intermediate and

long period regions the effect of ductility on *HE/IE* even becomes negligible resulting in an

overlap of the graphs for ductility value $\mu\geq3$ (see Figure 4.6b).

A comparison of the mean+σ and mean+2σ maximum *HE/IE* values shows almost no difference.

On average, the difference in the mean+σ and mean+2σ maximum *HE/IE* values were (0.036,

0.012, 0.007, 0.008) for BP, (0.007, 0.000, 0.002, 0.006) for SD, (0.013, 0.023, 0.008, 0.007) for

BF and (0.015, 0.026, 0.019, 0.029) for BS, for ductility values of $\mu=2,3,4$ and 5, respectively.

These values are relatively small compared to the maximum values of their respective spectra.

This observation is also true for site classes B and C so this further supports the argument that

HE/IE is a statistically stable parameter. It is therefore possible that the mean *HE/IE* spectra will

give more or less the same values as the mean+σ and mean+2σ *HE/IE* spectra if used for

calculating hysteretic energy from input energy. Although not part of this study, it has been

observed that all the mean, mean+ σ and mean+2σ *HE/IE* spectra tend to give very close values

for a given hysteretic model, ductility value and site class.
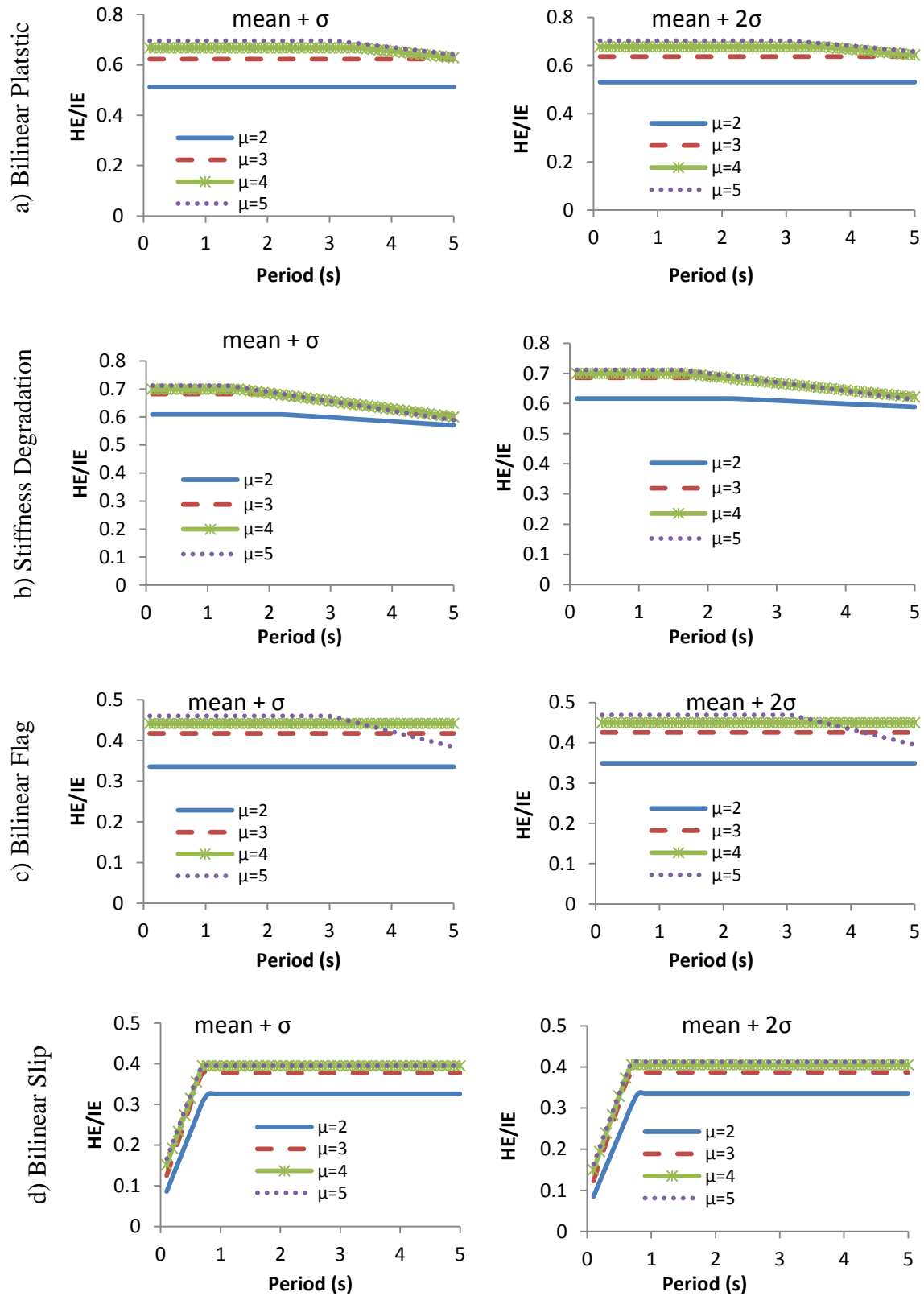
Figure 4.6 HE/IE spectra: site class D

4.6 *HE/IE* Spectra for Site Class E

Table 4.4 gives values of the constants used to define the *HE/IE* spectra for soil site class E.

Table 4.4 *HE/IE* spectra shape constants for site class E

	Hysteretic Model BP							
	mean+σ				mean+2σ			
μ	2	3	4	5	2	3	4	5
C	0.521	0.651	0.693	0.717	0.535	0.658	0.7	0.724
T_2	3.808	3.45	3.241	2.905	3.857	3.547	3.316	2.852
s	-0.0567	-0.07	-0.0575	-0.0483	-0.0571	-0.0771	-0.06	-0.0457
b	0.736	0.892	0.88	0.858	0.756	0.932	0.899	0.855
	Hysteretic Model SD							
	mean+σ				mean+2σ			
μ	2	3	4	5	2	3	4	5
C	0.633	0.708	0.736	0.746	0.631	0.704	0.73	0.741
T_2	2.307	1.867	1.317	1.2	2.4	1.861	1.357	1.353
s	-0.0483	-0.0471	-0.0459	-0.0521	-0.0483	-0.0471	-0.0395	-0.0476
b	0.745	0.796	0.796	0.809	0.739	0.780	0.783	0.805
	Hysteretic Model BF							
	mean+σ				mean+2σ			
μ	2	3	4	5	2	3	4	5
C	0.347	0.426	0.454	0.469	0.355	0.432	0.462	0.476
T_2	3.053	2.428	2.323	2.136	3.07	2.472	2.279	2.273
s	-0.021	-0.0225	-0.03	-0.035	-0.021	-0.0225	-0.0275	-0.035
b	0.411	0.481	0.524	0.544	0.419	0.481	0.525	0.555
	Hysteretic Model BS							
	mean+σ				mean+2σ			
μ	2	3	4	5	2	3	4	5
s_1	0.332	0.313	0.256	0.208	0.358	0.306	0.241	0.195
b_1	0.0591	0.0968	0.122	0.143	0.054	0.0945	0.118	0.139
T_1	0.767	0.824	0.956	1.095	0.748	0.867	1.096	1.334
C	0.314	0.355	0.367	0.372	0.322	0.359	0.382	0.3991
T_2	5	5	5	5	5	5	5	5
s_2								
b_2								

Figure 4.7 shows the *HE/IE* spectra for SDOF systems with hysteretic behavior types BP, SD, BF and BS having a pre-to-post yield stiffness ratio of α=0.05 and damping ζ=5% located at site class E generated using the spectral constants given in Table 4.4. Like those for site classes B, C and D, *HE/IE* values increase with ductility for site class E. Note that the region where the maximum *HE/IE* values lie for hysteretic model type SD is narrower compared to the other three hysteretic models. A similar phenomenon was observed for soil site class B. In a similar manner as for site classes B, C and D, the rate of increment for *HE/IE* values with ductility reduces at higher ductility values.

Whether it is extending towards the short period region (for hysteretic models BP, SD, and BF) or extending towards the long period region (for hysteretic model BS), the range of the intermediate region gets narrower as ductility value increases. This is in clear agreement with what has been observed for the input energy spectra of SDOF systems (See section 3.7). For instance, for hysteretic model type SD (see Figure 4.7b) the range is 2.31, 1.87, 1.31, 1.2 s for the mean+ σ spectra, and 2.4, 1.86, 1.36, 1.35 s for the mean+2σ spectra for ductility values of μ=2, 3, 4 and 5, respectively.
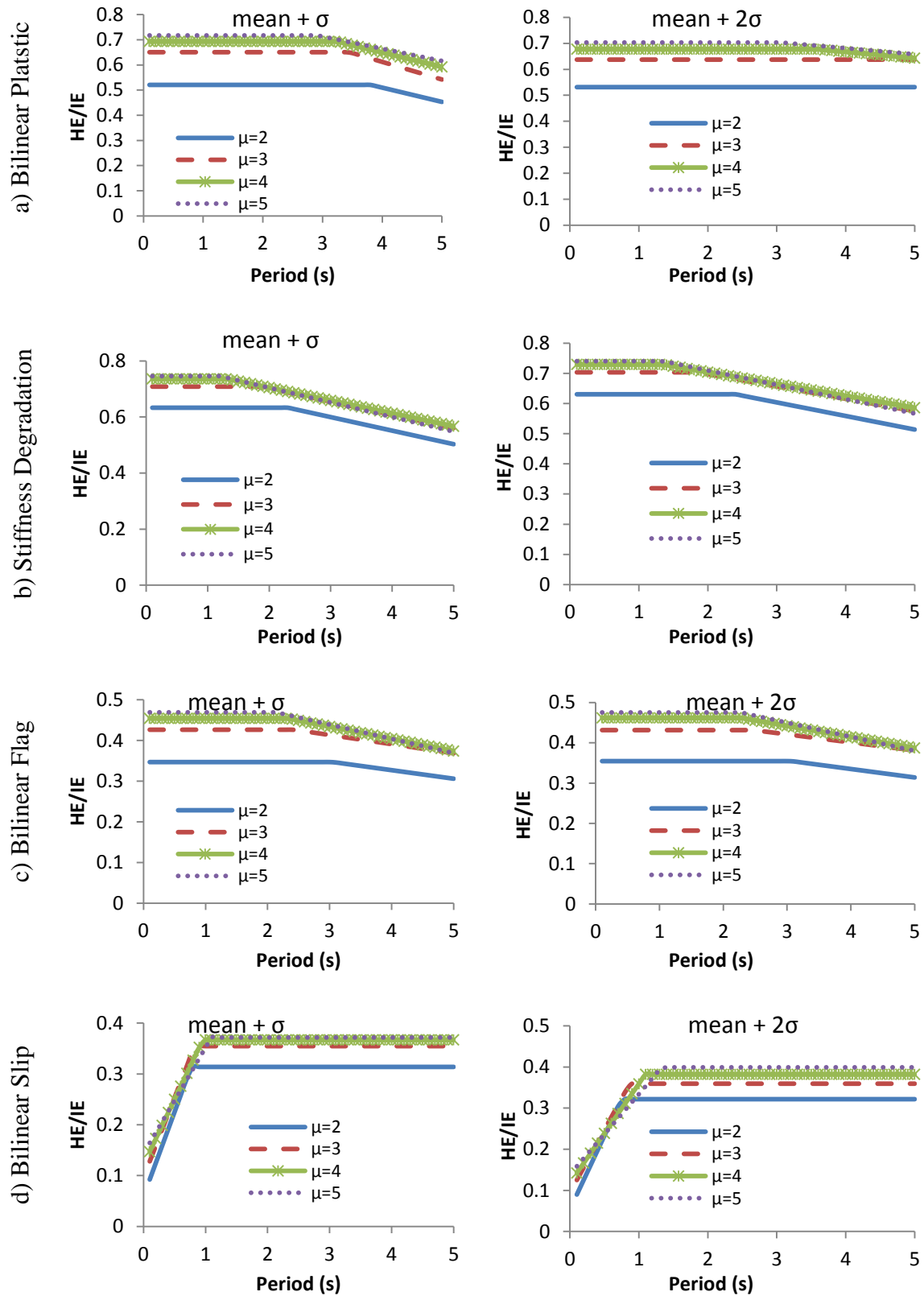
Figure 4.7 *HE/IE* spectra: site class E

4.7 Effect of Soil Site Type on *HE/IE*

In Section 3.8, the effect of site soil class on input energy spectra was discussed. Regardless of the hysteretic behavior considered, it has been found that the maximum spectral value of input energy increases and the range of the intermediate region becomes wider as the soil gets softer. Moreover, it has been observed that for a given ductility value, the input energy increases in the intermediate and long period regions but reduces in the short period region as the soil gets weaker (see Figures 3.30-33). In this section, the effect of site soil on *HE/IE* will be discussed.

Figure 4.8 shows *HE/IE* spectra for SDOF systems having ductility value of $\mu=3$ located at site classes B, C, D and E with the four hysteretic behavior types considered in this study. For a given hysteretic behavior and soil site class, *HE/IE* spectra for ductility values of $\mu=2, 4 \& 5$ exhibit a similar trend and variation as those of ductility value $\mu=3$. Consequently, observations made based on *HE/IE* spectra for ductility value $\mu=3$ (shown in Figure 4.8) will also apply to ductility values of $\mu=2, 4 \& 5$. From Figures 4.8(a), it can be seen that for SDOF systems with hysteretic behavior BP, *HE/IE* values increase as the site soil gets softer. However, for SDOF systems with hysteretic behaviors SD and BF (see Figures 4.8 (b&c), *HE/IE* values increase as the site soil gets softer only in the short and intermediate regions of the spectra. They show a mixed response in the long period region. For hysteretic behavior type BS, *HE/IE* values decrease as the soil gets softer. Upon further scrutiny, it can be observed that when compared to hysteretic types BP and BS, hysteretic types SD and BF tend to show less difference in the amount of *HE/IE* values among the different soil sites. As a result, it is not possible to make a general statement about the relationship of site class and hysteretic to input energy ratio without taking the hysteretic behavior of the system into consideration. This finding to a certain extent disagrees with the conclusion reached by Ye *et al (2009)* on the effect of site soil conditions on

the ratio of hysteretic energy to input energy. They concluded that the influence of soil site conditions and ground motion characteristics on the ratio of hysteretic energy (*HE*) to input energy (*IE*) is negligible. However, the differences are small enough that it may be concluded that the effect of site class on *HE/IE* spectra for a given hysteretic model can be neglected. For instance, for ductility value of μ=3, the mean square errors of *HE/IE* values between that of site class B and the other class sites ranges from 3.82E-05 to 5.34E-03 (see Table 4.5). The same order of magnitude for these values has been observed for the other ductility values as well. Thus, for a given hysteretic model a single *HE/IE* spectrum that envelops all the others and independent of site class can be conservatively proposed for practical design purposes.

Table 4.5 *HE/IE* mean square error values (μ=3)

Hysteretic Model	mean+2σ			mean+2σ		
	Site B&C	Site B&D	Site B&E	Site B&C	Site B&D	Site B&E
BP	9.04E-04	4.40E-03	5.34E-03	1.04E-03	4.32E-03	4.70E-03
SD	6.25E-03	3.51E-03	3.34E-03	4.12E-03	2.95E-03	1.96E-03
BF	2.25E-04	4.35E-04	9.20E-05	2.28E-04	1.86E-04	3.82E-05
BS	9.72E-04	1.02E-03	2.79E-03	7.36E-04	1.68E-03	4.44E-03
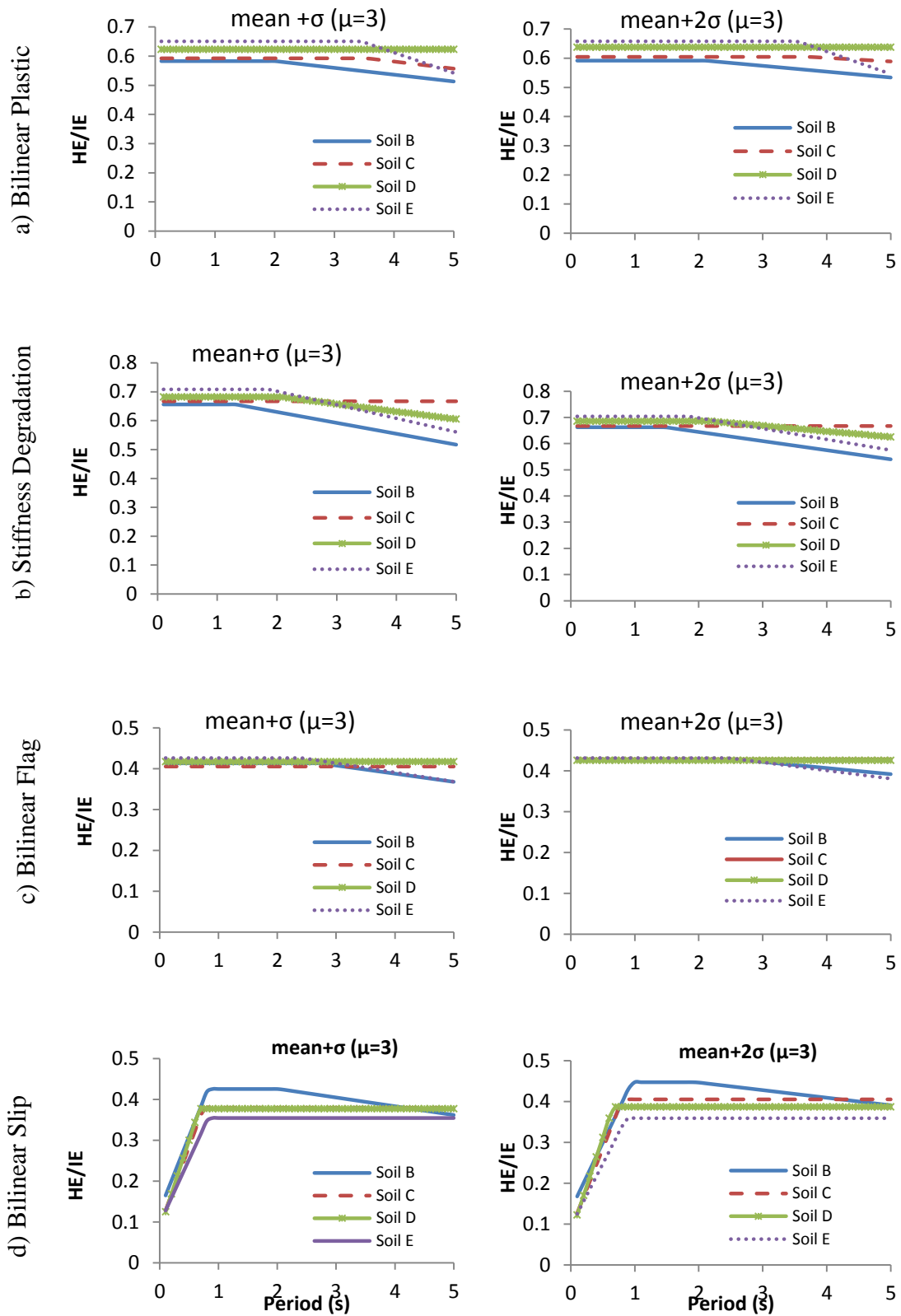
Figure 4.8 Effect of site soil on *HE/IE* spectra: ductility value μ=3

117

4.8 Effect of Hysteretic Behavior on *HE/IE*

Figure 4.9 shows the effect of hysteretic behavior on *HE/IE* spectra for SDOF structures with ductility value of $\mu=3$. It has been observed in Sections 4.3-4.6 that for a given hysteretic behavior, *HE/IE* spectra of SDOF systems with ductility values of $\mu \geq 3$ exhibit only small differences for all soil site classes considered in this study. In some cases, the *HE/IE* spectra graphs for ductility values $\mu \geq 3$ have been found to be overlapping in the intermediate and long period regions. In addition, *HE/IE* spectra for SDOF systems for ductility values of $\mu=2, 4, 5$ show similar pattern as those indicated in Figure 4.9 for ductility value of $\mu=3$. Thus, the inference made from Figure 4.9 is also applicable to SDOF systems with ductility values $\mu=2, 4, 5$.

As can be seen from Figure 4.9, SDOF systems with hysteretic behavior BP exhibit higher values of hysteretic to input energy ratio. For site classes C, D and E, it can be said that *HE/IE* generally varies with hysteretic behavior in the following order: BP>SD>BF>BS. However, except in the short period region, the same cannot be said for site class B where the graphs of *HE/IE* spectra overlap for hysteretic behavior types BF and BS in the intermediate and long period region. The *HE/IE* spectra reveal that for all soil site classes considered in this study, hysteretic models BP and SD often result in higher and almost equal *HE/IE* values when compared to hysteretic models BF and BS. This noticeable difference between the *HE/IE* values means for practical application the hysteretic models can be grouped into two groups with hysteretic models BP and SD in one group and BF and BS in another. Thus, for design purposes the maximum *HE/IE* value in each group could be used without significantly overestimating the energy demand on the structure.
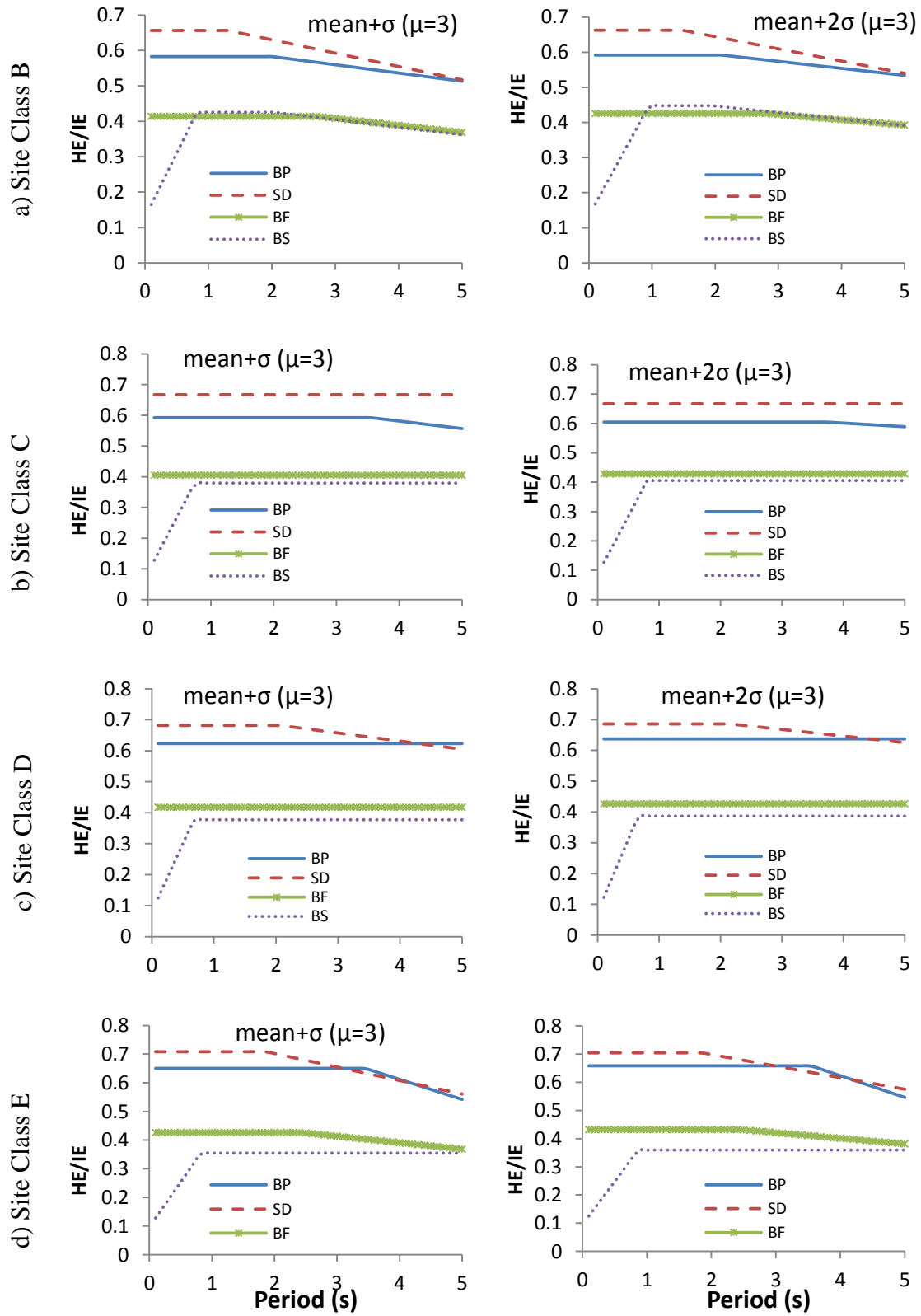
Figure 4.9 Effect of hysteretic model on *HE/IE* spectra: ductility value *μ=3*

4.9 Validation of Proposed Hysteretic Energy Spectra

Scaled earthquake records listed in Table 3.19 were used to examine the validity of the proposed *HE/IE* spectra. The same set of earthquakes has been used to investigate the performance of the proposed input energy spectra in Chapter 3. The validity of the proposed spectra is established through comparison with the corresponding "exact" spectra obtained from nonlinear time history analysis.

The mean+σ and mean+2σ "exact" hysteretic energy spectra shown in Figures 4.10 to 4.13 were obtained from the mean+σ and mean+2σ nonlinear time history analysis of SDOF systems subjected to the selected set of earthquakes that corresponds to each site class as shown in Table 3.19. The proposed mean+σ and mean+2σ hysteretic energy spectra were obtained using the following steps

Step1: For a given site, the mean+σ and mean+2σ values of the velocity index (VI) of the selected earthquakes were calculated.

Step2: For a given hysteretic model and ductility value, the corresponding input energy spectra was then obtained by multiplying the ordinates of normalized proposed energy spectra by the VI values obtained in Step 1, i.e.,

$$mean + \sigma \ (IE/m) = mean + \sigma \ (VI) \times \{mean + \sigma \ (N)\}^2 \quad and$$

$$mean + 2\sigma \ (IE/m) = mean + 2\sigma \ (VI) \times \{mean + 2\sigma \ (NE)\}^2$$

Step 3: The corresponding *mean+σ* and *mean+2σ* proposed hysteretic energy spectra were then obtained as a product of the values in Step 2 and corresponding (*HE/IE*) values proposed in sections 4.3 through 4.6.
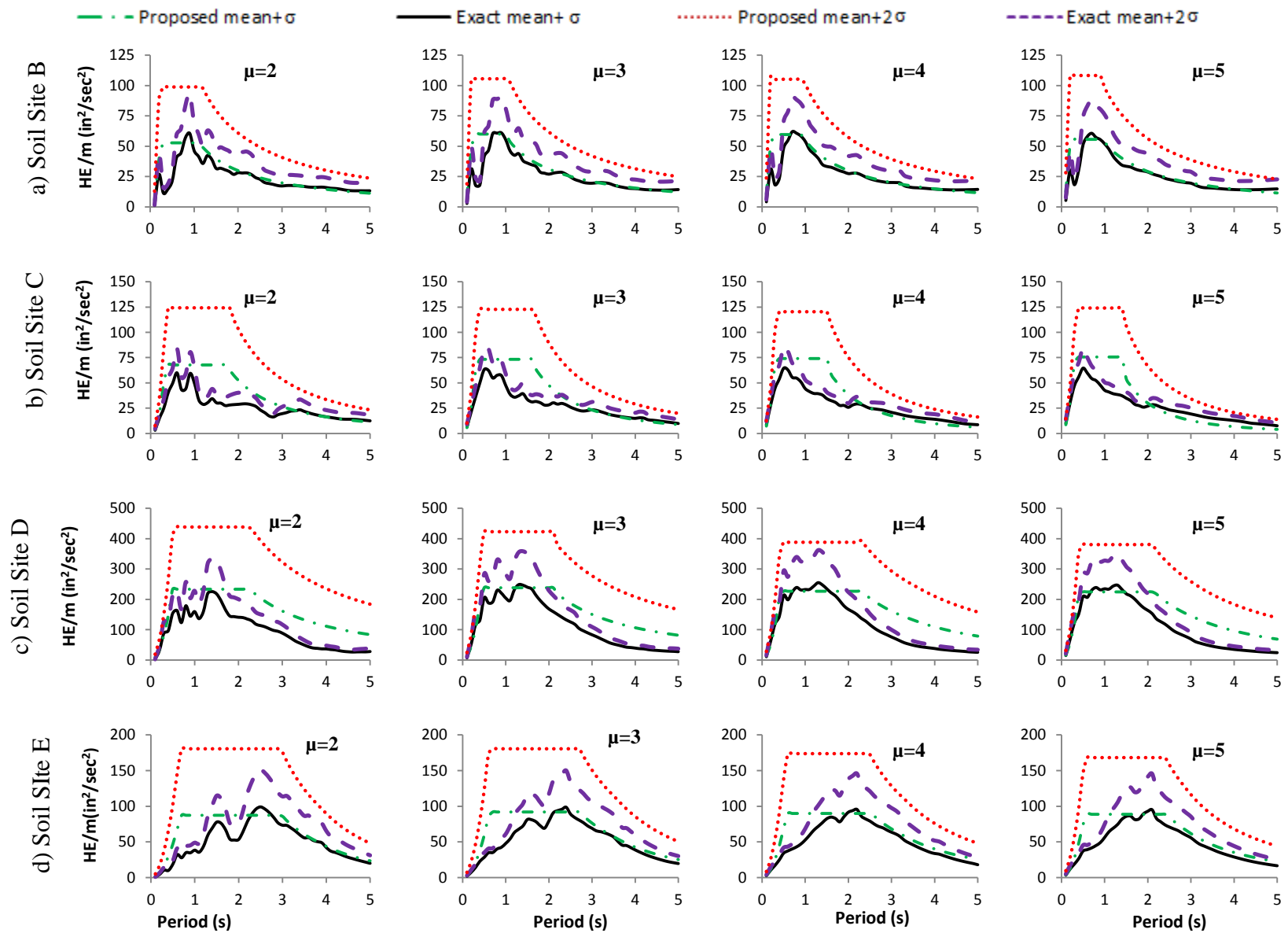
Figure 4.10 Verification of proposed spectra: hysteretic model BP

Figure 4.10 shows the *mean+σ* and *mean+2σ* hysteretic energy spectra (both proposed and

"exact") for SDOF systems with bilinear plastic (BP) hysteretic behavior, pre–to-post yield

stiffness ratio of α=0.05 and damping coefficient of ζ=5%. The six earthquake records selected

for each site class and presented in Table 3.19 were used to develop these spectra. For site class

B (Figure 4.10a), the proposed spectra reasonably match both the *mean+σ* and *mean+2σ* exact

spectra in all regions of the spectra for the period of vibration range 0-5 s. For the mean+σ

spectra a stronger agreement is observed between the proposed and the exact spectra, and only a

small value of root mean square error is noted. It is also observed that the proposed spectra

envelope the exact spectra obtained from nonlinear time history analysis for all ductility values.

This suggests that the use of the proposed spectra for design will produce safe results.

For site class C and hysteretic model BP, the proposed *mean+σ* spectra reasonably match the

mean+σ exact spectra (see Figure4.10b). However, the proposed *mean+2σ* spectra seem to

overestimate the spectral values regardless of the ductility value. If a designer chooses to use the

proposed *mean+2σ* spectra, the design will probably be overly conservative. For site classes D

and E, the proposed mean+σ spectra compare well with the exact *mean+σ* spectra. The

mean+2σ proposed spectra; however, appear to overestimate the hysteretic energy values over a

range of periods: In the intermediate and long period region for site class D and in the

intermediate region for site class E. Overall, the proposed spectra for most cases tend to envelope

the exact spectra, which is desirable as it leads to safe design.
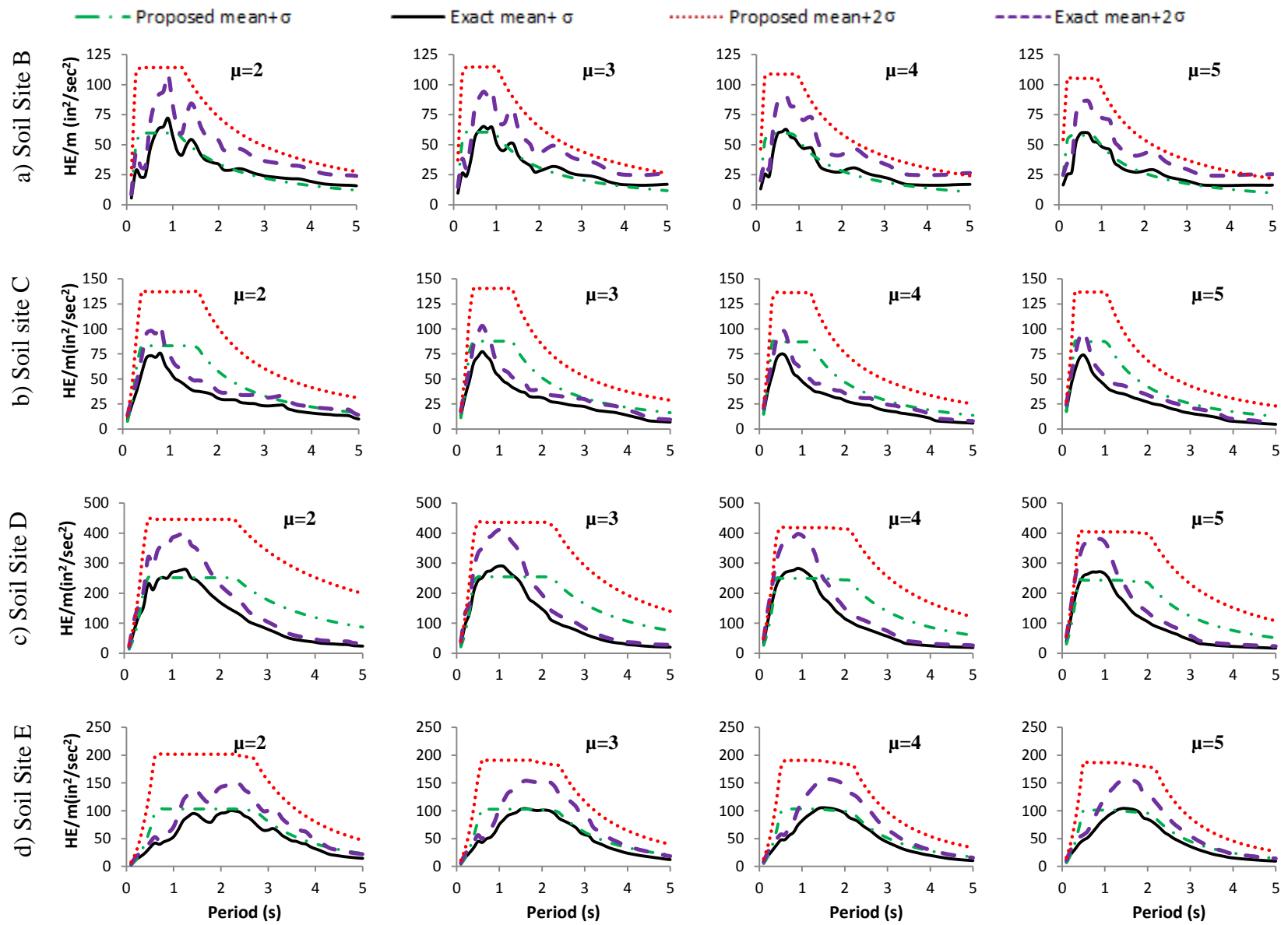
Figure 4.11 Verification of proposed spectra: hysteretic model SD

The verification graphs for both the proposed mean+σ and mean+2σ hysteretic energy spectra for SDOF systems with hysteretic behavior SD, pre-to-post yield stiffness ratio α=0.05, damping ratio ζ=5% and ductility values of μ=2,3,4, 5 located at site classes B, C, D and E are shown in Figure 4.11. For site class B, Figure 4.11(a), it can be seen that the proposed mean+σ and mean+2σ spectra adequately emulate the corresponding exact spectra. In fact, the proposed and exact mean+σ spectra match very well in all regions of the spectra for ductility values μ=2, 3, 4, 5. This is a good indication that a minimum of six earthquakes might be considered enough for seismic design of structures exhibiting a stiffness degradation hysteretic behavior and located in site class B. For site class C shown in Figure 4.11(b), it is evident that the proposed mean+σ hysteretic energy spectra give a good estimate of the exact spectra. However, the proposed mean+2σ spectra appear to overestimate the actual hysteretic energy spectra obtained from nonlinear time history analysis. The degree of overestimation is rather prominent in the intermediate region with about 35% increase on average over the spectral values from the exact spectra.

For site class D shown in Figure 4.11(c), both the proposed mean+σ and mean+2σ hysteretic energy spectra appear to match the exact spectra in the short and intermediate region. On the other hand, both spectra give overestimated values in the long period region. The proposed mean+σ hysteretic energy spectra for site class E shown in Figure 4.11(d) produce a reasonable estimate of the actual hysteretic energy in all regions. Except in the short period region where the spectra appear to overestimate the hysteretic energy values, the proposed mean+2σ spectra generally show a good estimate of the exact spectra in the intermediate and long period regions.
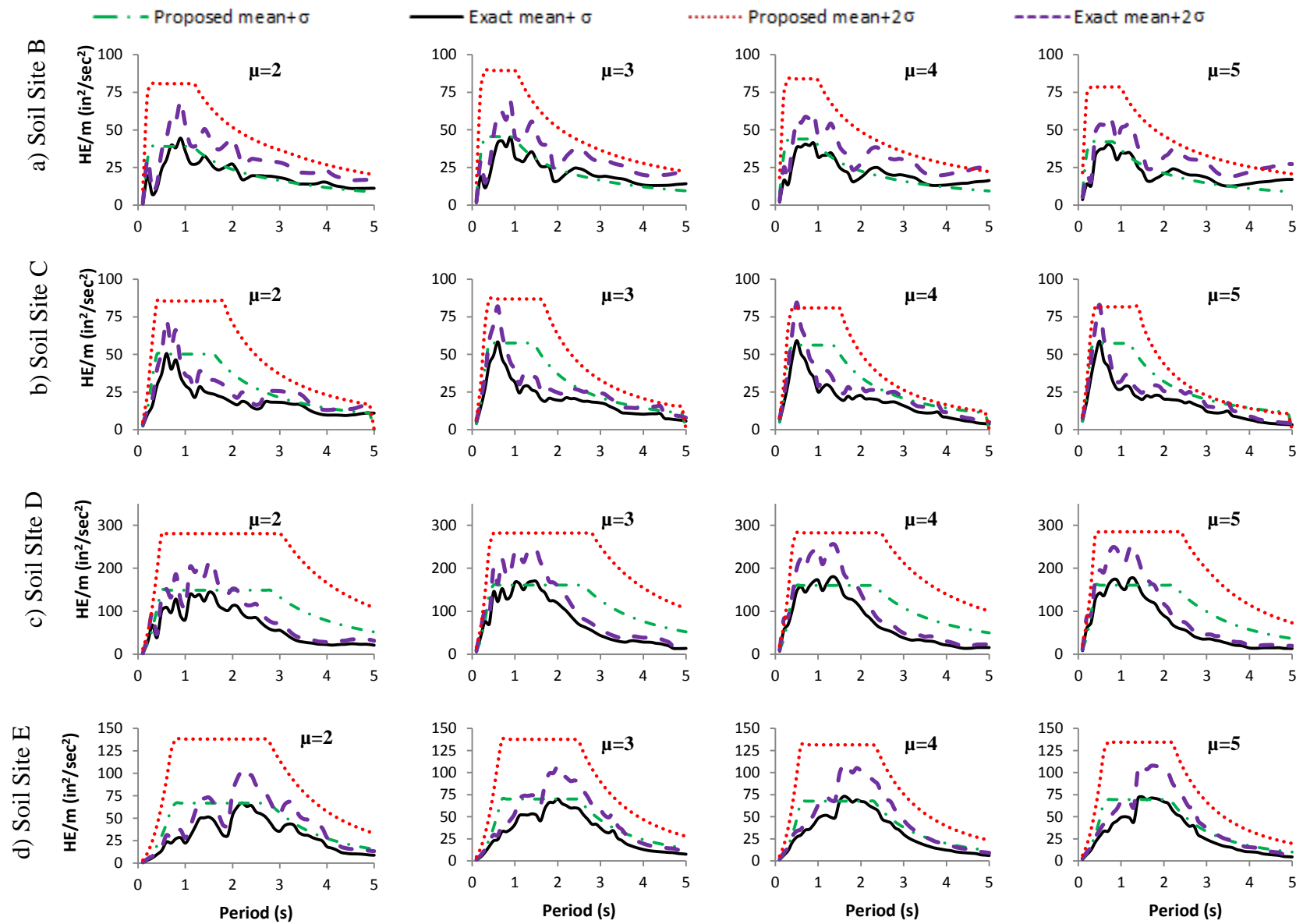
Figure 4.12 Verification of proposed spectra: hysteretic model BF

125

A comparison of the proposed and exact hysteretic energy spectra for SDOF systems with hysteretic behavior BF is shown in Figure 4.12(b)-(d) for soil site classes C, D and E. As can be seen, the proposed spectra envelop the exact hysteretic energy spectra for all ductility values. Similar to hysteretic model SD, the proposed spectra for site classes D and E exhibit relatively higher values of hysteretic energy when compared to the exact spectra in the long period and short period regions, respectively.

For site class B as shown in Figure 4.12(a), the proposed mean+σ spectra tend to underestimate the actual hysteretic energy especially in the long period region whereas the proposed mean+2σ spectra tend to overestimate the actual hysteretic energy. Also, for site class B the maximum mean+σ and mean+2σ spectral values for both the proposed and exact spectra are found to be nearly equal. The parity in the maximum spectral values indicates that the proposed spectra can effectively estimate the actual hysteretic energy in the worst case scenario. More importantly, the proposed spectra often produce conservative values over a large region of the spectra.

Similar results have been observed for hysteretic type BS (see Figure 4.13). The only exception is that for site class D, the proposed spectra tend to overly overestimate the hysteretic energy values. In particular the mean+2σ proposed hysteretic energy spectra are found to have values about 1.85 times the corresponding exact spectral values. Also, for site class B the shapes of the proposed spectra have uncharacteristically pointed maximums instead of plateaus but appeared to follow the trend of the exact spectra.
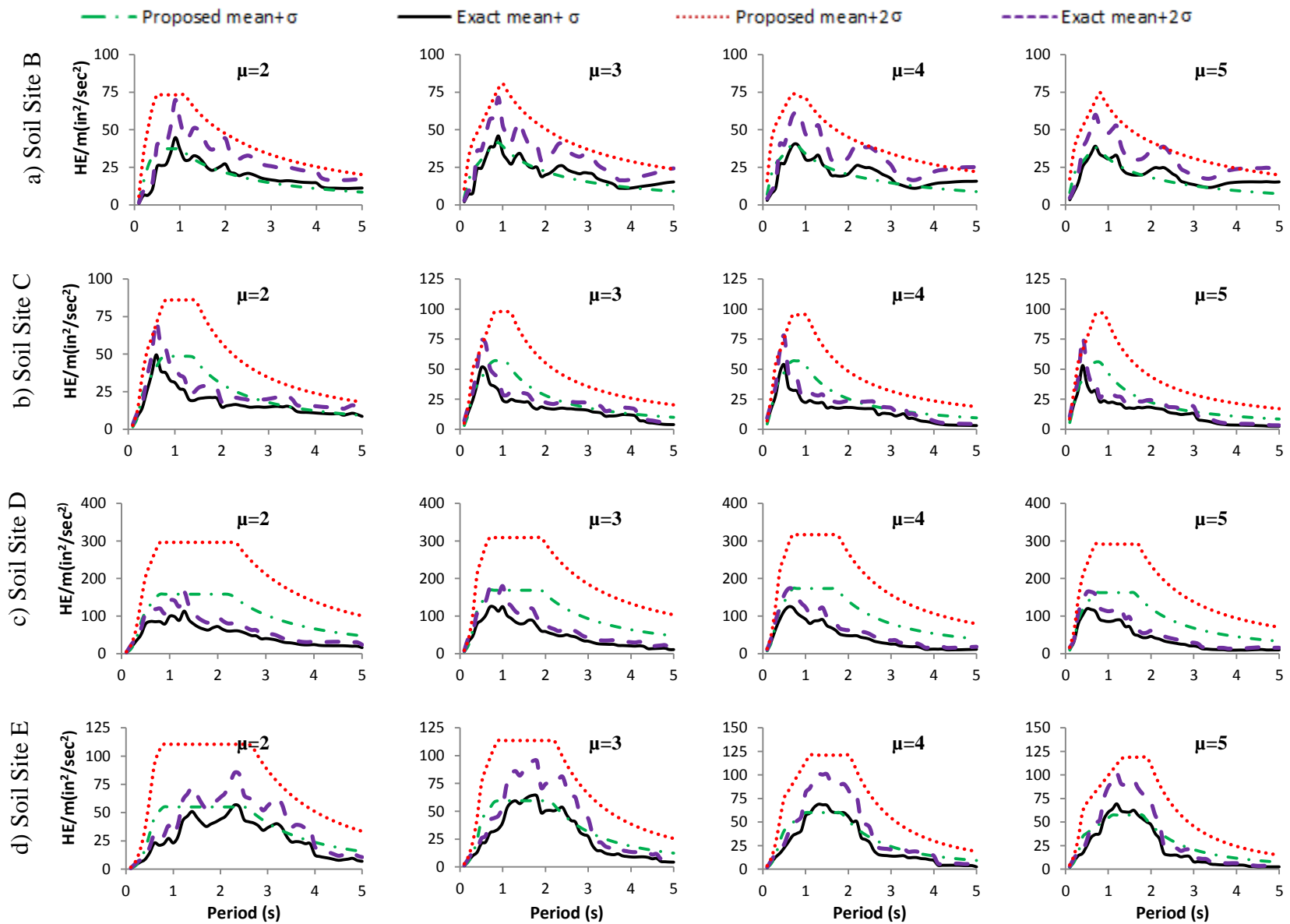
Figure 4.13 Verification of proposed spectra: hysteretic model BS

5   ESTIMATION OF SEISMIC INPUT ENERGY IN MDOF SYSTEMS

5.1 Introduction

In Chapters 3 and 4, simple expressions for input energy and hysteretic to input energy spectra

for SDOF systems have been developed. For a given design record and site condition, these

expressions will enable a designer to estimate the maximum hysteretic energy demand on SDOF

systems with a desired ductility value of $\mu \leq 5$ and with a damping ratio of 5%. In reality, the

designer often needs to deal with MDOF rather SDOF systems. Recognizing this fact, this

chapter aims to formulate relationships for estimating input energy and hysteretic demand for

MDOF systems using the equivalent single degree of freedom (ESDOF) system concept.

Section 5.2 presents a review of existing literature on input energy for MDOF systems. Section

5.3 discusses how a MDOF system can be discretized into a series of ESDOF systems based on

modal pushover analysis. Also in this section, a pushover based input energy relationship

between the MDOF system and its series of equivalent SDOF systems is to be developed.

Section 5.4 presents a description of the frames to be used for case study and the development of

the ESDOF systems based on the procedures outlined in Section 5.3. Finally, six earthquake

records were used to validate the proposed input energy relationships between the MDOF

systems and their associated series of ESDOF systems.

5.2 Input Energy in MDOF Structures: Literature Review

Regardless of the size of the structure, or whether it is a SDOF or an MDOF system, the first step

in energy-based seismic design is to determine the seismic energy demand on the structure due to

the design earthquake. Seismic energy demand or hysteretic energy, as explained in Chapter 2,

is the inelastic component of the absorbed energy of the total seismic input energy imparted onto

a structure and is a function of the hysteretic behavior of the structure. For a given design earthquake, as described in chapter 4, structures of equal weight/mass but have different hysteretic behavior will be subjected to different seismic energy demands. Expectedly, different seismic energy demands will require different energy dissipation capacities. In energy-based design, the structure has to be designed so its energy dissipation capacity will exceed the energy demand, i.e., the hysteretic energy. In the present study, hysteretic behavior dependent input energy and hysteretic energy expressions that are functions of ductility and period of vibration for SDOF systems with damping ratio of $\zeta=5\%$ have been developed in Chapter 3 and Chapter 4, respectively. The fact that almost all practical structures are MDOF systems means we need to go beyond SDOF systems and study the seismic input and hysteretic energy of MDOF systems. Compared to SDOF systems, seismic energy analysis of MDOF systems is relatively difficult to understand and carry out. The number of dynamic equations involved along with the coupling effect of different responses makes the determination of seismic input energy and the accompanying hysteretic energy in MDOF systems rather difficult to assess and comprehend. Clearly, one can say that the determination of seismic energy for MDOF systems in not as straightforward as that for SDOF structures. However the handiness of SDOF systems can be exploited to study the seismic energy of MDOF systems. Research performed up to now and presented below has enabled engineers to reach the conclusion that input energy for MDOF structures can be obtained from their equivalent SDOF components.

Akiyama *(1985)* used the S00E component of the 1940 El Centro record to compute the input energy using a Fourier Spectra for a five-story building. He compared it with an input energy of an equivalent one-story building having the same fundamental period of vibration, total mass, and yield strength. Based on his observation, he concluded that the input energy for MDOF

129

structures can be estimated from the input energy of equivalent SDOF systems. He also claimed that the parameters that affect earthquake input energy are mainly the mass and period of the structure. Nakakashima *et al* (1996) in their study on the energy behavior of structures with hysteretic dampers found that the total input energy and hysteretic energy for MDOF systems are approximately the same as those of the equivalent SDOF systems. They also found that this is true even for a large value of post-to-pre-yield stiffness ratio. The effect of post-to-pre-yield stiffness ratio was only seen on the distribution of hysteretic energy at different levels of the structure.

Shen and Akbas *(1999)* computed earthquake input energy for a three-, six- and ten-story moment resisting steel frames using equivalent SDOF systems. They compared the input energy expressions they formulated based on the energy balance equation and empirical equations by Housner *(1956)*, Akiyama *(1985)*, Fajfar *et al. (1989)*, Kuwambura and Galambos *(1989)* and Uang and Bertero *(1990)*. They found that energies for MDOF and their corresponding equivalent SDOF structures are significantly different since the empirical equations do not take into account structural properties such as period of vibration and hysteretic behavior. Chou and Uang *(2003)* developed an empirical formula to estimate the absorbed energy in multistory fames using an energy spectra developed for SDOF systems. They used a static pushover analysis to determine the yield force and ductility factor of an equivalent SDOF system. For low-to-medium rise buildings they showed that their expressions (Equation 5.1) can be used to estimate the absorbed energy in MDOF systems from their equivalent SDOF system.

$$E_a = \sum_{i=1}^{n} \tfrac{1}{2} m_i (V_{ai}\Gamma_i)^2 \tag{5.1}$$

where i is mode number, m_i is the modal mass of mode i, V_{ai} is the equivalent velocity obtained from the V_a spectra, Γ_i is the modal participation factor for mode i, and n is the number of modes considered. Chou and Uang *(2003)* used $n=2$ and they claimed that two modes were enough to give reasonably good results.

Li *et al. (2007)* and Ye *et al. (2009)* also proposed a procedure for obtaining hysteretic energy of MDOF structures from their equivalent SDOF structures. Their procedure takes into account only the first mode of the MDOF structures. They used eight examples (two regular and six irregular MDOF structures) and concluded that their procedure is an effective and simple way of obtaining the hysteretic energy demands of MDOF structures. Ye *et al. (2009)* also studied the energy-based seismic design and its application for steel braced frame structures. They proposed an inelastic input energy spectrum for SDOF structures and a relationship between hysteretic energy and input energy. They concluded that the input energy for MDOF structures can be estimated from their equivalent SDOF structures. For structures in the moderate and long period regions, they proposed expressions shown in Equations (5.2) and (5.3) for estimating the input energy for MDOF systems from their equivalent SDOF systems and the ratio of hysteretic energy to input energy for MDOF structures, respectively.

$$IE_{MODF} = IE_{SODF}\left(\zeta,\mu,T_o\right) \tag{5.2}$$

$$\frac{HE_{MODF}}{HE_{MDOF}} = \begin{cases} -43.6\zeta^3 + 29.87\zeta^2 - 7.22\zeta + 0.85 & (\zeta \neq 0, 1 < \mu \leq 2) \\ b_1 + (b_2 - b_1)(\mu - 2) & (2 < \mu < 3) \\ -17.48\zeta^3 + 15.69\zeta^2 - 5.25\zeta + 1 & (\mu \geq 3) \end{cases} \tag{5.3}$$

where IE_{SDOF} is the input energy for the equivalent SDOF system, T_o is the fundamental period of the MDOF system, HE_{SDOF} is the hysteretic energy of the ESDOF system, IE_{MDOF} is the input energy for the MDOF system and HE_{MDOF} is the hysteretic energy of the MDOF system.

In this study, aligned with the work done by Chou and Uang *(2003),* an analytical relationship between the energy balance for MDOF systems and their equivalent SDOF systems is formulated and investigated. This approach will result in a relationship between the input energy of the MDOF systems and their equivalent SDOF systems. The hysteretic energy for MDOF structures is then obtained from the calculated input energy by using equations of hysteretic to input energy ratio that were developed for SDOF structures. This approach is consistent with the approach used in estimating the hysteretic energy from the input energy developed for SDOF systems in Chapter 4.

5.3 Equivalent SDOF Systems for Determination of Input Energy in MDOF Systems

5.3.1 Equivalent SDOF Systems

The equations of motion for a MDOF system with *n* degrees of freedom subjected to earthquake ground motion, $\ddot{u}_g(t)$ can be expressed as in Equation (5.4).

$$M\ddot{u}(t) + C\dot{u}(t) + \tilde{K}u(t) = -M\iota\ddot{u}_g(t) \tag{5.4}$$

where $M,\ C, \tilde{K}$ are the mass, damping and stiffness matrices of size ($n \times n$), respectively; $\ddot{u}(t)$, $\dot{u}(t)$, $u(t)$ are the relative acceleration, velocity and displacement vectors of the *n*-degrees of freedom system, respectively and ι is the influence vector.

If we denote $u(t) = \Phi x(t) = \sum_{i=1}^{n} \phi_i x_i(t)$ where Φ is the mode shape matrix composed of mode

shape vectors ϕ_i, and $x(t)$ is the modal displacement vector composed of modal displacements

$x_i(t)$ for mode I, then upon substituting the terms for $u(t)$, Equation (5.4) will have the form of

Equation (5.5)

$$M \sum_{i=1}^{n} \phi_i \ddot{x}_i(t) + C \sum_{i=1}^{n} \phi_i \dot{x}_i(t) + \tilde{K} \sum_{i=1}^{n} \phi_i x_i(t) = -M \iota \ddot{u}_g(t) \tag{5.5}$$

For mode r, multiplying both sides of equation (5.5) by ϕ_r^T results in

$$\phi_r^T M \sum_{i=1}^{n} \phi_i \ddot{x}_i(t) + \phi_r^T C \sum_{i=1}^{n} \phi_i \dot{x}_i(t) + \phi_r^T \tilde{K} \sum_{i=1}^{n} \phi_i x_i(t) = -\phi_r^T M \iota \ddot{u}_g(t) \tag{5.6}$$

In nonlinear analysis, responses in different modes are coupled. In other words, the response in

one mode is affected by the response in another mode. However, in modal analysis, responses in

different modes are assumed to be independent. This assumption has been widely accepted for

linear analysis and has been found to give reasonable accurate results. Coupling of responses is

evident due to the non-linearity nature of the structural system. Though this is the reality, the

same assumption has been extended and used in nonlinear analysis of systems with material

nonlinearity. Chopra and Goel *(2002)*, Chou and Uang *(2003)*, Hernandes-Montes *et al (2004)*

and recently Prasanth *et al (2008)* have applied the assumption for determining seismic demand

in building and found that the assumption is reasonably acceptable. In this study, this basic

assumption is maintained in deriving input energy relationship between MDOF system and their

equivalent SDOF systems. Thus, responses in different modes are considered to be independent

and the modes are assumed to be orthogonal to one another. By using this assumption and by

assuming classical damping for the system, Equation (5.6) can be written for any mode r of an MDOF system as

$$\phi_r^T M \phi_r \ddot{x}_r(t) + \phi_r^T M \phi_r \dot{x}_r(t) + \phi_r^T \tilde{K} \phi_r x_r(t) = -\phi_r^T M \iota \ddot{u}_g(t) \qquad (5.7)$$

Defining $\phi_r^T M \phi_r = M_r$ and $\phi_r^T C \phi_r = C_r$, and substituting these equation in Equation (5.7) yields

$$M_r \ddot{x}_r(t) + C_r \dot{x}_r(t) + \phi_r^T \tilde{K} \phi_r x_r(t) = -\phi_r^T M \iota \ddot{u}_g(t) \qquad (5.8)$$

Dividing both sides of equation (5.8) by M_r, results

$$\ddot{x}_r(t) + 2\zeta_r \omega_r \dot{x}_r(t) + \frac{\phi_r^T \tilde{K} \phi_r}{M_r} x_r(t) = \frac{-\phi_r^T M \iota}{M_r} \ddot{u}_g(t) \qquad (5.9)$$

Defining a modal participation factor for mode r as $\Gamma_r = \dfrac{\phi_r^T M \iota}{M_r} = \dfrac{L_r}{M_r}$ and a nonlinear stiffness–

displacement relationship as $\phi_r^T \tilde{K} \phi_r x_r(t) = F_r(t)$, Equation (5.9) then becomes

$$\ddot{x}_r(t) + 2\zeta_r \omega_r \dot{x}_r(t) + \frac{F_r(t)}{M_r} = -\Gamma_r \ddot{u}_g(t) \qquad (5.10)$$

If the modal displacement is redefined as $x_r(t) = \Gamma_r D_r(t)$ where $D_r(t)$ is a generalized displacement for mode r, Equation (5.10) after simplification becomes

$$\ddot{D}_r(t) + 2\zeta_r \omega_r \dot{D}_r(t) + \frac{F_r(t)}{L_r} = -\ddot{u}_g(t) \qquad (5.11)$$

According to Chopra and Goel *(2002)*, Equation (5.11) can be interpreted as the governing equation for the rth- *mode* inelastic SDOF with the initial natural frequency ω_r and damping ratio ζ_r for the rth- *mode* linear MDOF system. Equation (5.11) can be conveniently solved by

134

standard software as it is similar to a standard equation of motion of a SDOF system. Chopra

and Goel *(2002)* named this approach of analysis as Uncoupled Modal Response History

Analysis (UMRHA).

5.3.2   Properties of rth-*mode* Inelastic SDOF System

The properties of an rth-*mode* inelastic SDOF system are determined using a pushover curve

obtained from a non-linear static analysis of the MDOF structure pushed to some predetermined

displacement using a lateral force distribution given by $S_r = M\phi_r$. The force distribution is set to

be proportional to the mode shape ϕ_r of the MDOF system. In a classical pushover analysis, the

roof displacement is considered to be a representative response and is taken as a predetermined

target displacement to which the structure is pushed. However, it is important to note that some

researchers (e.g., Manoukas *et al. (2011)*) have proposed energy-based static pushover analysis

procedures where the predetermined displacement will be independent of any particular story

displacement but a displacement pertinent to the energy.

Generally, the base shear (V_{br}) versus roof displacement u_{rr} plot obtained from a pushover

analysis of a MDOF system is converted into an $\dfrac{F_r}{L_r}$ versus D_r plot of an equivalent SDOF

(ESDOF) system. After Chopra *(2007),* where the proof can be found, the relationship between

(V_{br}, u_{rr}) of the MDOF system pushover curve and ($\dfrac{F_r}{L_r}$, D_r) of the ESDOF system are given by

Equation (5.12) shown below.

$$\frac{F_r}{L_r} = \frac{V_{br}}{M_r^*} = \frac{V_{br}}{L_r \Gamma_r} ; \ D_r = \frac{u_{rr}}{\Gamma_r \phi_{rr}} \tag{5.12}$$

where $M_r^* = L_r \Gamma_r$ is the mass participation factor or effective modal mass for mode r.
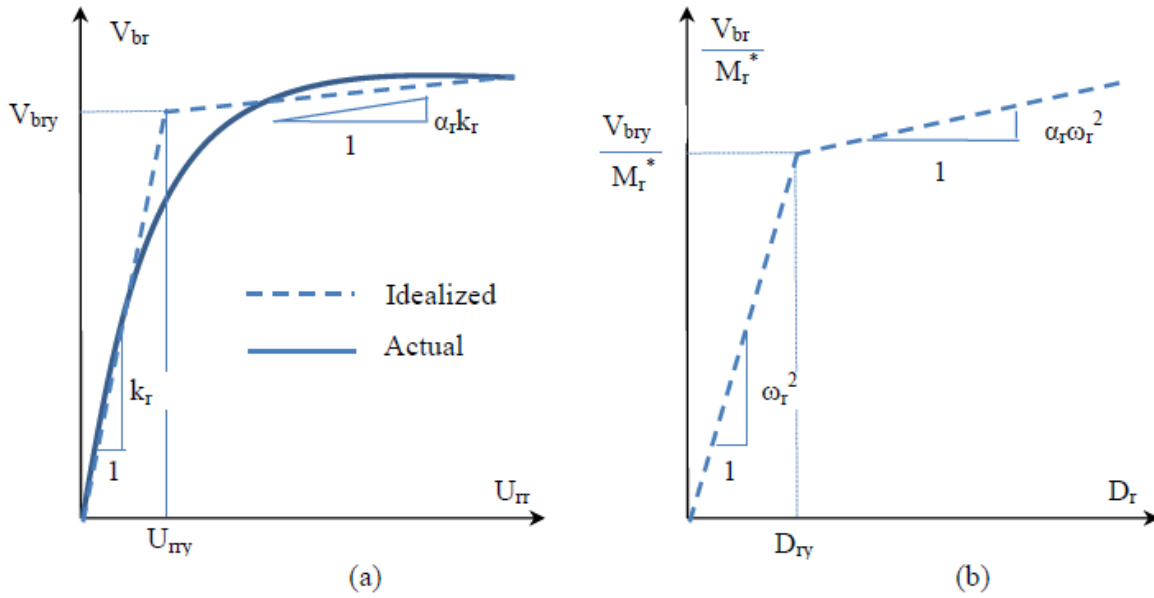
Figure 5.1 (a) an rth mode pushover curve (MDOF system); (b) Force-deformation relation for the rth mode inelastic SDOF system

Figure 5.1 (a) shows a typical actual and idealized pushover curve obtained from a pushover analysis of a MDOF system pushed to a predetermined roof displacement using a lateral force distribution specified for mode shape r. Figure 5.1(b) is a force-displacement relationship for the rth mode of an equivalent inelastic SDOF system generated from the actual pushover curve of Figure 5.1(a). The properties of the equivalent inelastic SDOF (α_r, ω_r, D_{ry}) are used in Equation (5.11) for the analysis of the equivalent SDOF system.

5.3.3   Energy Balance in MDOF Systems

The energy balance equation for SDOF systems was given in Equation (1.2). By the same logic and using the equation of motion for MDOF structures given in Equation (5.4), the energy balance equation for MDOF structures can be expressed as

$$\int_0^t M\ddot{u}(t)\dot{u}(t)d\tau + \int_0^t C\dot{u}(t)\dot{u}(t)d\tau + \int_0^t \tilde{K}u(t)\dot{u}(t)d\tau = \int_0^t -M\iota\ddot{u}_g(t)\dot{u}(t)d\tau \qquad (5.13)$$

Equation (5.13) can be rewritten as

$$E_{kr} + E_d + E_a = E_i \qquad (5.14)$$

where

$$E_{kr} = relative\ kinetic\ energy = \int_0^t M\ddot{u}(t)\dot{u}(t)d\tau$$

$$E_d = damping\ energy = \int_0^t C\dot{u}(t)\dot{u}(t)d\tau$$

$$E_a = absorbed\ energy = \int_0^t \tilde{K}u(t)\dot{u}(t)d\tau$$

$$IE = relative\ input\ energy = \int_0^t -M\iota\ddot{u}_g(t)\dot{u}(t)d\tau$$

For a particular mode r with the modal equation of motion shown in Equation (5.8), the modal

energy balance equation can be expressed as

$$\int_0^t M_r\ddot{x}_r(t)\dot{x}_r(t)d\tau + \int_0^t C_r\dot{x}_r(t)\dot{x}_r(t)d\tau + \int_0^t \phi_r^T \tilde{K}\phi_r x_r(t)\dot{x}_r(t)d\tau = \int_0^t -\phi_r^T M\iota\ddot{u}_g(t)\dot{x}_r(t)d\tau \quad (5.15)$$

or

$$E_{kr}^r + E_d^r + E_a^r = IE^r \qquad (5.16)$$

where $E_{kr}{}^r$, $E_d{}^r$, $E_{ar}{}^r$ and IE^r are the relative kinetic energy, damping energy, absorbed energy and

input energy contributions by mode r, respectively.

Equation (5.11) gives the equation of motion of a SDOF with unit mass corresponding to mode r.

The absorbed and input energy components for this equivalent SDOF system can be expressed as

$$E_{a,SDOF}^r = \int_0^t \frac{F_r(t)}{L_r} \dot{D}_r(t) d\tau \quad \text{and} \quad E_{i,SDOF}^r = \int_0^t -\ddot{u}_g(t)\dot{D}_r(t) d\tau \qquad (5.17)$$

Since $\phi_r^T \tilde{K} \phi_r x_r(t) = F_r(t)$ and $x_r(t) = \Gamma_r D_r(t)$, Equation (5.17) can be rewritten as

$$E_{a,SDOF}^r = \int_0^t \frac{F_r(t)}{L_r} \dot{D}_r(t) d\tau = \frac{1}{L_r \Gamma_r} \int_0^t F_r(t)\dot{x}_r(t) d\tau = \frac{1}{L_r \Gamma_r} E_a^r \quad \text{and}$$

$$IE_{SDOF}^r = \int_0^t -\ddot{u}_g(t)\dot{D}_r(t) d\tau = \frac{1}{L_r \Gamma_r} \int_0^t -\phi_r^T M \iota \ddot{u}_g(t)\dot{x}_r(t) d\tau = \frac{1}{L_r \Gamma_r} IE^r \qquad (5.18)$$

If the mode shapes are mass normalized, then $M_r = 1$ *and* $\Gamma_r = L_r$, the energy equation between MDOF and their equivalent SDOF systems with properties as described in Section 5.3.2 can be further simplified and given as follows

$$E_{a,SDOF}^r = \frac{1}{(\Gamma_r)^2} E_a^r \quad \text{and} \quad IE_{SDOF}^r = \frac{1}{(\Gamma_r)^2} IE^r \qquad (5.19)$$

The two expressions in Equation (5.19) are used to relate the input and absorbed energy of a given vibration mode for the MDOF system to that of its equivalent SDOF system. The amount of input energy and absorbed energy of a MDOF system obtained using these mode-based relationships is primarily dependent on the modal characteristics of the MDOF system besides the seismicity of the site.

5.3.4 Procedure for Estimating Hysteretic and Input Energies in MDOF Structures

In this study, a vibration mode-based procedure is proposed for estimating the input and hysteretic energy for MDOF structures from their equivalent SDOF structures. The proposed procedure involves a series of steps given below:

1. Determine the initial periods of vibrations of the MDOF structures and their corresponding effective modal masses.

2. Decide on the number of modes to be used so that the sum of effective modal masses considered is $\geq 90\%$ of the total mass of the structure.

3. For each mode considered, generate pushover curve by pushing the MDOF structure with a lateral load pattern that matches the respective mode shape.

4. For each mode, using the expressions given in Equation (5.12), develop a force-displacement relationship for an inelastic equivalent SDOF system from the modal pushover curve of the MDOF.

5. From the resulting pushover force displacement curve, determine the yield force, initial stiffness and post-yield stiffness ratio for each mode

6. Using the yield force, initial stiffness and post-yield stiffness ratio for each mode, determine the corresponding ductility factor. The ductility factor can be determined using one of the following approaches

   (a) by time history analysis of the SDOF for a given earthquake, or

   (b) from a ductility-based yield force spectra if readily available, or

   (c) from a prescribed desired ductility level

   Options (a) or (b) is used if the main objective is to determine the energy capacity of an MDOF systems, whereas option (c) is used if the objective is to design an energy dissipating mechanism for an MDOF system.

7. Using the ductility factor and period of vibration, determine the corresponding input and hysteretic energies for each mode using the input energy spectra (Chapter 3) and the hysteretic-to-input energy ratio spectra (Chapter 4), respectively.

8. The input energy and hysteretic energies of the MDOF structure are then given by

$$IE_{MDOF} = \sum_{r=1}^{n} (\Gamma_r)^2 \, IE_{SDOF}^r$$

$$HE_{MDOF} = \sum_{r=1}^{n} (\Gamma_r)^2 \, HE_{SDOF}^r$$

(5.20)

where

Γ_r = modal participation factor for mode r

n = number of modes considered

IE_{MDOF} = estimated input energy for the MDOF system

HE_{MDOF} = estimated hysteretic energy for the MDOF system

IE_{SDOF}^r = estimated input energy for the equivalent SDOF system for mode r

HE_{SDOF}^r = estimated hysteretic energy for the equivalent SDOF system for mode r

5.4 Description of Frames Used for Case study

Low and medium height moment resisting frames were used to investigate the validity of the expressions given in Equation (5.20) for estimating hysteretic and input energies for MDOF structures using equivalent SDOF systems. Four moment resisting frames with 3-, 5-, 7- and 9-stories were used in the study. The moment resisting frames have been previously used by researchers such as Gupta and Krawinkler *(1999)*, Chou and Uang *(2003)* and Prasanth *et al (2008)* for estimating the seismic responses of MDOF systems using equivalent SDOF systems. Their known physical and structural properties were used in checking the accuracy of the SAP 2000 and PERFORM 3D computer models the frames used in this study.

The 3-, 5-, and 7- story office building have ductile moment resisting frames in both directions to resist earthquake load as per the requirements of FEMA (1994). The design parameters used and

140

the design procedures involved can be found in Chou *(2001)*. The 9-story building has steel

moment resisting frames in both directions and was designed by a SAC commissioned

consulting firm based on the procedures of UBC (1994). The 3- story and 9-story building were

composed of steel columns and beams whereas the 5-story and 7-story buildings were designed

using steel encased reinforced concrete (SRC) columns and steel beams. For the 3-, 5- and 7-

story frames, a reduced beam section with 50% reduction in both the top and bottom flanges was

used to reduce the demand to the connections. Other than at the base of the columns, this

ensures that hinges do form first at beam ends for a given connection. The elevations, member

sizes and strengths of these four frames are listed in Appendix C.

5.4.1   Equivalent SDOF Systems

FEMA 273 *(1997)* recommends that the number of modes with a combined effective modal mass

of larger than 90% of the total mass be used in a modal analysis to estimate the dynamic

response of a structure. In addition, Filiatrault *(1998)* suggested that the effective modal mass

($L_r \Gamma_r$, or simply L_r^2 when modes shapes are mass normalized) can be used as an index for the

number of modes to be considered for elastic dynamic analysis. In this study, the

recommendation by FEMA 273 was adopted for determining the number of modes used for

comparing the input energy imparted to the MDOF systems (i.e., the frames described above) to

their equivalent SDOF systems. The periods of vibration, mass participation factors and

effective modal masses using two modes for each of the frames considered are shown in Table

5.1

141

Table 5.1 Periods of vibration and effective modal masses

Frame	3-Story	5-Story	7-Story	9-Story
Period T_1 (s)	1.06	1.48	1.85	2.14
Period T_2 (s)	0.35	0.53	0.66	0.80
L_1^2 (kip·s^2/in.)	2.195	3.654	5.175	21.241
L_2^2, kip·s^2/in.)	0.279	0.494	0.649	2.765
ΣL_r^2 (kip·s^2/in.)	2.474	4.148	5.824	24.006
Total Mass M (kip·s^2/in.)	2.527	4.349	6.172	25.723
$\Sigma L_r^2/M$	0.979	0.954	0.944	0.933

From Table 5.1, it can be seen that for all the frames considered in this study the total mass contribution from just two modes was found to exceed 90% of the total mass. Thus, according to FEMA 273 *(1997)*, it can be concluded that only two modes are needed for estimating the dynamic response of the frames. Based on the procedures outlined and the expressions formulated in Section 5.3, the equivalent SDOF systems of the first two modes for each frame were calculated and are presented below. Subsequently, these equivalent SDOF systems were used for estimating the input energies for the MDOF frame systems.

Static pushover analysis results for the 3-, 5-, 7- and 9-story frames for the first and second mode are shown in Figures 5.2 and 5.3, respectively. As mentioned earlier, the static pushover analyses were obtained by subjecting the frames to a pattern of lateral loads that emulate the modal shape of the respective mode until the roof displacement reaches a prescribed value. The prescribed displacement of each frame for each mode is limited to a drift ratio of 0.02. Drift ratio limit is often used as a criterion in the design of frames (see Appendix C).
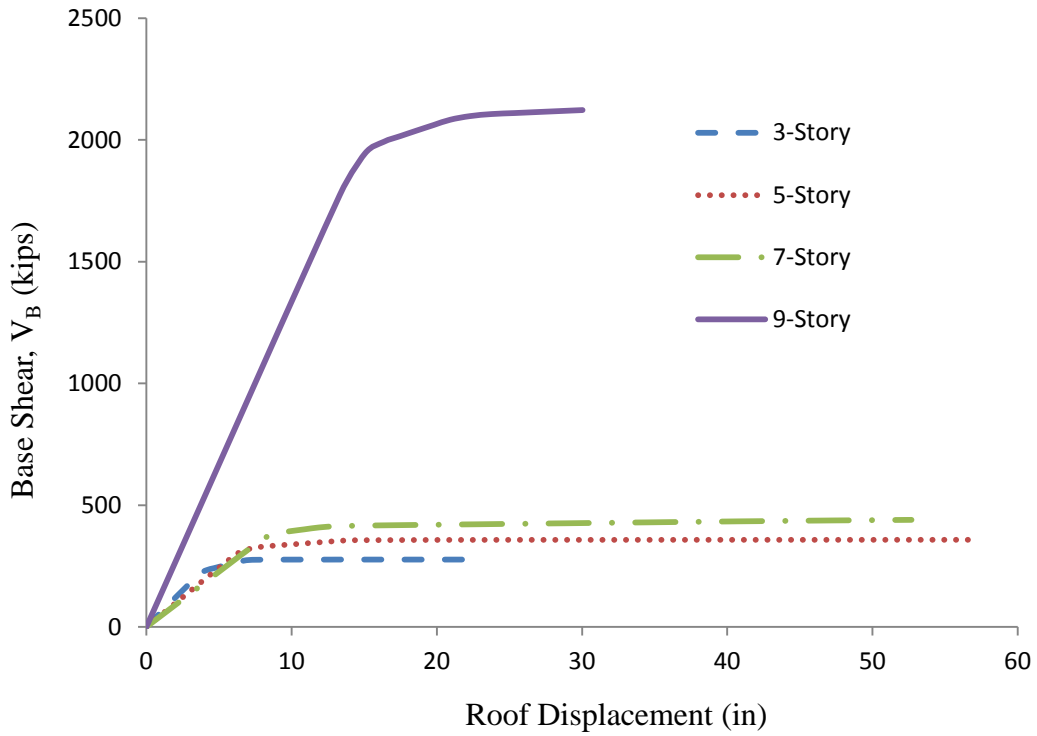
Figure 5.2 First mode MDOF system pushover curves
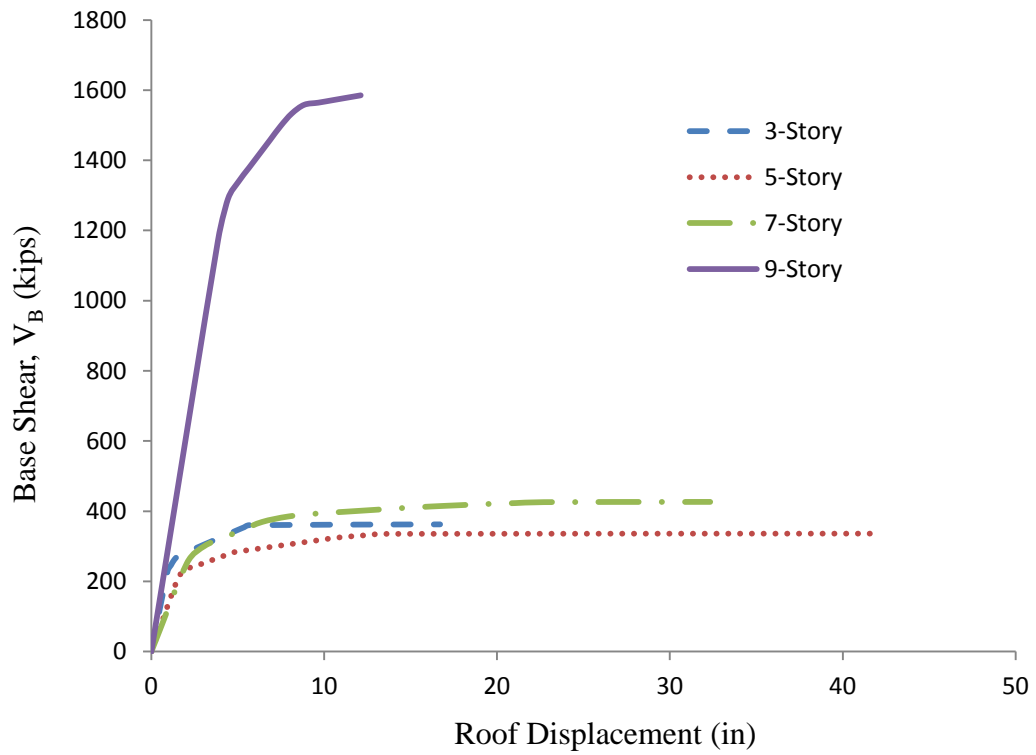
Figure 5.3 Second mode MDOF system pushover curves

143

The 9-story building was designed for site class D, which is higher than that of site class C to which the 3-story, 5-story, and 7-story frames were designed for. The higher yield force observed for the first and second modes of the 9-story frame when compared to the other three frames emanates from the inherent demand of higher yield force for a higher seismic coefficient. It has been observed that for the first mode pushover case most of the yielding occurred at lower stories with plastic hinges forming at base of columns and beams in the first and second stories, whereas in the second mode case much of the yielding happens at the upper stories, mainly concentrated approximately at level where the lateral force pattern for the second mode shape changes its sign.

Figures 5.4 and 5.5 show the force–displacement relations of the ESDOF components that correspond to the first and second modes of the corresponding MDOF systems. They were developed from pushover curves shown in Figures 5.2 and 5.3. Expressions given in Equation (5.12) were used to convert the MDOF pushover curves to the ESDOF force-displacement relationships. The ESDOF yield forces for the frames considered in the first and second modes (shown in Figures 5.4 and 5.5) indicate that the yield forces are higher for the second modes. This is in direct correlation to the notion that very limited yielding occurs in the second mode. It is probable that most of the yielding is contributed by the first mode, leaving the second mode to respond elastically. A summary of the yield forces and other parameters that were used in the input energy analysis for the ESDOF using BISPEC *(2010)* are listed in Tables 5.2 and 5.3.

Table 5.2 ESDOF parameters for the 1st mode

	Period (s)	D_{1y} (in.)	F_{1y}/L_1(in./s^2)	α	Γ_1
3-Story	1.06	3.23	114	0.07	1.481
5-Story	1.49	5.2	93	0.03	1.912
7-Story	1.85	6.7	77.3	0.02	5.175
9-Story	2.14	11	95	0.06	4.609

Table 5.3 ESDOF parameters for the 2nd mode

	Period (s)	D_{2y} (in.)	F_{2y}/L_2(in./s^2)	α	Γ_2
3-Story	0.342	3.2	1080	0.02	0.528
5-Story	0.537	3.85	528	0.05	0.703
7-Story	0.654	5.75	530	0.035	0.649
9-Story	0.781	8.5	550	0.01	1.663
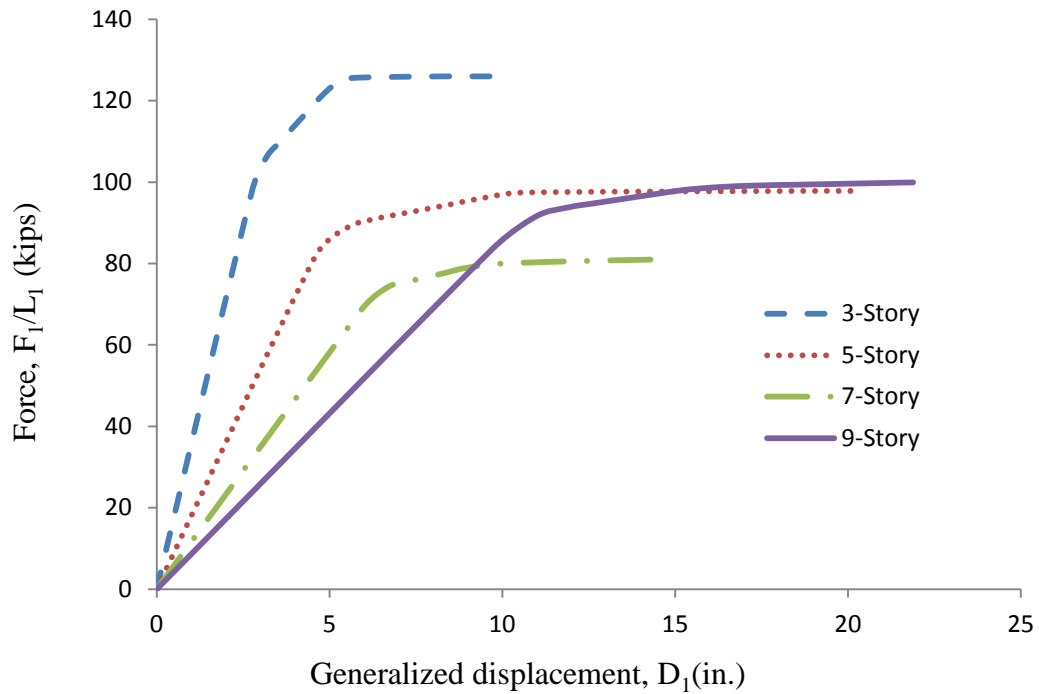
Figure 5.4 First mode force-deformation relationships for the inelastic ESDOF system
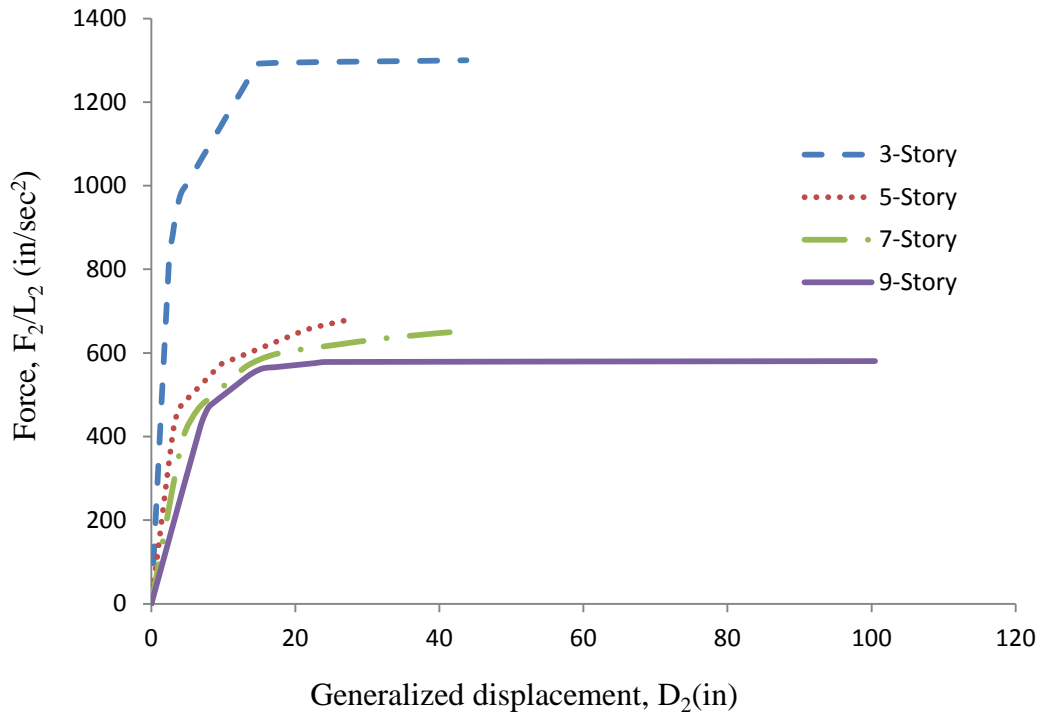
Figure 5.5 Second mode force-deformation relationships for the inelastic ESDOF system

5.5 Comparison of Input Energy in MDOF and ESDOF Systems

As shown in Equation (5.20), a simple relationship exists between earthquake input energy for MDOF system and its series of equivalent SDOF systems. In order to demonstrate the applicability and validity of these equations, the MDOF frames and their modal ESDOF systems have been subjected to three different earthquake ground motions. The earthquake ground motions selected for this purpose have both fault parallel and fault normal components. Their characteristics are as listed in Table 5.4.

Table 5.4 Ground motions used for demonstration

Ground motion	Fault Normal (FN) Component			Fault Parallel (FP) component		
	*CAV**	*PGA**	*PGV**	*CAV**	*PGA**	*PGV**
Loma Prieta	72.88	24.71	5.895	53.33	15.29	2.369
Northridge-01	90.82	25.22	1.242	67.86	14.05	0.7822
Chi-Chi Taiwan	122.2	27.38	2.956	107.5	19.96	2.875

* all units are in inches and seconds

The same earthquakes were used for all four frames. It is important to note that the frames need to behave non-linearly when subjected to the ground motions in order to capture their hysteretic behavior. Thus, the earthquakes listed in Table 5.4 were scaled in such a way that they will cause yielding in the frames without collapse and/or excessive distress. As a result, the ground motion components were scaled differently. The scale factors applied to each earthquake for each frame are shown in Table 5.5.

Table 5.5 Ground motion scaling factors

Ground motion	Loma Prieta (LP)		Northridge-01 (NR)		Chi-Chi-Chi Taiwan (CHI)	
	FN	FP	FN	FP	FN	FP
3-Story	7.14	12.5	5	11	7.14	10
5-Story	8.33	12.5	5	11	7.14	10
7-Story	8.33	12.5	5	11	7.14	10
9-Story	6.5	12.5	5	11	7.14	10

A total of 72 earthquake time history analyses were performed: 48 using BISPEC *(2010)* for the ESDOF components and 24 using PERFORM -3D *(2006)* for the MDOF systems. The results from both systems were analyzed and compared, and are presented below for each frame. As a side note, it has been found that in a linear analysis the expressions of Equation (5.20) are

capable of estimating the input energy in MDOF systems from their equivalent SDOF systems to an accuracy of about 95%.

5.5.1 Three-Story Frame

Input energy imparted to the three-story MDOF frame and its series of ESDOF components from the earthquakes given in Table 5.4 are shown in Figure 5.6. The combined ESDOF input energy from the first two modes is compared with the input energy obtained from a direct analysis of the MDOF system for each of the three earthquakes (two components each). As can be seen, the modal pushover based expressions of Equation (5.20) are able to estimate the input energy of the MDOF system with reasonable accuracy. The level of accuracy; however, is not uniform for all earthquakes considered. For instance, the MDOF and the combined ESDOF input energy time histories for the fault parallel components of the Loma Prieta and Northridge records match for the entire duration of the excitation, whereas the input energy time histories for the fault normal components of all three records and the fault parallel component of the Chi- Chi record slightly bifurcate after the maximum input energy is reached. This indicates that the input energy relationships of Equation (5.20) not only depend on the structural properties of the system but also on the characteristics of the ground motion.

In Chapter 3, site soil based input energy spectra were developed where the input energy was normalized through division by the velocity index (*VI*) and then taking the square root of the resulting quantity. Because the *VI* normalized input energy spectra are dimensionless, this allows the designer the flexibility to choose the proper intensity of the design earthquake. It is now of interest to investigate the effect of velocity index on the MDOF and the combined ESDOF systems maximum input energies and their ratio. For the three-story frame, the results are presented in Figure 5.7.

148
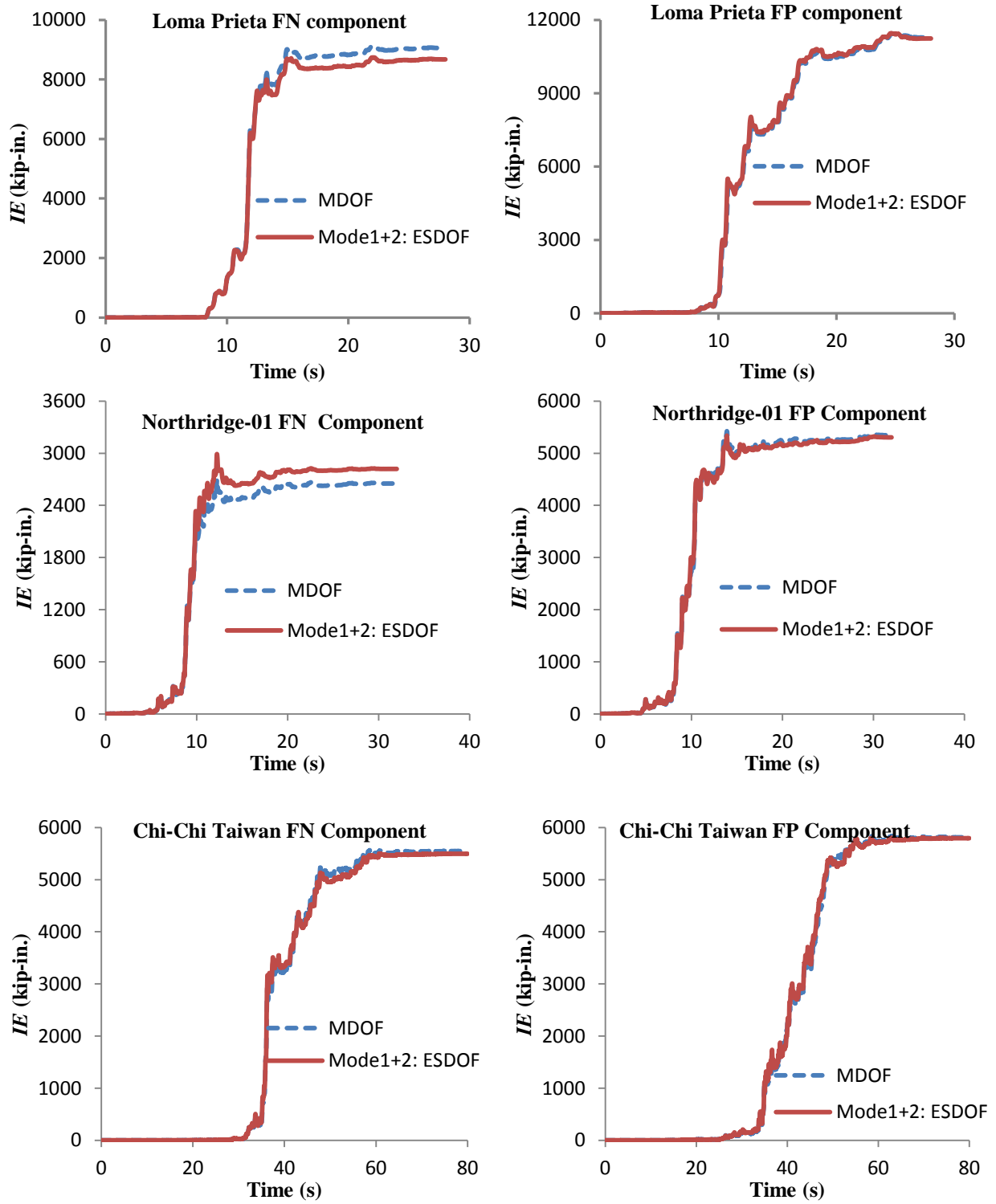
Figure 5.6 Input energy (*IE*) time histories: three-story frame

149
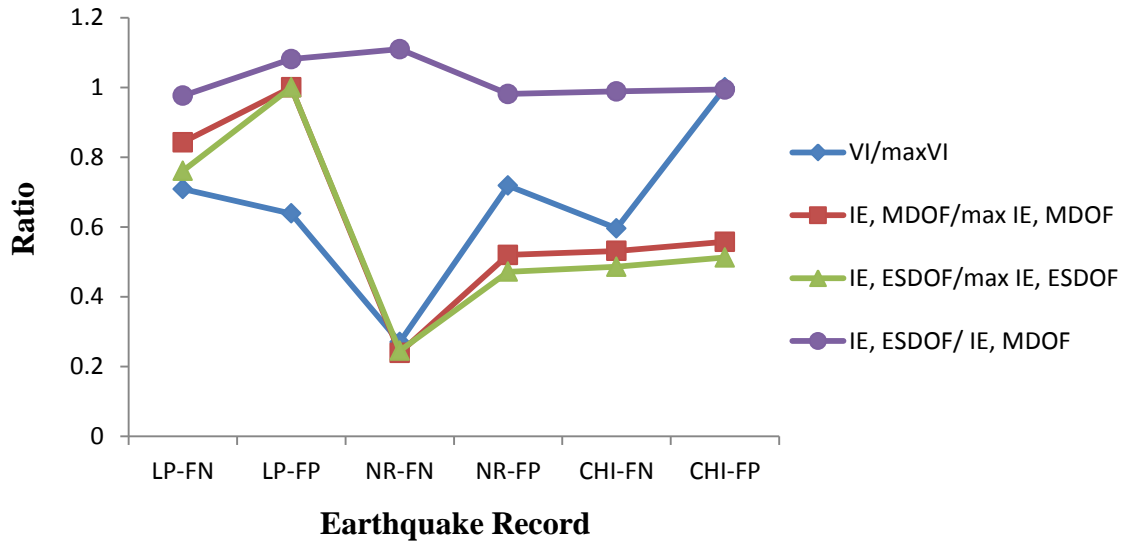
Figure 5.7 Velocity index (*VI*) - input energy (*IE*) relationships: three-story frame

Recall that the velocity index combines two characteristics of ground motion (*CAV* and *PGV*) that are closely related to the energy imparted by an earthquake to a structure. *CAV* and *PGV* show the cumulative effect of ground motion duration and the sudden jolt due to a spike in the magnitude of the earthquake, respectively. Generally, earthquakes with higher values are deemed as strong earthquakes. Thus, earthquakes with high *VI* values are anticipated to impart high input energy to a structure. From Figure 5.7; however, the effect of *VI* on input energy is rather unclear. For LP-FP, NR-FN, and NR-FP, a direct relationship is observed between the maximum input energy and *VI*. On the other hand, among the six records used, CHI-FP has the highest *VI* value but not necessarily the highest input energy value. This randomness in the *VI*-maximum input energy relationships could be attributed to the difference in the frequency content of the earthquakes and its effect on structural response. More importantly, the $IE_{\text{ESDOF}}/IE_{\text{MDOF}}$ plot in Figure 5.7 shows that for the three-story frame, only two modes are sufficient for estimating the input energy of the MDOF system from its series of equivalent

SDOF systems based on the expressions given in Equation (5.20). For the three-story frame, the IE_{ESDOF}/IE_{MDOF} values were obtained to be 0.98, 1.08, 1.11, 0.98, 0.99, and 0.99 for LP-LN, LP-FP, NR-FN, NR-FP, CHI-FN and CHI-FP earthquake records, respectively.

5.5.2 Five-Story Frame

Figure 5.8 shows a comparison of the input energies for the MDOF and its two ESDOF systems for the five-story frame subjected to the earthquakes given in Table 5.4. Like the three-story frame, the input energy of the MDOF system was obtained from a direct nonlinear analysis and then compared to that obtained from the sum of the input energies two ESDOF systems that correspond to the first two modes of the MDOF system. The corresponding input energy ratios, IE_{ESDOF}/IE_{MDOF}, were found to be 0.92, 1.12, 0.97, 0.96, 1.03 and 0.82 for the LP-FN, LP-FP, NR-FN, NR-FP, CHI-FN and CHI-FP earthquake records, respectively. Except for the CHI-FP record where the input energy obtained using the ESDOF systems underestimates the actual input energy; the input energy relations of Equation (5.20) produce a rather good estimate of the actual input energy of the MDOF system.

Table 5.6 IE_{ESDOF}/IE_{MDOF} for 3-Story and 5-Story Frames

	Input Energy Ratio, IE_{ESDOF}/IE_{MDOF}					
Record	LP-FN	LP-FP	NR-FN	NR-FP	CHI-FN	CHI-FP
3-Story	0.98	1	1.11	0.98	0.99	0.99
5-Story	0.92	1.12	0.97	0.96	1.03	0.82

Upon comparison of the IE_{ESDOF}/IE_{MDOF} ratios for the three- and five-story frames, some irregularities are observed for the different earthquakes. For instance, for the five-story frame the input energy relations produce an exact estimate for LP-FN with an energy ratio of unity,

whereas a less accurate estimate is obtained for the CHI-FP record (see Table 5.6).

Theoretically, with an increase in the number of stories, higher modes effect is anticipated and so the energy relationships are expected to give less accurate results. However, as shown in the above results, this theory does not always hold given the random nature of earthquakes.

The energy ratios IE_{MDOF} /max IE_{MDOF} and IE_{ESDOF} /max IE_{ESDOF} for the five-story frame are shown in Figure 5.9. As can be seen, they display similar characteristics as the three-story frame shown in Figure 5.7. For both frames, the maximum and minimum ratios occur for the same earthquake. This demonstrates that the input energy relationships are rather consistent in estimating input energy for MDOF systems from their ESDOF components. Form Figure 5.9, except for the CHI-FP record, it can also be observed that the variations of IE_{MDOF} /max IE_{MDOF} and IE_{ESDOF} /max IE_{ESDOF} follow a similar trend as VI/maxVI. This suggests that input energy estimation for MDOF structures from their ESDOF components is related to the VI value of the specific earthquake.
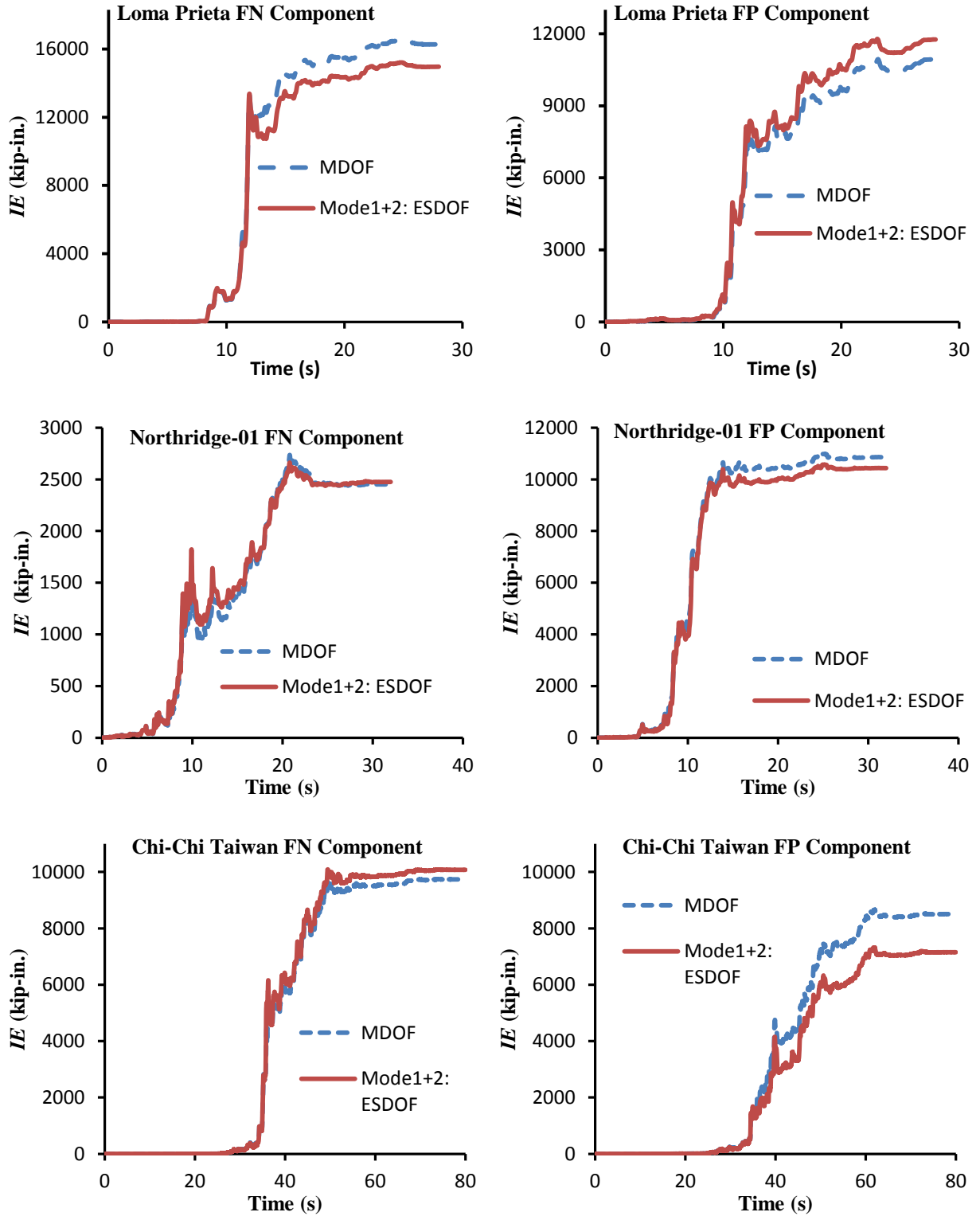
Figure 5.8 Input energy *IE* time histories: five-story frame
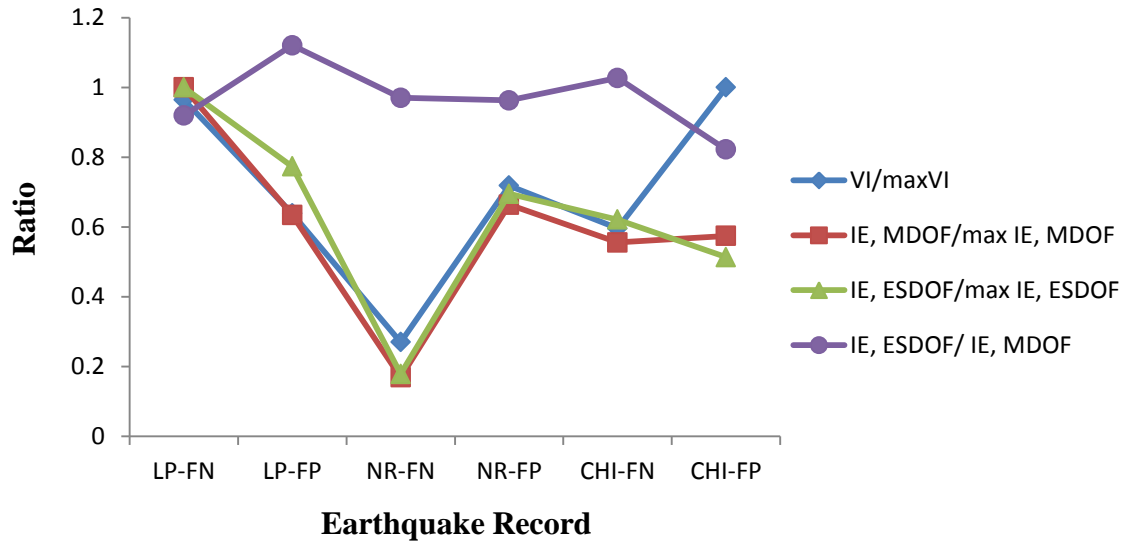
Figure 5.9 Velocity index (*VI*) - input energy (*IE*) relationships: five-story frame

5.5.3   Seven-Story Frame

Figure 5.11 shows a comparison of the input energy plots for the seven-story MDOF frame and its two ESDOF systems subjected to the six earthquakes given in Table 5.4. The input energy ratios, IE_{ESDOF} /IE_{MDOF}, for the seven-story frame are 1.11, 0.89, 0.94, 1.06, 0.81, 0.84 for the LP-FN, LP-FR, NR-FN, NR-FP, CHI-FN and CHI-FP earthquake records, respectively. Except for the Chi-Chi (both CHI-FN and CHI-PN) earthquake where the combined input energy of the two ESDOF systems underestimates the actual MDOF system input energy, a good estimate is obtained using the input energy relationships of Equation (5.20) for the rest of the records.

The IE_{ESDOF} /IE_{MDOF} ratios for the three-, five- and seven-story frames are summarized in Table 5.7. From the table, it can be concluded that the input energy relationship between the MDOF system and its ESDOF components is mainly affected by the nature of the earthquake. For the three frames, the input energy relationships for the CHI-FN and the CHI-FP records are

154

relatively weak compared to the other records. Clearly the performance of the proposed input energy relationships is dependent on the earthquake record –structure interaction.

Table 5.7 IE_{ESDOF} /IE_{MDOF} for 3-story, 5-story and 7-story frames

	Input Energy Ratio, IE_{ESDOF} /IE_{MDOF}					
Record	LP-FN	LP-FP	NR-FN	NR-FP	CHI-FN	CHI-FP
3-Story	0.98	1.08	1.11	0.98	0.99	0.99
5-Story	0.92	1.12	0.97	0.96	1.03	0.82
7-Story	1.11	0.89	0.94	1.06	0.81	0.84
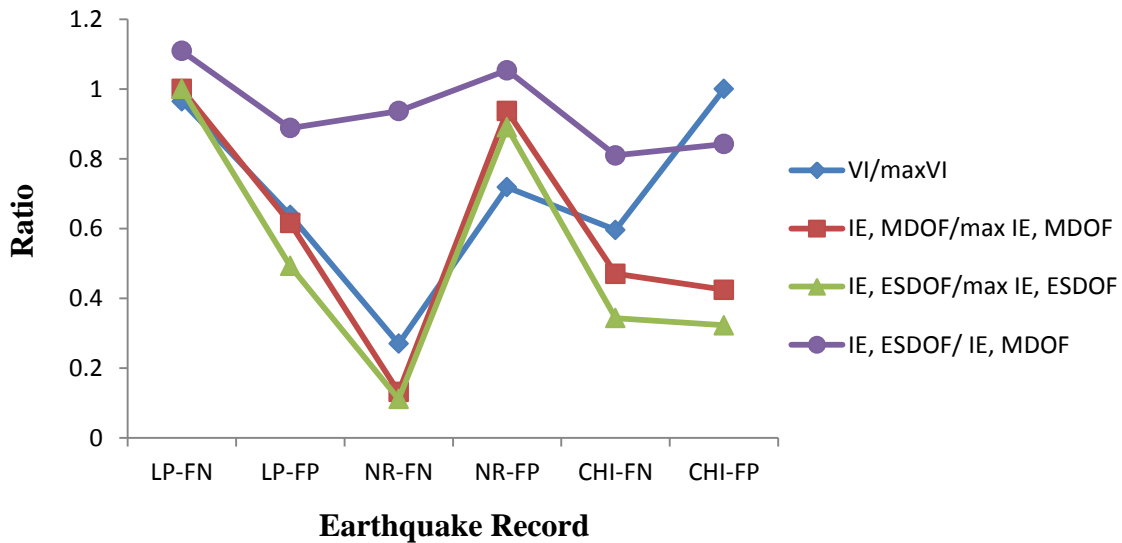
Figure 5.10 Velocity index (*VI*) - input energy (*IE*) relationships: seven-story frame

As can been seen from Figures 5.7, 5.9 and 5.10, the relationship between the IE_{MDOF}/max IE_{MDOF} and IE_{ESDOF}/max IE_{ESDOF} values exhibit similar characteristics for the 3-story, 5-story and 7-story frames. This further validates the use of Equation (5.20) and supports the use of the pushover based approach for estimation of input energy in MDOF system using its series of equivalent SDOF systems.
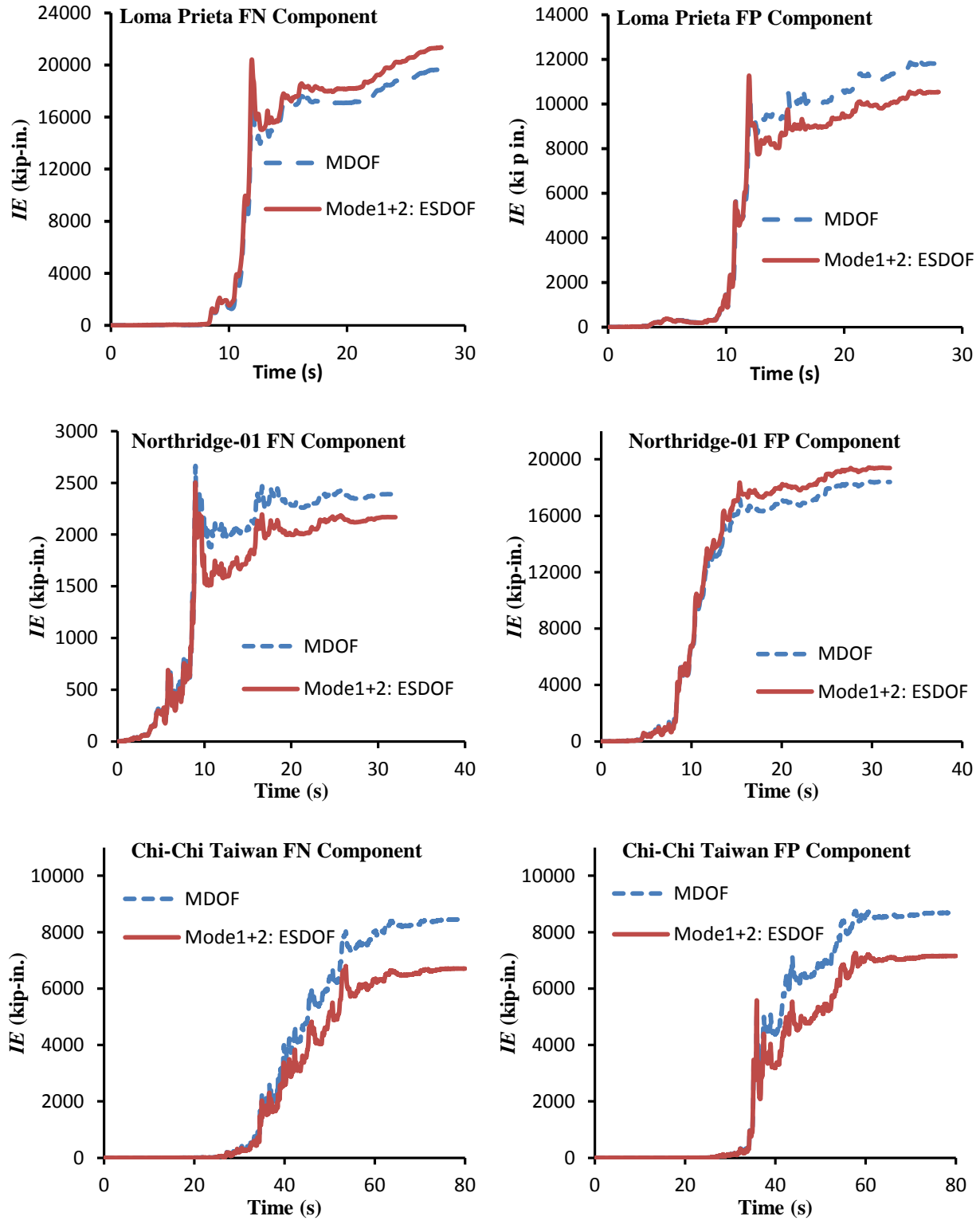
Figure 5.11 Input energy *IE* time histories: Seven-story frame

156

5.5.4 Nine-Story Frame

A comparison of the input energy time histories for the nine-story MDOF frame and its two ESDOF systems is shown in Figure 5.13. The max IE_{ESDOF} /max IE_{MDOF} ratios are 1.03, 1.11, 0.76, 1.00, 0.94, and 0.76 for the LP-FN, LP-FP, NR-FN,NR-FP, CHI-FN and CHI-FP earthquake records, respectively. Even though the input energy ratios for LP-FN, LP-FP, NR-FP and CHI-FN records show a good correlation, the same cannot be said about the input energy ratios for the NR-FN, and CHI-FP records. The NR-FN and CHI-FP input energies obtained using Equation (5.20) underestimate the actual input energy for this nine-story frame. As shown in Figure 5.12, the variations of IE_{MDOF} /max IE_{MDOF} and IE_{ESDOF} /max IE_{ESDOF} for the nine-story frame exhibited similar trend as the VI/maxVI variation. This was also the case for the 3-, 5- and 7-story frames discussed earlier.
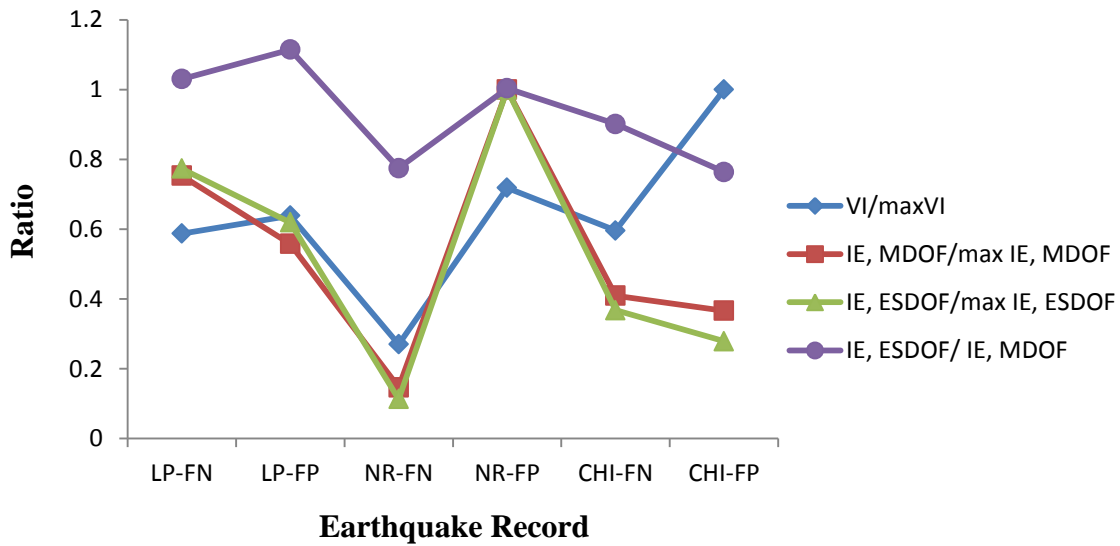
Figure 5.11 Velocity index (VI) – input energy (IE) relationships: nine-story frame
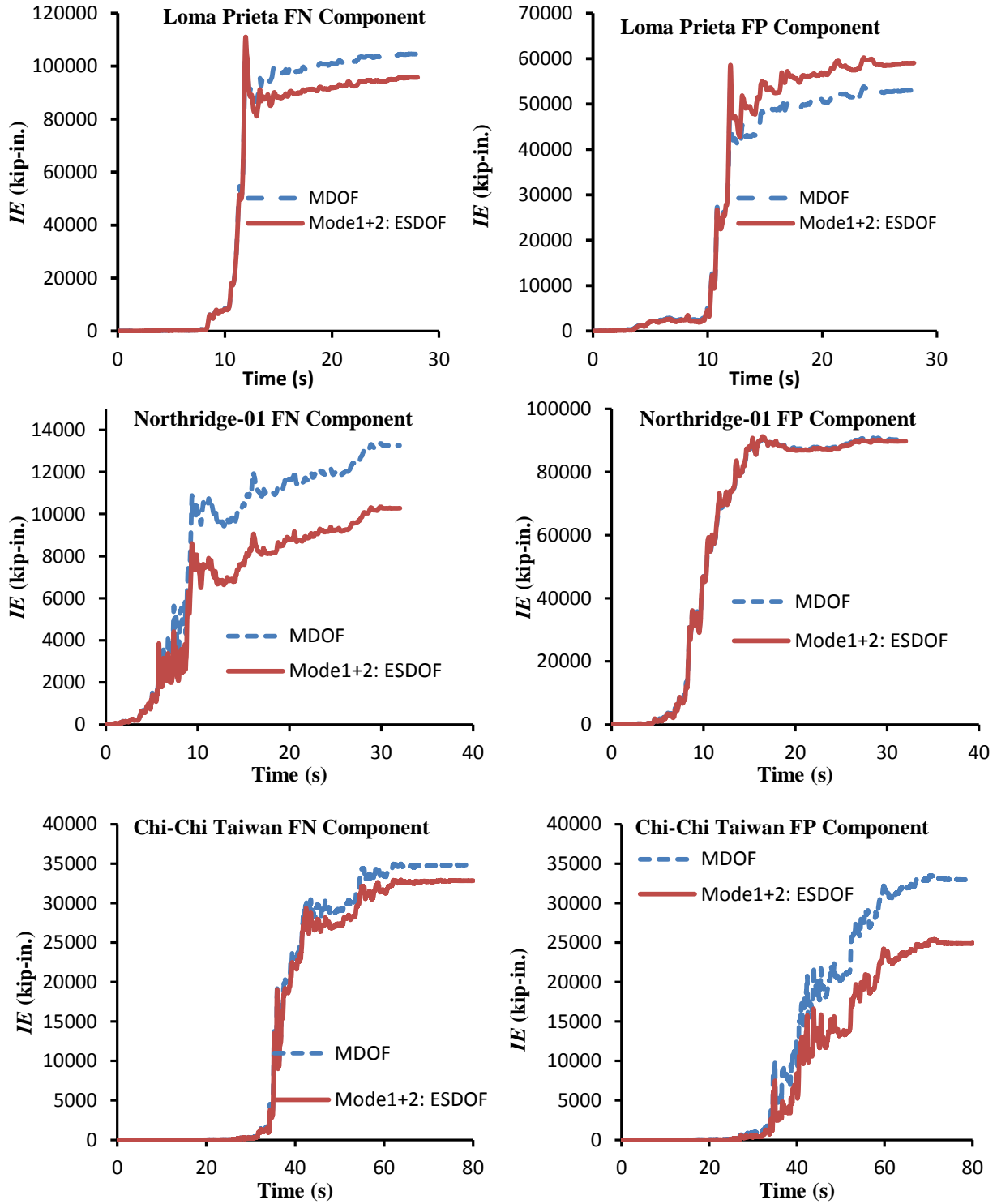
Figure 5.12 Input energy *IE* time histories: nine-Story Frame

Higher mode effects on the dynamic response of structures are well documented if not well quantified. The effect of higher modes on the seismic response of structures has been the subject of much research. It has been generally agreed that higher mode effects are more pronounced in high-rise and irregular structures as well as in structures where the responses from different modes are likely to be coupled. It is therefore reasonable to anticipate that the performance of the MDOF-ESDOF input energy relationships will deteriorate when the number of stories of the MDOF system increases. Thus, for a given earthquake, the max IE_{ESDOF} /max IE_{MDOF} ratio is expected to deviate further away from unity as the number of stories increases. However, from the results generated in this study using just two modes, this is not always the case. For instance, for the six earthquake records considered in this study and from the results summarized in Table 5.8, it can be seen that except for NR-FN and CHI-FP the max IE_{ESDOF} /max IE_{MDOF} ratios neither increase nor decrease as the number of stories increases. On the other hand, the max IE_{ESDOF} /max IE_{MDOF} ratios for NR-FN and CHI-FP do substantiate the theoretical expectation.

Table 5.8 IE_{ESDOF} /IE_{MDOF} for 3-story, 5-story, 7-story, and 9-story frames

	Input Energy Ratio, IE_{ESDOF} /IE_{MDOF}					
Record	LP-FN	LP-FP	NR-FN	NR-FP	CHI-FN	CHI-FP
3-Story	0.98	1.08	1.11	0.98	0.99	0.99
5-Story	0.92	1.12	0.97	0.96	1.03	0.82
7-Story	1.11	0.89	0.94	1.06	0.81	0.84
9-Story	1.03	1.11	0.77	1.00	0.90	0.76

From the discussions in Sections 5.4.1 through 5.4.4, it can be concluded that for the three-, five-, seven-, and nine-frames the energy relationships developed in Section 5.3.3 are capable of producing a reasonable estimate of the actual input energy for MDOF systems using input energy

from their associated ESDOF components. For the six earthquake ground motions used in this study, the average input energy estimation (both under and over estimation) errors are found to be 4.3%, 7.9%, 11.4% and 11.8% for the three-, five- , seven- and nine-story frames, respectively (see Table 5.9). Based on this observation, it can be concluded that using pushover-based modal combination, the input energy (and by extension the hysteretic energy) for MDOF system can be estimated from its ESDOF components to a reasonable accuracy even though the increase in error as the number of frame stories increases does suggest that the effect of higher modes on the input energy relationships can be significant.

Table 5.9 MDOF system input energy estimation error

$Error(\%) = \dfrac{|IE_{ESDOF} - IE_{MDOF}| * 100}{IE_{MDOF}}$						
LP-FN	LP-FP	NR-FN	NR-FP	CHI-FN	CHI-FP	Ave. Error
3-Story	2.4	8.1	10.9	1.9	1.2	0.6	4.2
5-Story	8.1	12.1	3.0	3.7	2.7	17.8	7.9
7-Story	10.9	11.2	6.3	5.4	19.0	15.8	11.4
9-Story	3.0	11.5	22.5	0.4	9.9	23.6	11.8

6 HYSTERETIC ENERGY DISTRIBUTION FOR MDOF SYSTEMS

6.1 Introduction

The advantage of energy-based seismic design (EBSD) over other code-based seismic design methods is its ability to capture the duration related cumulative damage effect of the seismic event. The duration related cumulative damage of a seismic event has been defined as hysteretic energy of the system. In Chapter 4, expressions for estimating hysteretic energy in SDOF systems have been developed. Subsequently, in Chapter 5 relationships between hysteretic energy of MDOF system and its series of equivalent SDOF systems have been established.

Hysteretic energy is the main design parameter in EBSD to determine member sizes. For a given earthquake, the hysteretic energy demand in a member depends on its relative location with respect to the structure. For multi-story frames, the distribution is made among the different stories instead of individual members. In Section 6.2, a literature review of some existing hysteretic distribution schemes for multistory frames is presented along with a proposed scheme which will be shown to be an improvement over the existing ones. Section 6.3 presents a relationship between the hysteretic energy demand due to earthquakes and the conventional plastic capacity of structures. Based on this relationship and other code related requirements, an EBSD procedure for the design of MDOF systems is proposed.

In Section 6.4, the entire work of this study is illustrated using two design examples: a three story single bay and a five story two bay frames. The design examples show each and every steps for determining the input energy and hysteretic energies for equivalent SDOF systems and the corresponding hysteretic energy for MDOF frames and its distribution along the height.

6.2 Hysteretic Energy Distribution

6.2.1 Literature Review

Using a statistical approach, Seneviratna and Krawinkler *(1997)*, and Shen and Akbas *(1999)* investigated the hysteretic energy (*HE*) distribution over the height of a building and were not able to identify any consistent pattern. However, Akbas *et al. (2003)* from their study of regular frames with a damping ratio of ζ=0.02 concluded that hysteretic energy distribution along the height is linear. Ye *et al. (2009)* counter argued that hysteretic energy distribution can be considered linear only for damping ratio ζ>0.1 and proposed the linear equations shown in equation (6.1) to distribute the *HE* over the building height for structures with damping ratio ζ>0.1. It is imperative to note that such high damping could only be attained if supplementary damping devices are installed in the structure.

$$\frac{HE_i}{HE} = \begin{cases} \dfrac{2(N+1-i)}{N(N+1)} & \text{for} \quad N < 5 \\[3mm] \dfrac{2(N-i)}{N(N-1)} & \text{for} \quad N \geq 5 \end{cases} \tag{6.1}$$

where *N* is the total number of stories; *i* is the story of interest; *HE* and *HE$_i$* are the total and story *i* hysteretic energies, respectively.

An attempt has been made by Chou and Uang *(2003)* to distribute hysteretic energy in multi-story frames based on a multi-mode pushover analysis approach. In their approach, *HE* for MDOF systems is distributed using a relationship between the end rotations and hysteretic energy of the elements in a particular story. They recommended distribution patterns which they referred to as energy shapes at different stages of loading. These energy shapes are functions of cumulative end rotations of each story. They proposed three different energy shapes for each of

the first two modes and distribute the hysteretic energy contribution by each mode to the different stories of the structure. From their study on 5-, 7- and 9-story frames, they concluded that their proposed procedure was able to predict damage distribution in low to medium-rise frames when the first two modes are considered. They also pointed out that the majority of the energy was contributed by the first mode for each of the frames considered in their study.

Peak responses have been dominantly taken as damage indices for structures subjected to earthquakes in most of the research on dynamic response of structures. Pushover analysis, also known as nonlinear static procedure, has been widely used in estimating structural peak responses. Over the years, different but complementary approaches of pushover analysis have been suggested by various researchers. Some examples include: adaptive pushover by Gupta and Kunnath *(2000)*, pushover result combination (PRC) by Monghadam and Tso *(2002)*, modal pushover analysis by Chopra and Goel *(2002)* and consecutive modal pushover (CMP) procedure by Poursha *et al. (2009)*. Although with some reservations, the above researchers concluded that pushover analysis is capable of estimating structural peak responses. This finding and findings from previous research on the topic made the static pushover analysis a widely accepted and used analysis for seismic performance evaluation of existing and new structures. However, as it was clearly stipulated in the problem statement in Chapter 1, it is the cumulative effect of earthquake throughout its duration of occurrence and not just the ultimate peak response that affects structures the most. In light of this, hysteretic energy which is a measure of the cumulative effect of earthquakes on structures is being considered as damage index in place of the peak structural responses.

There is no doubt that an earthquake that causes a substantial deformation in structures is going to impart high deformation energy. Thus, it is a forgone conclusion that there exist a relationship

163

between the structural peak responses and the hysteretic energy accumulated in structures during an earthquake event. To this end, Ye *et al.* *(2009)* established a relationship between the peak story responses and plastic deformation energy PE_i obtained from a pushover analysis. They proposed that the peak story responses and the corresponding story plastic deformation energy can be related by equation (6.2). They further pointed out that there is a direct relationship between *HE* distribution and *PE* in MDOF systems and proposed an expression for *HE* distribution in MDOF systems as shown in equation (6.3).

$$PE_i = (1 - \alpha_i)(\mu_i - 1)F_{yi}d_{yi} \tag{6.2}$$

$$\frac{HE_i}{\sum\limits_{i=1}^{N} HE_i} = \frac{PE_i}{\sum\limits_{i=1}^{N} PE_i} \tag{6.3}$$

where PE_i is the plastic energy, a_i is the post-yield stiffness ratio, μ_i is the ductility ratio, F_{yi} is the yield force, d_{yi} is the story yield deformation and i is the story number in question.

Recently, Wang and Yi *(2012)* developed a procedure for estimating the total hysteretic energy for MDOF systems from their equivalent SDOF systems. They also studied the relationship between hysteretic energy of a given story and its momentary story shear and story drift. Based on their findings, they proposed distribution equations of hysteretic energy for MDOF systems as follow.

$$HE_n = \frac{(\sum\limits_{i=n}^{N} m_i \phi_{k,i}) \Delta \phi_{k,n}}{\sum\limits_{i=1}^{N} m_i \phi_{k,i}^2} HE \tag{6.4}$$

164

where $\phi_{k,n}$ = the displacement at story n in mode k ; $\Delta\phi_{k,n} = \phi_{k,n} - \phi_{k,n-1}$; m_i = mass of story i ;

HE_n = hysteretic energy dissipated by story n in mode k and HE = total hysteretic energy in mode

k. They also proposed a hysteretic energy distribution for multi-story buildings with modes

shapes for different plastic stages, which is simply the expression in equation (6.4) except that

mode shapes $\phi_{k,n}$ to $\phi_{k,n-1}$ are replaced by $\phi_{p,k,n}$ to $\phi_{p,k,n-1}$ where p refers to the plastic stage

under consideration. They tested their formulations on three six-story pin supported buildings

subjected to a total of nine ground motions; three records each on hard, intermediate and soft

soils. They concluded that their proposed equations were suitable for hard soil site and for

buildings whose lateral displacement shape is controlled by the first mode shape.

The expression proposed by Wang and Yi *(2012)* is actually similar to the work done by external

forces applied at each story level during story displacements. For instance consider the lateral

force distribution and story displacement shown in Figure 6.1 below.
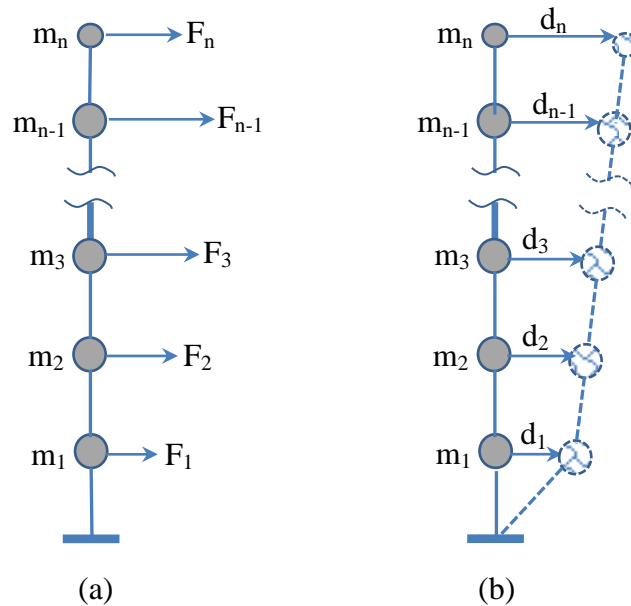
Figure 6.1 (a) Lateral forces and masses; (b) Lateral displacements

For the hypothetical story external forces and displacements shown in Figure 6.1, the external work done by the set of lateral forces due to the resulting story displacement can be obtained as follows. Let's define WE_i as the external work done by the set of lateral forces due to the displacement of story i, d_i, then we have:

$$WE_1 = F_1d_1 + F_2d_1 + F_3d_1 + ... + F_{n-1}d_1 + F_nd_1 = (\sum_{i=1}^{n} F_i)d_1$$

$$WE_2 = F_2(d_2 - d_1) + F_3(d_2 - d_1) + ... + F_{n-1}(d_2 - d_1) + F_n(d_2 - d_1) = (\sum_{i=2}^{n} F_i)(d_2 - d_1)$$

$$\vdots \qquad (6.5)$$

$$WE_{n-1} = F_{n-1}(d_{n-1} - d_{n-2}) + F_n(d_{n-1} - d_{n-2}) = (\sum_{i=n-1}^{n} F_i)(d_{n-1} - d_{d-2})$$

$$WE_n = F_n(d_n - d_{n-1})$$

From the above expressions, a general expression for the external work done by a set of lateral forces as shown in Figure 6.1 due to a story i drift, $\Delta d_i = d_i - d_{i-1}$ can be written as follows.

$$WE_i = (\sum_{k=i}^{n} F_k)\Delta d_i \qquad (6.6)$$

The total external work done by the set of lateral forces due to the resulting displacements shown in Figure 6.1 is then given as

$$WE_{total} = F_1d_1 + F_2d_2 + ... + F_{n-1}d_{n-1} + F_nd_n = \sum_{i=1}^{n} F_kd_k \qquad (6.7)$$

Then, the story-wise distribution of the total external work done expressed in terms of energy ratio, R; for story i, R_i is given by

$$R_i = \frac{WE_i}{WE_{total}} = \frac{(\sum\limits_{k=i}^{n} F_k)\Delta d_i}{\sum\limits_{i=1}^{n} F_i d_i} \qquad (6.8)$$

In modal pushover analysis, it is common practice to define the lateral load pattern as a product of the mass matrix and mode shape vector. In such cases, the story forces F_i are directly proportional to the product $m_i\phi_i$. If the story displacements, d_i, are assumed to be proportional the story mode shape values ϕ_i, then replacing F_i, d_i and Δd_i in equation (6.4) by $m_i\phi_i$, ϕ_i and $\Delta\phi_i$, respectively, the expression shown in Equation (6.9) can be obtained.

$$R_i = \frac{WE_i}{WE_{total}} = \frac{(\sum\limits_{k=i}^{n} m_k\phi_k)\Delta\phi_i}{\sum\limits_{i=1}^{n} m_i\phi_i\phi_i} = \frac{(\sum\limits_{k=i}^{n} m_k\phi_k)\Delta\phi_i}{\sum\limits_{i=1}^{n} m_i\phi_i^2} \qquad (6.9)$$

Equation (6.9) is the same as Equation (6.3), a hysteretic energy distribution scheme proposed by Wang and Yi *(2012)*. The only difference is that Wang and Yi's *(2012)* expression expands for mode shapes at different pushover stages; however, Equation (6.9) is based on the modes of the undeformed shape of the structure. In other words, Equation (6.9) doesn't capture the behavior of the structure beyond the yield point. Equation (6.8), on the other hand, is capable of simulating the nonlinearity behavior of the structures through the inelastic deformations that are used in calculating the external work done by the story forces. For this reason, the distribution scheme of Equation (6.8) is proposed for use in this study.

6.2.2   Comparison of Hysteretic Energy Distributions

The effect of structural properties on hysteretic energy distribution can be readily studied by changing the size, material and geometry of the structure. However, it is difficult to either qualitatively or quantitatively describe the effect of the nature of earthquake on hysteretic energy and its distribution for MDOF systems. Hysteretic energy distribution for MDOF systems due to a seismic excitation is erratic and frenzied. Such erratic hysteretic energy distributions were observed from a study made for 3-, 5-, 7- and 9-story frames subjected to six different earthquakes and are presented in Figure 6.2. The frames and the earthquakes were previously used in chapter 5. From Figure 6.2, it can be seen that the hysteretic energy demand distribution due to any of the earthquakes is neither peculiar nor follows any discernible pattern. For instance, the hysteretic energy demand distribution due to the Loma Prieta Fault Normal (LP-FN) component decreases with height for the 3-, 5- and 7- story fames but this decrease is not obvious for the 9-story frame. Similarly, the distribution patterns of the hysteretic energy due to the other five earthquakes for the different frames were found to be inconclusive. This observation contradicts a statement made by Shen and Akbas *(1999)* that hysteretic energy is insensitive to ground motion and is more uniformly distributed along the height of the structure when they did their study on 3-, 6- and 10-story regular moment resisting steel frames.

The time history analysis results shown in Figure 6.2 clearly indicate that there is no definitive way of distributing hysteretic energy along the height of MDOF structures. It can be said that hysteretic energy distribution is ground motion specific and is sensitive to the interaction between the nature of the earthquake and the structural properties of the MDOF system. Despite this observation, as outlined in Section 6.2, researchers have retorted to suggesting possible schemes of distributing hysteretic energy demand in MDOF systems. It is important to recall

that the main purpose of energy-based design is to ensure that the hysteretic energy demand is met by the energy dissipating capacity of the structure. In addition, because seismic load is just one of several design loads acting on a structure, a designer needs to consider the force effects of other design loads such as dead and live loads in sizing the structural elements while meeting the hysteretic energy demand of the seismic load. Generally, for multistory frames, the dead load and live load analysis would require stronger columns at lower stories. As a result, it is imperative to distribute the hysteretic energy in such a manner that takes the relative story stiffness and strength into account.

A close look at the hysteretic energy distributions discussed in Section 6.2 reveals that these distributions do implicitly take into account the story stiffness and strengths as they directly affect the story displacements and forces. In order to evaluate the relative suitability of the hysteretic energy distribution schemes stated in Section 6.2, they need to be compared to actual seismic hysteretic energy distribution. However, it was observed that hysteretic energy distributions obtained from exact time history analysis were erratic and cannot be taken as a benchmark for comparison. Alternatively, an actual hysteretic energy distribution obtained using a pushover analysis can be used. Hysteretic energy demand in a structure during a pushover analysis can be easily computed at each stage of pushover by multiplying the plastic moment capacity of the elements and the resulting plastic joint rotations.
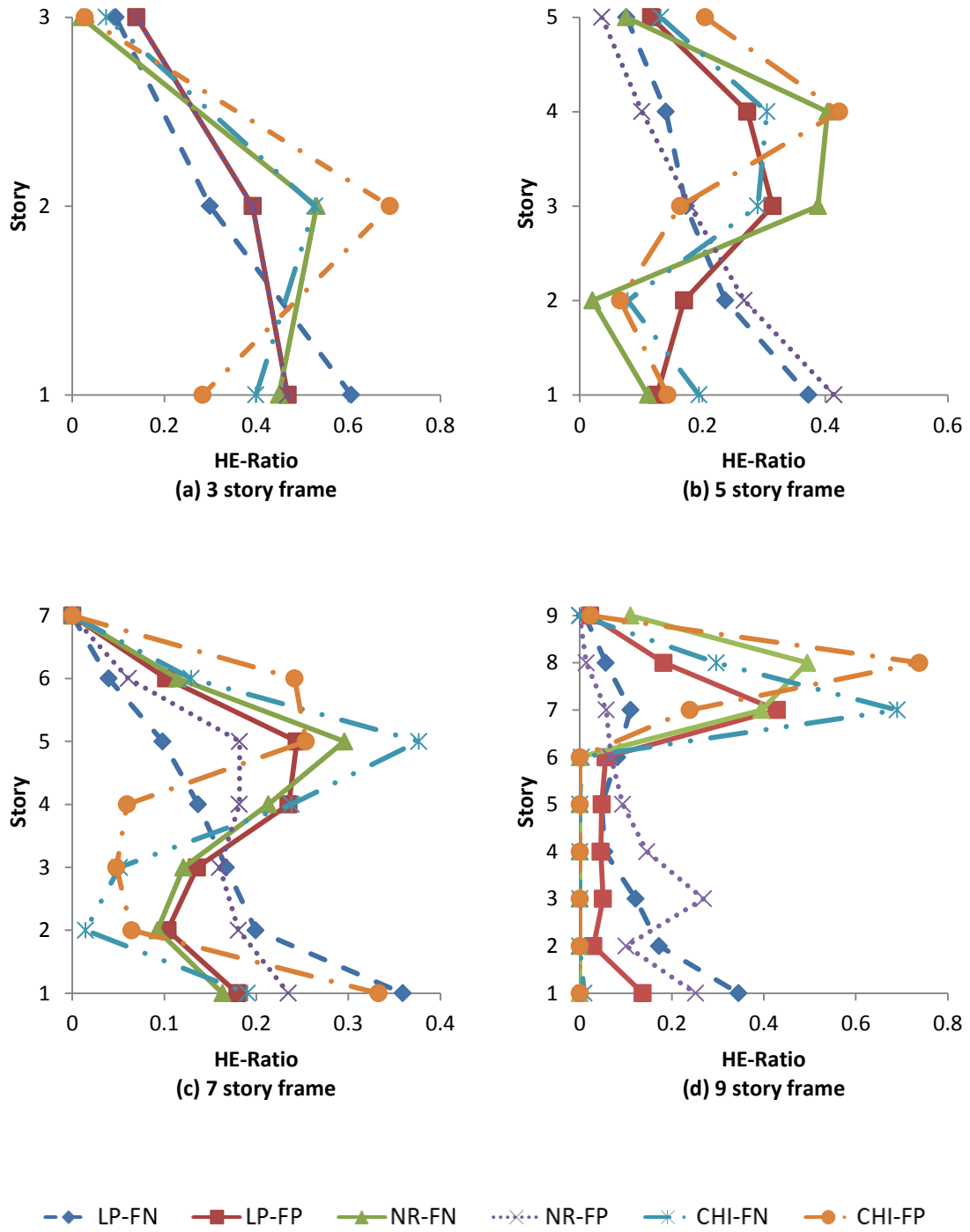
Figure 6.2 Hysteretic Energy Distribution Results from Time History Analysis

This is conceptually the same as the internal work done component in formulating the fundamental energy equation in plastic analysis of structures. By summing the energy contributions from all elements in a given story, it can be readily observed how hysteretic energy is distributed along the height of a given structure. Using this approach the hysteretic energy in each story can be obtained using the expression shown in equation (6.10).

$$HE_i = \sum_{k=1}^{nb} M_{pb,k}\theta_{pb,k} + \sum_{j=1}^{nc} M_{pc,j}\theta_{pc,j} \tag{6.10}$$

where

$M_{pb,k}$, $\theta_{pb,k}$ = plastic moment capacity and plastic rotation of beam at end k in story i

$M_{pc,j}$, $\theta_{pc,j}$= plastic moment capacity and plastic rotation of column at end j in story i

nb = number of plasticized beam ends in story i, and

nc = number of plasticized column ends in story i

In Figure 6.3, the actual hysteretic energy distribution based on Equation (6.10) is compared with the hysteretic energy distribution schemes stated in Section 6.2. As can be seen, the hysteretic energy distribution schemes by Ye *et al*. *(2009)*, Wang and Yi *(2012)* and the proposed method underestimate the hysteretic energy demand at the lower story and overestimate it at the upper stories. This can be clearly seen in Figures 6.3 (a), (b), (c) and (d) for the 3-, 5-, 7- and 9- story frames, respectively. The figures also show that the margin of error for estimating hysteretic energy demand is larger for Wang and Yi's *(2012)* distribution scheme when compared to that of Ye *et al*.'s *(2009)* and the proposed method given by Equation (6.8).

171
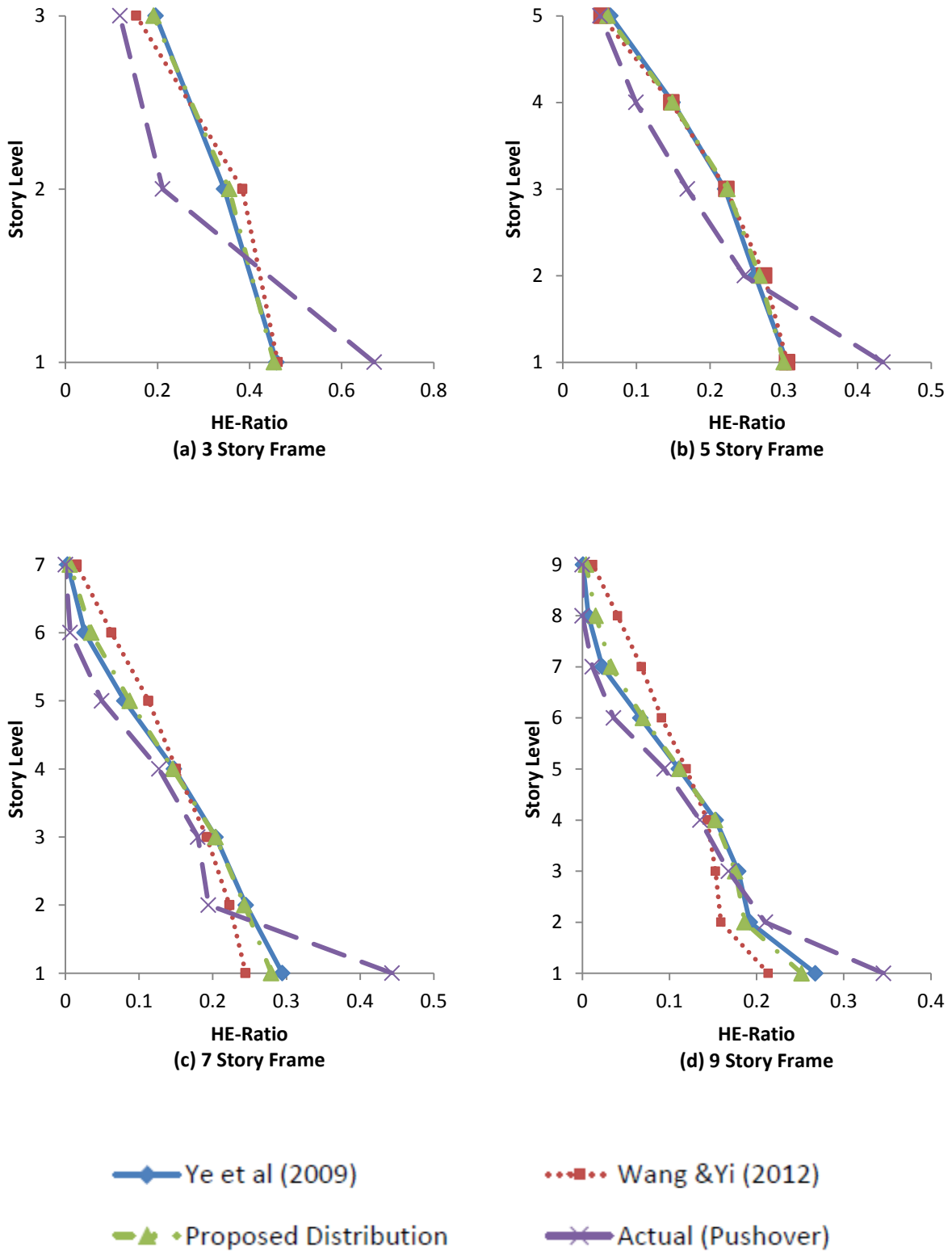
Figure 6.3 Comparison of hysteretic energy distribution in MDOF systems

The larger margin of error for the Wang and Yi's *(2012)* method, especially for the 7- and 9-story frames, may be attributed to the fact that the distribution does not take into account the effect of nonlinearity. This is clear from Equation (6.4) where the modes shapes only reflect the elastic behavior of the frames. However, it is also equally important to note that Wang and Yi *(2012)* did give an extension of their formulation if the structure goes into the plastic stage. They suggested that mode shapes for each stage of plasticity needed to be recalculated based on the stiffness and geometric condition of the structure and used in Equation (6.4). This is not a simple task because the reformulation of stiffness and mass matrices for different stages of plasticity is computationally demanding and impractical for design purposes.

On the other hand, Ye *et al. (2009*) and the proposed distribution schemes appear to match the actual distribution for the 2nd story and above fairly well despite a significant difference being observed for the 1st story. In order to explain why such substantial difference is exhibited only for the 1st story, we need to examine the formulation of the actual hysteretic energy distribution more carefully. Recall from Equation (6.9) that the hysteretic energy demand for the 1st story includes the hysteretic energy demand for the 1st floor beams and 1st floor columns. It was observed that when the frames were pushed beyond the performance limit of life safety, the hinges at the base of the frames start to form suddenly. This sudden increase in hinge deformation sharply increases the hysteretic energy demand in the first story and ultimately causing the structure to collapse.

Based on the above observation, some adjustment to the method by Ye *et al*. *(2009)* and the proposed method may result in a better distribution scheme when compared with the actual distribution given by Equation (6.10). With this in mind, the proposed method is to be adjusted and will be presented below. Nevertheless, it is important to consider the comparative advantage

173

of the proposed method over Ye *et al.*'s *(2009)* scheme. Both schemes required the computation

of story displacements and story forces/shears. In addition, Yet *et al.*'s *(2009)* approach involves

the following extra steps:

1. Development of story level pushover curves for each story

2. Computation of story yield forces, story pre-to-post yield stiffness ratio and story

    ductility ratio by idealizing the story level pushover curves

The story level pushover curves for the 3-, 5-, 7- and 9-story frames presented in Figure 6.4 were

used in developing the hysteretic energy distributions according to Ye *et al.*'s *(2009)* scheme

shown in Figure 6.3. Idealization of story level pushover curves and obtaining the corresponding

yield forces, pre-to-post stiffness ratio and ductility ratio are not that straightforward. It is rather

time consuming and the final values of the parameters that define the idealized pushover curves

are only approximates. It is also likely that the long mathematical manipulations are needed for

each story and these have the potential to introduce computational errors. It is possible that a

single error in computing one of the parameters used to define the story based pushover curves

could lead to a misleading hysteretic energy distribution.

On the other hand, the proposed method does not involve any of these additional computations

and only depends on the story forces and story displacements. Also, from the foregoing

discussion, it is evident that the proposed method is preferred for two reasons: (1) it is easier, i.e.,

less computation time, and (2) there is less chance of making errors that would have been

inevitable if computation was to involve a number of approximations and steps. Even though the

proposed distribution, Equation (6.8), is more desirable from these standpoints, modifications

still need to be made so it can better approximate the actual hysteretic energy distribution. The modifications are given below.
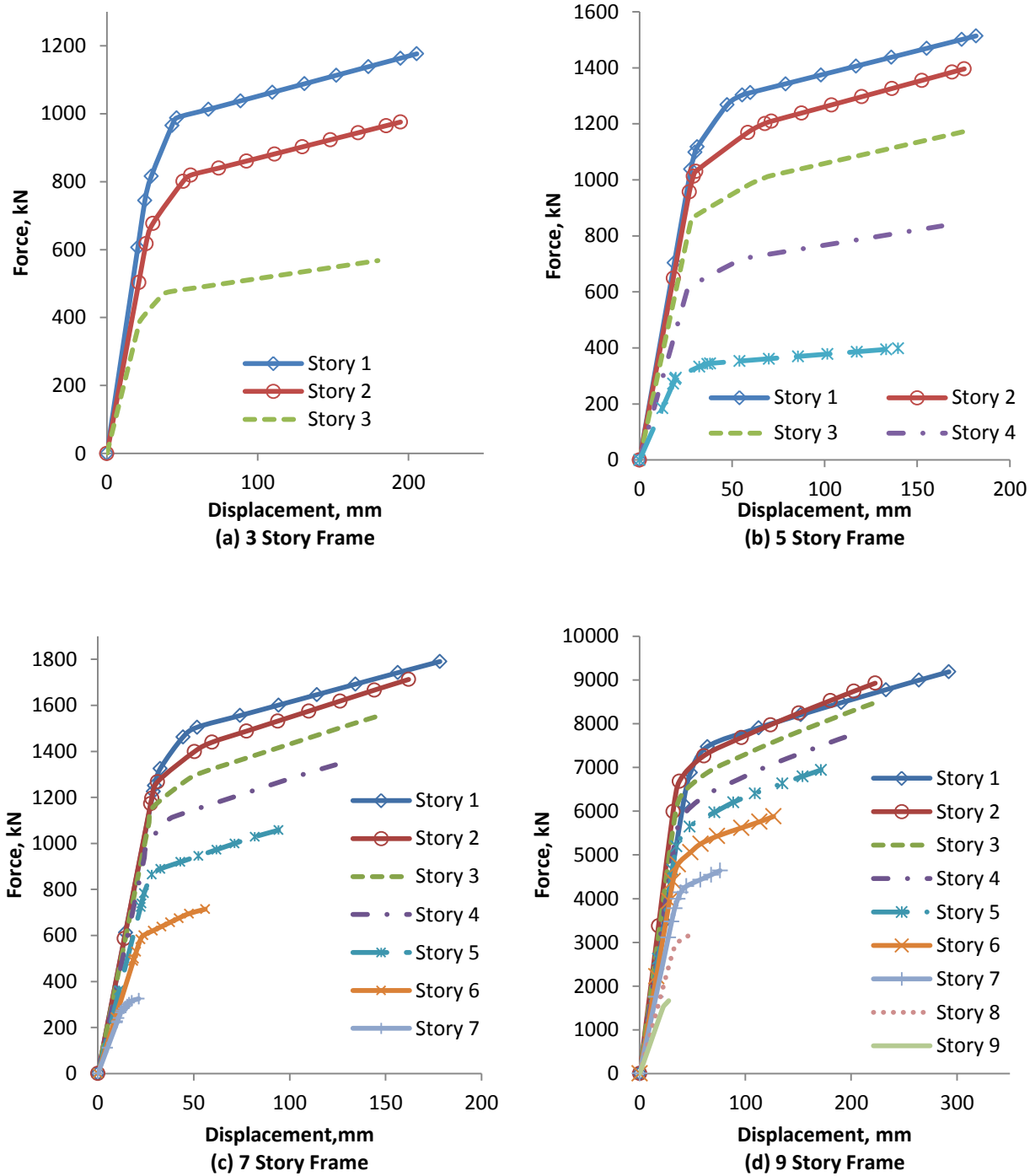
Figure 6.4 Story level pushover curves

175

In Figure 6.3 it was observed that the proposed energy distribution ratio for the first story was significantly lower than the actual value but they were slightly higher than the actual values for the upper stories. An attempt has been made to modify Equation (6.8) and the modified energy distribution equation is given in Equation (6.11).

$$R_i = \frac{WE_i}{WE_{total}} = \begin{cases} \dfrac{2(\sum\limits_{k=i}^{n} F_k)\Delta d_i}{(\sum\limits_{k=1}^{n} F_k)d_1 + \sum\limits_{i=1}^{n} F_i d_i} & \textit{for } i=1 \\[2em] \dfrac{(\sum\limits_{k=i}^{n} F_k)\Delta d_i}{(\sum\limits_{k=1}^{n} F_k)d_1 + \sum\limits_{i=1}^{n} F_i d_i} & \textit{for } i \geq 2 \end{cases} \qquad (6.11)$$

where R_i, i, Δd_i, d_i and F_i are as defined in Equation (6.8).

For comparison, the hysteretic energy distributions based on Equation (6.11) were plotted in Figure 6.5 along with the actual hysteretic distributions. From the figure, it can easily been seen that hysteretic energy distributions according to Equation (6.11) match reasonably well with the actual hysteretic energy distributions for the 3-, 5-, 7- and 9-story frames. Therefore, for design purposes the improved energy distribution equation will be used from now on to determine the hysteretic energy demand.
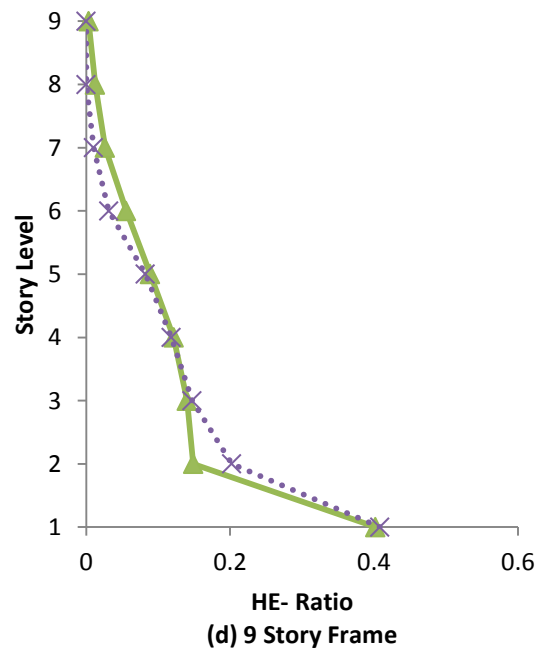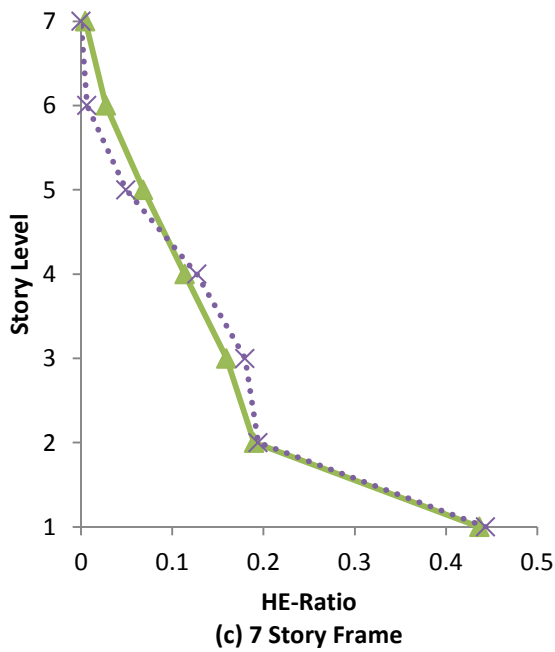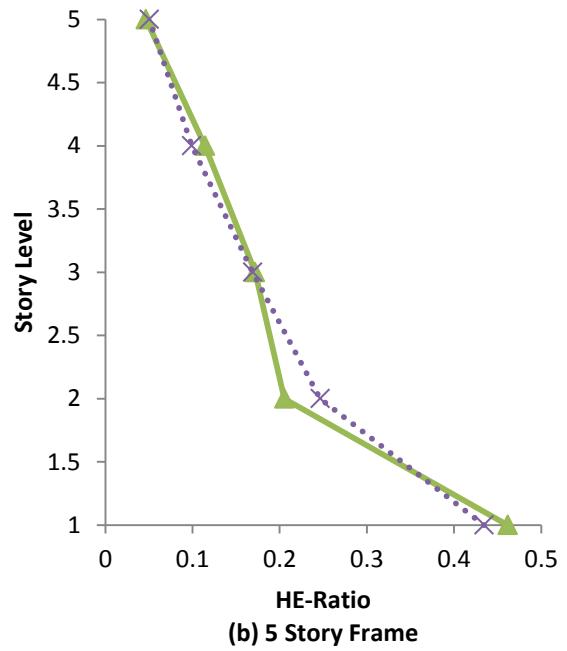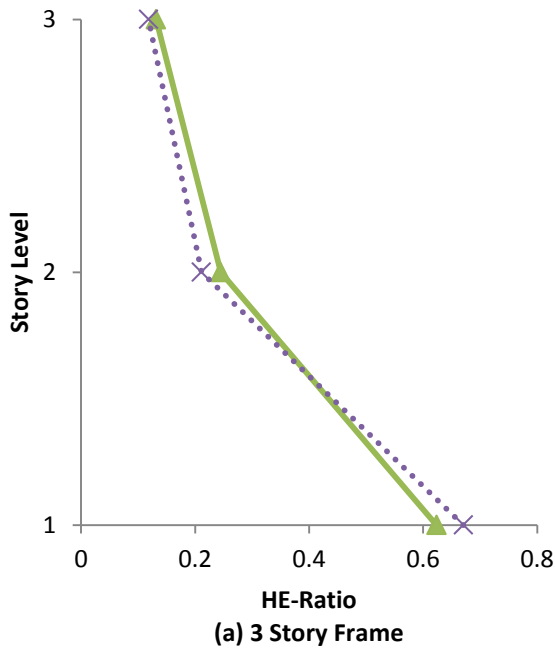
Figure 6.5 Hysteretic energy distribution comparison

6.3 Energy-based Seismic Design Procedure

6.3.1   General

Input energy and hysteretic energy spectra for different site classes and different hysteretic models have been developed in Chapter 3 and Chapter 4, respectively. These spectra can be used to determine the input energy imparted to and the hysteretic energy demand of a SDOF system due to an earthquake with far-fault characteristics. In reality, designers rarely deal with SDOF systems as most structures are MDOF systems. However, in order to minimize the complexity of having to carry out dynamic analysis for MDOF structures, researchers often opt to convert the MDOF to equivalent SDOF systems and relate the ESDOF results to MDOF systems. In Chapter 5, input and hysteretic energy relationships between MDOF and their equivalent SDOF systems have been developed. The ESDOF-MDOF relationships developed in Chapter 5 provide a means to estimate the total hysteretic energy demand for MDOF systems. Further, in Section 6.2 a distribution scheme for the total hysteretic energy demand along the height of a framed structure has been proposed.

At this juncture it is important to underline that the objective of EBSD is to design a structure in such a manner that its energy dissipation capacity exceeds the hysteretic energy demand from a design earthquake or a set of design earthquakes, i.e., mathematically the following inequality has to be satisfied.

$$(Hyteretic\ Energy)_{demand} \leq (Hysteretic\ Energy)_{capacity} \qquad (6.12)$$

For a structure subjected to a given earthquake, the left side of Equation (6.12) can be obtained using the expressions proposed in Chapter 3 through Section 6.2 of this study. The question here is what constitutes the right side of the equation. EBSD in essence is a plastic design; as it is an

ultimate/extreme state design that involves the formation of plastic hinges. Thus, the right hand side of Equation (6.12) can be formulated using the fundamental concepts of plastic design.

6.3.2 Energy-based Seismic Design and Plastic Design Relations

Recall that the underlining concept of plastic design of structures lies in the formation of plastic hinges and the resulting collapse mechanisms. Collapse mechanisms are said to have formed when a structure can no longer carry any load or is undergoing such excessive deform to a state where the integrity of the structure is severely compromised. Consider a sway mechanism, shown in Figure 6.6, of a portable frame subjected to a horizontal joint load and a concentrated span load. The work equations for the two collapse mechanisms using the geometry of the structure, plastic moment capacities of the beam and columns, the applied forces and the anticipated plastic rotations at collapse can be written as in Equation (6.13). The work done by the internal plastic moments is called the internal work, whereas the work done by the external forces is called the external work.

$$
\begin{array}{llll}
& External\,Work & = & Internal\,Work \\
Sway\,Mechanism & P \times (h \times \theta_p) & = & (2M_{pc} + 2M_{pb}) \times \theta_p \qquad (6.13) \\
Beam\,Mechanism & H \times (\dfrac{b}{2} \times \theta_p) & = & (6M_{pb}) \times \theta_p
\end{array}
$$

(a) Sway Mechanism　　　　**(b) Beam Mechanism**
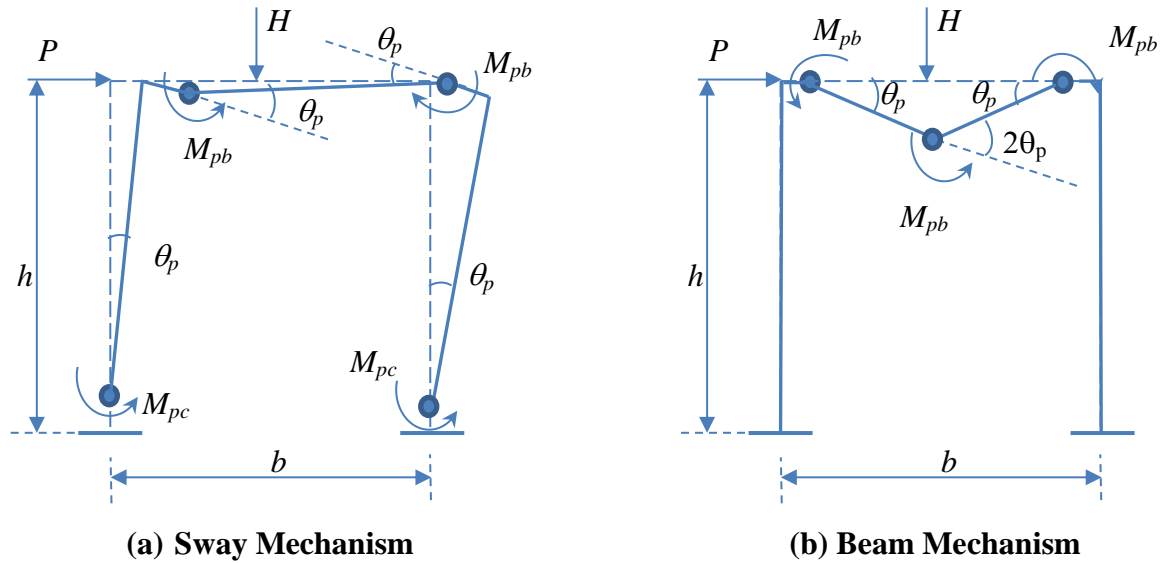
Figure 6.6 Collapse mechanisms of portable frame

For design purposes, it is rational to consider the external work done as the energy demand and the internal work as dissipation capacity. Henceforth, for energy-based seismic design the external work can be replaced by hysteretic energy demand. This approach has been used by Estes and Anderson *(2004)* in an energy-based seismic design of steel frames and Terapathana *(2012)* for an energy-based seismic design of reinforced concrete structures. Recall that the energy demand due to an earthquake involves cyclic load reversals that contribute to the cumulative hysteretic energy whereas the right hand side of Equation (6.13) does not involve load reversal and is monotonic. Thus, it is necessary to adjust the static monotonic hysteretic energy given by the right hand side of Equation (6.13) in order to correlate it to the dynamic hysteretic energy capacity of structures subjected to earthquake loads.

 For seismic evaluation of existing reinforced concrete structures, ATC 40 *(1996)* suggests the use of a dynamic to monotonic hysteretic energy ratio of four. In the same document it is also suggested that the factor of four be subjected to reduction factors to account for a reduction in the dynamic hysteretic energy due to pinching nature of the hysteresis behavior of concrete

sections. For moment resisting steel frames, with properly designed connections and stable

hysteresis, it is reasonable to consider a factor of four as the ratio of dynamic-to-monotonic

hysteretic energy. The justification behind the use of a factor of four can be better explained

from the energy calculation of one cycle of an idealized hysteresis loop as shown in Figure 6.7.
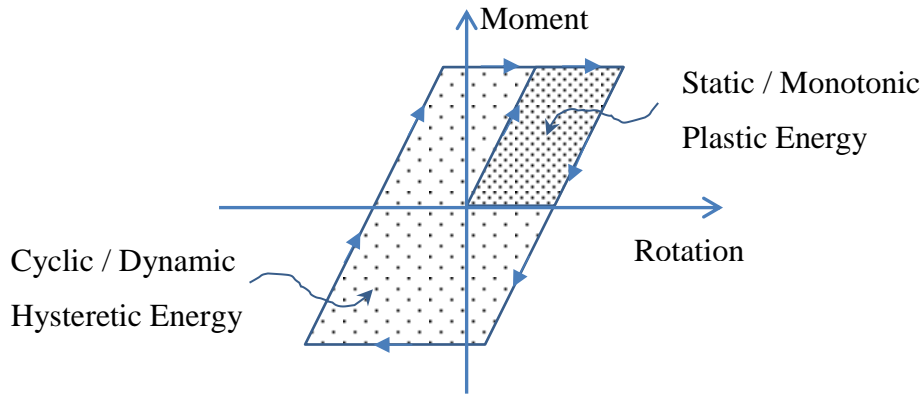
Figure 6.7 Elastic- plastic hysteresis cycle

From Figure 6.7, it can be readily seen that the full cycle area is four times the monotonic area.

This substantiates the assumption that for moment resisting steel frames with stable hysteresis

behavior which is devoid of any stiffness or strength degradation, the dynamic hysteretic energy

is approximately equal to four times the static plastic energy. Thus, a dynamic-to-static

hysteretic ratio of four will be used in this study to design an earthquake resistant moment

resisting steel frames based on energy method. For instance, for the frame mechanism shown in

Figure 6.6 (a), the hysteretic energy capacity given by the right hand side of Equation (6.13)

shall be greater than or equal to the hysteretic energy demand due to a design earthquake, i.e.,

$$(HE)_{demand} \leq 4.0 \times [(2M_{pc} + 2M_{pb}) \times \theta_p] \qquad (6.14)$$

where *(HE)_{demand}* = the hysteretic energy demand due to the design earthquake or suite of

earthquakes.

181

To a practicing engineer, the effect of earthquake on structures is more readily understandable when it is tied to the resulting horizontal motions/deformations of the structure. This is a useful observation to assess the applicability of Equation (6.14) to the different possible collapse mechanisms a structure may undergo. For the beam mechanism shown Figure 6.6 (b), it is obvious that the mechanism is related to vertical loads and is minimally affected by earthquake events. Thus, equating the external work causing a beam mechanism to a hysteretic energy demand due to an earthquake renders it unrealistic. Similarly, for a combined mechanism of sway and beam mechanisms, vertical loads are involved and the resulting external work cannot be fully related to the hysteretic energy demand due to an earthquake. As a result, the beam and combined collapse mechanisms will be discarded in the energy-based seismic design formulation without significantly affecting the final design result. This argument is supported by Estes and Anderson *(2004)* who showed that vertical load mechanisms are not significant when earthquake forces are considered.

It is important to highlight that a design method is deemed appropriate if it ensures that the resulting structure is safe against the design actions and is also cost effective. EBSD is no exception to this requirement. The cost of a structure, among others, is related to the final sizes of the members that form the structure. Obviously, as size and weight are directly related, the cost aspect of a design can be addressed by minimizing the weight of the structure. For moment resisting frames, in most cases the weight of beams and columns can be reasonably associated with their corresponding plastic moment capacity. Thus, a weight function can be expressed in terms of the length of the members and their plastic moment capacities. For instance, for the frame in Figure 6.6, the weight function can be written as

$$W = 2 \times h \times M_{pc} + b \times M_{pb} \tag{6.15}$$

By minimizing the weight function given in Equation (6.15), a cost effective energy-based seismic design of the portal frame can be achieved. This design concept practically reduces the energy- based seismic design to an optimization problem. In mathematics, an optimization problem involves minimization or maximization of an objective function which is subjected to certain constraint equations. For an energy-based seismic design, the objective function is the weight function whereas the inequalities of the collapse mechanisms form the constraint equations. For the frame shown in Figure 6.6, the objective function and the constraint equation are given by Equations (6.14) and (6.15), respectively. In moment resisting frame design, additional constraints such as beam to column capacity ratio, that arise from code or detailing requirements may need to be considered. For instance, for the frame in Figure 6.6 the mathematical formulation of the minimization problem will be described below.

Objective function:

Minimize the weight function: $W = 2 \times h \times M_{pc} + b \times M_{bc}$

Subjected to the constraint equations:

$4.0 \times [(2M_{pc} + 2M_{pb}) \times \theta_p] \geq (HE)_{demand}$; Strong Column – Weak Beam scenario

$4.0 \times [(2M_{pc} + 2M_{pc}) \times \theta_p] \geq (HE)_{demand}$; Strong Beam – Weak Column scenario

$M_{pc} - M_{pb} \geq 1.0$; Code Requirement

where $M_{pb}, M_{pc} \geq 0$

The above minimization for M_{pc} and M_{pb} can be easily achieved by using a Microsoft Excel built-in analysis function called Simplex Method. The Simplex method was developed by George Dantzig in 1947, and is a method for solving problems in linear programming.

6.3.3 Application to Multistory Frames

The application of an optimization problem for an energy-based seismic design of a single story portal frame is rather simple. However, for multistory frames the optimization problem involves many possible collapse mechanisms and many feasible constraint equations and becomes rather complex. Ridha and Wright *(1967)* proposed a classical safe approach called a story-wise optimization that reduces the plastic design of multistory frames into the design of a series of single story frames stacked vertically. In this approach, one story at a time is designed starting with the topmost story. The story-wise approach was also used by Disque *(1971)* for the design of multistory braced frames and recently adopted by Estes and Anderson *(2004)* and Terapathana *(2012)*.

Consider a four-story frame shown in Figure 6.8 (a) with possible sway mechanisms. According to Ridha and Wright *(1967)*, the design of the frame for safety against the sway mechanism occurring at the second story of the entire frame as shown in Figure 6.8(b) can be achieved by simultaneously satisfying the design requirements for the standalone story mechanism shown in Figure 6.8(d) and the resulting mechanism of the story above it as shown in Figure 6.8 (c). This can be easily verified by comparing the external and internal work equations of the collapse mechanisms shown in Figures 6.8 (b), (c) and (d). Let's assume that plastic hinges have formed in the second story at joints *i, j, k* and *l* and denote the plastic moment capacity of the columns as M_{nm} where *n* stands for the story and *m* is an index which equals 1 if the end of the column is

184

above and 2 if the end of the column is below the joint being considered. The corresponding

internal and external work equations are:
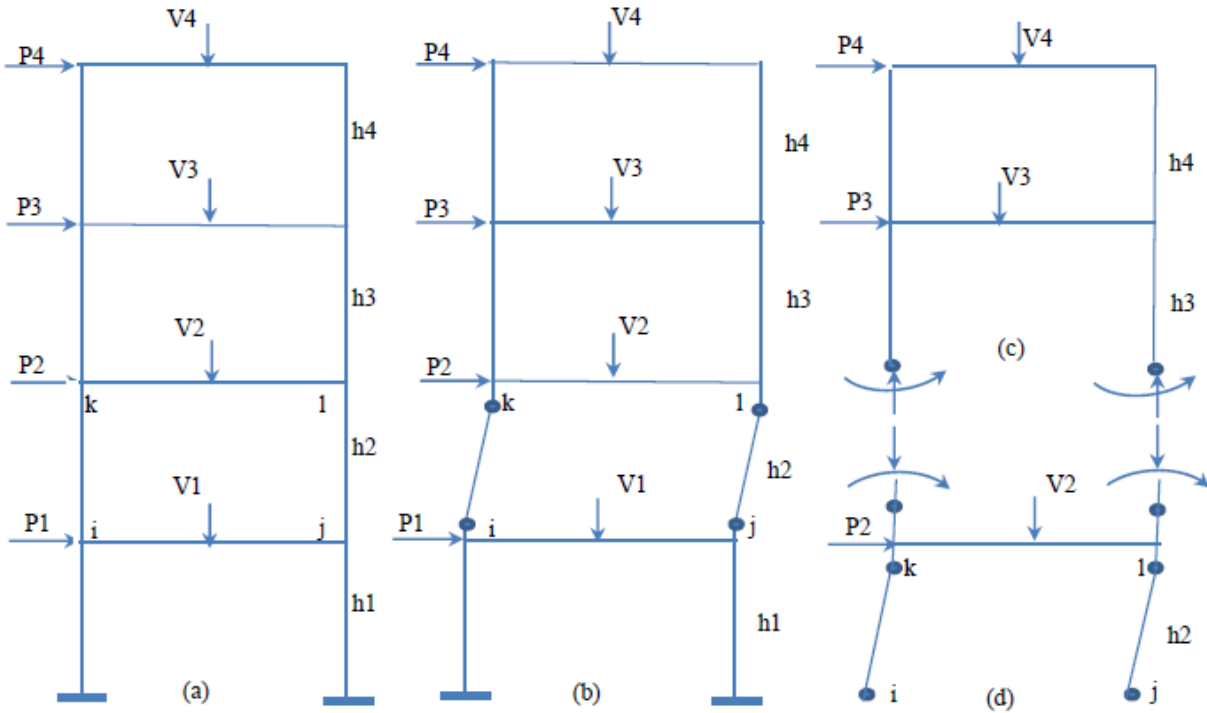
Figure 6.8 Standalone story and whole frame collapse mechanisms

For collapse mechanism shown in Figure 6.8 (b);

$$(P_4 + P_3 + P_2) \times h_2 \times \theta = (M_{21} + M_{21} + M_{22} + M_{22}) \times \theta \tag{6.16}$$

For collapse mechanism shown in Figure 6.8 (d);

$$P_2 \times h_2 \times \theta + (M_{31} + M_{31}) \times \theta = (M_{21} + M_{21} + M_{22} + M_{22}) \times \theta \tag{6.17}$$

For collapse mechanism shown in Figure 6.8 (c);

$$(P_4 + P_3) \times h_2 \times \theta = (M_{31} + M_{31}) \times \theta \tag{6.18}$$

185

The sum of Equations (6.17) and (6.18) gives Equation (6.16). This means that if the design requirements for the story sway mechanisms of Figures 6.8 (c) and (d) are met, the safety of the sway mechanism of the entire frame shown in Figure 6.8 (b) can be ensured.

Because the plastic capacity of compressive members is affected by the simultaneous action of axial force and bending moment, especially in multistory frames where gravity loads increase toward the lower stories. Thus, it is necessary to include the effect of axial force in the formulation of the energy-based seismic design. One way to incorporate axial force effect into EBSD is to use the code recommended axial force-bending moment interaction equations such as the one given in the American Institute of Steel Construction (AISC) manual. Per AISC *(2010)* steel construction manual's Chapter H, the interaction equations for doubly symmetric section in compression and flexure are given as follows.

$$
\begin{aligned}
\frac{P_r}{P_c} + \frac{8}{9}\left(\frac{M_{rx}}{M_{cx}} + \frac{M_{ry}}{M_{cy}}\right) &\leq 1.0 \qquad for \; \frac{P_r}{P_c} \geq 0.2 \\
\frac{P_r}{2P_c} + \left(\frac{M_{rx}}{M_{cx}} + \frac{M_{ry}}{M_{cy}}\right) &\leq 1.0 \qquad for \; \frac{P_r}{P_c} < 0.2
\end{aligned}
\tag{6.19}
$$

where the subscripts *c, r, x,* and *y* represent the available moment strength, required moment strength, strong axis and weak axis bending, respectively. For uniaxial bending about the strong axis, which is the often case for frame analysis and design, the subscripts *x* and *y* can be dropped from Equation (6.18) and after rearranging the interaction equation will take the form shown in Equation (6.19).

$$M_c \geq \frac{8}{9}\left(\frac{1}{(1-\frac{P_r}{P_c})}\right)M_r = \beta_m M_r \qquad for \ \frac{P_r}{P_c} \geq 0.2$$

$$M_c \geq \left(\frac{1}{(1-\frac{P_r}{2P_c})}\right)M_r = \beta_m M_r \qquad for \ \frac{P_r}{P_c} < 0.2$$

(6.20)

The modification factor β_m accounts for the reduction in moment capacity M_c due to the presence of an axial force by applying an amplification factor to the required plastic moment capacity M_r obtained per the energy-based seismic design procedure. According to AISC Load and Resistance Factor Design (LFRD) method, the design moment (M_c) and axial force (P_c) capacities of a column are given by $\phi_c P_n$ and $\phi_b M_n$, respectively where ϕ_c and ϕ_b are resistance factors for compression and bending, respectively. Because these factors are likely to be different for different specifications, they are both taken as unity in the following design examples. The primary objective here is to demonstrate how the energy-based design process can be applied without regard to the exact values of resistance factors used. The AISC LRFD design manual also gives detail procedures for determining the nominal capacities P_n and M_n for almost all commonly used structural shapes. However, for purpose of demonstrating the proposed EBSD procedure, the nominal capacities are calculated as follows.

$$M_n = \sigma_y Z \quad and \quad P_n = F_{cr} A_g$$

where Z = plastic section modulus about the axis of bending, F_{cr} = flexural buckling stress, and A_g = gross cross-sectional area of the member

6.3.4   Proposed Energy-Based Seismic Design Flowchart

The flowchart shown in Figure 6.9 summarizes the steps used in the proposed EBSD procedure

for the design of multistory frames. The details involved in each step will be described in the

following section through design examples of a three-story and five-story frames. The flow

chart shown in Figure 6.9 is simple and easy to follow but the design, like any other designs,

needs engineering judgment in its execution.
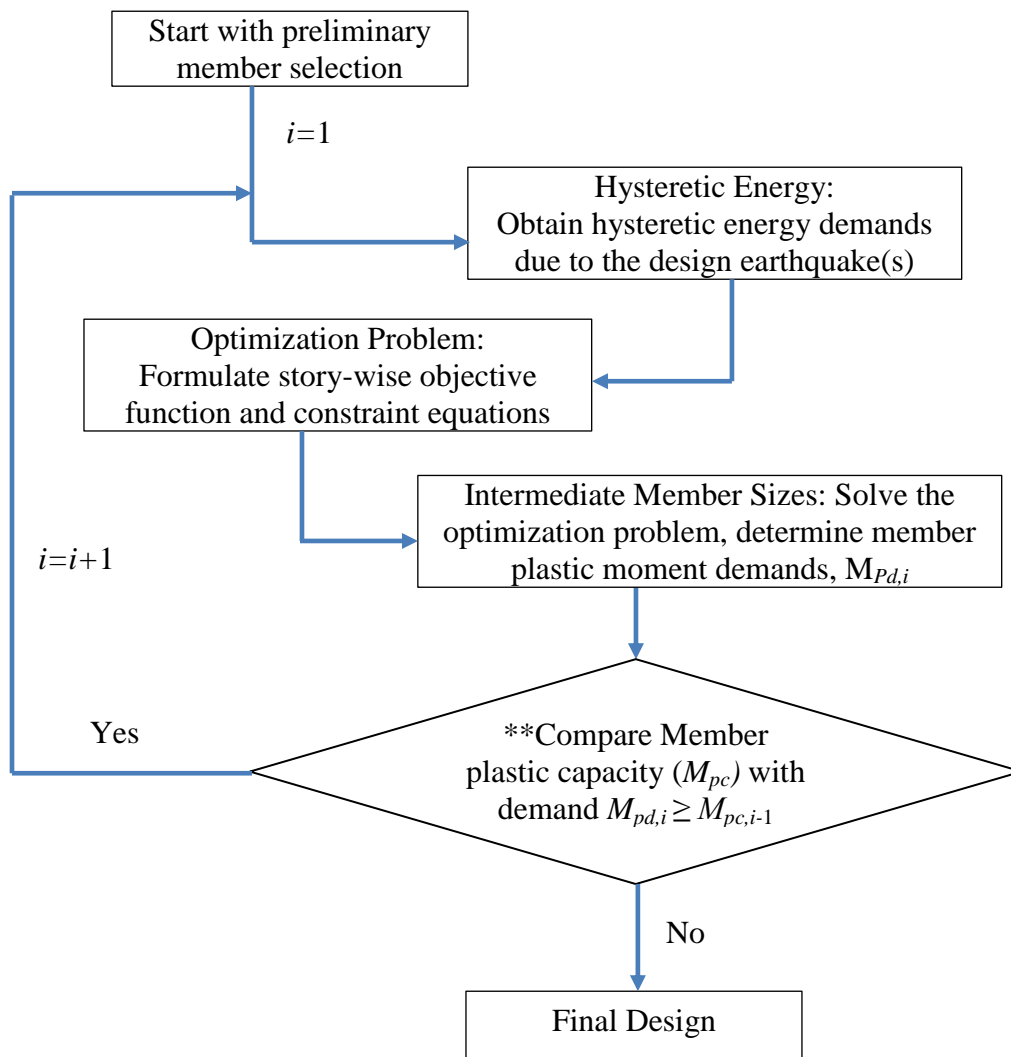
** It is also required to check that $M_{pc,i-1}$ is not excessively greater than $M_{pd,i}$

Figure 6.9 Flowchart: Energy based seismic design

6.4 Energy-based Seismic Design (EBSD): Design Examples

So far in this study, expressions for the input and hysteretic energies for SDOF and MDOF systems, the hysteretic energy distribution for MDOF systems and an energy-based seismic design procedure have been proposed. The next step is to demonstrate how all these concepts can be put together and applied to the design of real structures. For this purpose, two frames, a three-story and a five-story, will be designed. The design examples will show how the hysteretic energy demand for each frame is determined and how this demand is to be distributed to the different levels of the frame. The design examples will also elucidate how member sizes are optimized based on the Simplex method of linear optimization.

Both frames are assumed to be built in a location with site soil class C. The choice of the soil site classes is arbitrary, as the main purpose of these examples is to illustrate the different steps involved in applying the proposed EBSD procedure. A set of five earthquakes were selected from the PEER Beta Data Base and scaled to match an IBC 2009 response spectrum. The response spectrum is generated using a built-in procedure in SAP 2000 for soil class C at a site with zip code 94704. The location is chosen because it lies in one of the highly seismic active areas in the west coast of the United States and it is also where the headquarters of CSI Structures, the company that develops SAP 2000, is located. The design earthquakes are selected to be the Horizontal-1 (the main horizontal direction) component of the respective earthquake records. Details of the selected earthquakes are given in Table 6.1.

189

Table 6.1 List of selected design earthquakes

Earthquake Name	Station Name	Year	CAV*	PGA*	PGV*	Scale
Loma Prieta	Bear Valley #5	1989	114.84	26.3	3.64	11.5
Loma Prieta	Fremont - Mission San Jose	1989	210.17	48.9	5.55	7.5
Loma Prieta	Hayward City Hall - North	1989	80.76	18.88	2.21	18.5
Loma Prieta	SF - Telegraph Hill	1989	44.96	13.78	1.42	25.5
Loma Prieta	Yerba Buena Island	1989	49.44	11.36	1.71	28
Landers	Amboy	1992	362.91	44.43	7.17	6

* units are of inches and seconds

The normalized input energy spectra as described in Chapter 3 and the hysteretic-to-input energy ratio spectra as discussed in Chapter 4 have been formulated for SDOF systems with ductility level of $\mu = 2$, 3, 4 and 5. Later in Chapter 5, a relationship between the input energy for MDOF systems and their ESDOF systems was established. Thus, for the design of a structural system with a required level of ductility, the energy expressions and relationships formulated in Chapters 3, 4 and 5 can be used to estimate the hysteretic energy demand for use in the EBSD procedure.

Equation (6.13) shows the relationship between hysteretic energy demand and capacity. From the right hand side of the equation, it is clear that the capacity is dependent on the plastic moment and plastic rotation capacities. In EBSD, the plastic rotation capacity is considered as a known variable and needs to be determined before the design procedure is applied to optimize the member sizes. Intrinsically, the performance level of the structure is dependent on the performance level of each individual element that constitutes the structure. Per FEMA 350, moment resisting steel frames are capable of developing large plastic rotations, in the order of 0.02 radians or larger, without significant strength degradation. According to FEMA (1997)

Interim Advisory No.1, based on the work of SAC (a consortium of the Structural Engineers Association of California, the Applied Technology Council, and the California Universities for Research in Earthquake Engineering) and other researchers on full scale tests done after the Northridge earthquake, a plastic rotation of 0.025 to 0.030 was recommended for steel moment connections. Thus a design plastic rotation of 0.03 radians has been used in this study.

6.4.1   Design Example: Three Story One Bay Frame

The three story frame shown Figure 6.10 is one of the design examples considered for demonstrating the step by step procedures of the proposed EBSD. The moment resisting steel frame consists of beams and columns with rigid moment connections. The roof level beams were subjected to uniform dead and live loads of 2.5 *k/ft* and 1.75 *k/ft*, respectively. The loading on the remaining floor beams was considered to be 3.0 *k/ft* and 2.25 *k/ft* for dead and live loads, respectively. The seismic mass was taken to be a proportion of the gravity loads lumped at the joints. For this purpose a 100% of the dead loads and 25% the live loads are considered. To incorporate diaphragm action, as is the case of decks in frames for buildings, diaphragm constraints were employed to force the joints at a given floor to displace the same horizontally.

From the flow chart in Figure 6.9, it can be seen that the proposed EBSD method is an iterative procedure. Iterative procedures always start with a set of initial solutions or values. For the EBSD procedure, the initial values are the preliminary member sizes. For this example, the preliminary members of the frame were determined from a gravity load design of the frame using the AISC – LFRD procedure built in the SAP 2000 structural analysis and design software. The results are presented as Step 1 of Iteration 1 below.

Using these preliminary member sizes, modal properties for the first two modes that constitute more than 90% of the seismic mass were calculated and are given as Step 2 of Iteration 1.
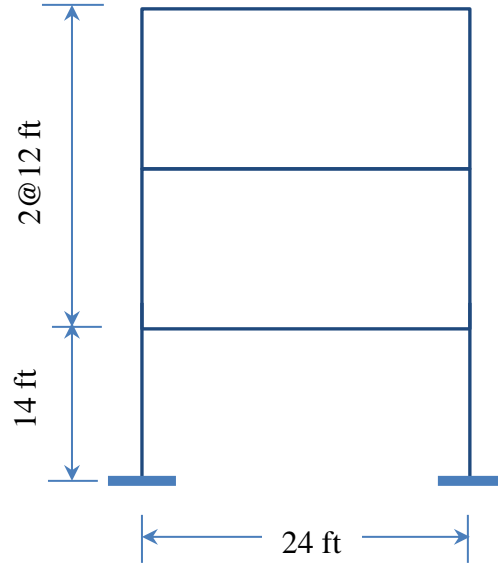
Figure 6.10 Design example: three story-one bay frame

Iteration 1

S*tep 1: Preliminary Member Sizes*

Preliminary Column Sizes		Preliminary Beam Sizes	
Story	Size	Floor Level	Size
1st	W14×90	2nd (1st story)	W18×76
2nd	W14×90	3rd	W18×76
3rd	W14×90	Roof (5th story)	W18×76

S*tep 2: Modal Properties*

	Period (s)	Γ^2, kip·s^2·in.$^{-1}$	$\Sigma\,\Gamma_i^2/\,M$	Ductility, μ
Mode 1	0.83	0.607	0.889	4
Mode 2	0.25	0.065	0.095	4
		$\Sigma\,\Gamma_i^2/\,M =$	98.4%	

Step 3: Normalized Input Energy per Unit Mass (NE)

Normalized input energy spectra for ESDOF for soil site class C and hysteretic model BP were developed and presented in Chapter 3. Using the expression for the *meant +σ NE* spectra, given by Equation 3.7, for a design ductility level μ=4, we have

$$
\begin{aligned}
s &= -0.0507\mu + 1.515 = -0.0507\times 4 - 1.515 = 1.312 \\
b &= 0.0137\mu - 0.0569 = 0.0137\times 4 - 0.0569 = -0.0021 \\
T_1 &= 0.374\mu^{-0.116} = 0.374\times 4^{-0.116} = 0.318\,\text{sec} \\
C &= 0.0069\mu^2 - 0.0657\mu + 0.563 = 0.0069\times 4^2 - 0.0657\times 4 + 0.563 = 0.411 \\
T_2 &= -0.102\mu + 1.978 = -0.102\times 4 - 1.978 = 1.57\,\text{sec}. \\
k &= 0.0089\mu^2 - 0.129\mu + 0.946 = 0.0089\times 4^2 - 0.129\times 4 = 0.572 \\
n &= 0.0072\mu^2 - 0.0124\mu - 0.786 = 0.0072\times 4^2 - 0.0124\times 4 - 0.786 = -0.702
\end{aligned}
$$

where μ is the ductility ratio and *s, b, T_1, C, T_2, k, n* are parameters used to define the *NE* spectra as shown in Figure 3.6 and Equation (3.1).

From Equation (3.1), the normalized energy is given as follows

For Mode 1: $(T_1= 0.318\text{ s }) \le (T= 0.83\text{ s}) < (T_2= 1.57\text{s})$

$$\Longrightarrow NE = C = 0.41$$

For Mode 1: $(T= 0.25\text{ s}) \le (T_1= 0.318\text{s})$

$$\Longrightarrow NE = sT + b = 1.3122\times 0.25\text{-}0.0021 = 0.326$$

Recall that *NE* is defined as the square root of the input energy per unit mass (*IE/m*) divided by the velocity index, *VI* (= *CAV*×*PGV*). Therefore, the input energy per unit mass is given by

$$IE/m = NE^2 \times CAV \times PGV$$

where *CAV* = Absolute Cumulative Velocity; *PGV* = Peak Ground Velocity of the design earthquake. Since the frame is to be designed for the *mean+σ* of the selected design earthquakes

listed in Table 6.1, the corresponding *mean+σ VI* needs to be calculated. The calculation of the

mean+σ VI is shown in the table below.

	(a)	(b)	(c)	(d)= $(a \times b \times c^2)$
Earthquake	*CAV* (in./s)	*PGV* (in./s)	Scale	*VI* (in.^{2}/s^2)
Loma Prieta	114.8	3.64	11.5	5.53×10^4
Loma Prieta	210.2	5.55	7.5	6.56×10^4
Loma Prieta	80.76	2.21	18.5	6.11×10^4
Loma Prieta	44.96	1.42	25.5	4.15×10^4
Loma Prieta	49.44	1.71	28	6.63×10^4
Landers	362.91	7.17	6	9.37×10^4
		mean+σ VI =		8.11×10^4

The input energy per unit mass (*IE/m*) for each mode is now obtained as follows:

$$\text{Mode 1: } IE/m = NE^{2 \times} VI = (0.41)^2 \times 8.11 \times 10^4 \text{ in.}^2/\text{s}^2 = 1.36 \times 10^4 \text{ in.}^2/\text{s}^2$$

$$\text{Mode 2: } IE/m = NE^2 \times VI = (0.326)^2 \times 8.11 \times 10^4 \text{ in.}^2/\text{s}^2 = 0.86 \times 10^4 \text{ in.}^2/\text{s}^2$$

Step 4: Hysteretic Energy per Unit Mass (HE/m)

Once the input energy per unit mass is obtained, the hysteretic energy per unit mass is calculated

using the hysteretic to input energy relationships developed in Chapter 4. For soil site class C

and hysteretic model BP, such relationships are given in Table 4.1. Using Figure 4.2 and Table

4.1, the ratio *HE/IE* for the two modes of the design example can be calculated as follows.

Entering Table 4.1 for hysteretic model BP, the *mean+σ HE/IE* spectra parameters for $\mu = 4$ are

given as below.

$$C = 0.651; \ T_2 = 2.674 \text{ s}; \ s = -0.0247 \text{ and } b = 0.717$$

where *C, T_2, s,* and *b* are as defined in Figure 4.2

194

According to the *HE/IE* spectra shown in Figure 4.2, since the periods of vibrations for mode 1 and mode 2 are less than T_2, the *HE/IE* ratio for both modes is within the constant region of the spectra and is equal to $C = 0.651$. The modal hysteretic energies per unit mass are then given by:

Mode 1: *HE/m*= (*IE/m*) $\times$ (*HE/IE*) = 1.36×10^4 in.^{2}/s$^2 \times 0.651 = 0.89 \times 10^4$ in.^{2}/s^2

Mode 2: *HE/m*= (*IE/m*) $\times$ (*HE/IE*) = 0.86×10^4 in.^{2}/s$^2 \times 0.651 = 0.56 \times 10^4$ in.^{2}/s^2

Step 5: MDOF System Total Hysteretic Energy Demand and its Distribution

The hysteretic energy demand for MDOF systems can be obtained using the hysteretic energy relationships between MDOF systems and their Equivalent SDOF systems developed in Chapter 5. Using Equation (5.20), the hysteretic energy demand for the three story frame is given as follows:

$$HE_{total} = (\Gamma^2 \times HE/m)_{mode\ 1} + (\Gamma^2 \times HE/m)_{mode\ 2}$$

$$HE_{total} = (0.607\ \text{k·s}^2\text{·in.}^{-1})\ (0.89 \times 10^4\ \text{in.}^2/\text{s}^2) + (0.065\ \text{k·s}^2\text{·in.}^{-1})\ (0.56 \times 10^4\ \text{in.}^2/\text{s}^2)$$

$$= 5752\ \text{kip-in.}$$

The total hysteretic energy demand should now be distributed to the different levels of the three story frame according to the hysteretic energy distribution proposed in Section 6.2 and given by Equation (6.10). The forces and displacements to be used in Equation (6.10) are obtained from modal pushover analysis results for Mode 1. The design ductility level 4 roughly corresponds to a roof drift ratio of 0.04, which is larger than the conventional value of 0.02 often used for the design of building frames for lateral loads. However, a properly designed frame per current codes rarely passes its elastic limit at a roof drift ratio of 0.02, in which case the use of the energy-based seismic design becomes irrelevant. Therefore, for better distribution of the

hysteretic energy demand to the different levels of the structure, the frame is pushed to roof drift ratio of 0.04. Presented below are the story level forces, displacements and story drifts obtained from the pushover analysis.

Story	Force (kips)	Displacement (in.)	Story Drift (in.)
Story 1	37.0	9.01	9.01
Story 2	72.0	15.74	6.73
Story 3	77.0	18.24	2.5

Using Equation (6.11), for purpose of hysteretic energy demand distribution, the total and story level external work done during the pushover are computed as follows.

$$For\ Story\ 1: \quad WE_1 = 2(\sum_{k=1}^{n} F_k)\Delta d_1 = 2\times(37+72+77)\times 9.01 = 3352 \text{ kip-in.}$$

$$For\ Story\ 2: \quad WE_2 = (\sum_{k=2}^{n} F_k)\Delta d_2 = (72+77)\times 6.73 = 1003 \text{ kip-in.}$$

$$For\ Story\ 3: \quad WE_3 = (\sum_{k=3}^{n} F_k)\Delta d_3 = 77\times 2.5 = 195.2 \text{ kip-in.}$$

$$WE_{total} = (\sum_{i=1}^{n} F_i)d_1 + \sum_{i=1}^{n} F_i d_i$$
$$= (37+72+77)\times 9.01 + (37\times 9.01) + (72\times 15.74) + (77\times 18.24) = 4547 \text{ kip-in.}$$

The hysteretic energy demands at different story levels are then given as:

$$Story\ 1: \quad R = \frac{HE_1}{HE_{total}} = \frac{WE_1}{WE_{total}} = \frac{3352}{4547} = 0.737 \Rightarrow HE_1 = 0.737\times 5752 \text{ kip-in.} = 4240 \text{ kip-in.}$$

$$Story\ 2: \quad R = \frac{HE_2}{HE_{total}} = \frac{WE_1}{WE_{total}} = \frac{1003}{4547} = 0.221 \Rightarrow HE_2 = 0.221\times 5752 \text{ kip-in.} = 1269 \text{ kip-in.}$$

$$Story\ 3: \quad R = \frac{HE_3}{HE_{total}} = \frac{WE_1}{WE_{total}} = \frac{192.5}{4547} = 0.042 \Rightarrow HE_3 = 0.042\times 5752 \text{ kip-in.} = 243.5 \text{ kip-in.}$$

Step 6: Member Size Optimization

The story-wise optimization of members involves formulating a series of story-wise collapse mechanisms and solving an optimization problem. The optimization problem relates the story level hysteretic energy demand to the collapse mechanism based on internal work done (treated in this study as plastic energy capacity or energy dissipating capacity). The steps involved in the EBSD method of optimization of member sizes are presented below starting with the third (i.e., top) story. Columns in the same story are assumed to have the same size and the following designation is used to denote a member.

M_{kC} = column member in story k, and M_{kB} = beam member in story k

Optimization of Members in the Third Story

(a)   (b)
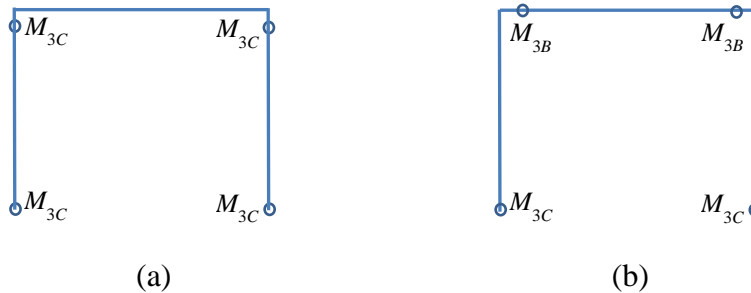
Constraint equation based on mechanism (a) – Strong beam and weak column

$$4\times(M_{3C}+M_{3C}+M_{3C}+M_{3C})\times0.03\geq243.5 \text{ kip-in.}$$

Constraint equation based on mechanism (b) – Strong column and weak beam

$$4\times(M_{3C}+M_{3C}+M_{3B}+M_{3B})\times0.03\geq243.5 \text{ kip-in.}$$

Additional constraint equation at joints – code requirement

$$M_{3C}-M_{3B}\geq0$$

Objective Function – Weight , W

$$W=2(144M_{3C})+288M_{3C}$$

Mathematical formulation of the minimization problem

Minimize :

$$W = 288 M_{3C} + 288 M_{3B}$$

Subjected to :

$$0.48 M_{3C} \geq 243.5 \text{ kip-in.}$$

$$0.24 M_{3C} + 0.24 M_{3B} \geq 243.5 \text{ kip-in.}$$

$$M_{3C} - M_{3B} \geq 0$$

where $\quad M_{3c} > 0, \quad M_{3b} > 0$

The optimized solution obtained using the Simplex linear solver built in Microsoft Excel is;

$$M_{3C} = 508 \text{ kip in. and } M_{3B} = 508 \text{ kip-in.}$$

Optimization of Members in the Second Story

(c) $\qquad\qquad\qquad\qquad\qquad$ (d)
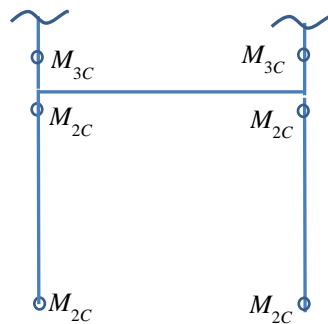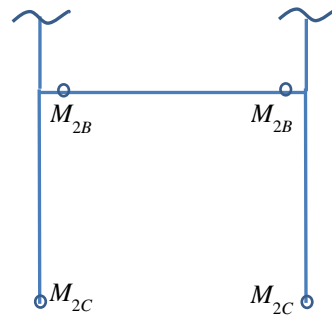
Constraint equation based on mechanism (c) – Strong beam and weak column

$$4 \times (M_{2C} + M_{2C} + M_{2C} + M_{2C}) \times 0.03 - 4 \times (508 + 508) \times 0.03 \geq 1269 \text{ kip-in.}$$

Constraint equation based on mechanism (d) – Strong column and weak beam

$$4 \times (M_{2C} + M_{2C} + M_{2B} + M_{2B}) \times 0.03 \geq 1269 \text{ kip-in.}$$

Additional constraint equation at joints – code requirement

$$M_{2C} + 508 - M_{2B} \geq 0$$

198

Objective Function – Weight, W

$$W = 144M_{2C} + 144M_{2C} + 288M_{2B}$$

Mathematical formulation of the minimization problem

Minimize :
$$W = 288M_{2C} + 288M_{2B}$$

Subjected to :
$$0.48M_{2C} \geq 1391 \text{kip-in.}$$
$$0.24M_{2c} + 0.24M_{2B} \geq 1269 \text{kip-in.}$$
$$M_{2C} - M_{2B} \geq -508 \text{kip-in.}$$

where $\quad M_{2C} > 0, \quad M_{2B} > 0$

The optimized solution obtained using the Simplex linear solver built in Microsoft Excel is

$$M_{2C} = 5286 \text{ kip-in. and } M_{2B} = 0 \text{ kip-in.}$$

The above solution for M_{2C} and M_{2B} is unrealistic, as the beam size cannot be zero. This is an intermediate solution and if accepted as is, the solution doesn't converge rapidly. As a result, additional constraint equation might be needed to tweak the optimization problem to give a realistic solution. In such cases, a constraint equation that requires the beam capacity to be at least greater than 60% of the column moment capacities may be used without adversely affecting the optimization problem. Employing such constraint yields a modified solution to the optimization problem given as

$$M_{2C} = 3304 \text{ kip-in. and } M_{2B} = 1982 \text{ kip-in.}$$

Optimization of Members in the First Story

(e)   (f)
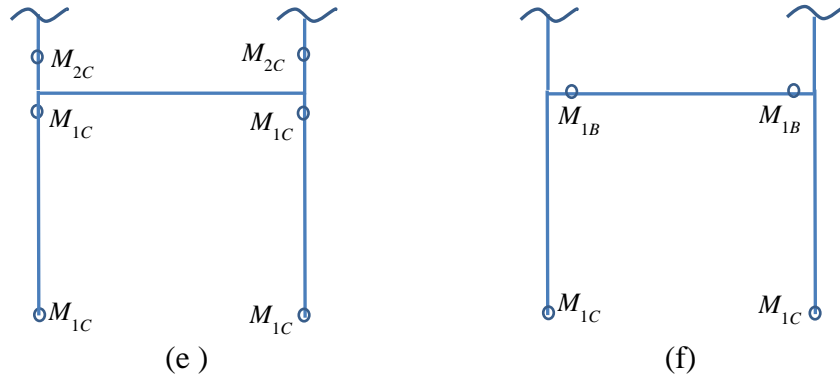
Constraint equation based on mechanism (e) – Strong beam and weak column

$$4\times(M_{1C}+M_{1C}+M_{1C}+M_{1C})\times0.03-4\times(3304+3304)\times0.03\geq4240\,\text{kip-in.}$$

Constraint equation based on mechanism (f) – Strong column and weak beam

$$4\times(M_{1C}+M_{1C}+M_{1B}+M_{1B})\times0.03\geq4240\,\text{kip-in.}$$

Additional constraint equation at joints – code requirement

$$M_{1C}+3304-M_{1B}\geq0$$

Objective Function – Weight, W

$$W=168M_{1C}+168M_{1C}+288M_{1B}$$

Mathematical formulation of the minimization problem

Minimize :
$$W=336M_{1C}+288M_{1B}$$

Subjected to :
$$0.48M_{1C}\geq5033\,\text{kip-in.}$$
$$0.24M_{1C}+0.24M_{1B}\geq4240\,\text{kip-in.}$$
$$M_{1C}-M_{1B}\geq-3304\,\text{kip-in.}$$

where $M_{1C}>0,\quad M_{1B}>0$

The optimized solution obtained using the Simplex linear solver built in Microsoft Excel is

$$M_{1C}=10490\text{ kip-in. and }M_{1B}=7181\text{ kip-in.}$$

200

Step 7: Effect of Axial Force on Plastic Capacity Demands

Per Equation (6.16), the plastic moment demands obtained in Step 6 need to be amplified by a

factor β_m to account for the reduction in the plastic moment capacities of columns due to the

presence of an axial compression force. The axial compressive force is present due to the

simultaneous actions of gravity and lateral loads during a seismic event.   The amplification

factor β_m is obtained as a ratio of the applied axial force during a seismic event to the axial

compression capacity of the member under consideration. In line with the load proportions

considered while determining the seismic mass, the axial forces were obtained from a

combination of 100% and 25% of the applied dead and the live loads, respectively.

Story	Column size	Axial Force (kips)		β_m	Plastic Moment (kip-in.)	
		Capacity	Applied		Required	Modified
1	W14×90	968	127	1.070	10490	11220
2	W14×90	1008	82	1.042	3304	3445
3	W14×90	1008	37	1.019	508	518

Step 8: Plastic Moment Capacity versus Demand Comparison

The last step of each iteration cycle for the proposed EBSD procedure is the selection of new

member sizes that meet the required plastic moment capacity obtained in Step 7. When selecting

new member sizes for columns, it is important to avoid the possibility of weak or extremely

strong story with respect to the story immediately above it. At this step the plastic moment

capacities of current member sizes are compared with the required plastic moment capacities

based on the energy-based seismic design. If the plastic moment required is less than the plastic

moment capacity of the current member size, then the current size remains unchanged.

However, this is not always true, as will be shown in the design example of the five story frame to be discussed in the next section. At the end of the first iteration the member sizes can be excessively large and need to be optimized in successive iterations. The plastic moment demand-capacity comparison and selection of new member sizes as required are tabulated below.

	Story	Current size	Plastic Moment (kip-in.)		Member Size	
			Capacity	Required	Decision	New
Columns	1	W14×90	7580	11220	Change	W14×132
	2	W14×90	7580	3445	Keep	W14×90
	3	W14×90	7580	518	Keep	W14×90
Beams	1	W18×76	8150	7071	Keep	W18×76
	2	W18×76	8150	1762	Keep	W18×76
	3	W18×76	8150	508	Keep	W18×76

Iteration 2

For brevity, detailed descriptions of the remaining iterations for each step including the different collapse mechanisms will not be repeated. Only important details along with the final results of each step will be presented.

S*tep 1: Member Sizes at end of Iteration 1*

Column Sizes @ end of Iteration 1	
Story	Size
1st	W14×132
2nd	W14×90
3rd	W14×90

Beam Sizes@ end of Iteration 1	
Floor Level	Size
2nd (1st story)	W18×76
3rd	W18×76
Roof (5th story)	W18×76

*S*t*ep 2: Modal Properties*

	Period (s)	Γ^2, kip·s^2·in.$^{-1}$	$\Sigma\,\Gamma_i^2/\,M$	Ductility, μ
Mode 1	0.77	0.589	0.859	4
Mode 2	0.24	0.077	0.112	4
		$\Sigma\,\Gamma_i^2/\,M =$	97.1%	

Step 3: Normalized Input Energy per Unit Mass (NE)

	μ	s	b	T_1	C	T_2	k	n	T	NE
Mode 1	4	1.312	-0.0021	0.318	0.411	1.57	0.572	-0.720	0.77	0.41
Mode 2	4	1.312	-0.0021	0.318	0.411	1.57	0.574	-0.720	0.24	0.31

Modal input energy per unit mass (*IE/m*):

Mode 1: $IE/m = NE^2 \times VI = (0.41)^2 \times 8.11 \times 10^4$ in.^{2}/s$^2 = 1.36 \times 10^4$ in.^{2}/s^2

Mode 2: $IE/m = NE^2 \times VI = (0.31)^2 \times 8.11 \times 10^4$ in.^{2}/s$^2 = 0.78 \times 10^4$ in.^{2}/s^2

Step 4: Hysteretic Energy per Unit Mass (HE/m)

	μ	C	T_2	s	b	T	EH/EI
Mode 1	4	0.651	2.674	-0.0247	0.717	0.77	0.651
Mode 2	4	0.651	2.674	-0.0247	0.717	0.24	0.651

Mode 1 : $EH/m = (EI/m) \times (EH/EI) = 1.36 \times 10^4$ in.^{2}/s$^2 \times 0.651 = 0.89 \times 10^4$ in.^{2}/s^2

Mode 2 : $HE/m = (IE/m) \times (HE/IE) = 0.78 \times 10^4$ in.^{2}/s$^2 \times 0.651 = 0.51 \times 10^4$ in.^{2}/s^2

Step 5: MDOF System Total Hysteretic Energy Demand and its Distribution

$$HE_{total} = (\Gamma^2 \times HE/m)_{mode1} + (\Gamma^2 \times HE/m)_{mode2}$$

$$HE_{total} = (0.589 \text{ k·s}^2\text{·in.}^{-1})(0.89 \times 10^4 \text{ in.}^2/\text{s}^2) + (0.077 \text{ k·s}^2\text{·in.}^{-1})(0.51 \times 10^4 \text{in.}^2/\text{s}^2)$$

$$= 5618 \text{ kip-in.}$$

Story forces, displacements, and hysteretic energies:

Story	Force (kips)	Displacement (in.)	Story Drift (in.)	External Work Done (kip-in.)	Hysteretic Energy (kip-in.)
Story 1	38.0	8.01	8.01	3428	3866
Story 2	84.0	15.3	7.29	1283	1447
Story 3	92.0	18.24	2.94	271	305

Step 6: Member Size Optimization

Optimization of Members in the Third Story

Objective Function – Weight, W

$$W = 144M_{3C} + 144M_{3C} + 288M_{3C}$$

Mathematical formulation of the minimization problem

Minimize :
$$W = 288M_{3C} + 288M_{3B}$$

Subjected to :
$$0.48M_{3C} \geq 305 \text{ kip-in.}$$
$$0.24M_{3C} + 0.24M_{3B} \geq 305 \text{ kip-in.}$$
$$M_{3C} - M_{3B} \geq 0$$

where $\quad M_{3c} > 0, \quad M_{3b} > 0$

The optimized solution obtained using the Simplex linear solver built in Microsoft Excel is

$$M_{3C} = 636 \text{ kip-in. and } M_{3B} = 636 \text{ kip-in.}$$

Optimization of Members in the Second Story

Objective Function – Weight, W

$$W = 144M_{2C} + 144M_{2C} + 288M_{2B}$$

Mathematical formulation of the minimization problem

Minimize :
$$W = 288M_{2C} + 288M_{2B}$$

Subjected to :
$$0.48M_{2C} \geq 1600\,\text{kip-in.}$$
$$0.24M_{2c} + 0.24M_{2B} \geq 1477\,\text{kip-in.}$$
$$M_{2C} - M_{2B} \geq -636\,\text{kip-in.}$$

where $\quad M_{2C} > 0, \quad M_{2B} > 0$

The optimized solution obtained using the Simplex linear solver built in Microsoft Excel is

$$M_{2C} = 3768 \text{ kip-in. and } M_{2B} = 2261 \text{ kip-in.}$$

Optimization of Members in the First Story

Objective Function – Weight, W

$$W = 168M_{1C} + 168M_{1C} + 288M_{1B}$$

Mathematical formulation of the minimization problem

Minimize :
$$W = 336M_{1C} + 288M_{1B}$$

Subjected to :
$$0.48M_{1C} \geq 4771\,\text{kip-in.}$$
$$0.24M_{1C} + 0.24M_{1B} \geq 3866\,\text{kip-in.}$$
$$M_{1C} - M_{1B} \geq -3768\,\text{kip-in.}$$

where $\quad M_{1C} > 0, \quad M_{1B} > 0$

The optimized solution obtained using the Simplex linear solver built in Microsoft Excel is

$$M_{1C} = 9940 \text{ kip-in. and } M_{1B} = 6169 \text{ kip-in.}$$

Step 7 : Effect of Axial Force on Plastic Capacity

Story	Column size	Axial Force (kips)		β_m	Plastic Moment (kip-in.)	
		capacity	Applied		Required	Modified
1	W14×132	1424	128	1.052	9940	10457
2	W14×90	1008	82	1.042	3768	3927
3	W14×90	1008	37	1.019	636	648

Step 8: Plastic Moment Capacity versus Demand Comparison

	Story	Current size	Plastic Moment (kip-in.)		Member Size	
			Capacity	Required	Decision	New
Columns	1	W14×132	11700	10457	Keep	W14×132
	2	W14×90	7580	3927	Keep	W14×90
	3	W14×90	7580	648	Keep	W14×90
Beams	1	W18×76	8150	6169	Keep	W18×76
	2	W18×76	8150	2261	Keep	W18×76
	3	W18×76	8150	636	Keep	W18×76

Because the current member sizes have more capacity than what is required as per the design, there is no need to continue the iterations. The current sizes can be taken as the final design sections.

6.4.2   Design Example 2: Five Story Two Bay Frame

The five story two bay frame shown in Figure 6.11 is formed by adding two stories and a bay to the three story one bay frame considered in the previous design example. The primary purpose of this example is to show the proposed energy-based seismic design method can be applied to the design of frames with more than one bay. Similar to the previous example, the roof beams for this frame were subjected to uniform dead and live loads of 2.5 k/ft and 1.75 k/ft, and the beams at other floor levels were subjected to uniform dead and live loads of 3.0 k/ft and 2.25 k/ft,

respectively. The sources of the seismic mass were considered to be the applied loads and the weight of the frame itself. 100% of the dead load and 25% of the live load were assumed to contribute to the seismic mass. Floor level diaphragm constraints were also employed to force the joints at a given floor to have equal horizontal displacement.
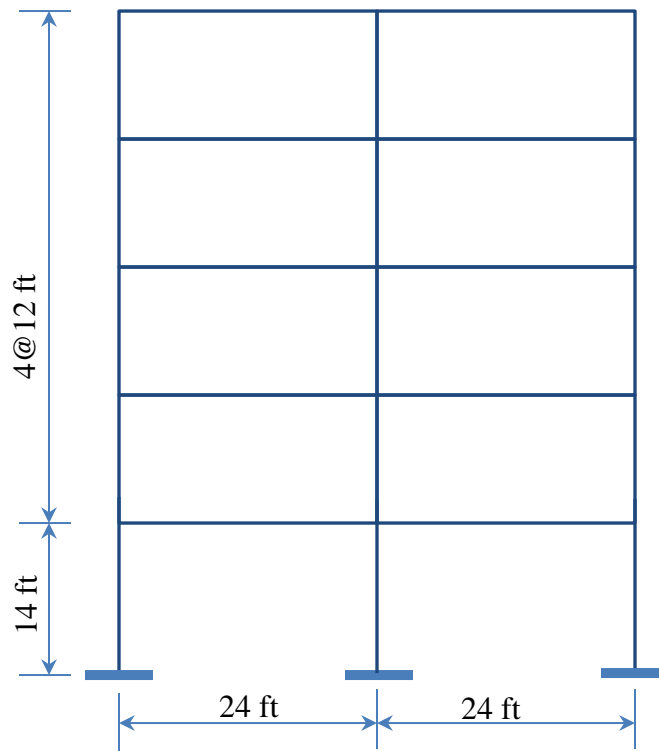
Figure 6.11 Design example: five story-two bay frame

The iterative design procedure for this five story frame is similar to the procedure followed in the design of the three story frame outlined in the preceding section. Thus, for brevity, only the important details and the final results of each step will be presented.

Iteration 1

S*tep 1: Preliminary Member Sizes*

The preliminary member sizes were determined by designing the frame for gravity loads using

the AISC – LFRD design procedures built in the SAP 2000 structural analysis and design

software. The resulting member sizes are shown below.

Preliminary Column Sizes			Preliminary Beam Sizes	
Story	Internal	External	Floor Level	Size
1st	W14×90	W14×74	2nd (1st story)	W18×65
2nd	W14×90	W14×74	3rd	W18×65
3rd	W14×90	W14×74	4th	W18×65
4th	W14×74	W14×74	5th	W18×65
5th	W14×74	W14×74	Roof (5th story)	W18×65

Step 2: Modal Properties

Using these preliminary member sizes, modal properties for the first two modes that constitute

more than 90% of the total seismic mass were calculated and are shown below. Like the three

story frame example, a ductility level of 4 is considered for each mode in the design of the frame.

	Period (s)	Γ^2, kip·s^2·in.$^{-1}$	$\Sigma \Gamma_i^2 / M$	Ductility, μ
Mode 1	1.59	1.596	0.86	4
Mode 2	0.51	0.222	0.097	4
		$\Sigma \Gamma_i^2 / M=$	95.7%	

 where M = total seismic mass

Step 3: Normalized Input Energy per Unit Mass (NE)

	μ	s	b	T_1	C	T_2	k	n	T	NE
Mode 1	4	1.312	-0.0021	0.318	0.411	1.57	0.572	-0.720	1.59	0.41
Mode 2	4	1.312	-0.0021	0.318	0.411	1.57	0.572	-0.720	0.51	0.41

The input energy per unit mass (IE/m) design earthquakes with a *mean*$+\sigma$ *VI* value of 8.11×10^4 in.^{2}/s^2 (see design example 6.4.1 above) are then computed as follows.

$$\text{Mode 1: } IE/m = NE^2 \times VI = (0.41)^2 \times 8.11 \times 10^4 \text{ in.}^2/\text{s}^2 = 1.36 \times 10^4 \text{ in.}^2/\text{s}^2$$

$$\text{Mode 2: } IE/m = NE^2 \times VI = (0.41)^2 \times 8.11 \times 10^4 \text{ in.}^2/\text{s}^2 = 1.36 \times 10^4 \text{ in.}^2/\text{s}^2$$

Step 4: Hysteretic Energy per Unit Mass (HE/m)

	μ	C	T_2	s	b	T	HE/IE
Mode 1	4	0.651	2.674	-0.0247	0.717	1.59	0.651
Mode 2	4	0.651	2.674	-0.0247	0.717	0.51	0.651

$$\text{Mode 1: } HE/m = (IE/m) \times (HE/IE) = 1.36 \times 10^4 \text{ in.}^2/\text{s}^2 \times 0.651 = 0.888 \times 10^4 \text{ in.}^2/\text{s}^2$$

$$\text{Mode 2: } HE/m = (IE/m) \times (HE/IE) = 1.36 \times 10^4 \text{ in.}^2/\text{s}^2 \times 0.651 = 0.888 \times 10^4 \text{ in.}^2/\text{s}^2$$

Step 5: MDOF System Total Hysteretic Energy Demand and its Distribution

$$HE_{total} = (\Gamma^2 \times HE/m)_{mode\ 1} + (\Gamma^2 \times HE/m)_{mode\ 2}$$

$$HE_{total} = (1.965 \text{ k·s}^2\text{·in.}^{-1})(0.888 \times 10^4 \text{ in.}^2/\text{s}^2) + (0.222 \text{ k·s}^2\text{·in.}^{-1})(0.888 \times 10^4 \text{ in.}^2/\text{s}^2)$$

$$= 1.94 \times 10^4 \text{ kip-in.}$$

Story forces, displacements and drifts;

Story	Force (kips)	Displacement (in.)	Story Drift (in.)
Story 1	21	10.16	10.16
Story 2	43	17.82	7.66
Story 3	62	22.22	4.4
Story 4	75	24.44	2.22
Story 5	68	25.52	1.08

External work done at each story:

$$\textit{For Story } 1: \quad WE_1 = 2(\sum_{k=1}^{5} F_k)\Delta d_1 = 2\times(21+43+62+75+68)\times10.16 = 5466 \text{ kip}-\text{in.}$$

$$\textit{For Story } 2: \quad WE_2 = (\sum_{k=2}^{5} F_k)\Delta d_2 = (43+62+75+68)\times7.66 = 1990 \text{ kip}-\text{in.}$$

$$\textit{For Story } 3: \quad WE_3 = (\sum_{k=3}^{5} F_k)\Delta d_3 = (62+75+68)\times4.4 = 902 \text{ kip}-\text{in.}$$

$$\textit{For Story } 4: \quad WE_4 = (\sum_{k=4}^{5} F_k)\Delta d_4 = (75+68)\times2.02 = 317.5 \text{ kip}-\text{in.}$$

$$\textit{For Story } 5: \quad WE_3 = (\sum_{k=5}^{5} F_k)\Delta d_5 = 68*1.08 = 73.4 \text{ } \textit{kip in.}$$

Total external work done:

$$WE_{total} = (\sum_{i=1}^{5} F_i)d_1 + \sum_{i=1}^{5} F_i d_i$$
$$= (21+43+62+75+68)\times10.16 + (21\times10.56) + (43\times17.82)$$
$$+ (62\times22.22) + (75\times24.44) + (68\times25.52)$$
$$= 8659 \text{ kip}-\text{in.}$$

Hysteretic energy distribution:

$$\textit{Story } 1: \quad R = \frac{HE_1}{HE_{total}} = \frac{WE_1}{WE_{total}} = \frac{5466}{8659} = 0.631 \Rightarrow HE_1 = 0.631\times1.91\times10^4 \text{ kip-in.} = 12250 \text{ kip-in.}$$

$$\textit{Story } 2: \quad R = \frac{HE_2}{HE_{total}} = \frac{WE_1}{WE_{total}} = \frac{1900}{8659} = 0.22 \Rightarrow HE_2 = 0.22\times1.91\times10^4 \text{ kip-in.} = 4259 \text{ kip-in.}$$

$$\textit{Story } 3: \quad R = \frac{HE_3}{HE_{total}} = \frac{WE_1}{WE_{total}} = \frac{902}{8659} = 0.104 \Rightarrow HE_3 = 0.104\times1.91\times10^4 \text{ kip-in.} = 2022 \text{ kip-in.}$$

$$\textit{Story } 4: \quad R = \frac{HE_4}{HE_{total}} = \frac{WE_1}{WE_{total}} = \frac{317.5}{8659} = 0.037 \Rightarrow HE_4 = 0.037\times1.91\times10^4 \text{ kip-in.} = 712 \text{ kip-in.}$$

$$\textit{Story } 5: \quad R = \frac{HE_5}{HE_{total}} = \frac{WE_1}{WE_{total}} = \frac{73.4}{8659} = 0.008 \Rightarrow HE_5 = 0.008\times1.91\times10^4 \text{ kip-in.} = 165 \text{ kip-in.}$$

Step 6: Member Size Optimization

For multi-story multi-bay frames, the formulation of the story level optimization problem inevitably involves many variables (i.e., unknown plastic moments). Thus, it is important to group members that are expected to be subjected to similar magnitudes of force actions and assign them the same member sizes. In this design example, it is suggested that for a given story the external columns will have the same size. Likewise, beams in a given floor level are designed to have the same plastic moment capacity. For easy manipulation, the plastic moment capacity of the different member groups is designated as follows.

$M_{IC,k}$ = plastic moment capacity of an internal column in story k

$M_{EC,k}$ = plastic moment capacity of an external column in story k

$M_{B,k}$ = plastic moment capacity of a floor beam in story k

Optimization of Members in the Fifth Story

(a)

(b)
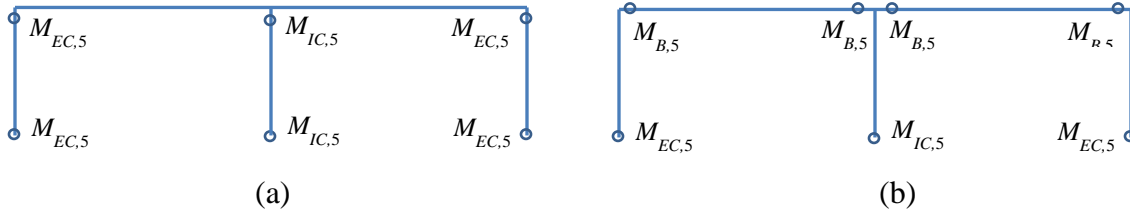
Constraint equation based on mechanism (a) – Strong beam and weak column

$$4 \times (4M_{EC,5} + 2M_{IC,5}) \times 0.03 \geq 165 \text{ kip-in.}$$

Constraint equation based on mechanism (b) – Strong column and weak beam

$$4 \times (2M_{EC,5} + M_{IC,5} + 4M_{B,5}) \times 0.03 \geq 165 \text{ kip-in.}$$

Additional constraint equations at joints – code requirement

$$M_{EC,5} - M_{B,5} \geq 0 \qquad \text{at an exterior joint}$$

$$M_{IC,5} - 2M_{B,5} \geq 0 \qquad \text{at an interior joint}$$

211

Objective Function - Weight, W

$$W = 288M_{EC,5} + 144M_{IC,5} + 576M_{B,5}$$

Mathematical formulation of the minimization problem

$$Minimize:$$

$$W = 288M_{EC,5} + 144M_{IC,5} + 288M_{B,5}$$

$$Subjected\ to:$$

$$0.48M_{EC,5} + 0.24M_{IC,5} \geq 165\,\text{kip-in.}$$

$$0.24M_{EC,5} + 0.12M_{IC,5} + 0.48M_{B,5} \geq 165\,\text{kip-in.}$$

$$M_{EC,5} - M_{B,5} \geq 0$$

$$M_{IC,5} - 2M_{B,5} \geq 0$$

$$where \quad M_{EC,5} > 0, M_{IC,5} > 0, M_{B,5} > 0$$

The optimized solution obtained using the Simplex linear solver built in Microsoft Excel is

$$M_{EC,5} = 172 \text{ kip-in.}, M_{IC,5} = 344 \text{ kip-in., and } M_{B,5} = 172 \text{ kip-in.}$$

Optimization of Members in the Fourth Story

(c)   (d)
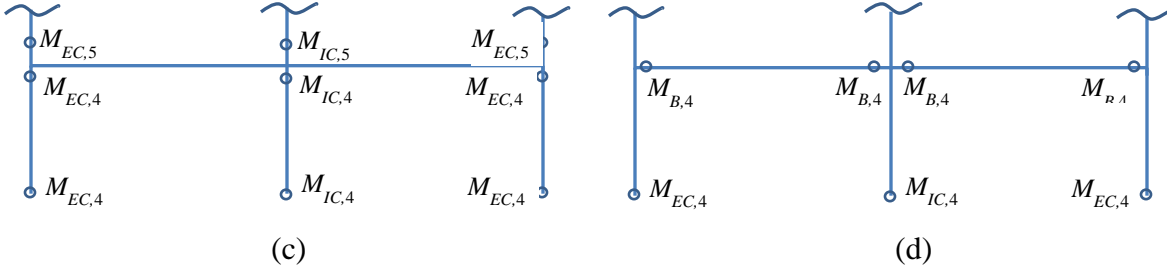
Constraint equation based on mechanism (c) – Strong beam and weak column

$$4 \times (4M_{EC,4} + 2M_{IC,4}) \times 0.03 - 4 \times (2 \times M_{EC,5} + M_{IC,5}) \times 0.03 \geq 712\,\text{kip-in.}$$

Constraint equation based on mechanism (d) – Strong column and weak beam

$$4 \times (2M_{EC,4} + M_{IC,4} + 4M_{B,4}) \times 0.03 \geq 712\,\text{kip-in.}$$

Additional constraint equations at joints – code requirement

$$M_{EC,4} + M_{EC,5} - M_{B,4} \geq 0 \qquad \text{at an exterior joint}$$

$$M_{IC,4} + M_{IC,5} - 2M_{B,4} \geq 0 \qquad \text{at an interior joint}$$

Objective Function - Weight, W

$$W = 288M_{EC,4} + 144M_{IC,4} + 576M_{B,4}$$

Mathematical formulation of the minimization problem

Minimize :
$$W = 288M_{EC,4} + 144M_{IC,4} + 576M_{B,4}$$

Subjected to :
$$0.48M_{EC,4} + 0.24M_{IC,4} \geq 794.6 \text{ kip-in.}$$
$$0.24M_{EC,4} + 0.12M_{IC,4} + 0.48M_{B,4} \geq 712 \text{ kip-in.}$$
$$M_{EC,4} - M_{B,4} \geq -172 \text{ kip-in.}$$
$$M_{IC,4} - 2M_{B,4} \geq -344 \text{ kip-in.}$$

where $\quad M_{EC,4} > 0, M_{IC,4} > 0, M_{B,4} > 0$

The optimized solution obtained using the Simplex linear solver built in Microsoft Excel is

$M_{EC,4}$ = 2967 kip-in., $M_{IC,4}$ = 0 kip-in., and $M_{B,4}$ = 0 kip-in.

Obviously, the above solution for $M_{EC,4}$, $M_{IC,4}$ and $M_{B,4}$ is unrealistic. Like the case of the three

story design example additional constraint equations are needed to tweak the optimization

problem to give a realistic solution. In this study, the additional constraint equations that will be

used are that the beam capacity to be at least greater than 60% and 40% of the external and

internal column moment capacities, respectively. In addition, the external columns are required

to have at least 60% of the internal moment capacities. Employing such constraints to the above

optimization problem gives a modified solution as follows.

$M_{EC,4}$ = 903 kip-in., $M_{IC,4}$ = 1505 kip-in., and $M_{B,4}$ = 656 kip-in.

Optimization of Members in the Third Story

(e)   (f)
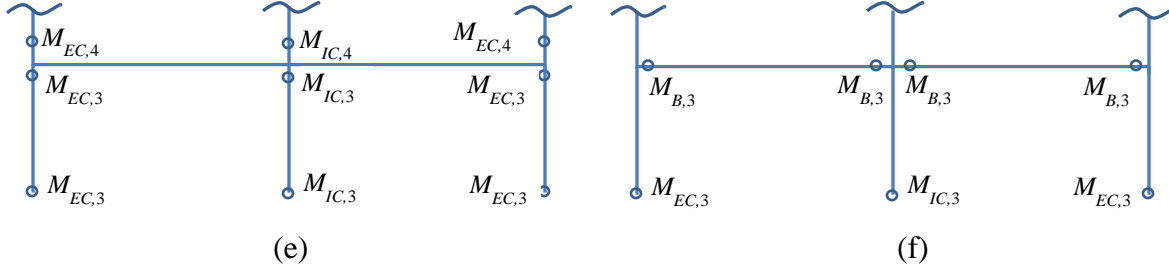
Constraint equation based on mechanism (e) – Strong beam and weak column

$$4 \times (4M_{EC,3} + 2M_{IC,3}) \times 0.03 - 4 \times (2 \times M_{EC,4} + M_{IC,4}) \times 0.03 \geq 2022 \, \text{kip-in.}$$

Constraint equation based on mechanism (f) – Strong column and weak beam

$$4 \times (2M_{EC,3} + M_{IC,3} + 4M_{B,3}) \times 0.03 \geq 2022 \, \text{kip-in.}$$

Additional constraint equation at joints – code requirement

$$M_{EC,3} + M_{EC,4} - M_{B,3} \geq 0 \qquad \text{at exterior joint}$$

$$M_{IC,3} + M_{IC,4} - 2M_{B,3} \geq 0 \qquad \text{at interior joint}$$

Objective Function - Weight, W

$$W = 288M_{EC,3} + 144M_{IC,3} + 576M_{B,3}$$

Mathematical formulation of the minimization problem

$$Minimize:$$
$$W = 288M_{EC,3} + 144M_{IC,3} + 576M_{B,3}$$
$$Subjected\ to:$$
$$0.48M_{EC,3} + 0.24M_{IC,3} \geq 2419 \, \text{kip-in.}$$
$$0.24M_{EC,3} + 0.12M_{IC,3} + 0.48M_{B,3} \geq 2022 \, \text{kip-in.}$$
$$M_{EC,3} - M_{B,3} \geq -903 \, \text{kip-in.}$$
$$M_{IC,3} - 2M_{B,3} \geq -1505 \, \text{kip-in.}$$
$$where \qquad M_{EC,3} > 0, M_{IC,3} > 0, M_{B,3} > 0$$

The optimized solution obtained using the Simplex linear solver built in Microsoft Excel is

$$M_{EC,3} = 2925 \text{ kip-in.}, M_{IC,3} = 4231 \text{ kip-in., and } M_{B,3} = 1693 \text{ kip-in.}$$

Optimization of Members in the Second Story

(g)   (h)
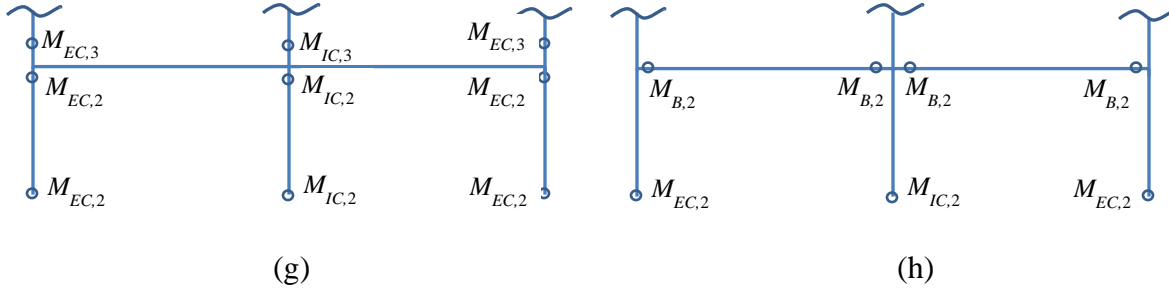
Constraint equation based on mechanism (g) – Strong beam and weak column

$$4 \times (4M_{EC,2} + 2M_{IC,2}) \times 0.03 - 4 \times (2 \times M_{EC,3} + M_{IC,3}) \times 0.03 \geq 4259 \text{ kip-in.}$$

Constraint equation based on mechanism (h) – Strong column and weak beam

$$4 \times (2M_{EC,2} + M_{IC,2} + 4M_{B,2}) \times 0.03 \geq 4259 \text{ kip-in.}$$

Additional constraint equations at joints – code requirement

$$M_{EC,2} + M_{EC,3} - M_{B,2} \geq 0 \qquad \text{at an exterior joint}$$

$$M_{IC,2} + M_{IC,3} - 2M_{B,2} \geq 0 \qquad \text{at an interior joint}$$

Objective Function - Weight, W

$$W = 288M_{EC,2} + 144M_{IC,2} + 576M_{B,2}$$

Mathematical formulation of the minimization problem

Minimize :
$$W = 288M_{EC,2} + 144M_{IC,2} + 576M_{B,2}$$

Subjected to :
$$0.48M_{EC,2} + 0.24M_{IC,2} \geq 5469 \text{ kip-in.}$$
$$0.24M_{EC,2} + 0.12M_{IC,2} + 0.48M_{B,2} \geq 4259 \text{ kip-in.}$$
$$M_{EC,2} - M_{B,2} \geq -2925 \text{ kip-in.}$$
$$M_{IC,2} - 2M_{B,2} \geq -4231 \text{ kip-in.}$$

where $\quad M_{EC,2} > 0, M_{IC,2} > 0, M_{B,2} > 0$

The optimized solution obtained using the Simplex linear solver built in Microsoft Excel is

$$M_{EC,2} = 7423 \text{ kip-in.}, \ M_{IC,2} = 7941 \text{ kip-in., and } M_{B,2} = 3176 \text{ kip-in.}$$

215

Optimization of Members in the First Story

(i)   (j)
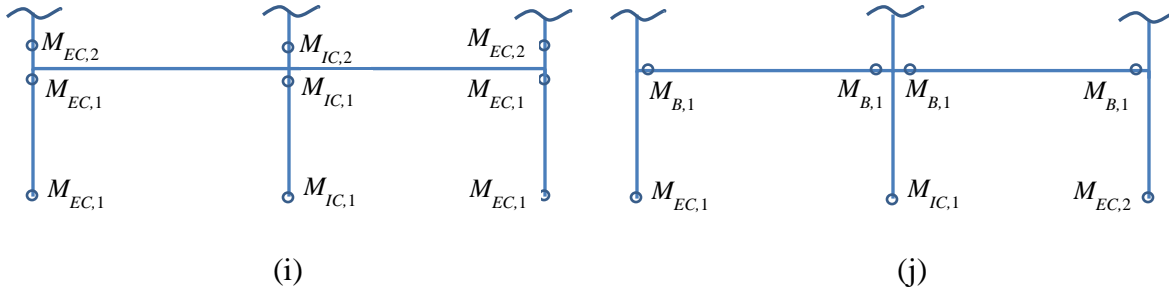
Constraint equation based on mechanism (i) – Strong beam and weak column

$$4 \times (4M_{EC,1} + 2M_{IC,1}) \times 0.03 - 4 \times (2 \times 7423 + 7941) \times 0.03 \geq 12250 \,\text{kip-in.}$$

Constraint equation based on mechanism (j) – Strong column and weak beam

$$4 \times (2M_{EC,1} + M_{IC,1} + 4M_{B,1}) \times 0.03 \geq 12250 \,\text{kip-in.}$$

Additional constraint equations at joints – code requirement

$$M_{EC,1} + 2942 - M_{B,1} \geq 0 \qquad \text{at an exterior joint}$$

$$M_{IC,1} + 9306 - 2M_{B,1} \geq 0 \qquad \text{at an interior joint}$$

Objective Function - Weight, W

$$W = 336M_{EC,1} + 168M_{IC,1} + 576M_{B,1}$$

Mathematical formulation of the minimization problem

Minimize :
$$W = 336M_{EC,1} + 168M_{IC,1} + 576M_{B,1}$$

Subjected to :
$$0.48M_{EC,1} + 0.24M_{IC,1} \geq 14100 \,\text{kip-in.}$$
$$0.24M_{EC,1} + 0.12M_{IC,1} + 0.48M_{B,1} \geq 12250 \,\text{kip-in.}$$
$$M_{EC,1} - M_{B,1} \geq -7423 \,\text{kip-in.}$$
$$M_{IC,1} - 2M_{B,1} \geq -7941 \,\text{kip-in.}$$

where $\quad M_{EC,1} > 0, M_{IC,1} > 0, M_{B,1} > 0$

The optimized solution obtained using the Simplex linear solver built in Microsoft Excel is

$$M_{EC,1} = 16020 \text{ kip-in.}, \; M_{IC,1} = 26700 \text{ kip-in., and } M_{B,1} = 10840 \text{ kip-in.}$$

Step 7: Effect of Axial Forces on Plastic Capacity Demands

Story		Column size	Axial Force (kips)		β_m	Plastic Moment (kip-in)	
			Capacity	Applied		Required	Modified
1	Internal	W14×90	969	440	1.628	26700	43470
	External	W14×74	663	208	1.295	16200	20980
2	Internal	W14×90	1008	348	1.358	7941	10780
	External	W14×74	724	166	1.153	7423	8561
3	Internal	W14×90	1008	257	1.193	4231	5048
	External	W14×74	724	123	1.093	2925	3197
4	Internal	W14×74	724	167	1.155	1505	1739
	External	W14×74	724	79	1.058	903	955
5	Internal	W14×74	724	77	1.056	344	363
	External	W14×74	724	35	1.025	172	176

Step 8: Plastic Moment Capacity versus Demand Comparison

When selecting new member sizes for columns, it is important to avoid the possibility of weak or extremely strong story with respect to the story immediately above it. The reason is very simple; weak story conditions are not allowed in frame design. On the other hand, extremely strong story could force most of the yielding to occur in the upper weaker stories where the hysteretic energy demand becomes larger. Unless the selection is done arbitrarily, the effect can be clearly seen in a subsequent iteration where the demand for members with large plastic moment capacity becomes smaller.

	Story	Current size	Plastic Moment (kip-in.)		Member Size	
			Capacity	Demand	Decision	New
Columns	1 Internal	W14×90	7850	43470	Change	W33×169
	1 External	W14×74	6300	20980	Change	W14×109
	2 Internal	W14×90	7850	10780	Change	W14×109
	2 External	W14×74	6300	8561	Change	W14×109
	3 Internal	W14×90	7850	5048	Change	W14×90
	3 External	W14×74	6300	3197	Keep	W14×74
	4 Internal	W14×74	6300	1739	Keep	W14×74
	4 External	W14×74	6300	955	Keep	W14×74
	5 Internal	W14×74	6300	363	Keep	W14×74
	5 External	W14×74	6300	176	Keep	W14×74
Beams	1	W18×65	6650	10840	Change	W18×97
	2	W18×65	6650	3176	Keep	W18×65
	3	W18×65	6650	1693	Keep	W18×65
	4	W18×65	6650	656	Keep	W18×65
	5 (Roof)	W18×65	6650	172	Keep	W18×65

Iteration 2

Step 1: Member Sizes at end of Iteration 1

Column Sizes @ end of Iteration 1		
Story	Internal	External
1st	W33×169	W14×109
2nd	W14×109	W14×109
3rd	W14×90	W14×74
4th	W14×74	W14×74
5th	W14×74	W14×74

Beam Sizes @ end of Iteration 1	
Floor Level	Size
2nd (1st story)	W18×97
3rd	W18×65
4th	W18×65
5th	W18×65
Roof (5th story)	W18×65

Step 2: Modal Properties

	Period (s)	Γ^2, kip·s^2·in.$^{-1}$	$\Sigma\,\Gamma_i^2/\,M$	Ductility, μ
Mode 1	1.34	1.758	0.759	4
Mode 2	0.44	0.293	0.126	4
Mode 3	0.25	0.135	0.058	4
		$\Sigma\,\Gamma_i^2/\,M=$	94.3%	

Step 3: Normalized Input Energy per Unit Mass (NE)

	μ	s	b	T_1	C	$T2$	k	n	T	NE
Mode 1	4	1.3122	-0.0021	0.318	0.411	1.57	0.572	-0.720	1.34	0.41
Mode 2	4	1.3122	-0.0021	0.318	0.411	1.57	0.572	-0.720	0.44	0.41
Mode 3	4	1.3122	-0.0021	0.318	0.411	1.57	0.572	-0.720	0.25	0.33

Modal input energy per unit mass (*IE/m*):

$$\text{Mode 1: } IE/m = NE^2 \times VI = (0.41)^2 \times 8.11 \times 10^4 \text{ in.}^2/\text{s}^2 = 1.36 \times 10^4 \text{ in.}^2/\text{s}^2$$

$$\text{Mode 2: } IE/m = NE^2 \times VI = (0.41)^2 \times 8.11 \times 10^4 \text{ in.}^2/\text{s}^2 = 1.36 \times 10^4 \text{ in}^2/\text{s}^2$$

$$\text{Mode 3: } IE/m = NE^2 \times VI = (0.33)^2 \times 8.11 \times 10^4 \text{ in.}^2/\text{s}^2 = 0.883 \times 10^4 \text{ in}^2/\text{s}^2$$

Step 4: Hysteretic Energy per Unit Mass (HE/m):

	μ	C	T_2	s	b	T	EH/EI
Mode 1	4	0.651	2.674	-0.0247	0.717	1.34	0.651
Mode2	4	0.651	2.674	-0.0247	0.717	0.44	0.651
Mode3	4	0.651	2.674	-0.0247	0.717	0.25	0.651

$$\text{Mode 1 : } HE/m = (IE/m) \times (HE/IE) = 1.36 \times 10^4 \text{ in.}^2/\text{s}^2 \times 0.651 = 0.888 \times 10^4 \text{ in.}^2/\text{s}^2$$

$$\text{Mode 2 : } HE/m = (IE/m) \times (HE/IE) = 1.36 \times 10^4 \text{ in.}^2/\text{s}^2 \times 0.651 = 0.888 \times 10^4 \text{ in.}^2/\text{s}^2$$

$$\text{Mode 3: } HE/m = (IE/m) \times (HE/IE) = 0.883 \times 10^4 \text{ in.}^2/\text{s}^2 \times 0.651 = 0.575 \times 10^4 \text{ in.}^2/\text{s}^2$$

Step 5: MDOF System Total Hysteretic Energy Demand and its Distribution

$$HE_{total} = (\Gamma^2 \times HE/m)_{mode\ 1} + (\Gamma^2 \times HE/m)_{mode\ 2} + (\Gamma^2 \times HE/m)_{mode\ 3}$$

$$HE_{total} = (1.758\ \text{kip·s}^2\text{·in.}^{-1})\,(0.888\times10^4\ \text{in.}^2/\text{s}^2) + (0.293\ \text{kip·s}^2\text{·in}^{-1})\,(0.888\times10^4\ \text{in.}^2/\text{s}^2)$$

$$+ (0.135\ \text{kip·s}^2\text{·in}^{-1})\,(0.575\times10^4\ \text{in}^2/\text{s}^2)$$

$$= 1.85\times10^4\ \text{kip-in.}$$

Story forces, displacements, and hysteretic energies:

Story	Force (kips)	Displacement (in.)	Story Drift (in.)	External Work Done (kip-in.)	Hysteretic Energy (kip-in.)
Story 1	21	1.82	1.82	1292	2716
Story 2	43	10.73	8.91	3029	6368
Story 3	62	20.6	9.87	2902	6100
Story 4	75	27.19	6.59	1404	2951
Story 5	68	28.88	1.69	174	366

Step 6: Member Size Optimization

Optimization of Members in the Fifth Story

Objective Function - Weight, W

$$W = 288M_{EC,5} + 144M_{IC,5} + 576M_{B,5}$$

Mathematical formulation of the minimization problem

Minimize :
$$W = 288M_{EC,5} + 144M_{IC,5} + 288M_{B,5}$$

Subjected to :
$$0.48M_{EC,5} + 0.24M_{IC,5} \geq 366\,\text{kip-in.}$$
$$0.24M_{EC,5} + 0.12M_{IC,5} + 0.48M_{B,5} \geq 366\,\text{kip-in.}$$
$$M_{EC,5} - M_{B,5} \geq 0$$
$$M_{IC,5} - 2M_{B,5} \geq 0$$

where $\quad M_{EC,5} > 0, M_{IC,5} > 0, M_{B,5} > 0$

The optimized solution obtained using the Simplex linear solver built in Microsoft Excel is

$$M_{EC,5} = 436\ \text{kip-in.},\ M_{IC,5} = 726\ \text{kip-in.,\ and}\ M_{B,5} = 363\ \text{kip-in.}$$

Optimization of Members in the Fourth Story

Objective Function - Weight, W

$$W = 288M_{EC,4} + 144M_{IC,4} + 576M_{B,4}$$

Mathematical formulation of the minimization problem

Minimize :

$$W = 288M_{EC,4} + 144M_{IC,4} + 576M_{B,4}$$

Subjected to :

$$0.48M_{EC,4} + 0.24M_{IC,4} \geq 3142.8\,\text{kip-in.}$$

$$0.24M_{EC,4} + 0.12M_{IC,4} + 0.48M_{B,4} \geq 2951\,\text{kip-in.}$$

$$M_{EC,4} - M_{B,4} \geq -436\,\text{kip-in.}$$

$$M_{IC,4} - 2M_{B,4} \geq -726\,\text{kip-in.}$$

where $\quad M_{EC,4} > 0, M_{IC,4} > 0, M_{B,4} > 0$

The optimized solution obtained using the Simplex linear solver built in Microsoft Excel is

$M_{EC,4} = 3883$ kip-in., $M_{IC,4} = 6472$ kip-in., and $M_{B,4} = 2589$ kip-in.

Optimization of Members in the Third Story

Objective Function - Weight, W

$$W = 288M_{EC,3} + 144M_{IC,3} + 576M_{B,3}$$

Mathematical formulation of the minimization problem

Minimize :

$$W = 288M_{EC,3} + 144M_{IC,3} + 576M_{B,3}$$

Subjected to :

$$0.48M_{EC,3} + 0.24M_{IC,3} \geq 7808.6\,\text{kip-in.}$$

$$0.24M_{EC,3} + 0.12M_{IC,3} + 0.48M_{B,3} \geq 6100\,\text{kip-in.}$$

$$M_{EC,3} - M_{B,3} \geq -3883\,\text{kip-in.}$$

$$M_{IC,3} - 2M_{B,3} \geq -6472\,\text{kip-in.}$$

where $\quad M_{EC,3} > 0, M_{IC,3} > 0, M_{B,3} > 0$

The optimized solution obtained using the Simplex linear solver built in Microsoft Excel is

$M_{EC,3} = 8873$ kip-in., $M_{IC,3} = 14790$ kip-in., and $M_{B,3} = 5916$ kip-in.

Optimization of Members in the Second Story

Objective Function - Weight, W

$$W = 288M_{EC,2} + 144M_{IC,2} + 576M_{B,2}$$

Mathematical formulation of the minimization problem

$\quad$ *Minimize* :

$$W = 288M_{EC,2} + 144M_{IC,2} + 576M_{B,2}$$

$\quad$ *Subjected to* :

$$0.48M_{EC,2} + 0.24M_{IC,2} \geq 10270\,\text{kip-in.}$$
$$0.24M_{EC,2} + 0.12M_{IC,2} + 0.48M_{B,2} \geq 6368\,\text{kip-in.}$$
$$M_{EC,2} - M_{B,2} \geq -8873\,\text{kip-in.}$$
$$M_{IC,2} - 2M_{B,2} \geq -14790\,\text{kip-in.}$$

$\quad$ *where* $\quad M_{EC,2} > 0, M_{IC,2} > 0, M_{B,2} > 0$

The optimized solution obtained using the Simplex linear solver built in Microsoft Excel is

$$M_{EC,2} = 11670 \text{ kip-in.}, \ M_{IC,2} = 19460 \text{ kip-in.}, \text{ and } M_{B,2} = 7782 \text{ kip-in.}$$

Optimization of Members in the First Story

Objective Function - Weight, W

$$W = 336M_{EC,1} + 168M_{IC,1} + 576M_{B,1}$$

Mathematical formulation of the minimization problem

$\quad$ *Minimize* :

$$W = 336M_{EC,1} + 168M_{IC,1} + 576M_{B,1}$$

$\quad$ *Subjected to* :

$$0.48M_{EC,1} + 0.24M_{IC,1} \geq 7852\,\text{kip-in.}$$
$$0.24M_{EC,1} + 0.12M_{IC,1} + 0.48M_{B,1} \geq 2716\,\text{kip-in.}$$
$$M_{EC,1} - M_{B,1} \geq -11670\,\text{kip-in.}$$
$$M_{IC,1} - 2M_{B,1} \geq -19460\,\text{kip-in.}$$

$\quad$ *where* $\quad M_{EC,1} > 0, M_{IC,1} > 0, M_{B,1} > 0$

The optimized solution obtained using the Simplex linear solver built in Microsoft Excel is

$$M_{EC,1} = 8923 \text{ kip-in.}, \ M_{IC,1} = 14871 \text{ kip-in.}, \text{ and } M_{B,1} = 5948 \text{ kip-in.}$$

Step 7 : Effect of Axial Forces on Plastic Capacity

Story		Column size	Axial Force (kips)		β_m	Plastic Moment (kip-in.)	
			Capacity	Applied		Required	Modified
1	Internal	W33×169	1514	445	1.259	14870	18720
	External	W14×109	1173	208	1.097	8923	9791
2	Internal	W14×109	1220	350	1.246	19460	24250
	External	W14×109	1220	165	1.073	11670	12520
3	Internal	W14×90	1008	259	1.196	14790	17690
	External	W14×74	724	121	1.091	8873	9682
4	Internal	W14×74	724	168	1.157	6472	7491
	External	W14×74	724	78	1.057	3883	4104
5	Internal	W14×74	724	78	1.057	726	767
	External	W14×74	724	35	1.025	436	447

Step 8: Plastic Moment Capacity versus Demand Comparison

	Story		Current size	Plastic Moment (kip-in.)		Member Size	
				Capacity	Required	Decision	New
Columns	1	Internal	W33×169	31450	18720	Change***	W14×176
		External	W14×109	9600	9791	Change	W14×132
	2	Internal	W14×109	9600	24250	Change	W14×176
		External	W14×109	9600	12520	Change	W14×132
	3	Internal	W14×90	7850	17690	Change	W14×176
		External	W14×74	6300	9682	Change	W14×120
	4	Internal	W14×74	6300	7491	Change	W14×109
		External	W14×74	6300	4104	Keep	W14×74
	5	Internal	W14×74	6300	767	Keep	W14×74
		External	W14×74	6300	447	Keep	W14×74
Beams	1		W18×97	10550	5948	Change***	W18×71
	2		W18×65	6650	7782	Change	W18×71
	3		W18×65	6650	5916	Change	W18×71
	4		W18×65	6650	2589	Change **	W18×71
	5 (Roof)		W18×65	6650	363	Keep	W18×65

*** Demand is too small compared to the capacity of the member

** Change is required as a result of design for gravity loads

Iteration 3

Step 1: Member Sizes at end of Iteration 2

Column Sizes @ end of Iteration 2			Beam Sizes @ end of Iteration 2	
Story	Internal	External	Floor Level	Size
1st	W14×176	W14×132	2nd (1st story)	W18×71
2nd	W14×176	W14×132	3rd	W18×71
3rd	W14×176	W14×120	4th	W18×71
4th	W14×109	W14×74	5th	W18×71
5th	W14×74	W14×74	Roof (5th story)	W18×65

Step 2: Modal Properties

	Period (s)	Γ^2, kip·s^2·in.$^{-1}$	$\Sigma \Gamma_i^2 / M$	Ductility, μ
Mode 1	1.37	1.93	0.831	4
Mode 2	0.45	0.251	0.108	4
Mode 3	0.25	0.087	0.038	4
		$\Sigma \Gamma_i^2 / M =$	97.7%	

Step 3: Normalized Input Energy per Unit Mass (NE)

	μ	s	b	T_1	C	T_2	k	n	T	NE
Mode 1	4	1.312	-0.0021	0.318	0.411	1.57	0.572	-0.720	1.37	0.41
Mode 2	4	1.312	-0.0021	0.318	0.411	1.57	0.572	-0.720	0.45	0.41
Mode 2	4	1.312	-0.0021	0.318	0.411	1.57	0.572	-0.720	0.25	0.33

Input energy per unit mass (*IE/m*):

$$\text{Mode 1: } IE/m = NE^2 \times VI = (0.41)^2 \times 0.811 \times 10^4 \text{ in.}^2/\text{s}^2 = 1.363 \times 10^4 \text{ in.}^2/\text{s}^2$$

$$\text{Mode 2: } IE/m = NE^2 \times VI = (0.41)^2 \times 0.811 \times 10^4 \text{ in.}^2/\text{s}^2 = 1.363 \times 10^4 \text{ in.}^2/\text{s}^2$$

$$\text{Mode 3: } IE/m = NE^2 \times VI = (0.33)^2 \times 0.811 \times 10^4 \text{ in.}^2/\text{s}^2 = 0.883 \times 10^4 \text{ in.}^2/\text{s}^2$$

Step 4: Hysteretic Energy per Unit Mass (HE/m)

	μ	C	T_2	s	b	T	EH/EI
Mode 1	4	0.651	2.674	-0.0247	0.717	1.34	0.651
Mode 2	4	0.651	2.674	-0.0247	0.717	0.44	0.651
Mode 3	4	0.651	2.674	-0.0247	0.717	0.25	0.651

Mode 1: $HE/m = (IE/m) \times (HE/IE) = 1.363 \times 10^4 \text{ in.}^2/\text{s}^2 \times 0.651 = 0.888 \times 10^4 \text{ in.}^2/\text{s}^2$

Mode 2: $HE/m = (IE/m) \times (HE/IE) = 1.363 \times 10^4 \text{ in.}^2/\text{s}^2 \times 0.651 = 0.888 \times 10^4 \text{ in.}^2/\text{s}^2$

Mode 3: $HE/m = (IE/m) \times (HE/IE) = 0.883 \times 10^4 \text{ in.}^2/\text{s}^2 \times 0.651 = 0.575 \times 10^4 \text{ in.}^2/\text{s}^2$

Step 5: MDOF System Total Hysteretic Energy Demand and its Distribution

$HE_{total} = (\Gamma^2 \times HE/m)_{mode\ 1} + (\Gamma^2 \times HE/m)_{mode\ 2} + (\Gamma^2 \times HE/m)_{mode\ 3}$

$HE_{total} = (1.93 \text{ kip·s}^2\text{·in}^{-1}) (0.888 \times 10^4 \text{ in.}^2/\text{s}^2) + (0.251 \text{ kip·s}^2\text{·in}^{-1}) (0.888 \times 10^4 \text{ in.}^2/\text{s}^2)$

$+ (0.087 \text{ kip. s}^2\text{.in}^{-1}) (0.575 \times 10^4 \text{ in.}^2/\text{s}^2) = 1.99 \times 10^4 \text{ kip-in.}$

Story forces, displacements, and hysteretic energies:

Story	Force (kips)	Displacement (in.)	Story Drift (in.)	External Work Done (kip-in.)	Hysteretic Energy (kip-in.)
Story 1	25.0	7.83	7.83	5669	9924
Story 2	55.0	15.62	7.79	2625	4596
Story 3	82.0	22.47	6.85	1932	3382
Story 4	104.0	27.3	4.83	966	1691
Story 5	96.0	28.88	1.58	152	266

Step 6: Member Size Optimization

Optimization of Members in the Fifth Story

Objective Function - Weight, W

$$W = 288M_{EC,5} + 144M_{IC,5} + 576M_{B,5}$$

Mathematical formulation of the minimization problem

      Minimize :

$$W = 288M_{EC,5} + 144M_{IC,5} + 288M_{B,5}$$

      Subjected to :

$$0.48M_{EC,5} + 0.24M_{IC,5} \geq 266\,\text{kip-in.}$$
$$0.24M_{EC,5} + 0.12M_{IC,5} + 0.48M_{B,5} \geq 266\,\text{kip-in.}$$
$$M_{EC,5} - M_{B,5} \geq 0$$
$$M_{IC,5} - 2M_{B,5} \geq 0$$

      where $M_{EC,5} > 0, M_{IC,5} > 0, M_{B,5} > 0$

The optimized solution obtained using the Simplex linear solver built in Microsoft Excel is

    $M_{EC,5} = 317$ kip-in., $M_{IC,5} = 528$ kip-in., and $M_{B,5} = 264$ kip-in.

Optimization of Members in the Fourth Story

Objective Function - Weight, W

$$W = 288M_{EC,4} + 144M_{IC,4} + 576M_{B,4}$$

Mathematical formulation of the minimization problem

      Minimize :

$$W = 288M_{EC,4} + 144M_{IC,4} + 576M_{B,4}$$

      Subjected to :

$$0.48M_{EC,4} + 0.24M_{IC,4} \geq 1830\,\text{kip-in.}$$
$$0.24M_{EC,4} + 0.12M_{IC,4} + 0.48M_{B,4} \geq 1691\,\text{kip-in.}$$
$$M_{EC,4} - M_{B,4} \geq -317\,\text{kip-in.}$$
$$M_{IC,4} - 2M_{B,4} \geq -528\,\text{kip-in.}$$

      where $M_{EC,4} > 0, M_{IC,4} > 0, M_{B,4} > 0$

The optimized solution obtained using the Simplex linear solver built in Microsoft Excel is;

    $M_{EC,4} = 2225$ kip-in., $M_{IC,4} = 3708$ kip-in., and $M_{B,4} = 1483$ kip-in.

Optimization of Members in the Third Story

Objective Function - Weight, W

$$W = 288M_{EC,3} + 144M_{IC,3} + 576M_{B,3}$$

Mathematical formulation of the minimization problem

Minimize :
$$W = 288M_{EC,3} + 144M_{IC,3} + 576M_{B,3}$$

Subjected to :
$$0.48M_{EC,3} + 0.24M_{IC,3} \geq 4361 \text{kip-in.}$$
$$0.24M_{EC,3} + 0.12M_{IC,3} + 0.48M_{B,3} \geq 3382 \text{kip-in.}$$
$$M_{EC,3} - M_{B,3} \geq -2225 \text{kip-in.}$$
$$M_{IC,3} - 2M_{B,3} \geq -3708 \text{kip-in.}$$
where $\quad M_{EC,3} > 0, M_{IC,3} > 0, M_{B,3} > 0$

The optimized solution obtained using the Simplex linear solver built in Microsoft Excel is

$M_{EC,3} = 4955$ kip-in., $M_{IC,3} = 8260$ kip-in., and $M_{B,3} = 3304$ kip-in.

Optimization of Members in the Second Story

Objective Function - Weight, W

$$W = 288M_{EC,2} + 144M_{IC,2} + 576M_{B,2}$$

Mathematical formulation of the minimization problem

Minimize :
$$W = 288M_{EC,2} + 144M_{IC,2} + 576M_{B,2}$$

Subjected to :
$$0.48M_{EC,2} + 0.24M_{IC,2} \geq 6676 \text{kip-in.}$$
$$0.24M_{EC,2} + 0.12M_{IC,2} + 0.48M_{B,2} \geq 4596 \text{kip-in.}$$
$$M_{EC,2} - M_{B,2} \geq -4955 \text{kip-in.}$$
$$M_{IC,2} - 2M_{B,2} \geq -8260 \text{kip-in.}$$
where $\quad M_{EC,2} > 0, M_{IC,2} > 0, M_{B,2} > 0$

The optimized solution obtained using the Simplex linear solver built in Microsoft Excel is

$M_{EC,2} = 7700$ kip-in., $M_{IC,2} = 12830$ kip-in., and $M_{B,2} = 5133$ kip-in.

Optimization of Members in the First Story

Objective Function - Weight, W

$$W = 336M_{EC,1} + 168M_{IC,1} + 576M_{B,1}$$

Mathematical formulation of the minimization problem

Minimize :

$$W = 336M_{EC,1} + 168M_{IC,1} + 576M_{B,1}$$

Subjected to :

$$0.48M_{EC,1} + 0.24M_{IC,1} \geq 13310 \text{ kip-in.}$$
$$0.24M_{EC,1} + 0.12M_{IC,1} + 0.48M_{B,1} \geq 9924 \text{ kip-in.}$$
$$M_{EC,1} - M_{B,1} \geq -7700 \text{ kip-in.}$$
$$M_{IC,1} - 2M_{B,1} \geq -12830 \text{ kip-in.}$$

where $\quad M_{EC,1} > 0, M_{IC,1} > 0, M_{B,1} > 0$

The optimized solution obtained using the Simplex linear solver built in Microsoft Excel is

$M_{EC,1}$ = 15130 kip-in., $M_{IC,1}$ = 25210 kip-in., and $M_{B,1}$ = 10080 kip-in.

Step 7 : Effect of Axial Forces on Plastic Capacity

Story		Column size	Axial Force (kips)		β_m	Plastic Moment (kip-in.)	
			Capacity	Applied		Required	Modified
1	Internal	W14×176	1938	446	1.155	25213	29111
	External	W14×132	1425	209	1.079	15128	16325
2	Internal	W14×176	2005	353	1.097	12834	14073
	External	W14×132	1481	165	1.059	7700	8154
3	Internal	W14×176	1938	262	1.072	8260	8859
	External	W14×120	1346	121	1.047	4955	5188
4	Internal	W14×109	1220	170	1.075	3708	3986
	External	W14×74	724	78	1.057	2225	2352
5	Internal	W14×74	724	78	1.057	528	558
	External	W14×74	724	35	1.025	317	325

Step 8: Plastic Moment Capacity versus Demand Comparison

			Current size	Plastic Moment (kip-in.)		Member Size	
	Story			Capacity	Required	Decision	New
Columns	1	Internal	W14×176	16000	29110	Change	W14×233
		External	W14×132	11700	16330	Change	W14×145
	2	Internal	W14×176	16000	14070	Keep	W14×176
		External	W14×132	11700	8154	Keep	W14×132
	3	Internal	W14×176	16000	8859	Change	W14×132
		External	W14×120	10600	5188	Keep	W14×120
	4	Internal	W14×109	9600	3986	Keep	W14×109
		External	W14×74	6300	2352	Keep	W14×74
	5	Internal	W14×74	6300	558	Keep	W14×74
		External	W14×74	6300	325	Keep	W14×74
Beams	1		W18×71	7300	10080	Change	W18×86
	2		W18×71	7300	5133	Change	W18×71
	3		W18×71	7300	3304	Change	W18×71
	4		W18×71	6650	1483	Keep	W18×71
	5 (Roof)		W18×65	6650	264	Keep	W18×65

Iteration 4

Step 1 Member Sizes at end of Iteration 3

Column Sizes @ end of Iteration 3		
Story	Internal	External
1st	W14×233	W14×145
2nd	W14×176	W14×132
3rd	W14×132	W14×120
4th	W14×109	W14×74
5th	W14×74	W14×74

Beam Sizes @ end of Iteration 3	
Floor Level	Size
2nd (1st story)	W18×86
3rd	W18×71
4th	W18×71
5th	W18×71
Roof (5th story)	W18×65

Step 2: Modal Properties

	Period (s)	Γ^2, kip·s²·in⁻¹	$\Sigma\,\Gamma_i^2/M$	Ductility, μ
Mode 1	1.32	1.879	0.808	4
Mode 2	0.44	0.278	0.12	4
Mode 3	0.25	0.103	0.044	4
		$\Sigma\,\Gamma_i^2/M =$	96.2%	

Step 3: Normalized Input Energy per Mass (NE)

	μ	s	b	T_1	C	T_2	k	n	T	NE
Mode 1	4	1.312	-0.0021	0.318	0.411	1.57	0.572	-0.720	1.32	0.41
Mode 2	4	1.312	-0.0021	0.318	0.411	1.57	0.572	-0.720	0.44	0.41
Mode 3	4	1.312	-0.0021	0.318	0.411	1.57	0.572	-0.720	0.25	0.33

Input energy per unit mass (*IE/m*):

$$\text{Mode 1: } IE/m = NE^2 \times VI = (0.41)^2 \times 8.11 \times 10^4 \text{ in.}^2/\text{s}^2 = 1.36 \times 10^4 \text{ in.}^2/\text{s}^2$$

$$\text{Mode 2: } IE/m = NE^2 \times VI = (0.41)^2 \times 8.11 \times 10^4 \text{ in.}^2/\text{s}^2 = 1.36 \times 10^4 \text{ in.}^2/\text{s}^2$$

$$\text{Mode 3: } IE/m = NE^2 \times VI = (0.33)^2 \times 8.11 \times 10^4 \text{ in.}^2/\text{s}^2 = 0.883 \times 10^4 \text{ in.}^2/\text{s}^2$$

Step 4: Hysteretic Energy per Unit mass (HE/m)

	μ	C	T_2	s	b	T	EH/EI
Mode 1	4	0.651	2.674	-0.0247	0.717	1.32	0.651
Mode 2	4	0.651	2.674	-0.0247	0.717	0.44	0.651
Mode 3	4	0.651	2.674	-0.0247	0.717	0.25	0.651

$$\text{Mode 1: } HE/m = (IE/m) \times (HE/IE) = 1.36 \times 10^4 \text{ in.}^2/\text{s}^2 \times 0.651 = 0.888 \times 10^4 \text{ in.}^2/\text{s}^2$$

$$\text{Mode 2: } HE/m = (IE/m) \times (HE/IE) = 1.36 \times 10^4 \text{ in.}^2/\text{s}^2 \times 0.651 = 0.888 \times 10^4 \text{ in.}^2/\text{s}^2$$

$$\text{Mode 3: } HE/m = (IE/m) \times (HE/IE) = 0.883 \times 10^4 \text{ in.}^2/\text{s}^2 \times 0.651 = 0.575 \times 10^4 \text{ in.}^2/\text{s}^2$$

Step 5: MDOF System Total Hysteretic Energy Demand and its Distribution

$HE_{total} = (\Gamma^2 \; x \; HE/m)_{mode \; 1} + (\Gamma^2 \; x \; HE/m)_{mode \; 2} + (\Gamma^2 \; x \; HE/m)_{mode \; 3}$

$HE_{total} = (1.879 \; \text{kip·s}^2\text{·in.}^{-1}) (0.888 \times 10^4 \; \text{in.}^2/\text{s}^2) + (0.279 \; \text{kip·s}^2\text{·in.}^{-1}) (0.888 \times 10^4 \; \text{in.}^2/\text{s}^2)$

$+ \; (0.103 \; \text{kip·s}^2\text{·in.}^{-1}) (0.575 \times 10^4 \; \text{in.}^2/\text{s}^2) = 1.97 \times 10^4 \; \text{kip-in.}$

Story forces, displacements, and hysteretic energies:

Story	Force (kips)	Displacement (in.)	Story Drift (in.)	External Work Done (kip-in.)	Hysteretic Energy (kip-in.)
Story 1	25.0	6.34	6.34	5009	8509
Story 2	57.0	13.8	7.46	5760	4689
Story 3	89.0	21.38	7.58	2373	4030
Story 4	116.0	27.17	5.79	1297	2203
Story 5	108.0	28.88	1.71	185	314

Step 6: Member Size Optimization

Optimization of Members in the Fifth Story

Objective Function - Weight, W

$$W = 288M_{EC,5} + 144M_{IC,5} + 576M_{B,5}$$

Mathematical formulation of the minimization problem

Minimize :

$$W = 288M_{EC,5} + 144M_{IC,5} + 288M_{B,5}$$

Subjected to :

$$0.48M_{EC,5} + 0.24M_{IC,5} \geq 314 \, \text{kip-in.}$$
$$0.24M_{EC,5} + 0.12M_{IC,5} + 0.48M_{B,5} \geq 314 \, \text{kip-in.}$$
$$M_{EC,5} - M_{B,5} \geq 0$$
$$M_{IC,5} - 2M_{B,5} \geq 0$$

where $\quad M_{EC,5} > 0, M_{IC,5} > 0, M_{B,5} > 0$

The optimized solution obtained using the Simplex linear solver built in Microsoft Excel is

$M_{EC,5} = 374$ kip-in., $M_{IC,5} = 623$ kip-in., and $M_{B,5} = 312$ kip-in.

Optimization of Members in the Fourth Story

Objective Function - Weight, *W*

$$W = 288M_{EC,4} + 144M_{IC,4} + 576M_{B,4}$$

Mathematical formulation of the minimization problem

Minimize :

$$W = 288M_{EC,4} + 144M_{IC,4} + 576M_{B,4}$$

Subjected to :

$$0.48M_{EC,4} + 0.24M_{IC,4} \geq 2367.5\,\text{kip-in.}$$
$$0.24M_{EC,4} + 0.12M_{IC,4} + 0.48M_{B,4} \geq 2203\,\text{kip-in.}$$
$$M_{EC,4} - M_{B,4} \geq -374\,\text{kip-in.}$$
$$M_{IC,4} - 2M_{B,4} \geq -623\,\text{kip-in.}$$

where $\quad M_{EC,4} > 0, M_{IC,4} > 0, M_{B,4} > 0$

The optimized solution obtained using the Simplex linear solver built in Microsoft Excel is

$M_{EC,4} = 2889$ kip-in., $M_{IC,4} = 4831$ kip-in., and $M_{B,4} = 1933$ kip-in.

Optimization of Members in the Third Story

Objective Function - Weight, *W*

$$W = 288M_{EC,3} + 144M_{IC,3} + 576M_{B,3}$$

Mathematical formulation of the minimization problem

Minimize :

$$W = 288M_{EC,3} + 144M_{IC,3} + 576M_{B,3}$$

Subjected to :

$$0.48M_{EC,3} + 0.24M_{IC,3} \geq 5305.5\,\text{kip-in.}$$
$$0.24M_{EC,3} + 0.12M_{IC,3} + 0.48M_{B,3} \geq 4030\,\text{kip-in.}$$
$$M_{EC,3} - M_{B,3} \geq -2899\,\text{kip-in.}$$
$$M_{IC,3} - 2M_{B,3} \geq -4831\,\text{kip-in.}$$

where $\quad M_{EC,3} > 0, M_{IC,3} > 0, M_{B,3} > 0$

The optimized solution obtained using the Simplex linear solver built in Microsoft Excel is

$M_{EC,3} = 6029$ kip-in., $M_{IC,3} = 10048$ kip-in., and $M_{B,3} = 4020$ kip-in.

Optimization of Members in the Second Story

Objective Function - Weight, W

$$W = 288M_{EC,2} + 144M_{IC,2} + 576M_{B,2}$$

Mathematical formulation of the minimization problem

$Minimize:$

$$W = 288M_{EC,2} + 144M_{IC,2} + 576M_{B,2}$$

$Subjected\ to:$

$$0.48M_{EC,2} + 0.24M_{IC,2} \geq 7342\,\text{kip-in.}$$
$$0.24M_{EC,2} + 0.12M_{IC,2} + 0.48M_{B,2} \geq 4689\,\text{kip-in.}$$
$$M_{EC,2} - M_{B,2} \geq -6029\,\text{kip-in.}$$
$$M_{IC,2} - 2M_{B,2} \geq -10050\,\text{kip-in.}$$

$where \qquad M_{EC,2} > 0, M_{IC,2} > 0, M_{B,2} > 0$

The optimized solution obtained using the Simplex linear solver built in Microsoft Excel is

$M_{EC,2} = 8342$ kip-in., $M_{IC,2} = 13905$ kip-in., and $M_{B,2} = 5562$ kip-in.

Optimization of Members in the First Story

Objective Function - Weight, W

$$W = 336M_{EC,1} + 168M_{IC,1} + 576M_{B,1}$$

Mathematical formulation of the minimization problem

$Minimize:$

$$W = 336M_{EC,1} + 168M_{IC,1} + 576M_{B,1}$$

$Subjected\ to:$

$$0.48M_{EC,1} + 0.24M_{IC,1} \geq 12180\,\text{kip-in.}$$
$$0.24M_{EC,1} + 0.12M_{IC,1} + 0.48M_{B,1} \geq 8509\,\text{kip-in.}$$
$$M_{EC,1} - M_{B,1} \geq -8342\,\text{kip-in.}$$
$$M_{IC,1} - 2M_{B,1} \geq -13905\,\text{kip-in.}$$

$where \qquad M_{EC,1} > 0, M_{IC,1} > 0, M_{B,1} > 0$

The optimized solution obtained using the Simplex linear solver built in Microsoft Excel is

$M_{EC,1} = 13840$ kip-in., $M_{IC,1} = 23070$ kip-in. and $M_{B,1} = 9227$ kip-in.

Step 7: Effect of Axial Forces on Plastic Capacity

	Story	Column size	Axial Force (kips)		β_m	Plastic Moment (kip-in.)	
			Capacity	Applied		Required	Modified
1	Internal	W14×233	2575	448	1.095	23070	25270
1	External	W14×145	1593	209	1.070	13840	14810
2	Internal	W14×176	2005	353	1.097	13905	15250
2	External	W14×132	1481	165	1.059	8342	8834
3	Internal	W14×132	1481	262	1.097	10050	11020
3	External	W14×120	1346	121	1.047	6029	6313
4	Internal	W14×109	1220	170	1.075	4831	5193
4	External	W14×74	724	78	1.057	2899	3064
5	Internal	W14×74	724	78	1.057	623	658
5	External	W14×74	724	35	1.025	374	383

Step 8: Plastic Moment Capacity versus Demand Comparison

		Story	Current size	Plastic Moment (kip-in)		Member Size	
				Capacity	Required	Decision	New
Columns	1	Internal	W14×233	21800	25270	Change	W14×257
Columns	1	External	W14×145	13000	14810	Change	W14×176
Columns	2	Internal	W14×176	16000	15250	Keep	W14×176
Columns	2	External	W14×132	11700	8834	Keep	W14×132
Columns	3	Internal	W14×132	11700	11020	Keep	W14×132
Columns	3	External	W14×120	10600	6313	Change	W14×109
Columns	4	Internal	W14×109	9600	5193	Keep	W14×109
Columns	4	External	W14×74	6300	3064	Keep	W14×74
Columns	5	Internal	W14×74	6300	658	Keep	W14×74
Columns	5	External	W14×74	6300	383	Keep	W14×74
Beams	1		W18×86	9300	9227	Keep	W18×86
Beams	2		W18×71	7300	5562	Keep	W18×71
Beams	3		W18×71	7300	4020	Keep	W18×71
Beams	4		W18×71	7300	1933	Keep	W18×71
Beams	5 (Roof)		W18×65	6650	312	Keep	W18×65

Iteration 5

Step 1: Member Sizes at end of Iteration 4

Column Sizes @ end of Iteration 4			Beam Sizes @ end of Iteration 4	
Story	Internal	External	Floor Level	Size
1st	W14×257	W14×176	2nd (1st story)	W18×86
2nd	W14×176	W14×132	3rd	W18×71
3rd	W14×132	W14×109	4th	W18×71
4th	W14×109	W14×74	5th	W18×71
5th	W14×74	W14×74	Roof (5th story)	W18×65

Step 2: Modal properties

	Period (s)	Γ^2, kip·s^2·in.$^{-1}$	$\Sigma \Gamma_i^2 / M$	Ductility, μ
Mode 1	1.30	1.855	0.797	4
Mode 2	0.43	0.283	0.121	4
Mode 3	0.24	0.11	0.047	4
		$\Sigma \Gamma_i^2 / M =$	96.5%	

Step 3: Normalized Input Energy per Unit Mass (NE)

	μ	s	b	T_1	C	T_2	k	n	T	NE
Mode 1	4	1.312	-0.0021	0.318	0.411	1.57	0.572	-0.720	1.32	0.41
Mode 2	4	1.312	-0.0021	0.318	0.411	1.57	0.572	-0.720	0.44	0.41
Mode 2	4	1.312	-0.0021	0.318	0.411	1.57	0.572	-0.720	0.24	0.31

Input energy per unit mass (*IE/m*):

$$\text{Mode 1: } IE/m = NE^2 \times VI = (0.41)^2 \times 8.11 \times 10^4 \text{ in.}^2/\text{s}^2 = 1.36 \times 10^4 \text{ in.}^2/\text{s}^2$$

$$\text{Mode 2: } IE/m = NE^2 \times VI = (0.41)^2 \times 8.11 \times 10^4 \text{ in.}^2/\text{s}^2 = 1.36 \times 10^4 \text{ in.}^2/\text{s}^2$$

$$\text{Mode 3: } IE/m = NE^2 \times VI = (0.31)^2 \times 8.11 \times 10^4 \text{ in.}^2/\text{s}^2 = .779 \times 10^4 \text{ in.}^2/\text{s}^2$$

Step 4: Hysteretic Energy per Unit mass (HE/m)

	μ	C	T_2	s	b	T	EH/EI
Mode 1	4	0.651	2.674	-0.0247	0.717	1.30	0.651
Mode 2	4	0.651	2.674	-0.0247	0.717	0.43	0.651
Mode 3	4	0.651	2.674	-0.0247	0.717	0.24	0.651

Mode 1: $HE/m = (IE/m)\times(HE/IE) = 1.36\times10^4 \text{ in.}^2/\text{s}^2\times0.651 = 0.888\times10^4 \text{ in.}^2/\text{s}^2$

Mode 2: $HE/m = (IE/m)\times(HE/IE) = 1.36\times10^4 \text{ in.}^2/\text{s}^2\times0.651 = 0.888\times10^4 \text{ in.}^2/\text{s}^2$

Mode 3: $HE/m = (IE/m)\times(HE/IE) = 0.779\times10^4 \text{ in.}^2/\text{s}^2\times0.651 = 0.507\times10^4 \text{ in.}^2/\text{s}^2$

Step 5: MDOF System Total Hysteretic Energy Demand and its Distribution

$HE_{total} = (\Gamma^2 \, x \, HE/m)_{mode\ 1} + (\Gamma^2 \, x \, HE/m)_{mode\ 2} + (\Gamma^2 \, x \, HE/m)_{mode\ 3}$

$HE_{total} = (1.855 \text{ kip·s}^2\text{·in.}^{-1}) (0.888\times10^4 \text{ in.}^2/\text{s}^2) + (0.283 \text{ kip·s}^2\text{·in.}^{-1}) (0.888\times10^4 \text{ in.}^2/\text{s}^2)$

$+ (0.11 \text{ kip·s}^2\text{·in.}^{-1}) (0.507\times10^4 \text{ in.}^2/\text{s}^2) = 19534 \text{ kip-in.}$

Story forces, displacements, and hysteretic energies:

Story	Force (kips)	Displacement (in.)	Story Drift (in.)	External Work Done (kip-in.)	Hysteretic Energy (kip-in.)
Story 1	24.0	5.33	5.33	4381	7400
Story 2	58.0	12.66	7.33	2837	4791
Story 3	93.0	20.63	7.97	2622	4429
Story 4	122.0	27.06	6.43	1518	2563
Story 5	114.0	28.88	1.82	207	350

Step 6: Member Size Optimization

Optimization of Members in the Fifth Story

Objective Function - Weight, W

$$W = 288M_{EC,5} + 144M_{IC,5} + 576M_{B,5}$$

Mathematical formulation of the minimization problem

$Minimize:$

$$W = 288M_{EC,5} + 144M_{IC,5} + 288M_{B,5}$$

$Subjected\ to:$

$$0.48M_{EC,5} + 0.24M_{IC,5} \geq 350\,\text{kip-in.}$$
$$0.24M_{EC,5} + 0.12M_{IC,5} + 0.48M_{B,5} \geq 350\,\text{kip-in.}$$
$$M_{EC,5} - M_{B,5} \geq 0$$
$$M_{IC,5} - 2M_{B,5} \geq 0$$

$where \quad M_{EC,5} > 0, M_{IC,5} > 0, M_{B,5} > 0$

The optimized solution obtained using the Simplex linear solver built in Microsoft Excel is

$M_{EC,5} = 417$ kip-in., $M_{IC,5} = 695$ kip-in., and $M_{B,5} = 348$ kip-in.

Optimization of Members in the Fourth Story

Objective Function - Weight, W

$$W = 288M_{EC,4} + 144M_{IC,4} + 576M_{B,4}$$

Mathematical formulation of the minimization problem

$Minimize:$

$$W = 288M_{EC,4} + 144M_{IC,4} + 576M_{B,4}$$

$Subjected\ to:$

$$0.48M_{EC,4} + 0.24M_{IC,4} \geq 2747\,\text{kip-in.}$$
$$0.24M_{EC,4} + 0.12M_{IC,4} + 0.48M_{B,4} \geq 2563\,\text{kip-in.}$$
$$M_{EC,4} - M_{B,4} \geq -417\,\text{kip-in.}$$
$$M_{IC,4} - 2M_{B,4} \geq -695\,\text{kip-in.}$$

$where \quad M_{EC,4} > 0, M_{IC,4} > 0, M_{B,4} > 0$

The optimized solution obtained using the Simplex linear solver built in Microsoft Excel is

$M_{EC,4} = 3373$ kip-in., $M_{IC,4} = 5621$ kip-in., and $M_{B,4} = 2249$ kip-in.

Optimization of Members in the Third Story

Objective Function - Weight, W

$$W = 288M_{EC,3} + 144M_{IC,3} + 576M_{B,3}$$

Mathematical formulation of the minimization problem

Minimize :

$$W = 288M_{EC,3} + 144M_{IC,3} + 576M_{B,3}$$

Subjected to :

$$0.48M_{EC,3} + 0.24M_{IC,3} \geq 5913 \text{ kip-in.}$$

$$0.24M_{EC,3} + 0.12M_{IC,3} + 0.48M_{B,3} \geq 4429 \text{ kip-in.}$$

$$M_{EC,3} - M_{B,3} \geq -3373 \text{ kip-in.}$$

$$M_{IC,3} - 2M_{B,3} \geq -5621 \text{ kip-in.}$$

where $\quad M_{EC,3} > 0, M_{IC,3} > 0, M_{B,3} > 0$

The optimized solution obtained using the Simplex linear solver built in Microsoft Excel is

$$M_{EC,3} = 6720 \text{ kip-in.}, M_{IC,3} = 11200 \text{ kip-in., and } M_{B,3} = 4480 \text{ kip-in.}$$

Optimization of Members in the Second Story

Objective Function - Weight, W

$$W = 288M_{EC,2} + 144M_{IC,2} + 576M_{B,2}$$

Mathematical formulation of the minimization problem

Minimize :

$$W = 288M_{EC,2} + 144M_{IC,2} + 576M_{B,2}$$

Subjected to :

$$0.48M_{EC,2} + 0.24M_{IC,2} \geq 7748 \text{ kip-in.}$$

$$0.24M_{EC,2} + 0.12M_{IC,2} + 0.48M_{B,2} \geq 4791 \text{ kip-in.}$$

$$M_{EC,2} - M_{B,2} \geq -6720 \text{ kip-in.}$$

$$M_{IC,2} - 2M_{B,2} \geq -11200 \text{ kip-in.}$$

where $\quad M_{EC,2} > 0, M_{IC,2} > 0, M_{B,2} > 0$

The optimized solution obtained using the Simplex linear solver built in Microsoft Excel is

$$M_{EC,2} = 8805 \text{ kip-in.}, M_{IC,2} = 14674 \text{ kip-in., and } M_{B,2} = 5870 \text{ kip-in.}$$

Optimization of Members in the First Story

Objective Function - Weight, *W*

$$W = 336M_{EC,1} + 168M_{IC,1} + 576M_{B,1}$$

Mathematical formulation of the minimization problem

$Minimize:$

$$W = 336M_{EC,1} + 168M_{IC,1} + 576M_{B,1}$$

$Subjected\ to:$

$$0.48M_{EC,1} + 0.24M_{IC,1} \geq 11270 \text{ kip-in.}$$
$$0.24M_{EC,1} + 0.12M_{IC,1} + 0.48M_{B,1} \geq 7400 \text{ kip-in.}$$
$$M_{EC,1} - M_{B,1} \geq -8805 \text{ kip-in.}$$
$$M_{IC,1} - 2M_{B,1} \geq -14670 \text{ kip-in.}$$

$where \qquad M_{EC,1} > 0, M_{IC,1} > 0, M_{B,1} > 0$

The optimized solution obtained using the Simplex linear solver built in Microsoft Excel is

$M_{EC,1} = 12810$ kip-in., $M_{IC,1} = 21350$ kip-in. and $M_{B,1} = 8541$ kip-in.

Step 7: Effect of Axial Forces on Plastic Capacity

Story		Column size	Axial Force (kips)		β_m	Plastic Moment (kip-in.)	
			Capacity	Applied		Required	Modified
1	Internal	W14×257	2847	448	1.085	21350	23180
	External	W14×176	1938	210	1.057	12810	13550
2	Internal	W14×176	2005	354	1.097	14670	16100
	External	W14×132	1481	165	1.059	8805	9324
3	Internal	W14×132	1481	262	1.097	11200	12290
	External	W14×109	1220	121	1.052	6720	7071
4	Internal	W14×109	1220	170	1.075	5621	6042
	External	W14×74	724	78	1.057	3373	3565
5	Internal	W14×74	724	78	1.057	695	735
	External	W14×74	724	35	1.025	417	427

Step 8: Plastic Moment Capacity versus Demand Comparison

	Story		Current size	Plastic Moment (kip-in.)		Member Size	
				Capacity	Required	Decision	New
Columns	1	Internal	W14×257	24350	23180	Keep	W14×257
		External	W14×176	16000	13550	Keep	W14×176
	2	Internal	W14×176	16000	16100	Keep	W14×176
		External	W14×132	11700	9324	Keep	W14×132
	3	Internal	W14×132	11700	12290	Change	W14×145
		External	W14×109	10600	7071	Keep	W14×109
	4	Internal	W14×109	9600	6042	Keep	W14×109
		External	W14×74	6300	3565	Keep	W14×74
	5	Internal	W14×74	6300	735	Keep	W14×74
		External	W14×74	6300	427	Keep	W14×74
Beams	1		W18×86	9300	8541	Keep	W18×86
	2		W18×71	7300	5870	keep	W18×71
	3		W18×71	7300	4480	keep	W18×71
	4		W18×71	7300	2249	Keep	W18×71
	5 (Roof)		W18×65	6650	348	Keep	W18×65

Iteration 6

Step 1: Member Sizes at end of Iteration 5

Column Sizes @ end of Iteration 5		
Story	Internal	External
1st	W14×257	W14x176
2nd	W14×176	W14x132
3rd	W14×145	W14x09
4th	W14×109	W14x74
5th	W14×74	W14x74

Beam Sizes @ end of Iteration 5	
Floor Level	Size
2nd (1st story)	W18×86
3rd	W18×71
4th	W18×71
5th	W18×71
Roof (5th story)	W18×65

Step 2: Modal Properties

	Period (s)	Γ^2, kip·s^2·in.$^{-1}$	$\Sigma\,\Gamma_i^2/\,M$	Ductility, μ
Mode 1	1.30	1.857	0.797	4
Mode 2	0.43	0.288	0.121	4
Mode 3	0.24	0.109	0.047	4
		$\Sigma\,\Gamma_i^2/\,M =$	96.5%	

Step 3: Normalized Input Energy per Unit Mass (NE)

	μ	s	b	T_1	C	T_2	k	n	T	NE
Mode 1	4	1.312	-0.0021	0.318	0.411	1.57	0.5724	-0.720	1.32	0.41
Mode 2	4	1.312	-0.0021	0.318	0.411	1.57	0.5724	-0.720	0.44	0.41
Mode 3	4	1.312	-0.0021	0.318	0.411	1.57	0.5724	-0.720	0.24	0.31

Input Energy per Unit Mass (IE/m):

$$\text{Mode1: } IE\,/m = NE^2 \times VI = (0.41)^2 \times 8.11 \times 10^4 \text{ in.}^2/\text{s}^2 = 1.36 \times 10^4 \text{ in.}^2/\text{s}^2$$

$$\text{Mode2: } IE\,/m = NE^2 \times VI = (0.41)^2 \times 8.11 \times 10^4 \text{ in.}^2/\text{s}^2 = 136 \times 10^4 \text{ in.}^2/\text{s}^2$$

$$\text{Mode3: } IE\,/m = NE^2 \times VI = (0.31)^2 \times 8.11 \times 10^4 \text{ in.}^2/\text{s}^2 = 0.779 \times 10^4 \text{ in.}^2/\text{s}^2$$

Step 4: Hysteretic Energy per Unit Mass (HE/m)

	μ	C	T_2	s	b	T	EH/EI
Mode 1	4	0.651	2.674	-0.0247	0.717	1.30	0.651
Mode 2	4	0.651	2.674	-0.0247	0.717	0.43	0.651
Mode 3	4	0.651	2.674	-0.0247	0.717	0.24	0.651

Mode 1: $HE/m = (IE/m) \times (HE/IE) = 1.36 \times 10^4 \text{ in.}^2/\text{s}^2 \times 0.651 = 0.888 \times 10^4 \text{ in.}^2/\text{s}^2$

Mode 2: $HE/m = (IE/m) \times (HE/IE) = 1.36 \times 10^4 \text{ in.}^2/\text{s}^2 \times 0.651 = 0.888 \times 10^4 \text{ in.}^2/\text{s}^2$

Mode 3: $HE/m = (IE/m) \times (HE/IE) = 0.779 \times 10^4 \text{ in.}^2/\text{s}^2 \times 0.651 = 0.507 \times 10^4 \text{ in.}^2/\text{s}^2$

Step 5: MDOF System Total Hysteretic Energy Demand and its Distribution

$$HE_{total} = (\Gamma^2 \times HE/m)_{mode\ 1} + (\Gamma^2 \times HE/m)_{mode\ 2} + (\Gamma^2 \times HE/m)_{mode\ 3}$$

$$HE_{total} = (1.857\ \text{kip·s}^2\text{·in.}^{-1})\ (0.888 \times 10^4\ \text{in.}^2/\text{s}^2) + (0.288\ \text{kip·s}^2\text{·in.}^{-1})\ (0.888 \times 10^4\ \text{in.}^2/\text{s}^2)$$

$$+ (0.109\ \text{kip·s}^2\text{·in}^{-1})\ (0.507 \times 10^4\ \text{in.}^2/\text{s}^2) = 1.96 \times 10^4\ \text{kip-in.}$$

Story forces, displacements, and hysteretic energies:

Story	Force (kips)	Displacement (in.)	Story Drift (in.)	External Work Done (kip-in.)	Hysteretic Energy (kip-in.)
Story 1	24.0	5.35	5.35	4394	7445
Story 2	58.0	12.68	7.33	2837	4802
Story 3	93.0	20.60	7.92	2606	4411
Story 4	122.0	27.06	6.46	1525	2581
Story 5	114.0	28.88	1.82	208	351

Step 6: Member Size Optimization

Optimization of Members in the Fifth Story

Objective Function - Weight, *W*

$$W = 288M_{EC,5} + 144M_{IC,5} + 576M_{B,5}$$

Mathematical formulation of the minimization problem

Minimize:
$$W = 288M_{EC,5} + 144M_{IC,5} + 288M_{B,5}$$

Subjected to:
$$0.48M_{EC,5} + 0.24M_{IC,5} \geq 351\text{kip-in.}$$
$$0.24M_{EC,5} + 0.12M_{IC,5} + 0.48M_{B,5} \geq 351\text{kip-in.}$$
$$M_{EC,5} - M_{B,5} \geq 0$$
$$M_{IC,5} - 2M_{B,5} \geq 0$$
where $\quad M_{EC,5} > 0, M_{IC,5} > 0, M_{B,5} > 0$

The optimized solution obtained using the Simplex linear solver built in Microsoft Excel is

$$M_{EC,5} = 418\ \text{kip-in.}, M_{IC,5} = 697\ \text{kip-in., and } M_{B,5} = 348\ \text{kip-in.}$$

Optimization of Members in the Fourth Story

Objective Function - Weight, *W*

$$W = 288M_{EC,4} + 144M_{IC,4} + 576M_{B,4}$$

Mathematical formulation of the minimization problem

Minimize :

$$W = 288M_{EC,4} + 144M_{IC,4} + 576M_{B,4}$$

Subjected to :

$$0.48M_{EC,4} + 0.24M_{IC,4} \geq 2765 \text{ kip-in.}$$

$$0.24M_{EC,4} + 0.12M_{IC,4} + 0.48M_{B,4} \geq 2581 \text{ kip-in.}$$

$$M_{EC,4} - M_{B,4} \geq -418 \text{ kip-in.}$$

$$M_{IC,4} - 2M_{B,4} \geq -697 \text{ kip-in.}$$

where $\quad M_{EC,4} > 0, M_{IC,4} > 0, M_{B,4} > 0$

The optimized solution obtained using the Simplex linear solver built in Microsoft Excel is

$M_{EC,4} = 3396$ kip-in., $M_{IC,4} = 5661$ kip-in., and $M_{B,4} = 2265$ kip-in.

Optimization of Members in the Third Story

Objective Function - Weight, *W*

$$W = 288M_{EC,3} + 144M_{IC,3} + 576M_{B,3}$$

Mathematical formulation of the minimization problem

Minimize :

$$W = 288M_{EC,3} + 144M_{IC,3} + 576M_{B,3}$$

Subjected to :

$$0.48M_{EC,3} + 0.24M_{IC,3} \geq 5905 \text{ kip-in.}$$

$$0.24M_{EC,3} + 0.12M_{IC,3} + 0.48M_{B,3} \geq 4411 \text{ kip-in.}$$

$$M_{EC,3} - M_{B,3} \geq -3396 \text{ kip-in.}$$

$$M_{IC,3} - 2M_{B,3} \geq -5661 \text{ kip-in.}$$

where $\quad M_{EC,3} > 0, M_{IC,3} > 0, M_{B,3} > 0$

The optimized solution obtained using the Simplex linear solver built in Microsoft Excel is

$M_{EC,3} = 6711$ kip-in., $M_{IC,3} = 11185$ kip-in., and $M_{B,3} = 4474$ kip-in.

Optimization of Members in the Second Story

Objective Function- Weight, W

$$W = 288M_{EC,2} + 144M_{IC,2} + 576M_{B,2}$$

Mathematical formulation of the minimization problem

Minimize :
$$W = 288M_{EC,2} + 144M_{IC,2} + 576M_{B,2}$$

Subjected to :
$$0.48M_{EC,2} + 0.24M_{IC,2} \geq 7755 \text{ kip-in.}$$
$$0.24M_{EC,2} + 0.12M_{IC,2} + 0.48M_{B,2} \geq 4802 \text{ kip-in.}$$
$$M_{EC,2} - M_{B,2} \geq -6711 \text{ kip-in.}$$
$$M_{IC,2} - 2M_{B,2} \geq -11190 \text{ kip-in.}$$

where $\quad M_{EC,2} > 0, M_{IC,2} > 0, M_{B,2} > 0$

The optimized solution obtained using the Simplex linear solver built in Microsoft Excel is

$M_{EC,2} = 8813$ kip-in., $M_{IC,2} = 14687$ kip-in. and $M_{B,2} = 5875$ kip-in.

Optimization of Members in the First Story

Objective Function - Weight, W

$$W = 336M_{EC,1} + 168M_{IC,1} + 576M_{B,1}$$

Mathematical formulation of the minimization problem

Minimize :
$$W = 336M_{EC,1} + 168M_{IC,1} + 576M_{B,1}$$

Subjected to :
$$0.48M_{EC,1} + 0.24M_{IC,1} \geq 11320 \text{ kip-in.}$$
$$0.24M_{EC,1} + 0.12M_{IC,1} + 0.48M_{B,1} \geq 7445 \text{ kip-in.}$$
$$M_{EC,1} - M_{B,1} \geq -8813 \text{ kip-in.}$$
$$M_{IC,1} - 2M_{B,1} \geq -14687 \text{ kip-in.}$$

where $\quad M_{EC,1} > 0, M_{IC,1} > 0, M_{B,1} > 0$

The optimized solution obtained using the Simplex linear solver built in Microsoft Excel is

$M_{EC,1} = 12870$ kip-in., $M_{IC,1} = 21450$ kip-in., and $M_{B,1} = 8578$ kip-in.

Step 7: Effect of Axial Forces on Plastic Capacity

Story		Column size	Axial Force (kips)		β_m	Plastic Moment (kip-in.)	
			Capacity	Applied		Required	Modified
1	Internal	W14×257	2847	449	1.086	21450	23280
	External	W14×176	1938	210	1.057	12870	13600
2	Internal	W14×176	2005	354	1.097	14690	16110
	External	W14×132	1481	165	1.059	8813	9333
3	Internal	W14×145	1650	262	1.086	11190	12150
	External	W14×109	1220	121	1.052	6711	7061
4	Internal	W14×109	1220	170	1.075	5661	6085
	External	W14×74	724	78	1.057	3396	3589
5	Internal	W14×74	724	78	1.057	697	737
	External	W14×74	724	35	1.025	418	428

Step 8: Plastic Moment Capacity versus Demand Comparison

			Current size	Plastic Moment (kip-in.)		Member Size	
		Story		Capacity	Required	Decision	New
Columns	1	Internal	W14×257	24350	23280	Keep	W14×257
		External	W14×176	16000	13600	Keep	W14×176
	2	Internal	W14×176	16000	16110	Keep	W14×176
		External	W14×132	11700	9333	Keep	W14×132
	3	Internal	W14×145	13000	12150	Keep	W14×145
		External	W14×109	10600	7061	Keep	W14×109
	4	Internal	W14×109	9600	6085	Keep	W14×109
		External	W14×74	6300	3589	Keep	W14×74
	5	Internal	W14×74	6300	737	Keep	W14×74
		External	W14×74	6300	428	Keep	W14×74
Beams	1		W18×86	9300	8578	Keep	W18×86
	2		W18×71	7300	5875	keep	W18×71
	3		W18×71	7300	4474	keep	W18×71
	4		W18×71	7300	2265	Keep	W18×71
	5 (Roof)		W18×65	6650	348	Keep	W18×65

6.4.3 Proposed EBSD Procedure: Observation

Like any iterative procedure, the rate of convergence of the proposed EBSD method is dependent on the quality of the first trial solution, i.e., the preliminary member sizes. Even though not explicitly mentioned in the design examples, it was observed that when designing the frames for gravity loads a lower value of force to moment (P-M) ratio for columns and a value closer to the desired P-M ratio for beams often help speed up the rate of convergence. Except for lower floor beams, it is likely that beam sizes mainly remain unchanged from their preliminary sizes during the iterative procedure. This supports the notion that the lateral force effect of earthquakes is mainly resisted by columns.

After the first iteration, the EBSD gives results that require an excessively large plastic moment capacity demand for the first story columns (see Iteration 1 of the five story two bay frame design example) and thus unnecessarily large member sizes. Therefore, the selection of member sizes after the first iteration shall not solely depend on the resulting plastic demand but should take into account the expected plastic demand for the subsequent iterations. Recall per the proposed EBSD procedure, the hysteretic energy distributions among the different stories depend on the story drifts. Say, if member sizes for the first story columns are chosen based on the plastic demand from the first iteration, the first story becomes stiff enough to force plastic hinges to form at upper stories, thus leaving the first story drift to be small. A small story drift is translated to a small hysteretic energy demand hence smaller member sizes. This phenomenon can be clearly seen from Figure 6.12, where the hysteretic energy demand and story drift of the first story for Iteration 2 are substantially smaller than those for Iteration 1. In addition, large member size means larger compressive capacity and smaller moment amplification factor, β_m. If

the member sizes for the first story columns are not selected wisely, they can be excessively

large, and thus more iterations are required to arrive at the final solution.
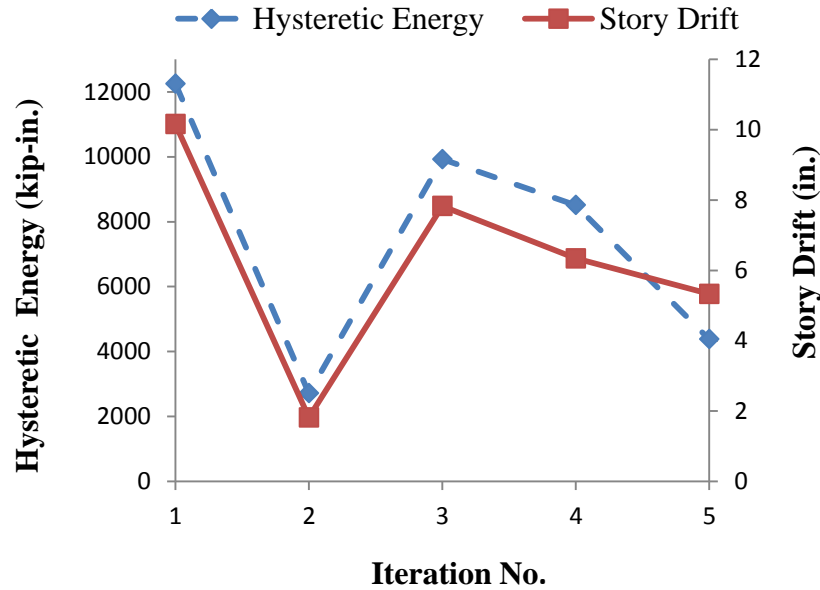
Figure 6.12 First story level hysteretic energy demand and drifts for five story frame

From a design perspective, the solution of the optimization problem using the Simplex method

can sometimes give unrealistic solutions. Examples are zero plastic moment demands for beams

or for columns. Zero plastic moment demands mean no plastic hinges are expected to form.

However, without the formation of plastic hinges, there will not be any collapse mechanisms and

the optimization problem cannot be formulated. In such cases, additional constraint equations

that do not change the integrity of the problem are added intuitively. Pending further research, it

is recommended that these constraint equations require that beams shall have at least 60% and

40% of the plastic moment demands of the external and internal columns, respectively; and

external columns shall have at least 60% of the plastic moment demands of the internal columns.

7 CONCLUSIONS AND RECOMMENDATIONS

7.1 Summary and Conclusions

1. The differences between the current seismic design procedures; namely, the force-based design (FBD) and displacement-based design (DBD), and the proposed energy-based seismic design (EBSD) were discussed. Unlike FBD and DBD, EBSD captures the duration dependent cumulative damage effect of earthquakes on structures. The main design parameters in FBD, DBD and EBSD are force, displacement and energy demand (hysteretic energy), respectively.

2. A new earthquake intensity index called velocity index (*VI*), obtained by multiplying two earthquake indices: the peak ground velocity (*PGV*) and the cumulative absolute velocity (*CAV*) and has dimensions of energy per unit mass, was introduced. *VI* is preferred over other existing earthquake intensity indexes for normalizing earthquake input energy per unit mass spectra for two reasons: (i) input energy per unit mass when normalized by *VI* becomes dimensionless, and (ii) the coefficient of variation of *VI* normalized input energies for a set of earthquakes is smaller when compared to the other normalization factors.

3. Soil site condition and structural hysteretic behavior dependent *VI* normalized input energy per unit mass (*NE*) spectra for SDOF systems with damping ratio of $\zeta = 0.05$ and ductility levels $\mu=1, 2, 3, 4$ and 5 were developed. The structural hysteretic models considered are: bilinear plastic (BP), stiffness degradation (SD), bilinear flag (BF) and bilinear slip (BS). They cover a wide range of hysteretic behavior of existing and new structures that encompass moment resisting to self-centering steel frames and reinforced concrete to prestressed concrete structures.

4. For hysteretic models BP, SD, BF and BS and soil site classes B, C, D and E, *NE* decreases with ductility. The rate of decrement with an increasing ductility value is more distinct at low ductility values (μ=1-3) than at higher ductility values (μ=3-5), suggesting that input energy in SDOF systems becomes relatively insensitive to ductility for ductility levels greater than 5.

5. *Mean+σ* and *mean+2σ NE* spectra for SDOF systems with hysteretic behavior types -BP, SD, BF and BS and site soil classes B, C, D and E were developed. For purpose of design, the normalized input energy spectra were divided into three regions: short period, intermediate period and long period. These are consistent with the customary design response spectra contained in various seismic codes and standards.

6. Irrespective of the hysteretic behavior, *NE* maximum spectral value (for both *mean+ σ* and *mean+2σ* spectra) and the corresponding period at which it occurs increase as the soil gets softer. In addition, the range of the intermediate period (region of maximum spectral value) of the normalized energy spectra becomes larger for sites with poor soil conditions.

7. When compared with the exact time history spectra, the proposed *NE* spectra provide conservative estimates of input energy for SDOF systems. An exception to this generalization is that for hysteretic behavior type BP in soil site classes B & C, and for hysteretic types SD, BF and BS in soil site class B, the proposed *mean +σ* spectra underestimate the input energy in the long period region by a slight margin.

8. *Mean+σ* and *mean+2σ* hysteretic energy to input energy ratio (*HE/IE*) spectra for SDOF systems with ductility levels μ= 2, 3, 4, and 5, hysteretic behavior types of BP, SD, BF and BS and site soil classes of B, C, D and E were developed. *HE/IE* values generally increase

with an increase in ductility. But, like the *NE* spectra, the *HE/IE* spectral values show very

small differences for ductility values $\mu \geq 3$ for soil site classes B, C, D and E.

9. For hysteretic behavior type BP, *HE/IE* spectral values tend to increase with decrease in the

stiffness of the foundation soil. However, the effect of soils on *HE/IE* spectra for SDOF

systems with hysteretic behavior types SD, BF and BS is neither significant nor shows a

specific trend.

10. For a given hysteretic behavior and ductility level, the difference in the magnitude of the

mean+σ and the *mean+2σ HE/IE* spectral values is negligible. As a result, either spectrum

can be used for estimating the hysteretic demand without a significant change in the final

value.

11. With respect to hysteretic behavior, *HE/IE* spectral values vary in the following order

BP>SD>BF>BS. Hysteretic energy demand for SDOF systems is highest for hysteretic

behavior type bilinear plastic (BP) and lowest for hysteretic behavior type BS.

12. The proposed *HE/IE* spectra yield conservative *mean+σ* and *mean+2σ* hysteretic energy

values for SDOF systems when compared to the exact *mean+σ* and *mean+2σ* hysteretic

energy values obtained from time history analysis. The only exception to this generalization

is that the proposed *mean+σ HE/IE* underestimates the hysteretic energy for SDOF systems

with hysteretic behavior type BF within the long period region of the spectra.

13. Simple vibration modes based expressions for estimating input and hysteretic energy for a

MDOF system from its equivalent SDOF systems were developed. The energy relationship

between the MDOF system and its ESDOF systems was derived from an energy balance

equation where the MDOF was discretized into its orthogonal modes. The properties of the

ESDOF system for each mode are determined using non-linear static (pushover) analysis of

the MDOF system subjected to a lateral force (with mode-based distribution) and pushed to a target (roof) displacement.

14. The simple input energy relationships between the MDOF system and its ESDOF systems were validated using four (a three, five, seven and nine story) frames. For each of the frames, two modes were enough to satisfy the 90% or greater effective modal mass requirement for mode based dynamic analysis. Using two modes, the proposed energy relationships provided a very good estimate for the three and five story frame with an estimation error of 4.5% and 6.5%, respectively. An acceptable result was also obtained for the seven and nine story frames with an estimation error of 10% and 11.5 %, respectively.

15. For low and medium height moment resisting frames, much of the input energy due to an earthquake is contributed by the 1st mode of vibration of the MDOF system.

16. Hysteretic energy distribution in moment resisting frames obtained from exact time history analysis is characteristically chaotic. It does not follow a specific trend nor is it consistent. An approximate pushover based hysteretic energy distribution is therefore proposed.

17. The proposed hysteretic energy distribution scheme is simpler and easy to use when compared with existing distribution schemes found in literature. It involves only story forces and displacements in determining the distribution ratios. When compared to the actual plastic energies ratios (product of plastic moment and plastic rotations), the proposed scheme produced very good results and is shown to be better than other distribution schemes.

18. A story-wise energy-based seismic design (EBSD) procedure was presented. The relationship that exists between EBSD and plastic analysis/design of structures was discussed. For moment resisting frames, the cyclic/dynamic hysteretic energy demand is approximately equal to four times the monotonic/static plastic energy.

19. The story-wise EBSD procedure reduces to an optimization problem, wherein the plastic moment capacities are determined by minimization of the weight function of the story subjected to a set of constraint equations (formulated using collapse mechanisms and code based requirements) using the Simplex method of linear optimization.

20. The expressions used for determining input energy, hysteretic energy and distribution scheme proposed in the present study were demonstrated using two design examples. The proposed expressions are easy to use and can significantly reduce the computational effort required for determining the hysteretic energy demand using nonlinear dynamic analysis.

21. Like any iterative procedure, the rate of convergence of the EBSD method is dependent on the quality of the first trial solution, i.e., the preliminary member sizes. Preliminary member sizes can be determined by designing the frame for gravity loads. It has been observed that the final member sizes for beams and columns in the upper stories do not significantly change from the preliminary sizes obtained by designing the frame for gravity loads.

22. The solution to an optimization problem using the Simplex method can sometimes produce unrealistic solutions, such as zero plastic moment demands for beams and/or columns. These solutions are obviously unacceptable, and additional constraint equations requiring that these plastic moment demands meet certain conditions and will not change the integrity of the problem should be added.

7.2 Recommendations for Future Research

1. Based on the distance from the source/fault, earthquake records are categorized as near-fault and far-fault records. Generally, seismic demand due to near-fault earthquakes is greater than far-fault earthquakes. In this study, only far-fault earthquakes were considered. A similar study on near-fault earthquakes will complement the current study.

252

2. Although the vibration mode based input and hysteretic energy relationships between a MDOF system and its equivalent SDOF systems developed in this study have been verified for regular low and medium rise moment resisting frames with hysteretic behavior type BP, applicability of the proposed method for high rise and irregular frames with hysteretic behavior type BP needs to be investigated. In addition, extension of the method to MDOF systems with hysteretic behaviors SD, BF and BS need to be performed.

3. The proposed scheme for distributing hysteretic energy was found to be sufficient for low and medium rise moment resisting frames when the overall dynamic response of the system is controlled predominantly by the first mode. In order to extend the distribution scheme to irregular and/or high rise frames, the distribution method needs further validation.

4. Even though the cost of moment resisting frames is directly related to the weight of the structure, joint detailing also significantly contributes to the cost of the structures. A better optimized design can be achieved if joint detailing cost is included in the optimization problem.

5. As demonstrated in the two design examples, the Simplex method of linear optimization can sometimes give unrealistic results. In such cases, the addition of supplementary constraint equations to the code-based and collapsed mechanism related constraint equations is needed. These supplementary equations can be added from design experience, but the final design would depend on the designer's choice of the conditions. For a more uniform design output, there is a need to formulate such equations based on plastic moment relationships between story external/internal column to floor beams and those between internal and external columns. These equations can also be used to replace the commonly used code-based joint constraint equations.

APPENDIX A   GROUND MOTION ENSEMBLES

A1. Site Class B – Summary of Selected Ground Motion Records

Comp.	NGA#	Scale Factor	D5-95(s)	Event	Year	Station	Mag	R_{rup}(km)	V_{s30}(m/s)
FN &FP	2107	0.8985	19.7 24.7	Denali- Alaska	2002	Carlo (temp)	7.9	50.9	963.9
FN &FP	946	1.7258	14.4 14.9	Northridge-01	1994	Antelope Buttes	6.69	46.9	821.7
FN &FP	804	0.9561	9.5 11.8	Loma Prieta	1989	So. San Francisco- Sierra Pt.	6.93	63.1	1020.6
FN &FP	283	2.1701	15.8 18.1	Irpinia- Italy-01	1980	Arienzo	6.9	52.9	1000
FN &FP	1033	1.2158	20.2 11.6	Northridge-01	1994	Littlerock - Brainard Can	6.69	46.6	821.7
FN &FP	2111	0.8937	18.8 23.7	Denali- Alaska	2002	R109 (temp)	7.9	43	963.9
FN &FP	1347	1.1725	25.6 21.1	Chi-Chi- Taiwan	1999	ILA063	7.62	61.1	996.5
FN &FP	1518	1.1402	19.8 22.2	Chi-Chi- Taiwan	1999	TCU085	7.62	58.1	999.7
FN &FP	788	1.0313	10.9 10.7	Loma Prieta	1989	Piedmont Jr High	6.93	73	895.4
FN &FP	1587	1.2211	33.6 34.7	Chi-Chi- Taiwan	1999	TTN042	7.62	65.2	845.3
FN &FP	797	0.8949	10.9 13.9	Loma Prieta	1989	SF - Rincon Hill	6.93	74.1	873.1
FN &FP	1021	1.2027	13.6 13.2	Northridge-01	1994	Lake Hughes #4 - Camp Mend	6.69	31.7	821.7
FN &FP	925	2.0055	26.5 22.5	Big Bear-01	1992	Rancho Cucamonga - Deer Can	6.46	[59.4]	821.7
FN &FP	1074	0.8161	17.4 13.5	Northridge-01	1994	Sandberg - Bald Mtn	6.69	41.6	821.7
FN &FP	1060	1.4735	15.1 16.2	Northridge-01	1994	Rancho Cucamonga - Deer Can	6.69	80	821.7
FN &FP	1096	1.5746	14.2 14.8	Northridge-01	1994	Wrightwood - Jackson Flat	6.69	64.7	821.7
FN &FP	2929	3.4843	17.4 18.3	Chi-Chi- Taiwan-04	1999	TTN042	6.2	69	845.3
FN &FP	943	2.4764	11.8 14.4	Northridge-01	1994	Anacapa Island	6.69	68.9	821.7
FN &FP	795	1.1371	8.6 11.4	Loma Prieta	1989	SF - Pacific Heights	6.93	76	1249.9
FN &FP	1041	1.0261	10.1 9.5	Northridge-01	1994	Mt Wilson - CIT Seis Sta	6.69	35.9	821.7

A2. Site Class C – Summary of Selected Ground Motion Records

Comp.	NGA#	Scale Factor	D5-95(s)	Event	Year	Station	Mag	Rrup(km)	Vs30(m/s)
FN&FP	299	2.4946	19.3 22.1	Irpinia- Italy-02	1980	Brienza	6.2	42.6	500
FN&FP	353	1.4575	18.8 19.4	Coalinga-01	1983	Parkfield - Gold Hill 4W	6.36	41.1	438.3
FN&FP	762	0.9005	18.3 16.4	Loma Prieta	1989	Fremont - Mission San Jose	6.93	39.5	367.6
FN&FP	798	2.182	9.2 8.4	Loma Prieta	1989	SF - Telegraph Hill	6.93	76.5	712.8
FN&FP	980	1.6481	29.1 26.9	Northridge-01	1994	Huntington Beach - Lake St	6.69	77.5	370.8
FN&FP	1015	1.3589	25.7 26.0	Northridge-01	1994	LB - Rancho Los Cerritos	6.69	51.9	405.2
FN&FP	1026	0.9721	23.3 23.5	Northridge-01	1994	Lawndale - Osage Ave	6.69	39.9	361.2
FN&FP	1027	1.5469	11.8 13.1	Northridge-01	1994	Leona Valley #1	6.69	37.2	684.9
FN&FP	1028	1.4716	13.2 12.5	Northridge-01	1994	Leona Valley #2	6.69	37.2	446
FN&FP	1029	1.3395	13.1 13.0	Northridge-01	1994	Leona Valley #3	6.69	37.3	684.9
FN&FP	1190	1.6949	38.0 38.7	Chi-Chi- Taiwan	1999	CHY019	7.62	50.5	478.3
FN&FP	1284	1.3759	22.2 21.6	Chi-Chi- Taiwan	1999	HWA035	7.62	48.4	500.8
FN&FP	1594	2.8355	36.5 37.0	Chi-Chi- Taiwan	1999	TTN051	7.62	36.7	680
FN&FP	2609	3.0711	61.4 59.5	Chi-Chi- Taiwan-03	1999	TCU053	6.2	40.6	454.6
FN&FP	2714	0.9412	16.8 12.8	Chi-Chi- Taiwan-04	1999	CHY046	6.2	38.1	442.1
FN&FP	2916	3.0915	20.0 23.2	Chi-Chi- Taiwan-04	1999	TTN022	6.2	56.3	507
FN&FP	2952	2.4116	16.8 17.3	Chi-Chi- Taiwan-05	1999	CHY042	6.2	67.7	680
FN&FP	3202	2.3519	21.7 22.9	Chi-Chi- Taiwan-05	1999	TCU102	6.2	52.8	714.3
FN&FP	3224	2.6425	18.6 25.5	Chi-Chi- Taiwan-05	1999	TTN001	6.2	59.2	424
FN&FP	3447	2.7129	31.9 25.0	Chi-Chi- Taiwan-06	1999	TCU032	6.3	59.6	454.4
FN&FP	3495	1.1679	34.9 36.4	Chi-Chi- Taiwan-06	1999	TCU109	6.3	37.9	424.2

A3. Site Class D – Summary of Selected Ground Motion Records

Comp.	NGA#	Scale Factor	D5-95(s)	Event	Year	Station	Mag	R_{rup}(km)	V_{s30}(m/s)
FN&FP	3271	1.2106	35.3 28.6	Chi-Chi- Taiwan-06	1999	CHY032	6.3	65	192.7
FN&FP	1816	1.9373	27.7 21.8	Hector Mine	1999	North Palm Springs Fire Sta #36	7.13	61.8	345.4
FN&FP	3276	1.0657	29.3 36.0	Chi-Chi- Taiwan-06	1999	CHY037	6.3	53.7	212.1
FN&FP	2695	2.9223	59.0 54.0	Chi-Chi- Taiwan-04	1999	CHY016	6.2	79.8	200.9
FN&FP	832	0.9457	25.2 29.9	Landers	1992	Amboy	7.28	69.2	271.4
FN&FP	1177	1.3668	39.3 38.9	Kocaeli- Turkey	1999	Zeytinburnu	7.51	53.9	274.5
FN&FP	1290	2.3407	25.7 26.1	Chi-Chi- Taiwan	1999	HWA043	7.62	58	228.6
FN&FP	1637	1.3285	27.8 27.7	Manjil- Iran	1990	Rudsar	7.37	64.5	274.5
FN&FP	862	1.3058	37.9 36.4	Landers	1992	Indio - Coachella Canal	7.28	54.2	345.4
FN&FP	3313	2.0942	55.7 48.4	Chi-Chi- Taiwan-06	1999	CHY094	6.3	59.6	221.9
FN&FP	941	2.7963	28.0 29.0	Big Bear-01	1992	Yermo Fire Station	6.46	[71.0]	353.6
FN&FP	907	2.2741	22.9 22.6	Big Bear-01	1992	Hesperia - 4th & Palm	6.46	[44.8]	345.4
FN&FP	3265	1.1293	16.7 16.5	Chi-Chi- Taiwan-06	1999	CHY025	6.3	40.3	277.5
FN&FP	958	1.1067	32.4 41.1	Northridge-01	1994	Camarillo	6.69	40.3	234.9
FN&FP	3480	2.7385	40.7 43.1	Chi-Chi- Taiwan-06	1999	TCU086	6.3	64.2	222.2
FN&FP	1762	0.7422	24.0 27.9	Hector Mine	1999	Amboy	7.13	43	271.4
FN&FP	1791	1.6048	23.6 32.9	Hector Mine	1999	Indio - Coachella Canal	7.13	73.5	345.4
FN&FP	1776	2.1505	24.7 19.4	Hector Mine	1999	Desert Hot Springs	7.13	56.4	345.4
FN&FP	2720	2.5407	39.9 27.2	Chi-Chi- Taiwan-04	1999	CHY056	6.2	79.4	193

A4. Site Class E – Summary of Selected Ground Motion Records

Comp.	NGA#	Scale Factor	D5-95(s)	Event	Year	Station	Mag	R_{rup}(km)	V_{s30}(m/s)
FN&FP	3319	1.8138	33.0 42.5	Chi-Chi- Taiwan-06	1999	CHY107	6.3	79.8	175.7
FN&FP	962	1.903	22.5 23.3	Northridge-01	1994	Carson - Water St	6.69	49.8	160.6
FN&FP	1147	0.7059	36.9 37.2	Kocaeli- Turkey	1999	Ambarli	7.51	69.6	175
FN&FP	1229	2.3854	38.6 41.2	Chi-Chi- Taiwan	1999	CHY078	7.62	77.2	160.7
FN&FP	3285	1.9532	27.8 34.5	Chi-Chi- Taiwan-06	1999	CHY054	6.3	77.6	172.1
FN&FP	2736	5.6455	42.1 39.2	Chi-Chi- Taiwan-04	1999	CHY076	6.2	56.4	169.8
FN&FP	3302	1.4669	41.3 38.3	Chi-Chi- Taiwan-06	1999	CHY076	6.3	70.4	169.8
FN&FP	2510	2.8682	37.6 45.4	Chi-Chi- Taiwan-03	1999	CHY107	6.2	72.5	175.7
FN&FP	1212	1.3432	39.9 36.4	Chi-Chi- Taiwan	1999	CHY054	7.62	48.5	172.1
FN&FP	2476	2.8264	33.3 44.3	Chi-Chi- Taiwan-03	1999	CHY054	6.2	70.4	172.1
FN&FP	808	1.0323	4.7 4.6	Loma Prieta	1989	Treasure Island	6.93	77.4	155.1
FN&FP	2755	2.7405	42.9 46.0	Chi-Chi- Taiwan-04	1999	CHY107	6.2	63.4	175.7
FN&FP	2718	2.6975	41.1 42.4	Chi-Chi- Taiwan-04	1999	CHY054	6.2	61.1	172.1

APPENDIX B: GRAPHICAL PRESENTATION OF SOIL EFFECT ON INPUT ENERGY

Figure B.1 Effect of soil on input energy of SDOF structures: hysteretic model BP

Figure B.2 Effect of soil on input energy of SDOF structures: hysteretic model SD
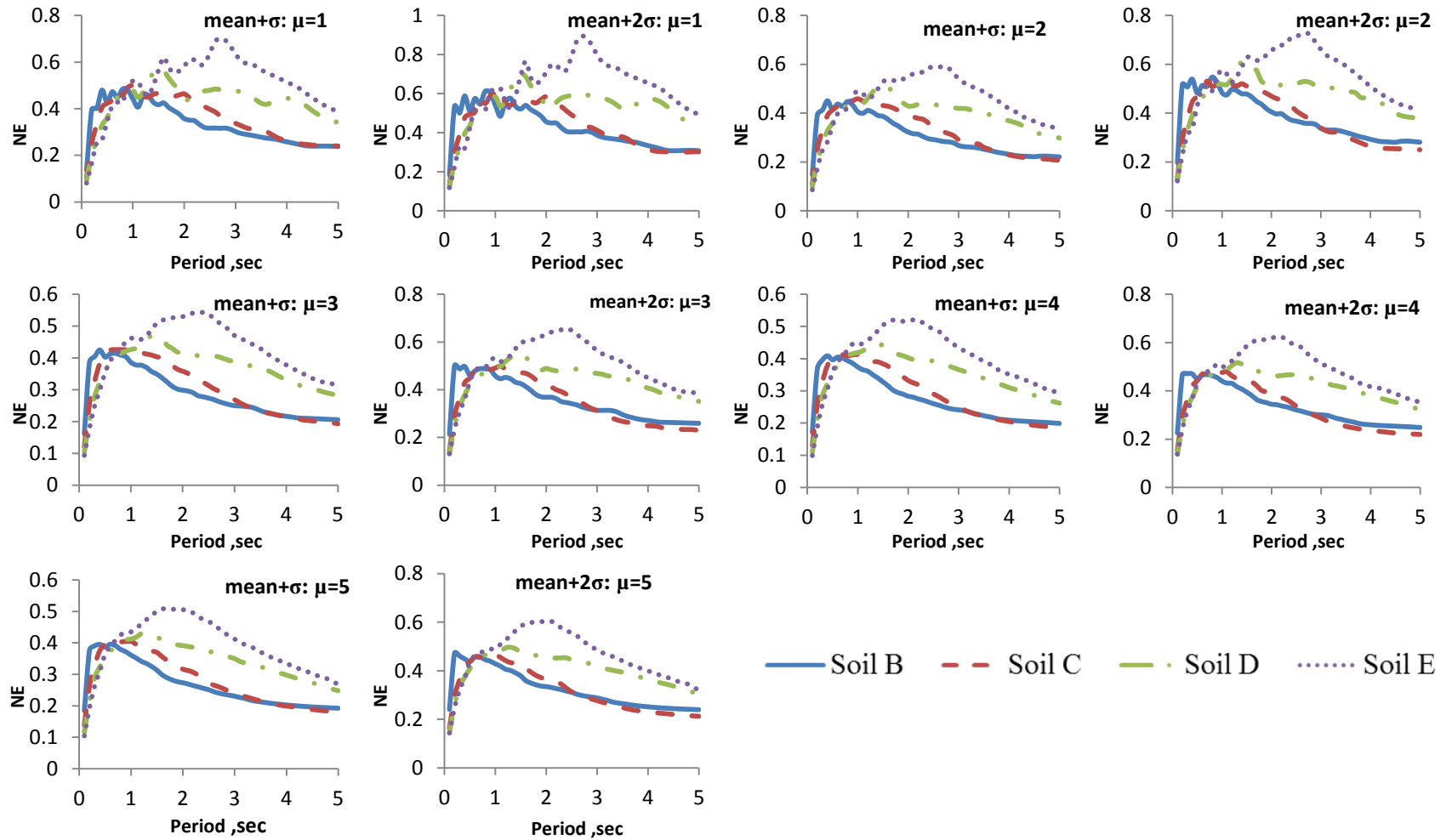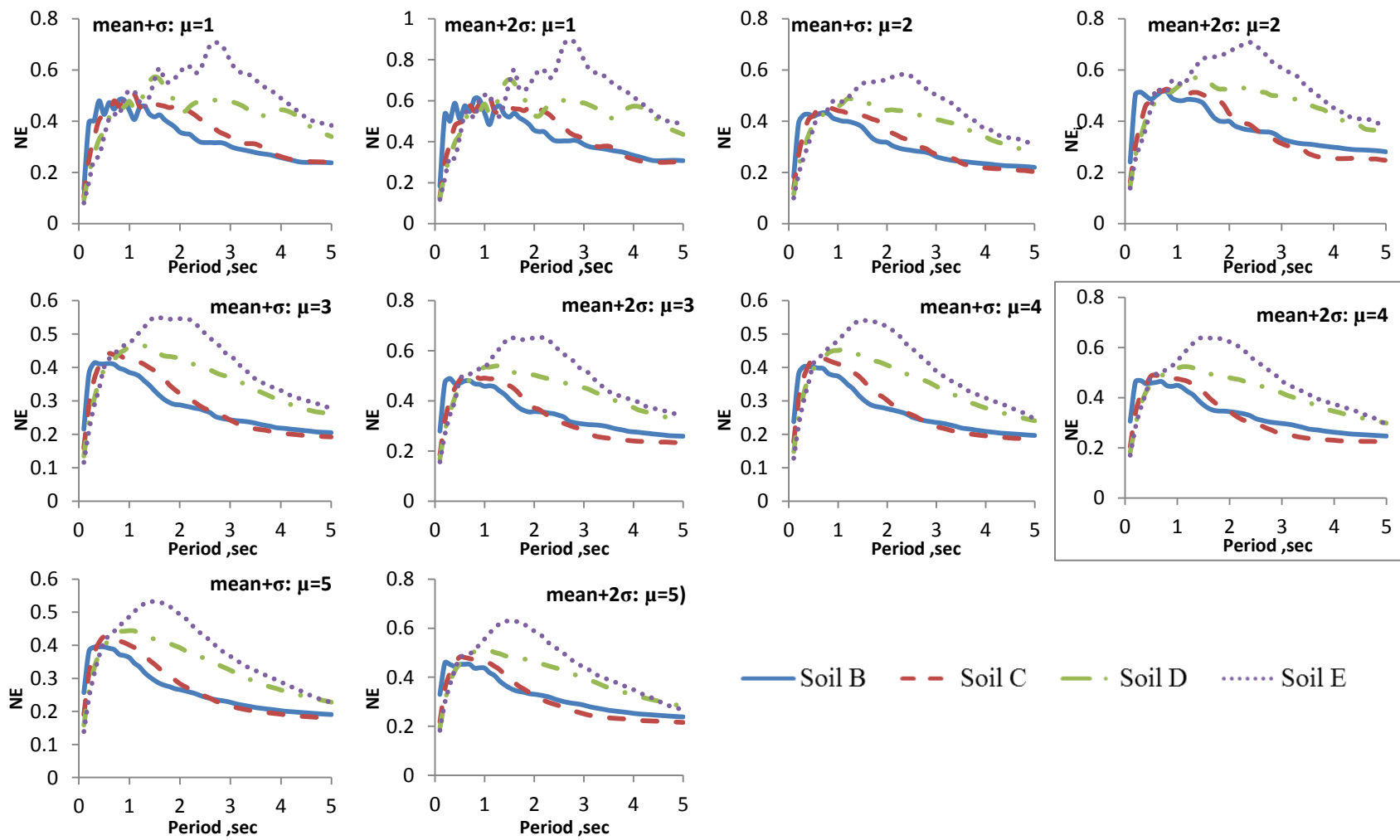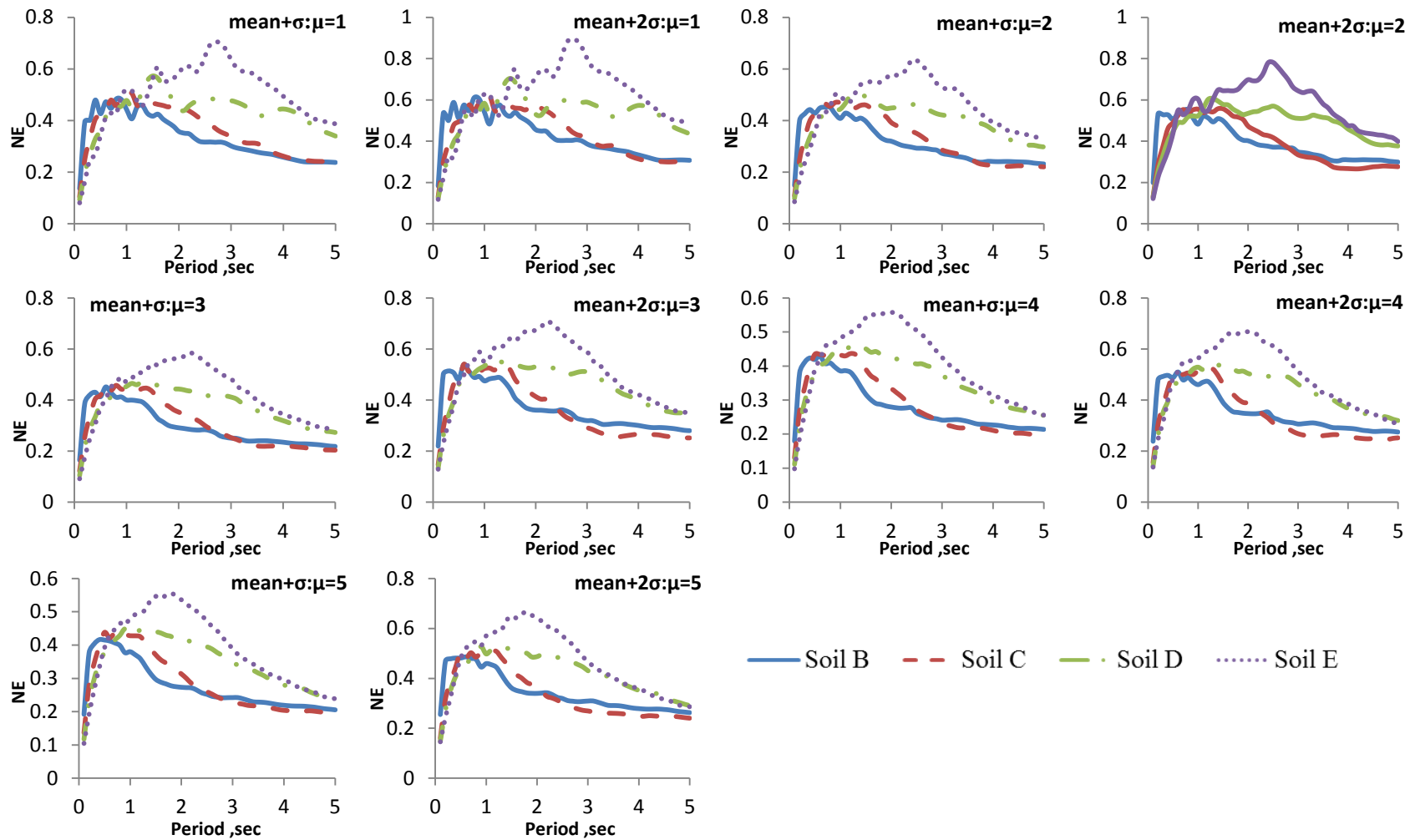
259

Figure B.3 Effect of soil on input energy of SDOF structures: hysteretic model BF
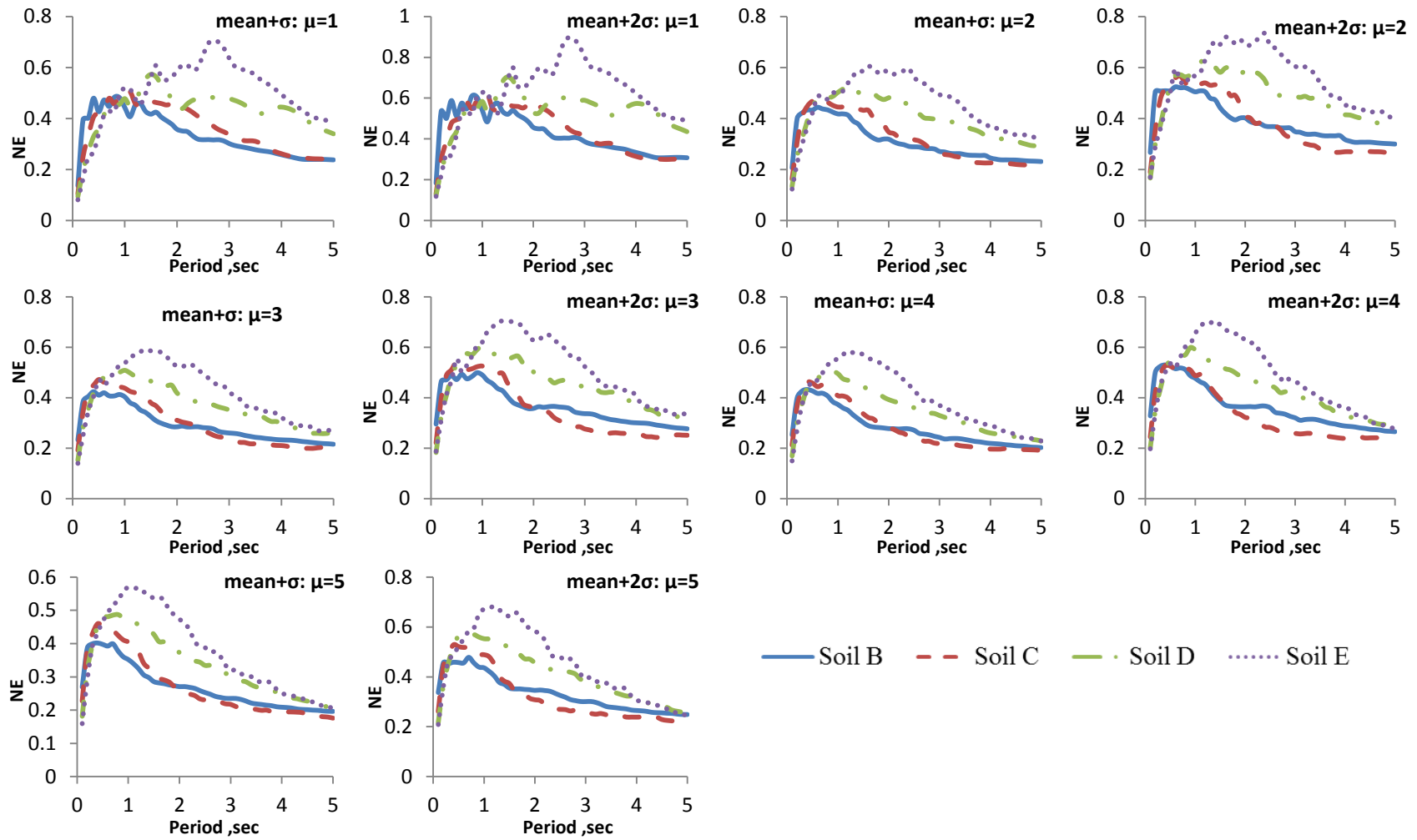
Figure B.4 Effect of soil on input energy of SDOF structures: hysteretic model BS

APPENDIX C: CASE STUDY FRAME DIMENSIONS AND SECTIONS

C1. Three-Story Moment-Resisting Frame (all dimensions in mm)
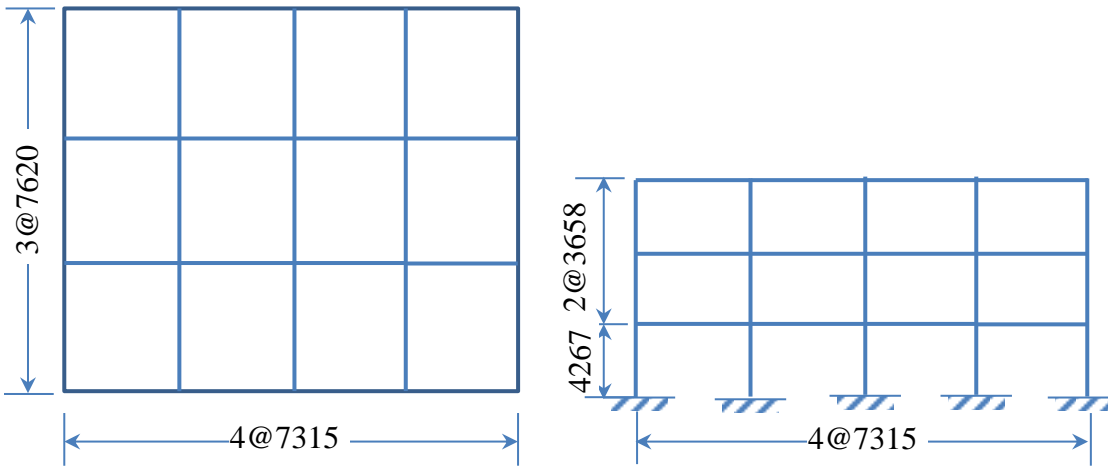
(a) Plan View   (b) Elevation View

Summary of Frame Design Parameters

Floor	Weight (kN)	Design Load (kN)	Drift (cm)	Drift Limit (cm)
2nd	1566	60	1.20	1.44
3rd	1566	130	1.27	1.33
Roof	1212	163	1.02	1.33

Steel Beam Moment Strength and Demand

Floor	Beam	M_{ub} (kN-m)	M_{pb} (kN-m))
2nd	W21x44	309	360
3rd	W18x40	251	282
Roof	W14x34	168	186

Steel Column Strength and Demand

Floor	Column		M_{pc} (kN-m)	
	Interior	Exterior	Interior	Exterior
1st	W14x109	W14x48	1085	443
2nd	W14x109	W14x48	1085	443
3rd	W14x109	W14x46	1085	443

C2. Five-Story Composite Special Moment- Resisting Frame (all dimensions in mm)
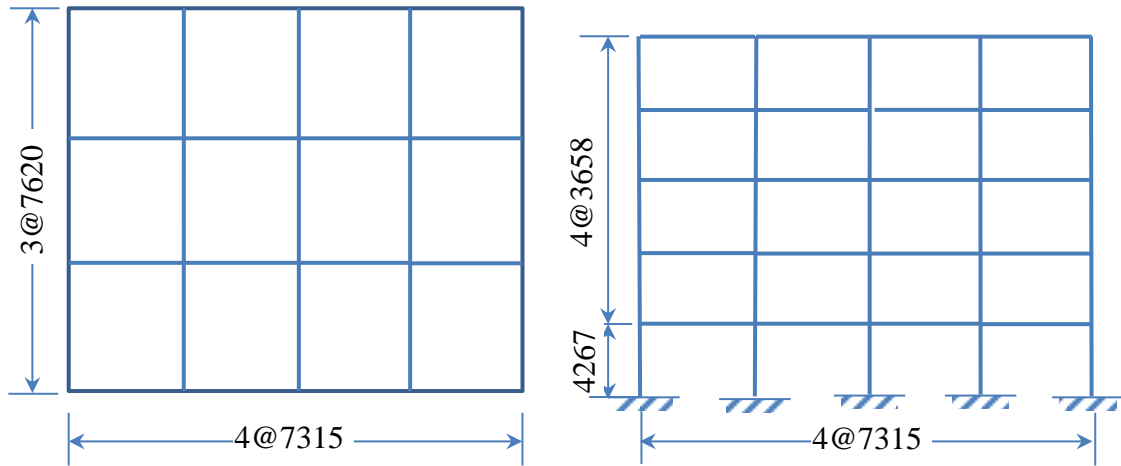
(a) Plan View

(b) Elevation View

Summary of Frame Design Parameters

Floor	Weight (kN)	Design Load (kN)	Drift (cm)	Drift Limit (cm)
2nd	1566	23	1.23	1.44
3rd	1566	57	1.25	1.33
4th	1566	100	1.29	1.33
5th	1566	150	1.28	1.33
Roof	1212	160	1.01	1.33

Steel Beam Moment Strength and Demand

Floor	Beam	M_{ub} (kN-m)	M_{pb} (kN-m))
2nd	W24x62	393	581
3rd	W24x62	378	581
4th	W21x50	319	411
5th	W18x40	257	282
Roof	W14x34	164	186

Steel Column Strength and Demand

Floor	Column		M_{pc} (kN-m)		E_m ($\times 10^8$ kN/m^2)	
	Interior	Exterior	Interior	Exterior	Interior	Exterior
1st	W14x74 (508x559)	W12x53 (508x508)	1180	777	3.018	3.306
2nd	W14x74 (508x559)	W12x53 (508x508)	1180	777	3.018	3.306
3rd	W14x74 (508x559)	W12x53 (508x508)	1180	777	3.018	3.306
	W14x68 (508x559)	W12x45 (457x508)	1097	694	3.114	3.394
4th	W14x68 (508x559)	W12x45 (457x508)	1097	694	3.114	3.394
5th	W14x68 (508x559)	W12x45 (457x508)	1097	694	3.114	3.394

( ) is the SRC column dimension in millimeters

Em Elastic modulus of composite section

C3. Seven-Story Composite Special Moment-Resisting Frame (all dimension in mm)
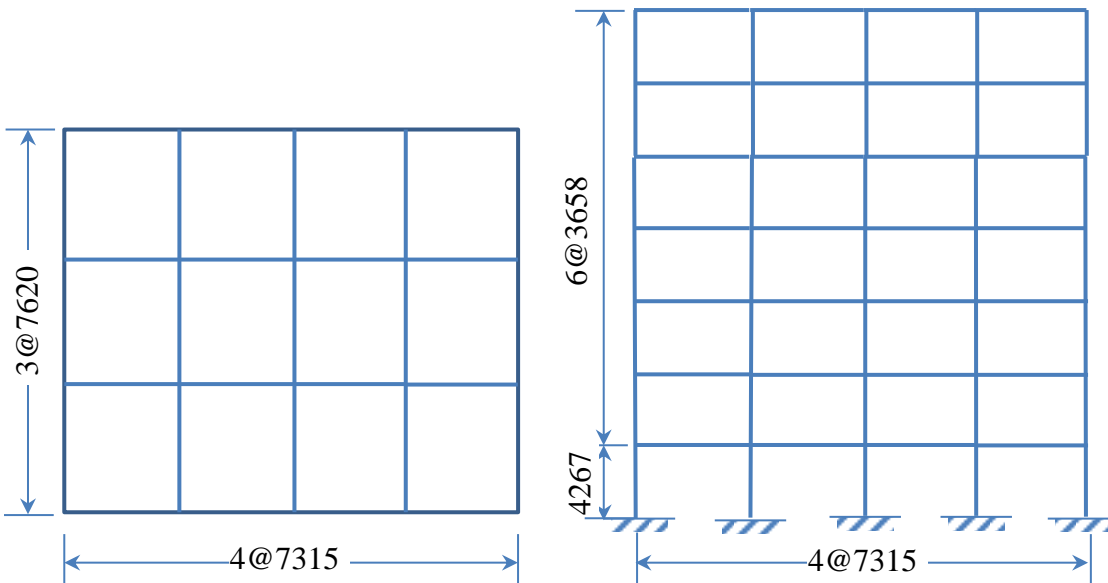
(a) Plan View

(b) Elevation View

Summary of Frame Design Parameters

Floor	Weight (kN)	Design Load (kN)	Drift (cm)	Drift Limit (cm)
2nd	1566	9	1.40	1.44
3rd	1566	27	1.36	1.33
4th	1566	51	1.35	1.33
5th	1566	80	1.29	1.33
6th	1566	115	1.30	1.33
7th	1566	155	1.15	1.33
Roof	1212	154	0.66	1.33

Steel Beam Moment Strength and Demand

Floor	Beam	M_{ub} (kN-m)	M_{pb} (kN-m))
2nd	W24x76	461	718
3rd	W24x76	422	718
4th	W24x68	407	642
5th	W24x68	375	642
6th	W21x50	326	411
7th	W21x50	255	411
Roof	W21x50	145	411

Steel Column Strength and Demand

Floor	Column		M_{pc} (kN-m)		E_m ($\times 10^8$ kN/m^2)	
	Interior	Exterior	Interior	Exterior	Interior	Exterior
1st	W14x82 (508x559)	W12x58 (508x508)	1284	830	2.915	3.197
2nd	W14x82 (508x559)	W12x58 (508x508)	1284	830	2.915	3.197
3rd	W14x82 (508x559)	W12x58 (508x508)	1284	830	2.915	3.197
4th	W14x82 (508x559)	W12x58 (508x508)	1284	830	2.915	3.197
5th	W14x82 (508x559)	W12x58 (508x508)	1284	830	2.915	3.197
	W14x68 (508x559)	W12x45 (457x508)	1097	694	3.114	3.394
6th	W14x68 (508x559)	W12x45 (457x508)	1097	694	3.114	3.394
7th	W14x68 (508x559)	W12x45 (457x508)	1097	694	3.114	3.394

( ) is the SRC column dimension in millimeters

E_m Elastic modulus of composite section

265

C4. Nine-Story Composite Special Moment-Resisting Frame (all dimensions in mm)
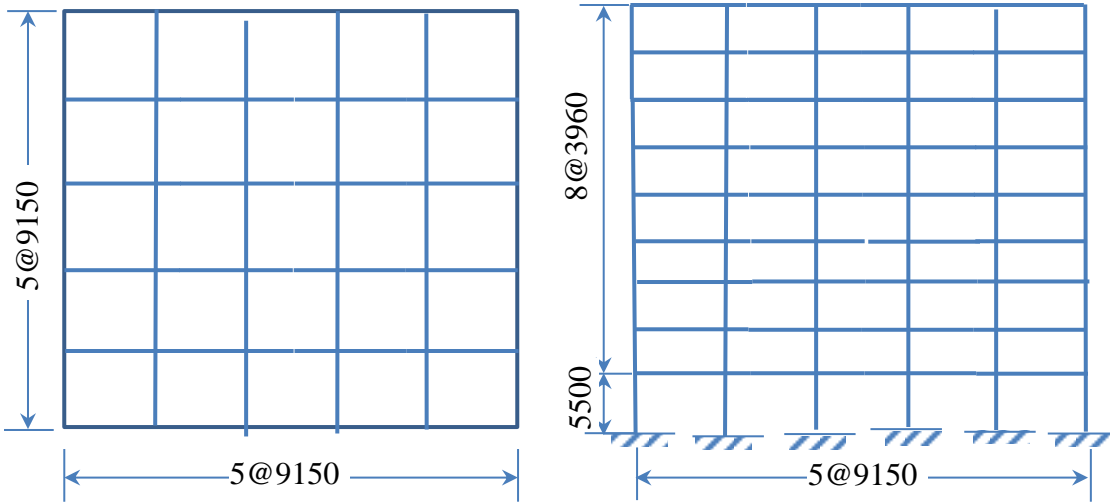
(a) Plan View (b) Elevation View

Summary of Frame Design Parameters

Floor	Weight (kN)	Design Load (kN)	Drift (cm)	Drift Limit (cm)
2nd	5053	21.92	1.71	2.0
3rd	5053	58.85	1.34	1.44
4th	5053	111.24	1.41	1.44
5th	5053	178.14	1.49	1.44
6th	5053	258.87	1.47	1.44
7th	5053	352.94	1.41	1.44
8th	5053	459.95	1.43	1.44
9th	5053	579.55	1.35	1.44
Roof	3790	533.6	0.94	1.44

Steel Beam Moment Strength and Demand

Floor	Beam	M_{ub} (kN-m)	M_{pb} (kN-m)
2nd	W36x160	1755	3470
3rd	W36x160	1742	3470
4th	W36x135	1707	2832
5th	W36x135	1642	2832
6th	W36x135	1537	2832
7th	W36x135	1384	2832
8th	W30x99	1176	1735
9th	W27x84	905	1357
Roof	W24x68	564	985

Steel Column Strength and Demand

Floor	Column		M_{pc} (kN-m)	
	Interior	Exterior	Interior	Exterior
1st	W14x500	W14x370	6836	4792
2nd	W14x500	W14x370	6836	4792
	W14x455		6094	
3rd	W14x455	W14x370	6094	4792
4th	W14x455	W14x370	6094	4792
	W14x370	W14x283	4792	3529
5th	W14x370	W14x283	4792	3529
6th	W14x370	W14x283	4792	3529
	W14x283	W14x257	3529	3171
7th	W14x283	W14x257	3529	3171
8th	W14x283	W14x257	3529	3171
	W14x257	W14x233	3171	2839
9th	W14x257	W14x233	3171	2839

REFERENCES

Abrahamson, N., and Silva, W., "*Summary of the Abrahamson & Silva NGA ground-motion relation,."* Earthquake Spectra, 2008, Vol. 24, No. 1, pp. 67-97

Akiyama H., "Earthquake-resistant limit state design for building". University of Tokyo Press, Tokyo, 1985

Arias, A., "*A Measure of the Earthquake Intensity in Seismic Design for Nuclear Power Plants"*, MIT Press: Cambridge, MA, (1970)

ASCE/SEI 7-10, "Minimum Design Loads for Building and Other Structures", ASCE Standard

Bazzurro, P., and Luco, N.,"*Damage Potential of Near-Source Ground Motion Records,"* Proceedings of the 8th US national Conference on Earthquake Engineering, Curran Associates, San Francisco,2006, pp. 5061-5070

BISPEC, Bispec version 2.03, www.eqsols.com, 2010

Boore, D. M., and Atkinson, G. M., *"Ground-motion Prediction Equations for the Average Horizontal Component of PGA, PGV, and 5%-Damped PSA at Spectral Periods between 0.01 s and 10.0 s,"* Earthquake Spectra, 2008, Vol. 24, No. 1, pp. 99-138

Bradley, B. A., *"Empirical Correlations Between Cumulative Absolute Velocity and Amplitude-Based Ground Motion Intensity Measures,"* Earthquake Spectra,2012, Vol.28, No.1, pp.37-54

Bruneau M., and Wang N., "*Some Aspects of Energy Methods for the Inelastic Seismic Response of Ductile SDOF Structures,"* Engineering Structures, 1996, Vol. 18, No.1, pp. 1-12

Campbell, K. W., & Bozorgnia, Y., *"A Ground Motion Prediction Equation for the Horizontal Component of Cumulative Absolute Velocity (CAV) Based on the PEER-NGA Strong Motion Database,"* Earthquake Spectra, 2012, Vol. 26, No. 3, pp. 635-650

Campbell, K. W., and Bozorgnia, Y., *"NGA ground motion model for the geometric mean horizontal component of PGA, PGV, PGD and 5% damped linear elastic response spectra for periods ranging from 0.01 to 10 s,"* Earthquake Spectra, 2008, Vol. 24, No.1, pp. 139-171

Campbell, K.W, *"Empirical Near-Source Attenuation Relationships for Horizontal and Vertical Components of Peak Ground Acceleration, Peak Ground Velocity and Pseudo-Absolute Acceleration Response Spectra,"* Seismological Research Letters, 1997, Vol. 68, No. 1, pp. 154-179

Chen, K., Liu, Z., & Shen, P., *"Study on the Effect of Ductility Coefficient on Input Energy Time Histories for Inelastic SDOF Systems,"* Journal of Earthquake Engineering and Engineering Vibration, 2010, Vol.6, No. 11

Chiou, B. J., and Youngs, R. R., *"An NGA Model for the Average Horizontal Component of Peak Ground Motion and Response Spectra,"* Earthquake Spectra, 2008, Vol. 24, No.1, pp. 173-215

Chopra, A. K., & Goel, R. K., *"Capacity-Demand-Diagram Methods Based on Inelastic Design Spectrum,"* Earthquake Spectra, (1999)., Vol. 15, No. 4, pp. 637-656

Decanini, L. D. and Mollaioli, F., *"Formulation of elastic earthquake input energy spectra"* Earthquake Engineering and Structural Dynamics, 1998: Vol. 27, No. 12, pp.1503-1522

Disque, Robert O., *"Applied Plastic Design in Steel"*, Van Nostrand Reinhold Company, 1971

EPRC, *"A Criterion for Determining Exceedance of the Operating Basis Earthquake,"* Electric Power Research Corporation, EPRC Report 2848-16., (1988)

Estes, K. R., and Anderson, J.C., *"Earthquake resistant design using hysteretic energy demands for low rise buildings,"* Proceeding of the 13th World Conference on Earthquake Engineering: Vancouver, B. C., Canada, 2004

Fajfar P., Vidic T., *"Consistent Inelastic Design Spectra: Hysteretic and Input Energy,"* Earthquake Engineering and Structural Dynamics, 1994, Vol.23: pp. 523-537

Fajfar, P., Vidic, T., and Fischinger, M., "*Seismic Design in Medium- and Long-Period Structures*," Earthquake Engineering and Structural Dynamics, 1989, Vol. 18, pp. 1133-1144.

FEMA 267A, "*Interim Guidelines Advisory No. 1*", USA Federal Emergency Management Agency, 1997

FEMA 350, "*Recommended Seismic Design Criteria for New Steel Moment-Frame Buildings*" USA Federal Emergency Management Agency, 200)

FEMA 356, "*Prestandard and Commentary for the Seismic Rehabilitation of Buildings*", USA Federal Emergency Management Agency, 2000

FEMA P695, "*Recommended Methodology for Quantification of Building System Performance and Response Parameters*", NEHRP (National Earthquake Hazards Reduction Program and Applied Technology Council: Redwood City, CA, 2009

Gazetas, G., "*Seismic Design of Foundations and Soil–Structure Interaction*," First European Conference on Earthquake Engineering and Seismology, Geneva, Switzerland, Sept. 2006

Hall, J. F., Heaton, T. H., Halling, M. W., and Wald, D. J., "*Near-Source Ground Motion and Its Effects on Flexible Buildings,*" Earthquake spectra, 1995, Vol. 11, No. 4, pp. 569-605

Hernandez-Montes, E., Kwon, O., and Aschheim, M. A., "*An Energy Based Formulation for First and Multiple Mode Nonlinear Static (Pushover) analysis,*" Journal of Earthquake Engineering, 2004, Vol. 8, No.1, pp. 69-88

Housner, G.W., "*Limit design of structures to resist earthquakes*," Proceedings of the 1st World Conference on Earthquake Engineering, California, USA, 1956, Vol. 5, pp. 1 – 13

IBC, ICC "*International Building Code*", International Code Council Inc., 2009

IBC, ICC. "*International Building Code*", International Code Council, 2012

Inel, M., Aschheim, M. A., & Abrams, D. P., "*An Agorithm for Computing Isoductile Response Spectra,*" Journal of Earthquake Engineering, 2002, Vol. 6, No. 3, pp. 375-390

Khashaee, *"Energy–Based Seismic Design and Damage Assessment for Structures"*, PhD dissertation, Southern Methodist University, Dallas, Texas, 2004, 266 pages

Kuwamura, H., and Galambos, T.V., *"Earthquake Load for Structural reliability"*, Journal of Structural Engineering, ASCE, 1989; Vol. 115, No. 6, pp. 1446-1462

Lieping Ye, Guanggyu Cheng, and Xhe Qu., "*Study on energy based seismic design method and the application for steel braced frame structures*", Sixth International Conference on Urban Earthquake Engineering, Tokyo Institute of Technology, Tokyo, Japan, 2009; pp. 417-428

Luco, J. E., *"Linear Soil-Structure Interaction: A Review,"* Earthquake Ground Motion and its Effects on Structures, ASME, AMD, 1982, Vol. 53, pp. 41-57

Manfredi, Gaetano, "*Evaluation of Seismic Energy Demand*," Earthquake Engineering and Structural Dynamics, 2001; Vol. 30, pp. 485-499

Manoukas G., Athannatopoulou A., and Avramidis, I.,*"Static Pushover Analysis Based on Energy Equivalent SDOF System,"* Earthquake Spectra, 2011, Vol. 27, No. 1, pp. 89-105

Nakashima, M., Saburi, K., and Tsuji, B., "*Energy input and dissipation behavior of Structures with Hysteretic Dampers*," Earthquake Engineering and Structural Dynamics, 1996; Vol. 19, No.1: pp. 77-90

Park, Y. and Ang, A., *"Mechanistic Seismic Damage Model for Reinforced Concrete,"* Journal of Structural Engineering, 1985, Vol. 111, No. 4, pp. 722-739

PEER (Pacific Earthquake Engineering Research Center), Nov. 2011 Beta version Data Base, http://peer.berkeley.edu/peer_ground_motion_database,

Peng, B. F., & Conte, J. P*.," Statistical Insight into Constant-Ductility Design using a Non-Stationary Earthquake Ground Motion Model,"* Earthquake engineering & structural dynamics, 1997, Vol. 26, No.9, pp. 895-916

Poland, C., Sougles, J., Sun, J., and Mejia, L., *"Quantifying the Effect of Soil-Structure Interaction for Use in Building Design"*, California Division of Mines and Geology, Office of Strong Motion Studies, 2000

Power, M., Chiou, B., Abrahamson, N., Bozorgnia, Y., Shantz, T., & Roblee, C., *"An Overview of the NGA Project,"* Earthquake Spectra, 2008, Vol. 24, No. 1, pp. 3-21

Prasanth, T, Siddhartha G, and Kevin R. C., "*Estimation of Hysteretic Energy Demand using Concepts of Modal Pushover Analysis*," Earthquake Engineering & Structural Dynamics, 2008; Vol. 37, No. 6, pp. 975-990

Priestley, M.J.N., Calvi, G.M., and Kowalsky, M.J. *"Displacement-Based Seismic Design of Structures,"* IUSS Press, Pavia, 2007, 721 pages

Ramirez, O. M., Constantinou, M. C., Whittaker, A. S., Kircher, C. A., & Chrysostomou, C. Z. *"Elastic and Inelastic Seismic Response of Buildings with Damping Systems,"* Earthquake Spectra, (2002), Vol. 18, No. 3, pp. 531-547

Shen, J. and Akbas, B., "*Seismic Energy Demand in Steel Moment Frames*", Journal of Earthquake Engineering, 1999; Vol. 3, No. 4: pp. 519-559.

Smith, R.S.H. and Tso, W.K. *"Inconsistency of Force-Based Design Procedure,"* JSEE, 2002, Vol. 4, No.1, pp. 46-54

Spyrakos, C.C. and Vlassis, A.G., *"Effect of Soil-Structure Interaction on Seismically Isolated Bridges,"* Journal of Earthquake Engineering, 2002, Vol. 6, No. 3, pp. 391-429

Stewart, J. P., Fenves, G.L. and Seed, R. B., "*Seismic Soil-Structure Interaction in Buildings I: Analytical Methods,"* Journal of Geotechnical and Geoenvironmental Engineering., 1999, Vol. 125, No.1, pp. 26-37

Terapathana, S, *"An Energy method for Earthquake Resistant Design of RC Structures"*, PhD dissertation, University of Southern California, Los Angeles, CA, 2012, 211pages

Tongaonkar, N. P., and Jangid, R. S., *"Seismic Response of Isolated Bridges with Soil–Structure Interaction,"* Soil Dynamics and Earthquake Engineering, 2003, Vol. 23, No. 4, pp. 287-302

Trifunac, M.D., and Brady, A.G., "*A Study on the Duration of Strong Earthquake Ground Motion*," Bulletin of Seismological Society of America, 1975; Vol. 65, pp. 581-626

Uang, C.-M., and Bertero, V.V., "Evaluation of Seismic Energy in Structures", Earthquake Engineering and Structural Dynamics, 1990; Vol.19, No.1, pp. 77-90

UBC, *"Uniform Building Code,"* International Conference of Building Officials, (1997)

Wang, Feng, and Tinghua Yi., "*A Methodology for Estimating Seismic Hysteretic Energy of Buildings.*" In Civil Engineering and Urban Planning 2012, pp. 17-21. ASCE, 2012.

Zhai, C., and Lili Xie. "*Constant-Ductility Strength Demand Spectra for Seismic Design of Structures.*" Earthquake Engineering and Engineering Vibration,2005; Vol. 4, No. 2, pp 243-250.

VITA

Name: Mebrahtom Gebrekirstos Mezgebo

Date and Place of Birth: June 18, 1979, Bizet, Tigray, Ethiopia

Education:

- B. Sc., Civil Engineering July 2000, Addis Ababa University, Addis Ababa, Ethiopia
- M. Tech., Civil Engineering August 2004, Indian Institute of Technology Bombay, India

Academic Experience:

- Lecturer, July 2000-July 2002 and Sep. 2004 – June 2008, Department of Civil Engineering, Mekelle University, Ethiopia
- Teaching Assistant, August 2008 –December 2012, Department of Civil and Environmental Engineering, Syracuse University, Syracuse New York.

Professional Experience:

- Structural Designer, Jan 2013-Present, Michael Baker International, Hamilton New Jersey.
- Part time Structural Engineer, Sept 2004 – June 2008, Net Consult Plc and Ahadu Consult Plc, Mekelle, Ethiopia

Honor and Awards

- Nominated for Civil & Environmental Engineering Outstanding Achievement Award in Graduate Study, May 2015
- Outstanding Teaching Assistant, Syracuse University, April 2012
- Tuition Scholarship, August 2008- May 2013, Department of Civil and Environmental Engineering, Syracuse University.
- Best Academic Staff award , Mekelle University, Ethiopia, August 2007
- Government of Ethiopia Scholarship for students to study a Master's Degree, July 2002- July 2004, Indian Institute of Technology Bombay, India
- Class Topper, B. Sc. Civil Engineering Graduates, Addis Ababa University, Ethiopia, July 2000
- Best Performer of All Civil Engineering Students, Addis Ababa University, Ethiopia, February 1998